Study of the environment of comet 67P/Churyumov-Gerasimenko based on the data of ROSINA/RTOF onboard the Rosetta mission.

Margaux Hoang

To cite this version:

Margaux Hoang. Study of the environment of comet 67P/Churyumov-Gerasimenko based on the data of ROSINA/RTOF onboard the Rosetta mission.. Astrophysics [astro-ph]. Université toulouse 3 Paul Sabatier, 2018. English. NNT : . tel-02268406

HAL Id: tel-02268406
https://theses.hal.science/tel-02268406

Submitted on 20 Aug 2019

THÈSE

En vue de l'obtention du

DOCTORAT DE L'UNIVERSITÉ DE TOULOUSE

Délivré par : *l'Université Toulouse 3 Paul Sabatier (UT3 Paul Sabatier)*

Présentée et soutenue le *12/10/2018* **par :**

Margaux HOANG

Étude de la coma de la comète 67P/Churyumov-Gerasimenko à l'aide des données de l'instrument ROSINA/RTOF à bord de la mission spatiale Rosetta.

JURY

Henri REME	Professeur émérite	Président du Jury
Philippe GARNIER	Maître de conférence	Membre du Jury
Jérémie LASUE	Astronome adjoint	Membre du Jury
Dominique BOCKELEE-MORVAN	Directrice de recherche	Membre du Jury
Valérie CIARLETTI	Professeure	Membre du Jury
Nicolas BIVER	Chargé de recherche	Membre du Jury
Anny-Chantal LEVASSEUR-REGOURD	Professeure émérite	Membre du Jury

---

École doctorale et spécialité :
SDU2E : Astrophysique, Sciences de l'Espace, Planétologie
Unité de Recherche :
Institut de Recherche en Astrophysique et Planétologie (UMR 5277)
Directeur(s) de Thèse :
Philippe GARNIER et *Jérémie LASUE*
Rapporteurs :
Dominique BOCKELEE-MORVAN et *Valérie CIARLETTI*

Le travail présenté dans cette thèse a été réalisé à l'Institut de Recherche en Astrophysique et Planétologie de Toulouse, et encadré par Philippe Garnier et Jérémie Lasue, mes directeurs de thèse, que je remercie ici sincèrement. Je remercie également Henri, Dominique, Arnaud, ainsi que Benoît, Josette, Dorine, Henda et toutes les personnes du laboratoire qui m'ont aidée et soutenue durant ces trois ans.

Je remercie l'équipe ROSINA du Center for Space and Habitability de l'Université de Bern, en particulier Sébastien Gasc, Kathrin Altwegg et Martin Rubin. Je remercie également Maria Teresa Capria de l'Istituto Naziolane di Astrofisica de Rome.

Je remercie Dominique Bockelée-Morvan et Valérie Ciarletti d'avoir accepté d'être rapportrices de ma thèse, ainsi que Nicolas Biver et Anny-Chantal Levasseur-Regourd d'avoir fait partie de mon jury.

Enfin, cette aventure m'a permise de rencontrer une pléiade de personnes exceptionnelles: Merci à Cricri, Gab, Jason, Marina, Zizi, Sinon, Sacha, Mathieu, Ilane, Victor, Tonio, Henda, Sophie, Rémi, Jacqueline et Gilbert.

Merci à mes parents, à Emma, Guillaume et May.

Far above the world
Planet Earth is blue
And there's nothing I can do

Major Tom (1947-2016)

Contents

I Comets: small icy bodies of the Solar System 1

List of Figures

Abstract

The comet 67P/Churyumov-Gerasimenko (67P/C-G) has been investigated by the Rosetta space mission over two years from August 2014 to September 2016. Onboard the spacecraft, the Rosetta Orbiter Spectrometer for Ion and Neutral Analysis (ROSINA) experiment included two mass spectrometers – Double Focusing Mass Spectrometer (DFMS) and Reflectron-type Time-Of-Flight mass spectrometer (RTOF) – to detect the composition of neutrals and ions, and a Comet Pressure Sensor (COPS) to monitor the density and velocity of neutrals in the coma. This thesis details an analysis and discussion of the data of the Reflectron-type Time-Of-Flight instrument during the comet escort phase. We analyse 67P/C-G's coma over the mission in terms of the main volatiles concentrations (H_2O, CO_2 and CO) and their ratios. The 2-years-long Rosetta mission allows us to observe the diurnal and seasonal variabilities in the atmosphere of 67P/C-G and the strong heterogeneities showed by the main volatiles. We study the correlation between the spectrometers' results to confirm the measurements consistency and compare the observations with predictions based on a Direct Simulation Monte Carlo (DSMC) model. We also study in details the influence of the illumination and the orbitography parameters. This analysis shows that the illumination conditions do not explain all the coma observations, revealing the presence of surface or sub-surface heterogoeneities. Therefore, we use a thermo-physical nucleus model applied to the case of 67P/C-G to investigate the physical processes occurring inside the nucleus and leading to complex coma observations, and interpret the measurements of RTOF in terms of nucleus structure and physical processes.

Résumé

La mission spatiale Rosetta a étudié la comète 67P/Churyumov-Gerasimenko (67P/C-G) pendant deux ans, d'août 2014 à septembre 2016. À bord de la sonde, l'expérience *Rosetta Orbiter for Ion and Neutral Analysis* (ROSINA) était composée de deux spectromètres de masse – *Double Focusing Mass Spectrometer* (DFMS) et *Reflectron-type Time-Of-Flight mass spectrometer* (RTOF) – pour étudier la composition des neutres et des ions présents dans la coma, et d'un senseur de pression – *Comet Pressure Sensor* (COPS) – pour mesurer la densité et la vitesse du gaz cométaire. Le travail présenté a pour objectif l'étude de la coma de la comète 67P/C-G grâce à l'analyse et l'interprètation des données de l'instrument RTOF, en particulier des mesures des principaux volatiles (H_2O, CO_2 et CO) et de leurs abondances relatives. Les mesures récoltées pendant les deux années de mission nous permettent d'étudier les variations diurnes et saisonnières de la coma de 67P/C-G et de mettre en évidence des hétérogénéités spatiales. Nous étudions la corrélation entre les résultats des deux spectromètres de ROSINA pour confirmer la cohérence des mesures, et comparons ensuite les données avec les prédictions d'un modèle Monte Carlo (Direct Simulation Monte Carlo, DSMC). De plus, nous étudions en détail l'influence des conditions d'illumination du noyau et des paramètres orbitaux. Cette analyse révèle que les conditions d'illumination n'expliquent pas en totalité les observations et suggère la présence d'hétérogénéités de surface ou sous-surface. Nous appliquons un modèle thermo-physique de noyau cométaire au cas de 67P/C-G pour étudier les processus physiques à l'intérieur du noyau responsable de la complexité des observations de la coma, et pour interpréter les mesures faites par RTOF en termes de structure du noyau et de processus physiques.

General introduction

The goal of the ESA's Rosetta mission has been the study of a comet, a small icy body evolving in our Solar System. Formed in the proto-planetary disk during the Solar System's formation, comets are believed to have spent most of their lifetime far from the Sun, avoiding transformations due to heating. Thus, comets are considered as the most primitive objects in our Solar System, and the cometary material is a key to investigate the chemical composition of the protosolar nebula and better understand the conditions that allowed life to appear on Earth. If ground-based observations and a few spacecraft's fly-bys brought elements of knowledge about comets, the Rosetta mission represents a major step in cometary exploration.

The Rosetta spacecraft and its lander Philae were launched in 2004 and arrived at their targeted comet 67P/Churyumov-Gerasimenko (67P/C-G) after ten years of travel. At close distance from the nucleus, Philae separated itself from Rosetta and, after a slow descent towards the surface, unexpectedly rebounded on the comet's surface and ended its landing in a poorly illuminated area. After almost 60 hours of operations, the internal batteries were emptied and the solar panels remained unable to produce the energy required to operate the instruments aboard the lander any longer. The Rosetta spacecraft investigated comet 67P/C-G over two years from August 2014 to September 2016, with eleven instruments on board. Among them, the ROSINA experiment included two mass spectrometers to derive the composition of neutrals and ions, and a COmet Pressure Sensor (COPS) to monitor the density and velocity of the neutrals in the coma. ROSINA's instruments combine high performances in term of mass resolution, sensitivity and temporal resolution and recorded an unprecedented amount of in-situ measurements of a coma. The Institut de Recherche en Astrophysique et Planétologie (IRAP) of Toulouse participated in the development of the ROSINA's Reflectron-type Time-of-Flight mass spectrometer (RTOF).

In this work, we achieve the calibration of the RTOF spectra and we propose an analysis and interpretation of the measurements of the coma's main volatiles: H_2O, CO_2 and CO through the two-years of mission. In addition to the study of in situ data, we investigated the interior of the nucleus with a thermo-physical model applied to the case of 67P/C-G to constrain its nucleus' properties.

To cover the different aspects of the thesis, this manuscript is structured in four parts.

In the first one, we briefly describe the actual knowledge about comets, as well as the previous space missions and the Rosetta mission. Chapter 1 gives an overview of the history of the comets' studies, details their origin, classification and structure (nucleus, coma and tails), as well as the observation of comets before the Rosetta mission. As the cometary coma and nucleus will be the center of the study proposed in Part III and Part IV, we detail our knowledge of those two elements before the Rosetta mission in Chapter

2. Chapter 3 presents the Rosetta mission, its target the comet 67P/C-G, its on-board instruments and its trajectory, and summarises the main scientific results obtained.

The second part focuses on the Rosetta Orbiter Spectrometer for Ion and Neutral Analysis (ROSINA) and the data analysis used for the study of the Reflectron-type Time-Of-Flight mass spectrometer (RTOF)'s spectra. Chapter 4 gives a presentation of the experiment and its performances, an introduction to mass spectroscopy, as well as a description of the three ROSINA instruments, in particular the operating principle and modes and the in-flight performances of RTOF. Chapter 5 details the different steps of the spectral analysis: the RTOF raw spectra, the correction applied, the mass calibration and the conversion from the counts measured inside the instrument to species' densities.

The third part of this work is the study of the heterogeneous coma of 67P/Churyumov-Gerasimenko seen by ROSINA/RTOF. Chapter 6 presents the orbitography parameters, in particular the comet-spacecraft distance, the heliocentric distance, the sub-spacecraft point coordinates and the nadir off-pointing, which largely influence the RTOF detections. Chapter 7 studies the global dynamics of the three main volatiles, H_2O, CO_2 and CO and the influence of the orbitography parameters. The strong seasonal variations, due to the inclination of the spin of the nucleus, are analysed through the densities of the three volatiles and their relative ratios. The chapter 8 investigates the coma and possibly surface/sub-surface heterogeneities, by presenting 2D latitude-longitude maps of the illumination of the nucleus at different heliocentric distances and 2D maps of densities for the three main volatiles as seen by RTOF. Chapter 9 and 10 show respectively a comparison between the RTOF results with the other instruments of ROSINA and with a Direct Simulation Monte Carlo model applied to the case of 67P/C-G.

The fourth part is dedicated to the modeling of the nucleus with a thermo-physical model to interpret the observations. In chapter 11, we describe the actual model and some previous studies, and our application of the model. In chapter 12, we study the evolution of the temperatures at different depths, of the internal structure and of the fluxes of the main species at different positions on the orbit and for different initial parameters. In particular, we discuss the variations in outgassing rates based on changes of an initial dust layer in the northern hemisphere, of the presence of CO trapped in the amorphous ice and of the initial CO_2/H_2O and CO/H_2O ratios. The chapter 13 presents 2D and 3D visualisations of fluxes for the three volatiles and compares them to fluxes derived from RTOF data to constrain several properties of the comet nucleus.

Finally, this thesis work is briefly resumed in a final conclusion.

Introduction générale

La mission Rosetta (ESA) a eu pour objectif l'étude d'une comète, un petit corps glacé de notre système solaire. Formées dans le disque proto-planétaire lors de la formation du système solaire, les comètes évoluent la plupart du temps loin du soleil, à l'abri des hausses de température pouvant altérer sa composition. Par conséquent, elles sont considérées comme les objets les plus primitifs du système solaire, et l'étude de leur composition nous permet d'approcher la composition de la nébuleuse proto-planétaire et de mieux comprendre les conditions d'apparition de la vie sur Terre. Les observations de comètes faites depuis le sol, ainsi que les quelques survols réalisés par des sondes spatiales, ont permis d'améliorer nos connaissances des comètes. Cependant, la mission Rosetta représente une étape sans précédent dans l'exploration cométaire.

La sonde Rosetta et l'atterrisseur Philae ont été lancés en 2004 et ont atteint leur cible, la comète 67P/Churyumov-Gerasimenko (67P/C-G), après un voyage long de dix ans. Arrivé près du noyau cométaire, Philae s'est détaché de Rosetta, a opéré une lente descente vers la surface, où il a rebondi à plusieurs reprises avant de terminer sa course dans une zone peu illuminée. Après quelques 60 heures d'opération, les batteries internes de l'atterrisseur étaient déchargées et les panneaux solaires n'ont pas été capable de produire l'énergie nécessaire à la suite des opérations. La sonde Rosetta a étudié, à l'aide de ses onze instruments, la comète 67P/C-G pendant deux ans, d'août 2014 à septembre 2016. À bord de la sonde, l'expérience ROSINA (pour *Rosetta Orbiter Spectrometer for Ion and Neutral Analysis*) était composée de deux spectromètres de masse pour étudier la composition des neutres et des ions, et d'un senseur de pression pour analyser la densité et la vitesse du gaz cométaire. Ces trois instruments ont permis à ROSINA de combiner de hautes performances en termes de résolution massique, de sensibilité et de résolution temporelle. L'expérience ROSINA a récolté un nombre sans précédent de données in situ. L'Institut de Recherche en Astrophysique et Planétologie (IRAP) de Toulouse a participé au développement du spectromètre de masse RTOF (pour *Reflectron-type Time-Of-Flight*) de l'expérience ROSINA.

Durant cette thèse, nous avons calibré les spectres enregistrés par RTOF dans la coma de 67P/C-G, et présentons l'analyse et l'interprétation des mesures des principaux volatiles (H_2O, CO_2 and CO), et de leur évolution durant les deux années de mission. En plus de l'étude des données in situ, nous avons simuler l'intérieur du noyau cométaire à l'aide d'un modèle thermo-physique appliqué au cas de 67P/C-G pour contraindre les propriétés de son noyau.

Pour parcourir les différents aspects de cette thèse, ce manuscrit est structuré en quatre parties.

Dans la première partie, nous résumons brièvement nos connaissances actuelles des comètes et présentons les missions spatiales cométaires, en particulier la mission Rosetta.

Le chapitre 1 parcourt l'étude des comètes dans l'histoire, détaille l'origine des comètes, leur classification et leur structure (le noyau, la coma et les queues), et présente les observations cométaires avant la mission Rosetta. Le chapitre 2 décrit en détails nos connaissances concernant la coma et le noyau, qui constitueront le centre d'intérêt de notre travail dans les parties III et IV. Le chapitre 3 présente la mission Rosetta, sa cible (la comète 67P/C-G), ses instruments, sa trajectoire, ainsi qu'un résumé des principaux résultats scientifiques obtenus.

La seconde partie décrit l'expérience ROSINA et la méthode d'analyse des données utilisée pour l'étude des spectres de l'instrument ROSINA/RTOF. Le chapitre 4 présente l'expérience et ses performances techniques, une introduction à la spectrométrie de masse, et une description des trois instruments de ROSINA, en particulier le principe de fonctionnement de RTOF, ses modes opérationnels et ses performances de vol. Dans le chapitre 5, nous détaillons les étapes de l'analyse des spectres: la description des spectres bruts, les diverses corrections, la calibration de masse et la conversion des coups mesurés par l'instrument en densités d'espèces volatiles.

La troisième partie concerne l'étude de la coma de 67P/Churyumov-Gerasimenko et de ses hétérogénéités, mesurées par RTOF. Le chapitre 6 présente les paramètres orbitaux qui influencent les détections de RTOF et leurs variations, notamment la distance entre la comète et la sonde, la distance héliocentrique, les coordonnées géographiques de la sonde dans le repère cométaire et le nadir off-pointing. Le chapitre 7 étudie la dynamique globale des principaux volatiles: H_2O, CO_2 and CO et l'influence des paramètres orbitaux. L'analyse des variations de densités des espèces et de leurs abondances relatives révèle d'importantes variations saisonnières, dues à l'inclinaison de l'axe de rotation du noyau. Le chapitre 8 analyse la coma et les éventuelles hétérogénéités en surface et en sous-surface, en présentant des cartes 2D latitude-longitude de l'illumination du noyau à différentes positions sur l'orbite, ainsi que des cartes 2D de densités des trois volatiles principaux. Les chapitres 9 et 10 montrent respectivement une comparaison des résultats de RTOF avec les résultats des autres instruments de ROSINA et avec les prédictions d'un modèle de simulation Monte Carlo appliqué au cas de 67P/C-G.

La quatrième et dernière partie de ce manuscrit est dédiée à la modélisation du noyau cométaire grâce à un modèle thermo-physique dans le but d'interpréter les observations in situ de RTOF. Le chapitre 11 décrit le modèle de noyau et les détails de notre utilisation du modèle. Dans le chapitre 12, nous étudions l'évolution des températures à différentes profondeurs à l'intérieur du noyau, la structure interne et les flux des volatiles principaux, et ce, à différentes distances héliocentriques et pour différents paramètres initiaux. Plus spécifiquement, nous discutons des variations des taux de dégazages en fonction de l'épaisseur d'une couche de poussière recouvrant l'hémisphère nord, de la présence de CO piégé dans la glace amorphe et de différentes valeurs pour les rapports CO_2/H_2O et CO/H_2O. Dans le chapitre 13, nous présentons des visualisations en 2D et 3D des flux des trois volatiles et les comparons aux flux estimés à partir des données RTOF pour contraindre certaines propriétés du noyau cométaire.

Une conclusion finale vient enfin clore le travail réalisé durant cette thèse.

Part I

Comets: small icy bodies of the Solar System

Chapter 1

From naked-eye observation to in situ measurements

In this first chapter, we present an overview of the general knowledge about comets. We start with the observations and descriptions of comets through History. Then, we describe a scenario of formation of our Solar System to explain the origin of comets, their location and why studying comets is important for the comprehension of the Solar System and Earth's history. We detail the comet's types and classification defined by the International Astronomical Union (IAU), and the structure of a comet (nucleus, coma and tails). We then present the previous space missions targeting comets and their main results.

1.1 Observations through the ages

For ages, a spectacular phenomenon has been observed with fascination and anxiety. Once in a while, unpredictable bright stars with tails appeared in the night sky, sometimes shined for days or months and finally faded away. The imagination of observers associated those apparitions to various interpretations, which supported thoughts and beliefs, augured bad omens or important changes. We summarise the comet's observations through history which were detailed in Brandt and Chapman (2004).

These mysterious objects were named *comets*. This English name came from the Latin *cometa*, which came from the greek *kometes*, and literally means *long-hair star*. Before the use of telescopes, one observer on Earth could only detect a comet close to the Sun, when it developed a huge bright cometary tail, visible with the naked-eye. At the time, astronomers reported precisely their observations, but they only had assumptions concerning the nature, the size, the orbit or the origin of those bodies.

Until the Renaissance period, following a suggestion of the greek scientist and philosopher Aristotle (384 BC - 322 BC), comets were generally considered to be closer than the Moon, suggesting they were atmospheric events. In 1577, Tycho Brahe (1546 - 1601), a Danish astronomer, observed precisely the trajectory of comet C/1577 V1 (i.e. The Great Comet of 1577), relative to the Moon and stars by triangulation. His calculations lead to the conclusion that this comet was located much further than the distance to the Moon. He suggested that comets orbited around the Sun in circular trajectories, in a helio-geocentric system, where the Moon and the Sun orbit the Earth and the other planets orbit the Sun (Brahe, 1602).

Finally, the periodicity of these small objects was proved by Edmond Halley (1656 - 1742) in *A synopsis of the astronomy of comets*, published in 1705. Born in 1656, this English scientist studied tables of orbital parameters of comets and realized the similarity between the values obtained for three observations, in 1531, 1607, and 1682. Halley used Newton's theory (later published in 1687 in *Philosophiae naturalis principia of mathematica*) to calculate the orbital parameters of historical comets and discovered that three reported observations described the same object with a periodicity of about 76 years. He predicted the return of the comet, which appeared in the Christmas night of 1758 and became the most famous comet in history. This brought an additional proof of Newton's gravitational theory and the comet was named Halley. This discovery changed completely the study of comets and allowed scientists to tentatively connect the old observations with the more recent ones.

Comets were well described and represented in the literature and arts. Their apparitions were often linked to mythological, religious or historical scenes. Figure 1.1 shows a part of the Bayeux embroideries (a tapestry of 70 m long dating back to the 11th century), which represents men observing a passage of Halley's comet during the Hastings battle in 1066, six centuries before the birth of Halley.

In the 19th century, study of comets benefited from the developments of astrophysics, in particular polarimetry (Arago, 1843) and spectroscopy (Donati, 1858; Huggins, 1868). The modern era in cometary science began in the 1950s, when Fred Whipple predicted the existence of the cometary nucleus and first described it with the model of icy conglomerate, which will be further detailed in Section 2.2.1.

Figure 1.1: Representation of the Halley's comet passage of 1066 in a part of the Bayeux embroideries where the text says: *Isti mirant stella*, Those men wonder at the star (1070) (Archeurope Educational Resources, 2018).

1.2 Origin of comets and their importance

To investigate the origin of comets, we summarise the classical theory of formation of the Solar System (see Armitage (2010) and De Pater and Lissauer (2015) for a detailed introduction). The starting point of the Solar System formation happened about 4.6 billion years ago. An interstellar molecular cloud called the *protosolar nebula* (PSN) was disturbed by an important perturbation, probably the explosion of a supernova (Cameron and Truran, 1977). The explosion's resulting shock wave initiated irreversible perturbations of the nebula, starting with the collapse of the cloud and the associated acceleration of the rotation speed which induced a flattening of the cloud by conservation of momentum. Inside, the temperature and the density increased considerably, in particular in the center of the disk, where the condensation of the matter lead to the birth of a proto-star. The interaction between gas and dust implies that the dust settled in a very thin plane (smaller than the disk) and started the hierarchical accretion, i.e. small interstellar particle of about 10-100 nm accreted into cm-size and larger aggregates (Rietmeijer, 1998, 2002).

The largest bodies are called *planetesimals*. They gravitationally draw the surrounding materials and continued to grow. When their diameter reached hundreds of kilometers, planetesimals became proto-planets which have evolved in one of the eight *planets* of our Solar System, Mercury, Venus, Mars or the Earth, the four terrestrials planets, or Jupiter, Saturn, Uranus or Neptune, the four Giant gaseous planets. The planets were formed rapidly, in about 10 million years (Yin et al., 2002). In the center of the disk, the proto-star started the nuclear fusion of hydrogen and became the Sun. At this time, the disk remained full of debris, and the planets were the targets of intense bombardments which cleaned the Solar System of a fraction of the small bodies. The remaining bodies became the comets, asteroids, moons and dwarf planets located in various reservoirs in the Solar System. As the temperature decreases with the distance to the Sun, small bodies formed at a distance where the temperature will aggregate dust and solid ice became the icy small bodies of the Solar System.

The Grand Tack is an hypothesis proposed by Walsh et al. (2011), based on hydrodynamical simulations of a protoplanetary disk, simulating the migration of planets. They suggested that Jupiter was formed around 3 - 4 AU[1] from the Sun and migrated inward, followed by Saturn. Around 1.5 AU, Jupiter was captured in resonance with the orbit of Saturn, whose period corresponds exactly to 3/2 that of Jupiter. The mean motion resonance reversed their directions of migration and the two giant planets migrated outward, beyond 5.5 AU. As a consequence, the main asteroid belt was depleted of bodies and Neptune and Uranus moved outward. After the Grand Tack, the four giant planets were in a compact configuration, in resonant nearly circular orbits. A scenario of the evolution of this configuration is given by the Nice Model, described in a series of papers (Morbidelli et al., 2005; Tsiganis et al., 2005; Gomes et al., 2005; Morbidelli et al., 2007). They suggested the presence of a massive disk of icy planetesimals, located further than the giant planets. After about 600 million years, the cumulative gravitational interactions between the planets and the disk perturbed the resonant configuration and destabilised the entire planetary system. In particular, a close encounter between Jupiter and Saturn provoked a shift of Uranus and Neptune, which moved much further than their previous

---

[1] AU for astronomical unit, equals to the average Sun-Earth distance, i.e. about 150.10^9 km

orbits, to their current orbits. The two giant planets were propelled far from their initial position, inside the planetesimal disk. They induced a scattering of the small icy bodies, which were ejected in the outer Solar System or injected in the inner Solar System. Those small bodies impacted intensely the terrestrial planets during this period which is called the Late Heavy Bombardment (LHB). This probably explains the apparent simultaneous formation of impact basins on the Moon, Mars and Mercury (Morbidelli et al., 2001). The dynamical history of the Solar System described above is illustrated in Figure 1.2 from DeMeo and Carry (2014).

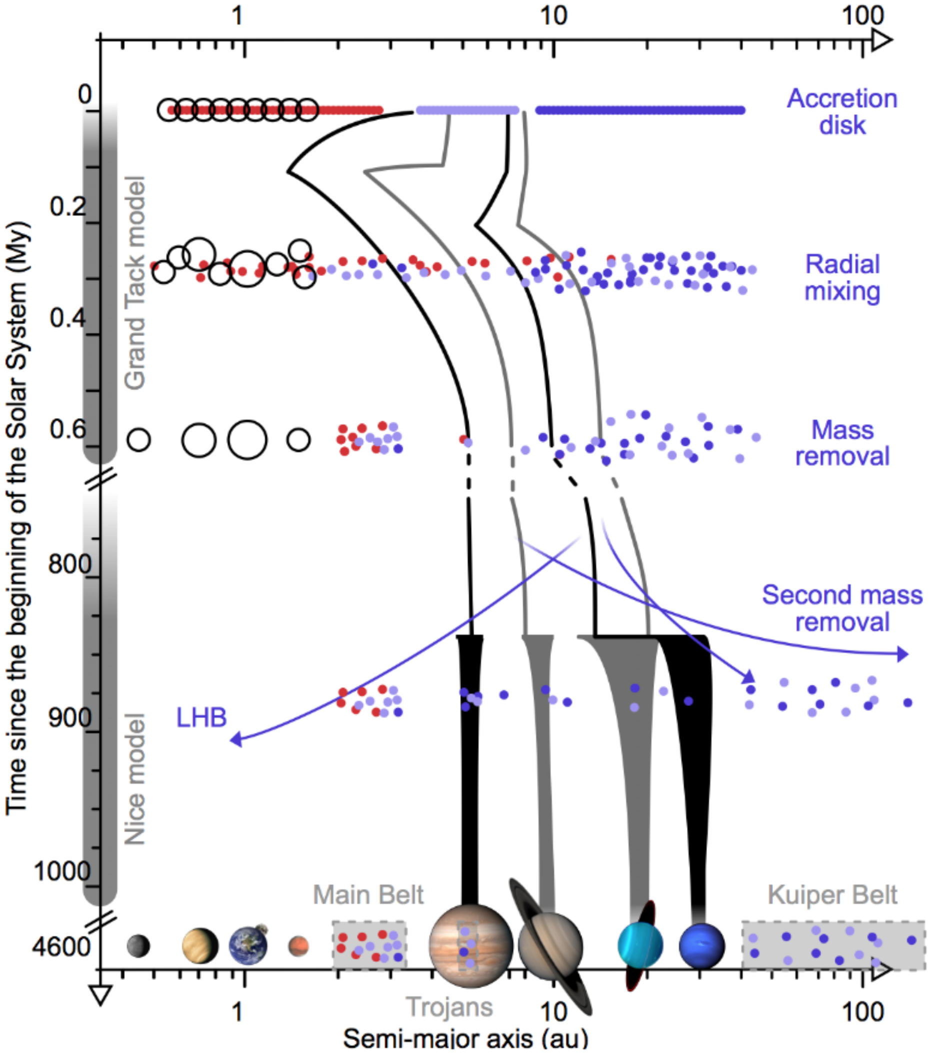

Figure 1.2: Representation of the planetary migration and their effect on the small bodies of the Solar System, as described by the Grand Tack and the Nice model (DeMeo and Carry, 2014).

Small bodies of the Solar System are located in different regions of the Solar System, as seen in Figure 1.3:

- The Main Belt or Asteroid Belt is situated between the orbit of Mars and Jupiter, with a semi-major axis ranging from 1.7 - 4.5 AU. The space mission Dawn explored the asteroids (1) Ceres (the largest object of the Main Belt, with a diameter of 946 km) and (4) Vesta (530 m of diameter).

- The Kuiper Belt, or Edgeworth-Kuiper belt, is located beyond Neptune's orbit, between 30 to 50 AU, and contains small bodies and dwarf planets (including Pluto). It was predicted by Edgeworth (1943) and named after Gerard Kuiper, who suggested the existence of small bodies beyond Pluto but actually rejected the presence of the Kuiper belt at its actual position, due to the presence of Pluto (Hynek, 1952). Except Pluto and Charon, respectively detected in 1930 and 1978, the first two objects of the Kuiper belt were discovered in 1992 by Jewitt et al. (1992) and Luu et al. (1993). Two distinct populations of Kuiper belt objects have been described by Tegler and Romanishin (1998), based on the surface color of the objects, the reddest object and the object slightly redder than the Sun. The populations are recognized today as dynamically hot and dynamically cold, and we expect the hot population to have been emplaced by the Late Heavy Bombardment event. In addition to the difference of surface color, the objects of the two populations have different physical properties, such as albedo, inclination and eccentricity.

- The Oort Cloud is an hypothetical reservoir of icy bodies inferred from the distribution of semi-major axis of long period comets (Oort et al., 1950). They described it as a large shell-shaped structure extending up to the limit of our Solar System (from 50 000 to 150 000 AU, i.e. 0.8 to 2.4-light years).

- Minor other groups of small bodies circulate in the Solar System. The Jupiter Trojans are on the orbit of Jupiter, at the Lagrangian points, the Hilda asteroids are situated between the asteroid belt and Jupiter, on a 3:2 orbital resonance with Jupiter (Armitage, 2010).

- The Scattered Disk contains icy objects with large range of eccentricities and inclinations (Duncan and Levison, 1997). It extends from beyond the Kuiper belt up to hundreds of AU.

The Kuiper Belt and the Oort Cloud are the two largest reservoirs of icy bodies. Some of them were injected into the inner Solar System, probably because of a gravitational perturbation, and became detectable from Earth due to their activity and became comets.

Figure 1.3: Schematic of the Solar System, showing the Main Asteroid Belt (between the orbits of Mars and Jupiter), the Kuiper belt (from 30 to 50 AU from the Sun) and the Oort cloud (up to 50 000-100 000 AU). Modified from an illustration from Schwamb (2014).

1.3 Interest of the cometary science

The study of comets is motivated by several reasons. One of them is the possibility to look back in the past of our Solar System. Comets are formed from the most pristine material of the protosolar disk (since they did not become larger bodies), and they spent most of their lifetime far from the Sun, too far to be affected by solar temperature. The comets' current composition should be very close to their original composition. Thus, comets are among the most pristine objects of the Solar System and their study may reveal important missing clues on the conditions of planets' formation and on the composition of our planetary system. The study of the initial composition of the nucleus is the ultimate goal to investigate those issues. The in situ data and remote sensing observations recorded by instruments can only access the coma composition. The composition and relative abundance of the coma can however be very different from those inside the nucleus, due to molecular dissociation, dust fragmentation, chemical processes, etc., as described later in Section 2.1.2. The presence of specific molecules, abundances and isotopic ratios can give clues to the origin and formation process of the nucleus.

Another reason concerns the Earth, its oceans and the origin of life. During the formation of the Solar System, the young planets have been intensely heated by impacts from small bodies, including comets, which should have removed most of the primitive volatile inventory of the Earth (including water) (Raymond et al., 2004; Morbidelli et al., 2012). It is then probable that later impacts from comets brought some materials to the Earth. Since they contain a large amount of water -D/H ratio have been in situ measured in comet Halley by the spacecraft Giotto (Balsiger et al., 1995; Eberhardt et al., 1995)- and organic molecules, comets' input on the surface of young Earth could help form oceans. As far as we know, life on Earth began in the oceans and comets could have brought pre-biotic materials in the form of complex molecules. Two other possibilities are considered for the origin of terrestrial water: 1) the gravitational capture of an hydrogen-rich atmosphere of nebular gas at the end of Earth's formation (Ikoma and Genda, 2006); 2) the delivery of water by water-rich bodies (like C-type asteroids) from the outer asteroid belt during the formation of the planets (Lunine et al., 2007; Raymond et al., 2007).

1.4 Comet types and classification

Different classifications exist to determine the different types of comets. The most commonly used are the dynamical classifications, that order comets according to their orbits. One of them is the one proposed by Levison (1996). When a comet achieves an orbit around the Sun in less than 200 years, it is referred to as a *short-period comet*. A period of revolution higher than 200 years characterizes a *long-period comet*, which probably comes from the Oort Cloud. In this category, we distinguish the new (incoming) ones and the returning ones.

The short-period comets are divided in two groups: Jupiter family comets and Halley-type comets. Jupiter family comets have periods of less than 20 years, a flat inclination (up to 30 deg) and a prograde orbit. These are strongly affected by Jupiter's gravitational influence and are supposed to come from the Kuiper Belt. Halley-type comets have more inclined orbits (up to more than 90 deg) with larger periods between 20 to 200 years. Their orbit suggested that they were initially long-period comet.

Observed comets are officially named following three information. The name contains: a number, the number of named comets since the first discovered comet or the date of discovery; a letter, for the type of comet (P/ for periodic comet, C/ for non-periodic, D/ for disappeared comet and X/ for the others). Finally, the name of the discoverer is often associated. For example: 1P/Halley is the first named comet, its orbit is periodic and has been discovered by Halley.

Since 1995, the International Astronomical Union (IAU)'s Minor Planet Center (The International Astronomical Union, 2018) approved a new nomenclature, which contains the information of the nomenclature above cited, with a few added information. The name contains: a letter for the type of comet, the year of discovery, a letter for the half-month of the discovery (A for the first half of January, B for the second half, C for the first half of February, etc.), a number for the order of discovery during the same half-month and finally the name of the discoverer. For example: C/1995 O1 Hale-Bopp is a long-period comet discovered in 1995, in the second half of July by Alan Hale and Thomas Bopp.

Comets receive a permanent number and are named by the IAU's Minor Planet Center after their second apparition. The new discoveries are announced through the website of the Central Bureau for Astronomical Telegrams (Harvard University, 2018).

1.5 Structure

Comets are composed of: a solid nucleus (up to $\sim$ 10 km), a coma ($\sim$ 10 000 km, which can be compared to an extended tenuous atmosphere), and tails ($\sim 10^6$ km), as indicated in Figure 1.4. As this thesis deals exclusively with the nucleus and the coma, these will be described in details in Chapter 2, after a brief description below.

1.5.1 Nucleus

The idea of a solid nucleus was predicted by Whipple (1950) (in a model detailed in Section 2.2.1) and confirmed in 1986 with the mission to 1P/Halley (see Section 1.6).

The cometary nucleus is typically a few kilometers long object, composed of ices and dust. Most of the time, comets evolve far from the Sun on elliptical orbits where they remain quiet, with no activity, thus the nucleus is difficult to detect by ground-based observations. When the comet approaches the Sun, the solar illumination heats the surface of the nucleus. Its activity starts approximately between 2.5 and 3 AU, when the temperature reaches levels sufficient to sublimate water. The heat wave propagates inside the nucleus and when the temperature reaches the temperature of sublimation of the ices. The sublimation releases volatiles which form an atmosphere around the nucleus called the coma. As the comet progressively approaches the Sun, the outgassing strongly increases, the gases and dust escape and form cometary tails. Rapid increases of brightness have been observed as the result of outbursts (as described for example in Sekanina (1982); Trigo-Rodríguez et al. (2008)). They are characterised by sudden jets of gases and dust. Locally situated on the surface of the nucleus, they expand more or less widely in space and carry dusts, ices and gases.

Comets inevitably lose mass through the sublimation processes and their size diminishes with the erosion of the nucleus. They end up their life in different possible ways. The comet becomes invisible due to an intense erosion; the comet becomes dormant (no more

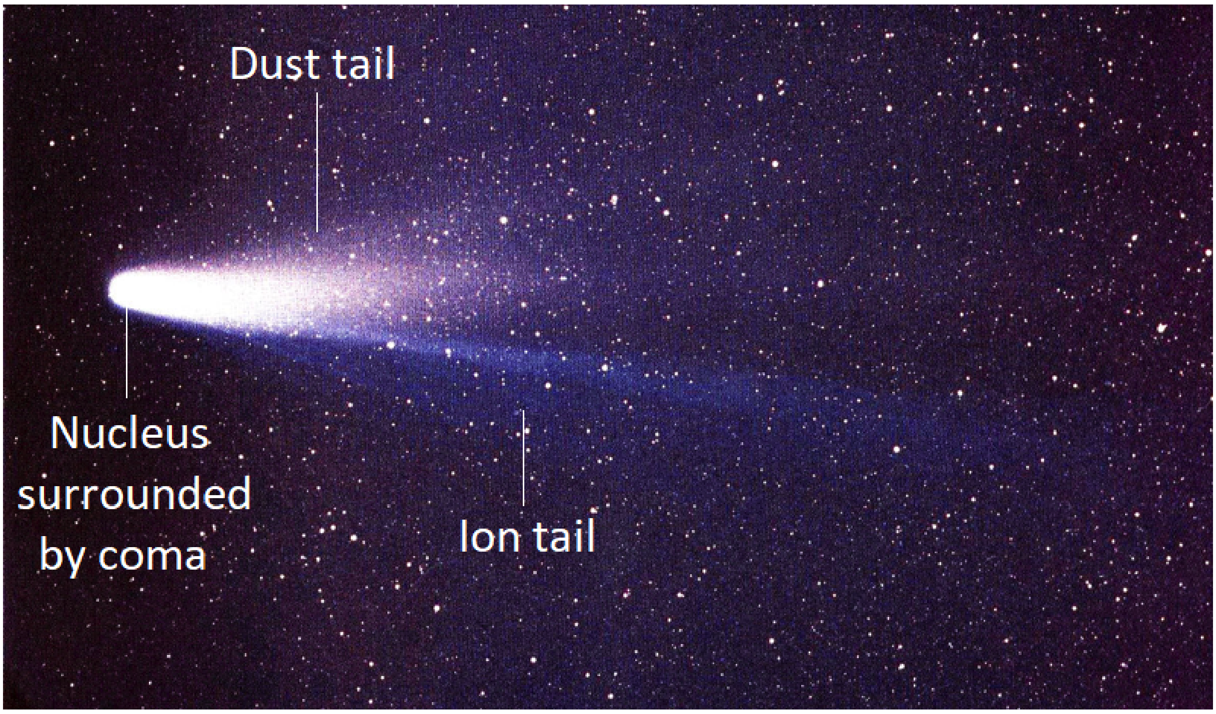

Figure 1.4: Structure of a comet, annotated on a picture of 1P/Halley taken in 1986 (Credits: W: Liller). Cometary tails are the only visible part of the comet from Earth.

activity, the size of the nucleus remains constant); or the nucleus fragments in chunks and it gets destroyed (Keller and Jorda, 2001), like D/1993 F2 (Shoemaker-Levy 9) whose fragments ended up in Jupiter's atmosphere in 1994 (see Figure 1.5) or the disrupted comet 73P/Schwassmann-Wachmann.

1.5.2 Coma

The coma is the gaseous surrounding of the cometary nucleus, composed by the ejected dust, neutral molecules and ions. Its size and density evolve along the orbit, growing as the comet approaches the Sun to reach a typical size of 10^4 kilometres and decreases in size and intensity in the outbound part of the orbit. The composition of the coma gives information on the composition of the nucleus (Huebner and Benkhoff, 1999), but the link between both is complex to analyse in details (see Section 2.2.2).

Dusty organic aggregates ejected from the nucleus may also release gas in the coma , which explains the radial distribution of volatiles that differ from distributions expected for sublimation (Fulle et al., 2000; Cottin et al., 2004; Lasue and Levasseur-Regourd, 2006; Levasseur-Regourd et al., 2018). Those external sources are called distributed sources or extended sources.

1.5.3 Tails

Two tails are formed by the interaction between the comet and its environment. The ion tail or Type I tail is composed by charged molecules and atoms repealed by the solar wind (high speed stream of solar ionized particles). Its direction is opposite to the solar direction. The abundant charged CO^+ molecules absorb solar energy and re-emit by fluorescence, in a blue color (Magnani and A'Hearn, 1986). The dust tail or Type II contains dust particles pushed by the radiation pressure, as the different size particles have different forces applied to them and different velocities, which results in a large curved tail along the orbit of the comet. The dust tail is the most visible part of the comet from Earth and appears yellow because of the scattering of the solar light. Both tails have a typical size of 10^6 kilometers and can expand to hundreds of millions of kilometer (literally 1 AU).

1.6 Observations before Rosetta

The ground-based observations were, at first, visual and then spectroscopic. Obviously, the space exploration considerably improved our knowledge concerning small bodies of the Solar System. A review of the observations from 1P/Halley to 67P/Churyumov-Gerasimenko is provided in Brandt and Chapman (2004). Ground-based and space-based instruments studied comets at different wavelengths, from X-ray to radio wavelengths.

The Orbiting Astronomical Observatory (OAO-2) and Orbiting Geophysical Observatory (OGO-5) made for example the first ultraviolet observations of comets (C/1969 T1, C/1969 Y1,..) in 1970, from above the atmosphere. They studied the Lyman-α emission cloud surrounding comets and the hydroxyl and oxygen emissions, which are now known as the daughter products of H_2O dissociation.

The Kuiper Airborne Observatory (KAO) allowed to detect for the first time water vapour in comets from the Earth's upper atmosphere in the infrared (Mumma et al., 1986). Observations from the upper atmosphere were required, as the fundamental infrared vibration emission of H_2O is absorbed in our atmosphere. The Infrared Space Observatory (ISO) observed C/1995 O1 Hale-Bopp and recorded spectra of H_2O, CO_2 and CO bands and the evolution of their relative abundance (Crovisier et al., 1999).

The International Ultraviolet Explorer (IUE) observed 26 comets from a geosynchronous orbit between 1978 and 1996. They observed the dominance of hydrogen Lyman α and hydroxyl bands in the spectra and made the first discovery of S_2 in comets. X-ray emissions have been observed firstly on C/1996 B2 Hyakutake by the Rontgen Satellite (ROSAT) and the Extreme UltraViolet Explorer (EUVE) (Mumma et al., 1997), and later, in several others comets. They are produced by the charge-exchange collision between the charged solar wind ions and the neutral species in the coma. Observations of numerous comets have been made with ground-based radio-telescopes, such as the Very Large Array (see a summary in De Pater and Lissauer (2015). The Hubble Space Telescope, in a low Earth orbit since 1990, observed, amongs others, 19P/Borrelly (Lamy et al., 1998), the fragmentation of D/1993 F2 Shoemaker-Levy 9 (Weaver et al., 1995), C/1995 O1 Hale-Bopp (Weaver et al., 1999) and 67P/Churyumov-Gerasimenko (Lamy et al., 2006).

The first in situ data were collected in 1985 by the *International Cometary Explorer* (ICE) lead by NASA. It studied the comet Giacobini-Zinner's plasma tail with an approach at 7800 kilometers from the nucleus.

The passage of the comet Halley in 1986 has been an important time in the cometary study history, followed by a number of ground observations and spacecrafts. The European Space Agency (ESA), Japan and the Soviet Union sent five spacecrafts (the "Halley

Armada") to comet Halley: *Giotto* (ESA) (Reinhard, 1986), *Vega*-1 and *Vega*-2 (URSS) (Sagdeev et al., 1986), *Sakigake* and *Suisei* (Japan) (Hirao and Itoh, 1988). The spacecrafts carried multiple instruments and were able to measure the emissions, chemical composition, magnetic field, solar wind, plasma waves, as well as the distribution of dust particles and more. *Vega-1* and *Vega-2* approached the nucleus at a distance of 8 890 km, *Suisei* at a distance of 151 000 km and *Sakigake* at a distance of 7.10^6 km. With 14 instruments onboard, the VEGA spacecraft imaged the Halley's nucleus, estimated its size, shape and reflectivity, and observed the gas and dust of the inner coma (Sagdeev et al., 1986). The analysed dust particles contained the light elements H, C, N, O (such a composition is referred to as CHON). They observed large quantities of very small dust particles $\sim 0.01 \mu m$. The european spacecraft *Giotto*, flew close to 1P/Halley comet at an altitude of 596 km. After a 6 years long hibernation, it then approached the comet Grigg-Skjellerup at 200 km, which, among other results, observed modification of dust particles' properties in the coma (Levasseur-Regourd et al., 1993). The spacecraft carried 10 experiments, including three spectrometers (Reinhard, 1986). This mission gave close-up pictures of Halley's nucleus: an ellipsoidal shape of 16 × 8 × 8 km, with a very irregular surface, and the first in situ data of the gas and dust particles surrounding a nucleus. An important discovery was the darkness of the nucleus' surface, with an albedo lower than 0.04, the nucleus being much darker than expected. Keller et al. (1986) observed that 10% of the surface was active, the rest was covered of non-volatile material. The coma abundance of neutrals and ions was analysed by the spectrometers (Altwegg et al., 1999; Balsiger et al., 1986). The main volatiles detected in the coma were H_2O ($\sim$ 80%), CO ($\sim$ 10%) and CO_2 ($\sim$ 3.5%). The spectrometers also found, in minor abundance, methane, ammonia, hydrocarbons, iron and sodium (Eberhardt, 1999). Halley showed outbursts from isolated active regions and extended sources of H_2CO and CO, associated with dust (A'Hearn et al., 1986; Festou, 1999).

The next visited comet was 19P/Borelly in 2001 by the mission *Deep Space 1* (NASA), launched in 1998. 19P/Borelly has a bilobate elongated nucleus of about 8 × 3 × 3 km. The image revealed an albedo between 0.01 and 0.03, a dry surface (< 10% of sublimating areas) and two types (broad and collimated) jets of activity (Soderblom et al., 2002). An asymmetry of dust between the dayside and the nightside suggested a lateral flow which carried dust in the nightside (Boice et al., 2000).

In 2004, the mission *Stardust* (NASA) collected the first sample of a comet during a flyby at comet 81P/Wild 2, at a distance of 236 km, and brought it back to Earth in 2006. The mission allowed to study thousands of particles in the laboratory. Sampled materials revealed micrometer sized or larger grains, of a high-temperature meteoritic materials (formed in the inner regions of the Solar System and then transported in colder regions) (Brownlee et al., 2006). The nucleus of 81P/Wild 2 presented an ellipsoidal shape, with a diameter of about 4 km.

In 2005, *Deep Impact* sent an impactor of 372 kg on the surface of Jupiter-family comet 9P/Tempel 1. The low albedo nucleus suggested the presence of a layer of organic compounds (Strazzulla et al., 1991). Deep impact brought the first evidence of that hypothesis. The analysis of the ejected materials revealed a surface layer of fine particles (1 to 10 μm) and estimated the density of the nucleus at 600 $kg.m^{-3}$ (A'Hearn et al., 2005). Eight parent volatiles had been studied by infrared spectroscopy, with relative ratios similar to the Oort cloud comets, but lower abundance in acetylene and methane

(Mumma et al., 2005). Its nucleus has an approximate size of about 7 × 5 × 5 km. A dust/ice ratio >1 indicates that dust was dominant, which suggested a description of the nucleus as an 'icy dirtball' instead of a 'dirty snowball', model proposed by Whipple (see Section 2.2.1) (Küppers et al., 2005).

Several years later, the *Deep Impact* mission was extended and the spacecraft, newly named *EPOXI* for Extrasolar Planet Observation and Deep Impact Extended Investigation, visited the comet 103P/Hartley 2 in 2010 at 700 km from the nucleus. 103P/Hartley 2 is a comet originating the Kuiper belt. It appeared as a small bilobate nucleus of 2.33 km long with lobes of about 0.5 km of diameter, and an intense activity (A'Hearn et al., 2011). Hartogh et al. (2011) reported a D/H ratio of $1.61 \pm 0.24 \cdot 10^{-4}$, which is very close to the D/H ratio of water on Earth, i.e $1.558 \pm 0.001 \cdot 10^{-4}$. The standard isotopic composition of water on Earth is defined by Standard Mean Ocean Water (SMOW) (Craig, 1961). The D/H ratios measured on six comets from the Oort cloud present a higher ratio.

Pictures of the comet 1P/Halley, recorded by the Halley Multicolour Camera (HCM) in March 1986 are visible in Figure 1.6. The five pictured cometary nuclei to scale are shown in Figure 1.7.

Typical properties of cometary nucleus can be resumed as following: a low albedo ($\sim$0.04), low density ($\sim$0.5), composed of ices (H_2O, CO_2, CO and some organics compounds CHON) and dust (silicates and organics) with a dust to ice ratio (in volume) of $\sim$ 1 and $\sim$ 10% of active surface.

The space missions considerably improve our knowledge concerning the coma and the structure of the comet's nucleus, as detailed in Section 2. Nevertheless, all those space missions investigated comets through fly-bys; a study of the evolution of the comet along its trajectory and a landing on the surface were not achieved until the Rosetta mission (see Section 3).

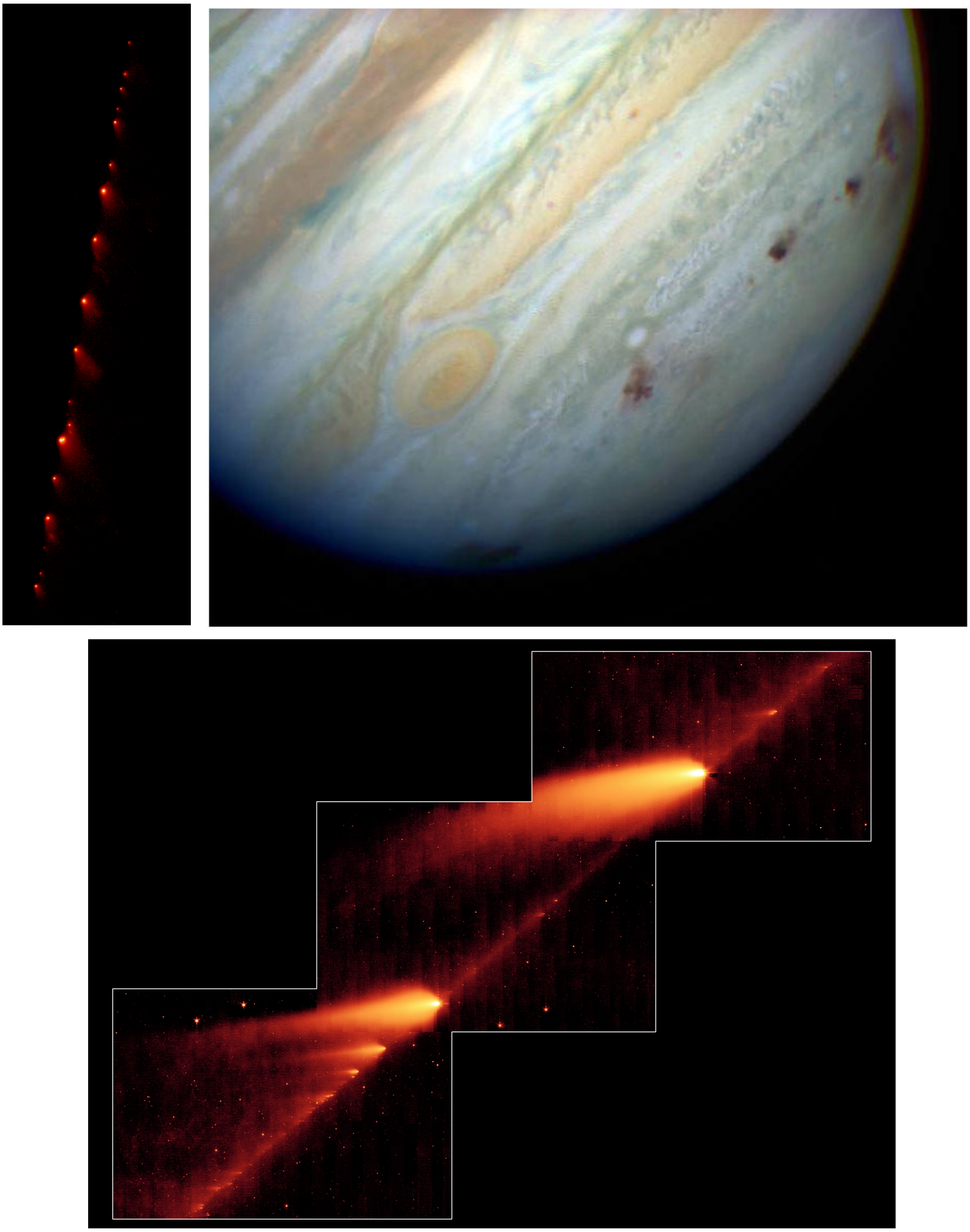

Figure 1.5: Top left: The 21 fragments of the disrupted D/1993 F2 (Shoemaker-Levy 9), taken on the 17 May 1994. NASA/ESA. Top right: Dark patches on the southern hemisphere of Jupiter's atmosphere, following the impact of the fragments, pictured by the Hubble Space Telescope in July 1994. Bottom: Trail of debris of the disrupted comet 73P/Schwassmann-Wachmann 3, pictured by the Spitzer Space Telescope in May 2006.

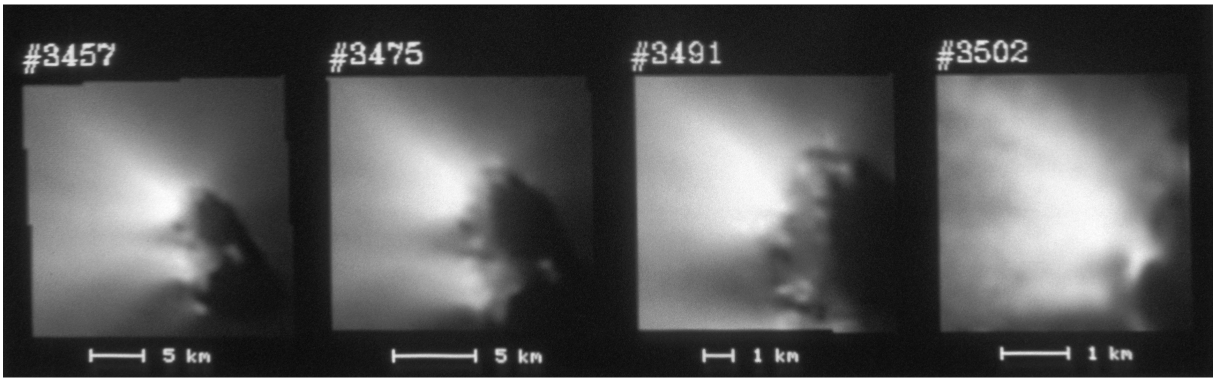

Figure 1.6: Six pictures of comet 1P/Halley taken by the Halley Multicolour Camera (HCM) in March 1986.

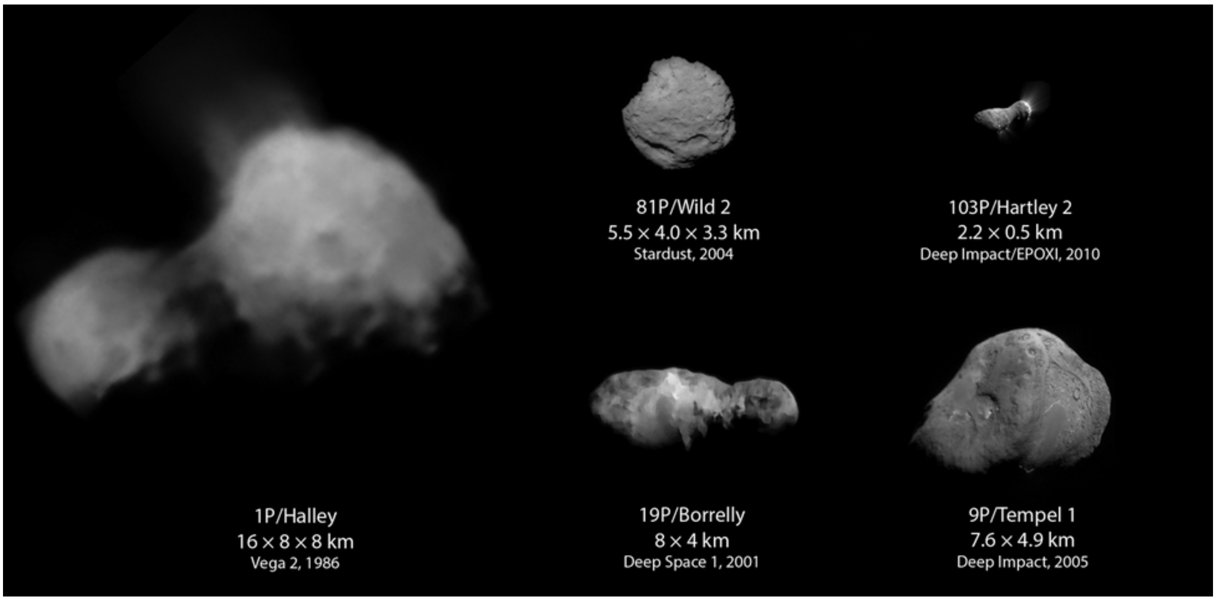

Figure 1.7: Nuclei of the visited (and pictured) comets 1P/Halley, 81P/Wild 2, 16P/Borrelly, 9P/Tempel 1, 103P/Hartley 2. Montage based on a work from Emily Lakdawalla. Picture credits: Russian Academy of Sciences (Halley), NASA/JPL (Borelly, Tempel 1, Hartley 2 and Wild 2).

Chapter 2

Our vision of the coma and the nucleus before Rosetta

This chapter proposes a description of our current knowledge concerning the coma and the nucleus properties before the Rosetta space mission. In a first section, we review the current knowledge regarding the coma. We summarise the different reactions occurring in the coma and its chemical composition. We also detail different models of the gas expansion in the coma. In a second section, we list different models of the cometary nucleus proposed since 1950. Before the space missions, nuclei were notably difficult to observe. We also give an overview of the physical processes induced by the heat diffusion in the interior of a nucleus.

2.1 Coma

2.1.1 Chemical composition of the coma

The inventory of the molecules found in the coma is crucial to understand the composition and the formation conditions of the material in the solar nebula. Cometary comae have been first studied by remote spectroscopic observations using ultraviolet, infrared or radio wavelengths, thanks to instruments on-board spacecrafts or from ground-based observatories. Bockelée-Morvan et al. (2004) and Mumma and Charnley (2011) provided a review of molecules found by the spectral observations of comets. H_2O is the major component of the cometary gas. Combined study in laboratory and spectroscopic observations brought the demonstration that OH radicals and H atoms, observed in comets, were the products of H_2O photodissociation. The H_2O molecules were finally observed in 1P/Halley by the Kuiper Airborne Observatory and Vega's spectrometers and in C/1995 O1 Hale-Bopp and 103P/Hartley 2 by ISO. The minor species of the cometary gas include CO, CO_2, CH_3OH, CH_4 and NH3.

The observations of C/1995 O1 (Hale-Bopp) and C/1996 B2 (Hyakutake), two comets originating from the Oort cloud (period > 200 years), showed similar volatile compositions and allowed the identification of more than 25 parent species. The passage of comet C/1995 O1 (Hale-Bopp) has been observed from the ground, from 1995 to 1997. For the first time, the outgassing pattern of a comet is observed with the detailed production rate of each molecule (Biver et al., 1997). Figure 2.1 shows the production rates of OH, CO, CH_3OH, H_2S, H_2CO, HCN, CS, CH_3CN and HNC with respect to the heliocentric distance, from radiotelescopic observations of comet C/1995 O1 (Hale-Bopp). One can notice the typical behavior of species ejection due to the increase in illumination close to the Sun (the 'Christmas tree' pattern). The CO outgassing appeared dominant at large heliocentric distances while, from 2.5 AU, the outgassing was driven by H_2O.

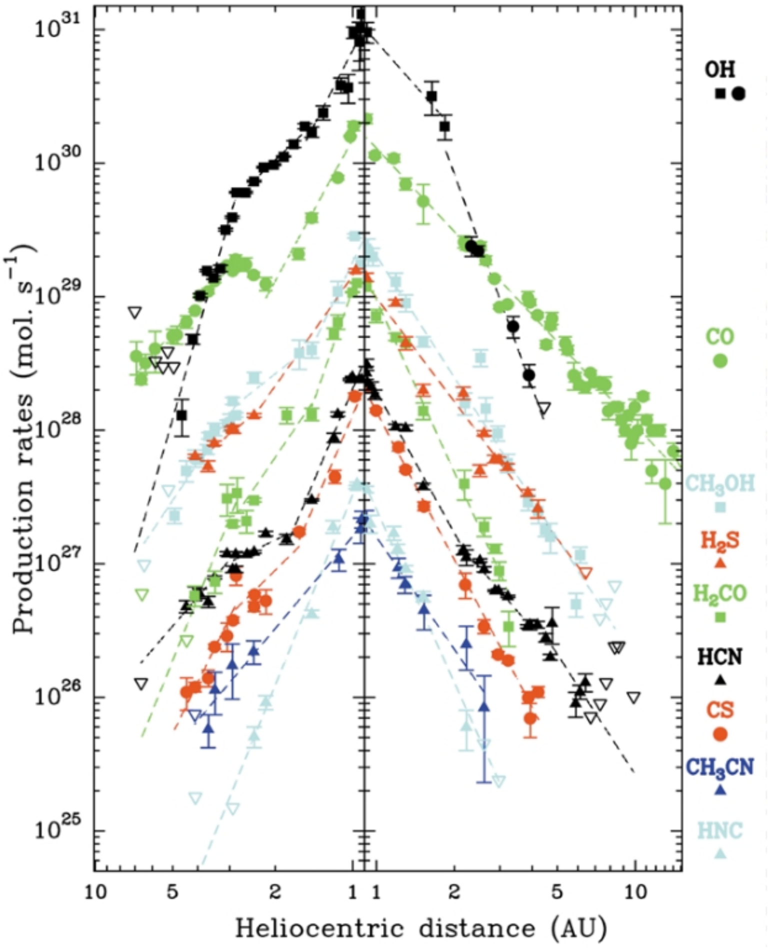

Figure 2.1: Production rate of volatiles with respect to the heliocentric distance of comet C/1995 O1 (Hale-Bopp) (Biver et al., 2002).

The study of comet 1P/Halley gave the first in situ data on the composition of the gas and the dust particles in a coma (Eberhardt et al., 1994; Kissel et al., 1986; Balsiger et al., 1986). Giotto's mass spectrometer identified water, hydrocarbons (CO, CO_2, H_2CO, CH_3OH values of ratio to H_2O), hydrogen cyanide (HCN) and hydrogen sulfide (H_2S). Heavy water (HDO) was also found in the coma. The D/H ratio has been estimated at $3.08 \cdot 10^{-4}$ (Balsiger et al., 1995), enriched in deuterium compared to the protosolar D/H (2 ± 10^{-5}), and to the terrestrial water ($1.5 \cdot 10^{-4}$, defined for Earth as Standard Mean Ocean Water) to identify the similarities between the bodies.

The table 2.1 (Bockelée-Morvan et al., 2004) summarised the abundances of the volatiles species relative to H_2O, based on the observations (IR, UV and Radio) of 1P/Halley, C/1995 O1 Hale-Bopp and C/1996 B2 Hyakutake.

Le Roy et al. (2015) gave an inventory of the volatiles of 67P/C-G coma, measured

Molecule	**1P/Halley**	**C/1995 O1 Hale-Bopp**	**C/1996 B2 Hyakutake**
H_2O	100	100	100
CO	3.5,11	12,23	14,19-30
CO_2	3-4	6	
CH_4	<0.8	1.5	0.8
C_2H_2	0.3	0.1-0.3	0.2-0.5
C_2H_6	0.4	0.6	0.6
CH_3OH	1.8	2.4	2
H_2CO	4	1.1	1
HCOOH		0.09	
$HCOOCH_3$		0.08	
CH_3CHO		0.02	
NH_2CHO		0.015	
NH_3	1.5	0.7	0.5
HCN	0.1	0.25	0.1-0.2
HNCO		0.10	0.07
HNC		0.04	0.01
CH_3CN		0.02	0.01
HC_3N		0.02	
H_2S	0.4	1.5	0.8
OCS		0.4	0.1
SO_2		0.2	
CS_2	0.2	0.2	0.1
H_2CS		0.05	
NS		$\geqslant 0.02$	
S_2			0.005

Table 2.1: Production rate of species observed in comets 1P/Halley, C/1995 O1 Hale-Bopp and C/1996 B2 Hyakutake, relative to water (Bockelée-Morvan et al., 2004).

in situ by ROSINA as well as the volatiles measured by the missions to 1P/Halley, 9P/Tempel 1, and 103P/Hartley 2. They confirmed H_2O, CO_2 and CO as the dominant volatiles in the coma of 67P/C-G. The study of those three main volatiles as seen by ROSINA is provided in Part IV.

2.1.2 Photo-reactions and chemical reactions

The coma is composed of dust and gas originating from the nucleus. The neutral molecules, after ejection from the surface, suffer transformations due to solar radiations destruction and chemical reactions. The transformations are cumulative and increase with the distance traveled by the molecules in the coma. We differentiate three sorts of processes occurring in the coma:

- Dissociation: a molecule can split in several parts due to energetic photons (photodissociation) or due to impact with other neutrals or ions, or even with energetic electrons.

- Ionisation: one or more electrons can be removed from a neutral molecule, leading to the presence of positive ions. The most important ionisation processes are photoionisation and electron impact ionisation. Ionisation eventually leads to radiative or dissociative reactions.
- Other chemical reactions that can alter the parent molecule (its charge state, momentum or excitation level): charge transfer process, neutral-neutral or ion-neutral collisions,...

A detailed list of possible reactions in the inner coma is given in Table 2.2, from Huebner et al. (1991), in order of importance. Impacts with energetic photons or electrons occurs the most and lead to dissociation, ionisation or dissociative ionisation of neutrals (examples are given for H_2O, CO_2 and CO for a photon impact and N_2, CO and CO_2 for an electron impact). The other reactions listed in the table are possible, but occurs more rarely.

Photodissociation	$h\nu + H_2O \rightarrow H + OH$
Photoionisation	$h\nu + CO \rightarrow CO^+ + e$
Photodissociative ionisation	$h\nu + CO_2 \rightarrow O + CO^+ + e$
Electron impact dissociation	$e + N_2 \rightarrow N + N + e$
Electron impact ionisation	$e + CO \rightarrow CO^+ + e + e$
Electron impact dissociative ionisation	$e + CO_2 \rightarrow O + CO^+ + e + e$
Positive ion-atom interchange	$CO_2 + H_2O \rightarrow HCO^+ + OH$
Electron dissociative recombination	$C_2H^+ + e \rightarrow C_2 + H$
Three-body positive ion-neutral association	$C_2H_2^+ + H_2 + M \rightarrow C_2H_4^+ + M$
Neutral rearrangement	$N + CH \rightarrow CN + H$
Three-body neutral recombination	$C_2H_2 + H + M \rightarrow C_2H_3 + M$
Radiative electronic state deexcitation	$O(^1D) \rightarrow O(^3P) + h\nu$
Radiative recombination	$e + H^+ \rightarrow H + h\nu$
Radiative positive ion-neutral association	$C^+ + H \rightarrow CH^+ + h\nu$
Radiative neutral recombination	$C + C \rightarrow C_2 + h\nu$
Neutral-neutral associative ionisation	$CH + O \rightarrow HCO^+ + e$

Table 2.2: Possible photo-reactions and chemical reactions in the coma (left) and corresponding examples (right) (Huebner et al., 1991).

2.1.3 Models of gas expansion in the coma

The expansion of gas in the coma is a complex problem of first importance due to the paucity of in-situ chemical information from the nucleus. We describe a few models of coma (as reviewed in Brandt and Chapman (2004)).

Haser (1957), from the Institut of Astrophysics of Liège, presented the first model of radial distribution of the molecules in the coma. The Haser model allows to derive the outgassing rate of a gas from a number of molecules detected and is widely used to help interpretation. The application of the model requires different assumptions:

- A spherical nucleus with a radial symmetry for the coma.
- Molecules come from the sublimation of the nucleus and are, eventually, photo-dissociated into daughter's molecules, with a lifetime τ.
- Gases escape radially, with constant velocity.

The variation of density due to the dissociation of the parent's molecules are described by the relation 2.1:

$$\frac{dN}{dt} = -\frac{N}{\tau_0} \tag{2.1}$$

with N the density, τ_0 the time needed for a decrease of 1/e of the initial number density.

One particle travels on average a distance r_0 equal to $\tau_0 v_0$ before a dissociation, for a constant speed of the flow v_0.

With the assumption of a spherical nucleus, a constant speed and no dissociation, the outgassing rate Q of a gas with a density n $[m^{-3}]$ is given by the relation 2.2:

$$Q = 4\pi r^2 v_0 n(r) \tag{2.2}$$

Integrating the relation along the line of sight gives the expression of the column density N_ρ, where ρ is the projected distance, as in relation (2.3):

$$N_\rho = \frac{Q}{4v\rho} \tag{2.3}$$

Taking into account the possible dissociation, the radial density distribution of the parent's molecules at a distance r from the nucleus is described in relation 2.4 and the distribution for the daughter's molecules (velocity v_1 and lifetime τ_0) is given in 2.5, with k, a scale factor equal to $v_0\tau_0/(v_1\tau_1 - v_0\tau_0)$:

$$n(r) = \frac{Q}{4\pi r^2 v_0} e^{-\frac{r}{\tau_0 v_0}} \tag{2.4}$$

$$n_1(r) = \frac{Q}{4\pi r^2 v_1} k(e^{-\frac{r}{v_0\tau_0}} - e^{-\frac{r}{v_1\tau_1}}) \tag{2.5}$$

A comparison between the Haser model and observations was performed for comet 1P/Halley. Figure 2.2 shows indeed the variation of the surface brightness (proportional to column density N_ρ) as a function of the projected distance ρ. The variation would have been linear, with a slope -1, without creation and destruction processes. The slope of the curve is first less steep due to the creation of molecules close to the surface, and then steeper due to the dissociation in the coma.

The Haser model is a very simplified model which does neither take into account the real shape of a comet, nor the non radial speed of gases due to collisions close to the surface. However, it can be used as a good approximation for a low active nucleus, with no significant collisional zone.

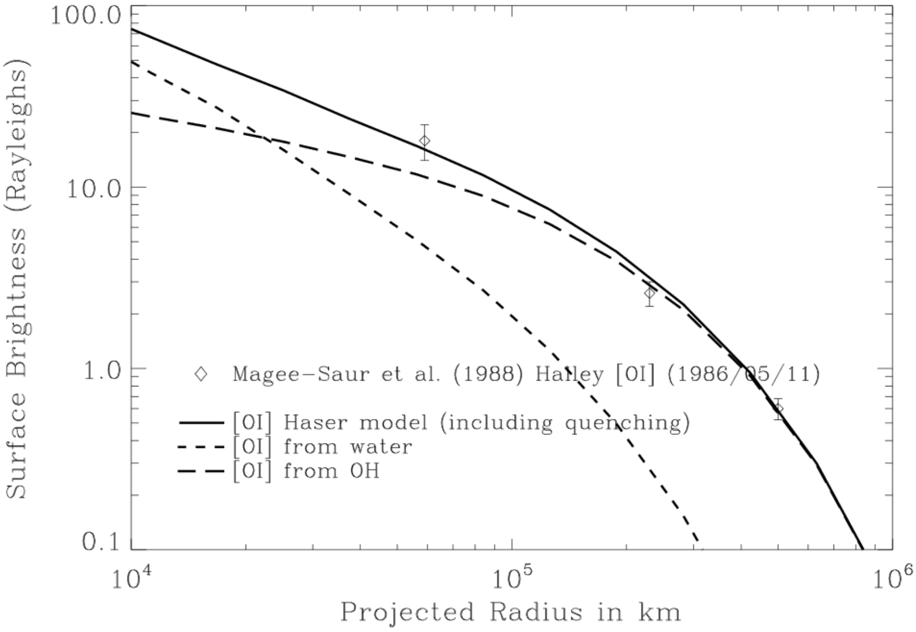

Figure 2.2: Observation of the O I line from water (short-dashed curve) and from OH (long-dashed curve) observed in comet 1P/Halley and the curve obtained with the Haser model (solid curve) (Magee-Sauer et al., 1988).

Instead of a purely radial description, Combi and Delsemme (1980) proposed a more realistic approach (called MCPTM for Monte Carlo Particle-Trajectory Model), using an average random walk model simulated by a Monte Carlo method. The model calculated the individual trajectory of the particles, taking into account the photo-dissociations, collisions and decays occurring in the coma. They applied the model to the Lyman-α cloud and to heavy species (mass comparable to HO) (Combi and Smyth, 1988; Combi et al., 1993). Richter et al. (2000) used an improved version of the model, which took into account the radiative transport in the coma, as the excitation processes are dominated by the solar radiation beyond the inner coma. This approach has been recently extended by Fougere et al. (2016) who applied a 3D direct simulation Monte Carlo model to the shape model of 67P/C-G to reproduce the VIRTIS and ROSINA's observations (see Chapter IV).

2.2 Cometary nucleus

2.2.1 Model of the internal structure

Fred L. Whipple published in 1950 and 1955 ”A Comet Model” (Whipple, 1950, 1955), a series of papers where he described the comet nucleus as a *conglomerate of ices, such as* H_2O*,* NH_3*,* CH_4*,* CO_2 *or CO, (*C_2N_2*?) and other possible material volatile at room temperature, combined in a conglomerate with meteoric materials, all initially at extremely low temperatures (*$\leqslant$*50 K).* This description is also referred to as the ”dirty snowball model”.

The assumption of an icy nucleus model is an important step in cometary science, as it solved several problems. Before 1950, comets were described with a ”sand bank” model, an aggregate of different size solid particles carrying gas. Whipple’s idea allows to solve an observation unexplained by the sand bank model: the non-gravitational acceleration of comet 2P/Encke. Johann Encke studied the orbital observations collected in 1786, 1795, 1805 and 1818, and understood that they were previous passages of the same comet. He estimated its period of rotation at 3.3 years and successfully predicted the return of the comet in 1822. However, the comet’s period appeared to unexpectedly decrease, and the comet arrived at perihelion earlier than predicted. The explanation was proposed by Friedrich Bessel, who observed extensive fine structures at the head of comet 1P/Halley, initially in direction of the Sun and then backward away. For Bessel, the expulsion of material lead to a ’rocket effect’ and modified the orbit of comet 2P/Encke. In Whipple’s model, the icy nature of the body explained the release of the estimated amount of gas. The solar radiation induces the sublimation of the icy material at the illuminated surface. The motion of the comet could be modified by jets of activity out of a dirty snowball-like solid nucleus. Whipple also mentioned the eventual formation of a dust mantle on some parts of the nucleus. In summary, the icy-conglomerate explains the observation of volatile species gases, the nongravitational forces and the dust ejection. The model showed limitations to explain the production of gas with respect to the heliocentric distance. In particular, the observations of species like CN, C_3, NH_2 in the coma and the tails from 3 AU were not consistent with the model.

Delsemme and Swings (1952) suggested the presence of a crystal structure of water able to trap molecules: the clathrate hydrates. They indicated that some species could be trapped in clathrate hydrates form (cage made of 6 molecules of H_2O). In this case, the trapped species are released at the sublimation temperature of water, which explained the increase of activity observed at 3 AU. This hypothesis faced an unsolved problem: the formation of clathrate hydrates requires high pressures (Lewis, 2012), which is not indicated by any model of cometary formation so far.

Another possible way to trap species is the amorphous water ice, which is a non-crystalline form of ice (Bar-Nun et al., 1988). Amorphous ice requires a low temperature environment (< 120 K), where fast condensation freezes the water molecules in their random orientation (they do not have time to orient themselves). Gas molecules present at the time of condensation may be trapped in the amorphous ice. The increase of temperature due to solar illumination allows the crystallisation, i.e. the reorientation of the hexagonal lattice. The crystallisation is an exothermic[1]. and irreversible reaction which characterizes the transition from amorphous ice to crystalline ice, and eventually releases the gas previously trapped in the structure. The phase transition occurs around ~ 140 K (from amorphous to cubic ice) and around 160 K (from cubic to hexagonal) (Bar-Nun et al., 1985; Hudson and Donn, 1991). Mekler and Podolak (1994) claimed that comets contain amorphous ice as the comet was formed in a low temperature and low pressure environment. They investigated the formation of amorphous ice in the protoplanetary nebula, and, based on the required temperature conditions, they proposed that comet nuclei composed of amorphous ice were formed beyond 7 AU. The physico-chemical processes occurring in the near surface layers of comets have been investigated for different cases of ice mixtures and different temperatures in Schmitt et al. (1989).

---

[1] An experiment showed that the transition may be endothermic for a certain amount of impurities in the ice (Kouchi and Sirono, 2001), but this observation has never been confirmed

They concluded that the first three meters are composed of crystalline pure water ice, and the volatiles molecules are trapped in the nucleus in the gas phase. They pointed an exception for the case of CO_2, which may be present as a clathrate hydrate structure that recondensed in the upper layers.

Greenberg et al. (1972) studied the chemical composition of interstellar grains and found out that complex organic molecules can be formed thanks to ultraviolet radiation on icy grains composed of H, C, O and N. Greenberg (1977) proposed the "interstellar dust model", where comet nuclei are aggregated interstellar dust particles.

The physical structure of the nucleus also remained poorly known. A modification was proposed by Weissman in 1986 known as the rubble-pile model (Weissman, 1986). Instead of a single large icy body, nuclei would preferentially be aggregates of small icy conglomerates, weakly tied together. On the first hand, the accretion theory of small bodies in the solar nebula implies collisions of materials at low velocity of $\sim$ 1 m/s (Weidenschilling, 1997). Plus, it is very likely that these aggregates never collect enough energy to modify their original composition. This model is very convenient to explain the splitting events observed on several comets, like Shoemaker-Levy 9 approaching Jupiter in July 1994.

Gombosi and Houpis (1986) proposed another model for the cometary nucleus, called the icy-glue model. They suggested that the nucleus is composed of boulders of large size - from tens of centimeters to hundred of meters- glued together by a matrix of ice and dust.

In agreement with the concept of accretion of grains in the primordial solar nebula, Donn (1990) realized numerical simulations and suggested that the structure of the aggregates are low density fractals of irregular shapes. In more recent simulations, Lasue et al. (2009) took into account disruptive and sticking effects and the temporal evolution of cohesive strength due to sintering processes. They observed a radial variation of density and porosity, with a more compact material in the core (Lasue et al., 2011).

Belton et al. (2007) proposed a model of nucleus characterised by layers for the Jupiter family cometary nuclei: the layered pile model, based on observations of 9P/Tempel 1. They described the nucleus as a number of layers stacked around a core. The layers are remnants of the accretion of small bodies of the solar nebula and differ in composition and physical properties. This leads to an onion-like internal structure and to an inhomogeneous surface, erosion, topography and activity all over the nucleus.

Schematics of four of the cited models are shown in Figure 2.3.

More recently, a new model was introduced by Jansson and Johansen (2014), 'pebble-pile model'. In this model, nuclei are homogeneous millimeter and centimeter-size pebble-pile planetesimals. These pebble-pile are constituted of primordial remnants from the solar nebula. During the planet formation, the relative drift between gas and solid particles lead to streaming instabilities, which allow the collapse of small particles into bigger ones.

Origin of the cometary material

The cometary nuclei are assumed to be constituted of, under an eventual alterated layer, an homogeneous aggregates of ices and dust. The origin of the material, the possible processing in the interstellar medium (ISM) or in the protosolar nebula PSN, and the fraction of pristine interstellar materials are currently investigated.

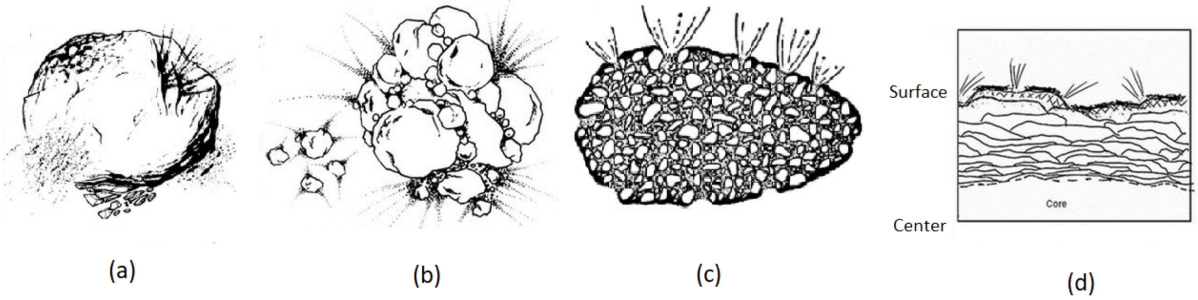

Figure 2.3: Representations of four models of cometary nucleus: (a) the icy conglomerate model (Whipple, 1950), (b) the rubble pile model (Weissman, 1986), (c) the icy-glue model (Gombosi and Houpis, 1986) and (d) the layered pile model (Belton et al., 2007). Credits: unknown.

Ehrenfreund and Charnley (2000) gave a review of the evolution of organic molecules, from the ISM to the Solar System's bodies, based on the ground-based and space-based observations of C/1996 B2 (Hyakutake) and C/1995 O1 (Hale-Bopp), laboratory experiments, and results of the missions to Halley. They investigated the link between the composition of nuclei and the pristine interstellar ice and dust by comparing the inventory of molecules and relative abundances observed in comets and in the ISM. The ISM is made of gas (mainly H, and 10% of He, 0.1% of C, N and O, and traces of other elements) and dust. Observations revealed hundreds of molecules, including a large number of organics. The low temperature (10 - 30 K) and high densities conditions (10^{4-8} H/cm^{-3}) allowed to form simple species (mainly CO, N_2, O_2, C_2H_2, C_2H_4, HCN) (Herbst, 1995), which formed molecules through simple addition reactions (such as H_2, NH_3, CH_4). In dense clouds, dust grains are an efficient support for the formation of ices, like CO, CO_2 and CH_3OH (Wooden et al., 2004). Complex chemistry takes place in those icy grains, altered by ultraviolet irradiation, cosmic ray and variations of temperature. They conclude that the composition of interstellar clouds are consistent with the composition of comets, with notable differences in relative abundance for some trace species, which may suggest a processing of interstellar volatiles. Ehrenfreund and Charnley (2000) advanced evidence that cometary material are a mixing between unprocessed interstellar material (Greenberg et al., 1998) and material processed in the protosolar nebula (Fegley, 1999). Thus, the possible fraction of pristine material in cometary nuclei remains to be investigated. The analysis of the sampled dust of 81P/Wild 2 captured by Stardust is consistent with the hypothesis of a mixing (Keller et al., 2006).

2.2.2 Heat diffusion and physical processes

The comet nuclei are low density bodies (< 0.5 g.cm^{-3}, inducing a high porosity $\sim$ 70%), mostly composed of water ice (and other minor volatile species like CO and CO_2) and dust. The minor species may be mixed in the water ice. In this section, we give the description of heat and gas diffusion inside the cometary nucleus as detailed by Huebner et al. (2006), to link the composition of the nucleus with the observations of the coma.

A first source of energy is the radioactivity of elements such as ^{26}Al (Prialnik and Podolak, 1995). Depending on the abundance of those elements and the decays occurring during the formation, the nucleus experiences a radioactive heating of its interior. This effect is the dominant source of heating for the comet which evolves far from the Sun, but appears very weak, except for large bodies (Guilbert-Lepoutre et al., 2011).

The second source of energy is the solar illumination of the nucleus, which heats the surface. The heat wave propagates from the surface through the interior and induces different physical processes. The surface is directly impacted by the heat wave and experiences the stronger change of temperature. The surface heating results in sublimation of gas, see ① in Figure 2.4. Outgassing will be composed of volatiles (water molecules and eventually minor species if present) and dust. The sublimation of ices induces an erosion of the surface and a mass loss. The activity of the nucleus with respect to heliocentric distance increases when approaching the Sun (inbound part of the orbit) and decreases when moving away (outbound part of the orbit). The loss mass experienced during each orbit eventually leads to the disruption or extinction of the comet. The splitting of the nucleus can occur at a close encounter with a massive object, as experienced by D1/1993 F2 Shoemaker-Levy 9 and 73P/Schwassmann-Wachmann 3 (Zahnle and Mac Low, 1994; Crovisier et al., 1996).

Underneath the surface, the heat wave penetrates the interior of the nucleus and increases the temperature of the sub-surface layers ②. As a high porosity medium ($\sim$ 70 - 80 %) is not a good conductor for heat, the heat wave is not able to propagate very deeply in the body. The thermal properties of such a material indicates an orbital skin depth ($\sim$ few meters) very small compared to the size of the nucleus (Prialnik et al., 2004). If we consider the close surface nucleus as a porous structure containing water ice and minor molecules -like CO and CO_2-, these can sublimate before water considering their lower sublimation temperature. With sublimation temperatures of approximately 35 K for CO and 100 K for CO_2, the surface layers are rapidly depleted of very volatile molecules and become a layer of pure water ice ($T_{sub} \sim 160$ K) (Huebner et al., 2006). This process creates a chemical differentiation of the upper layers. The first layer containing CO_2 will stand below the pure water ice layer, and the first layer with CO will be located even deeper. The differentiation of the bodies can be observed in the activity pattern of the centaurs, which probably contain amorphous ice (Jewitt, 2009).

In the hypothesis of the presence of amorphous ice, the heating will induce a phase transition, i.e. the crystallisation of amorphous ice, at a temperature around 120 K with a maximum around 137 K (Prialnik and Bar-Nun, 1990). The crystallisation represents the third important source of energy. The transition which causes the reorientation of the frozen ice molecules and releases the eventually trapped minor species (Prialnik, 1992) (represented with the colored points in the schematic) ③. The released molecules are then carried away by a pressure gradient which diffuses the gas component above and under the crystallisation front. They are either pushed outward, and eventually make their tortuous way through the porous structure and reach the surface ④, or either pushed inward, deeper in the interior and will recondensate quickly below the sublimation front on the pores walls. Dust particles carried in the flow can obstruct pores or reach the surface.

The dust particles released at the surface are subject to the drag force (induced by the escaping gas) and the gravitational forces. Depending on its size (compared to a modeled critical radius, see Chapter IV) the dust particle will either escape to the coma or fall back on the surface. If the number of large particles is sufficient, an area on the surface can be covered by a dust layer, called a dust mantle ⑤.

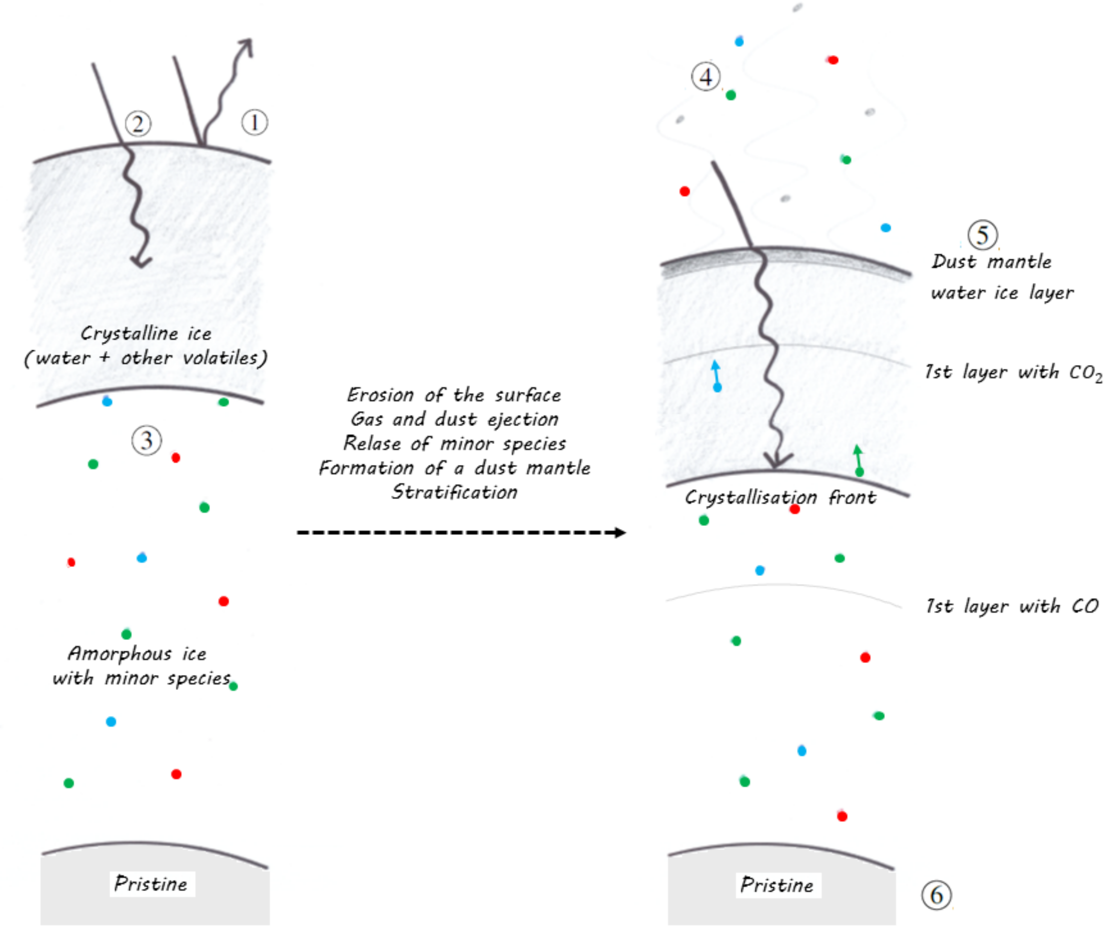

Figure 2.4: Effect of the solar illumination on an hypothetical nucleus model containing amorphous ice, and example of induced stratification, based on Prialnik (2004). The heat wave propagation leads to an erosion of the surface, gas and dust ejection with eventual release of minor species, the formation of a dust mantle and a stratification of the nucleus' interior. The colored points represented eventual volatiles species trapped in the amorphous ice. The depth of the layers are not scaled, the heating decreases exponentially with the depth, therefore the layers are closer to each other near the surface, the pristine material being located at an unknown depth.

In conclusion, the outgassing contains water essentially from the surface which causes erosion. Other volatiles eventually mixed in the matrix, dust particles and minor species are released. The near-structure of the nucleus is expected to be stratified. Under the subsurface layer affected by the propagation of the heat wave, the composition should be pristine ⑥.

The diffusion and gas release processes taking place in the nucleus depend on a series of parameters (porosity, thermal inertia, dust/ice ratio, distributed sizes of dust particles, etc...) that are still largely debated today. Modeling the cometary nucleus is complex but allows to study the influence of the different parameters and constrain the comet structure, as described in more details in Part IV.

Chapter 3

The Rosetta mission (2014-2016)

In this chapter, we present the Rosetta mission in details. In particular, we describe its development and goals, as well as its target − the comet 67P/Churyumov-Gerasimenko (hereafter 67P/C-G) −, the on-board instruments, the trajectory timeline and the main scientific results.

3.1 Introduction

The Rosetta mission is a mission of the European Space Agency (ESA) designed to meet a comet, to escort it along its orbit around the Sun and to drop a lander on its surface. It was approved in 1993 by the program committee. Fourteen European countries and the United States participated in the building of the orbiter, lead by Astrium, while the lander Philae was developed by the German Aerospace Research Institute and a European consortium. The Rosetta Mission Operation Center (RMOC) controlled the mission operations from ESAC (European Space Astronomy Centre) in Madrid, and the European Space Operations Centre (ESOC) was based at ESOC (European Space Operations Centre) in Darmstadt. The landing operation were controlled by the Rosetta Lander Ground Segment (RLGS), based at the DLR (Deutsches Zentrum für Luft- und Raumfahrt) in Cologne and at the CNES (Centre National d'Études Spatiales) in Toulouse.

The name Rosetta refers to the Rosetta stone which allowed Jean-Francois Champollion to decrypt hieroglyphs in 1822. In the same way, the mission has been built to decipher the mysteries comets conceal and more widely, the clues about the history of the Solar System formation. The Rosetta mission's scientific objectives were numerous and required to study the nucleus and the coma (Glassmeier et al., 2007). Among the goals of the mission, we can mention the relation between the nucleus and the coma composition, the comet interaction with the solar wind, the origin of comets (do they originate from the interstellar medium (ISM) or were they formed in the protosolar nebula (PSN)?), the chemical composition of the protosolar nebula, but also the origin of terrestrial life, water oceans, atmosphere, ...

To achieve this ambitious mission, an orbiter and a lander were sent to the comet 67P/Churyumov-Gerasimenko. For the first time, a spacecraft was orbiting around a comet, as an escort along its travel inside the internal Solar System until its perihelion, after an initial launch beyond Jupiter's orbit thanks to the largest solar panels ever built for a planetary science mission (64 m^2) and four gravitational assists around planets (3 around the Earth and 1 around Mars). For the first time, a lander was dropped successfully on the surface of a comet. Finally, the spacecraft ended its mission on the surface of the comet on 30 September 2016 after two years of work.

3.2 Comet 67P/Churyumov-Gerasimenko

The comet investigated by the Rosetta mission was discovered in 1969 by Klim Churyumov on a photographic plate taken by Svetlana Gerasimenko. This periodic comet was the 67th discovered comet and was named after the two soviet astronomers: 67P/Churyumov-Gerasimenko (67P/C-G). The comet has been intensely observed by ground-based and space-based telescopes at each perihelion with a periodicity of about 6.45 years. Its current orbit has a semi-major axis of 3.46 AU with a perihelion at 1.24 AU and an aphelion at 5.68 AU (Lamy et al., 2007). 67P/C-G is a Jupiter family comet (JFC), most probably issued from the Kuiper Belt. The past orbits and planetary encounters of comets are difficult to investigate, as their trajectories are easily deviated by the planets. The only certainties concerning the previous orbits of 67P/C-G are two encounters with Jupiter in 1840 and in 1959. The orbital parameters of the comet before this time remain unknown with large error bars (Maquet, 2015). The rotation period of the comet has been estimated at 12.404 hr after the perihelion of 2009 and at 12.0 hr after the perihelion of 2015 (Mottola et al., 2014). Before the Rosetta mission, the only information on the shape of the comet were given by the Hubble Space Telescope. The shape of the nucleus was inferred from the light curve of the nucleus far away from the Sun (when inactive) (Lamy et al., 2006, 2007).

The Rosetta mission closely studied 67P/C-G during two years and was able to observe its last perihelion passage on 13 August 2015, at a distance of 1.2432 AU, or 186 millions of kilometers from the Sun.

3.3 On-board instruments

The Rosetta mission was composed of an orbiter named Rosetta and a lander named Philae. We describe in this section the list of instruments carried on the orbiter and the lander, as represented in Figure 3.1.

The orbiter weighed 2900 kg for a volume of about ten cubic meters. 11 Instruments were carried by the satellite.

- OSIRIS, for Optical, Spectroscopic, and Infrared Remote Imaging System, consists in two high resolution cameras, operating in the visible, the near infrared and the near ultraviolet wavelengths (Keller et al., 2007).

- ROSINA, for Rosetta Orbiter Spectrometer for Ion and Neutral Analysis, is an experiment consisting of three instruments (two mass spectrometers and one pressure sensor, described in Part 4) to analyse the composition of the coma's neutral gas and ions (Balsiger et al., 2007).

- COSIMA, for Cometary Secondary Ion Mass Analyser, analysed the dust particle's composition thanks to a dust collector, an ion mass spectrometer and a microscope (Kissel et al., 2007).

- GIADA, for Grain Impact Analyser and Dust Accumulator, characterised the dust grains's velocity, momentum and mass (Colangeli et al., 2007).

- MIDAS, for Micro-Imaging Dust Analysis System, analysed the dust with a spatial resolution of 4 nm, which allowed for a microtextural analysis of the dust particles (Riedler et al., 2007).

- RPC, for Rosetta Plasma Consortium, is an ensemble of five instruments for the study of the plasma environment: ICA, for Ion Composition Analyser; IES, for Ion and Electron Sensor; LAP, for Langmuir Probe; MAG, for fluxgate Magnetometer; MIP, for Mutual Impedance Probe (Carr et al., 2007).

- CONSERT, for Comet Nucleus Sounding Experiment by Radiowave Transmission, is a two components instrument (one onboard the spacecraft and the other onboard the lander), which studied the dielectric properties of the nucleus. The antenna onboard the orbiter sent a radio signal through the nucleus to the lander, which transmits it back to the orbiter. The double propagation gives a higher SNR than a single antenna sounder would have (Kofman et al., 2007).

- Alice, the ultraviolet imaging spectrometer, is an imaging spectrometer which studied the composition of the nucleus and the coma in the extreme and far ultraviolet (Stern et al., 2007), particularly useful to characterize the lyman alpha line distribution associated with H atoms.

- RSI, for Radio Science Investigation, analysed the non-dispersive and dispersive frequency shifts, the power and polarization of the radio carrier waves, to study the gravity field, characterize the nucleus and the coma, and determines the most precise values of the density and density distribution in the nucleus (Pätzold et al., 2007).

- VIRTIS, for Visible and Infrared Thermal Imaging Spectrometer is an imaging spectrometer, with three channels: two mappings channels (VIRTIS-M) and one high resolution channel (VIRTIS-H) (Coradini et al., 2007). The instrument analyse the composition of the nucleus' surface and the coma, and the surface temperature by remote sensing.

- MIRO, for Microwave Instrument for the Rosetta Orbiter, studied the abundances and the outgassing rate of the main volatiles, measured isotopic ratios, and analysed the subsurface temperature of the nucleus down to a few centimeters (Gulkis et al., 2007).

The lander Philae contained 10 instruments to study the surface of the comet.

- APXS, for Alpha Proton X-ray Spectrometer, was a spectrometer for the analysis of the composition of the solid surface material but did not function (Klingelhöfer et al., 2007).

- CIVA, for Comet Infrared and Visible Analyser, was a combination of six micro-cameras to picture the surface of the nucleus. It was also concieved to analyse the composition, texture and albedo of cometary material (Bibring et al., 2007).

- CONSERT, the other part of the instrument described onboard the orbiter.
- COSAC, for COmetary SAmpling and Composition experiment, consisted in a gas chromatograph and a time-of-flight mass spectrometer to study the composition of complex organic molecules (Goesmann et al., 2007).
- MUPUS, for MUlti-PUrpose Sensors, contained different temperature sensors and a 35 cm penetrator to analyse the surface and sub-surface properties (Spohn et al., 2007).
- Ptolemy, an experiment to analyse the composition of light elements including isotopes (Morse et al., 2009).
- ROLIS, for Rosetta Lander Imaging System, was built for the imaging of the landing site during the descent (Mottola et al., 2007).
- ROMAP, for Rosetta Lander Magnetometer and Plasma Monitor, was a multi-sensor experiment, containing a fluxgate magnometer, an electrostatic analyzer and two sensors to study the local magnetic field and the comet-solar wind interaction (Auster et al., 2007).
- SD2, for Sampling, Drilling and Distribution, was built to bore up to 250 mm on the surface and to analyse the samples with microscopes and to analyse the environment with a spectrometer (Finzi et al., 2007).
- SESAME, for Surface Electric Sounding and Acoustic Monitoring Experiment, contained three instruments to probe the surface: SESAME/CASSE, for Surface Electric Sounding and Acoustic Monitoring Experiment/Comet Acoustic Surface Sounding Experiment, which analysed the propagation of the sounds through the surface; SESAME/DIM, for SESAME/Dust Impact Monitor, which measured the dust particle redeposited on the surface; and SESAME/PP, for SESAME/Permittivity Probe which analysed the electrical properties of the nucleus (Seidensticker et al., 2007).

This work concerns the calibration, analysis and interpretation of the ROSINA data. Thus, the ROSINA experiment and its three instruments will be described in details in the next part 4.

3.4 Trajectory

When the program committee approved the mission in 1993, the initial target was the comet 46P/Wirtanen and the launch was planned for January 2003. Unfortunately, one month before, the mission was suspended due to the failure of a previous flight of Ariane 5 (flight 157). Once the launch window was missed, a new target was chosen: the comet 67P/Churyumov-Gerasimenko, and a new trajectory was calculated. The new trajectory included four gravitational assists and fly-bys of two other small bodies: the asteroids (2867) Steins and (21) Lutetia.

On the 2nd of March 2004, Ariane 5 took off from the Kourou launch site, carrying the European spacecraft for a long travel of about 6.4 billions of kilometres and 10 years.

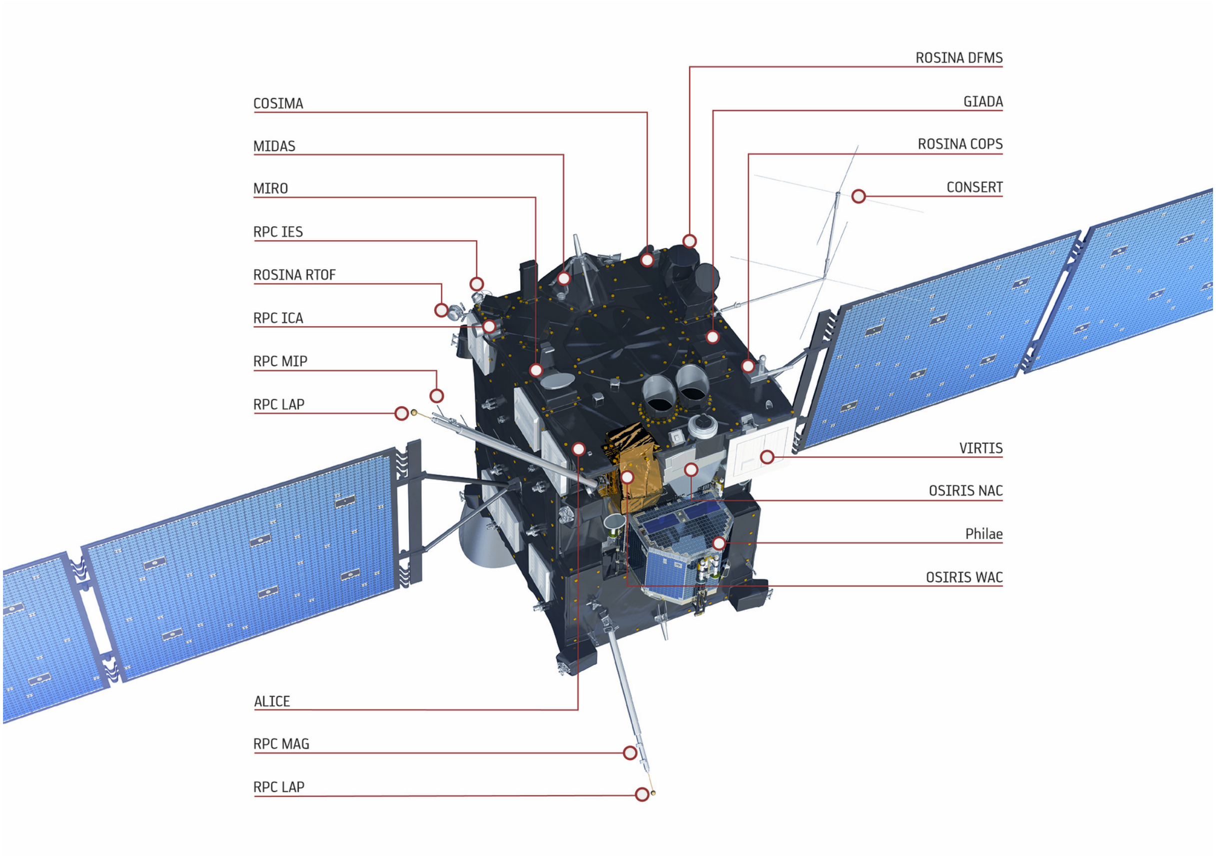

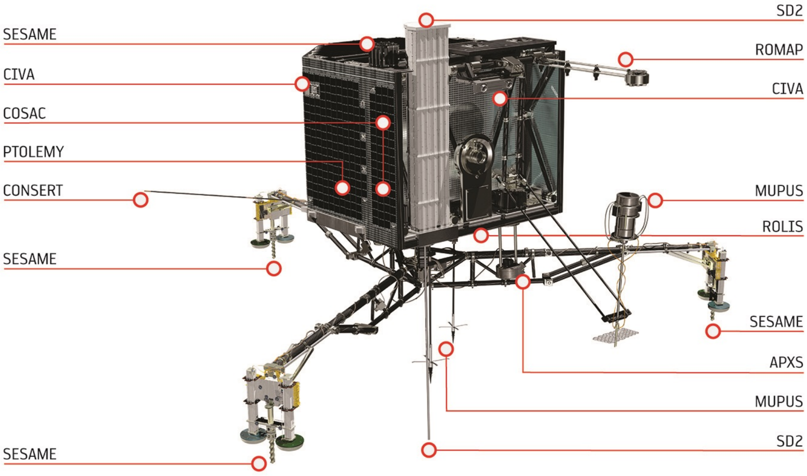

Figure 3.1: Schematics of the Rosetta orbiter, with the location of the 11 instruments (upper figure) and the lander Philae, with the location of its 10 instruments (lower figure) (Balsiger et al., 2007).

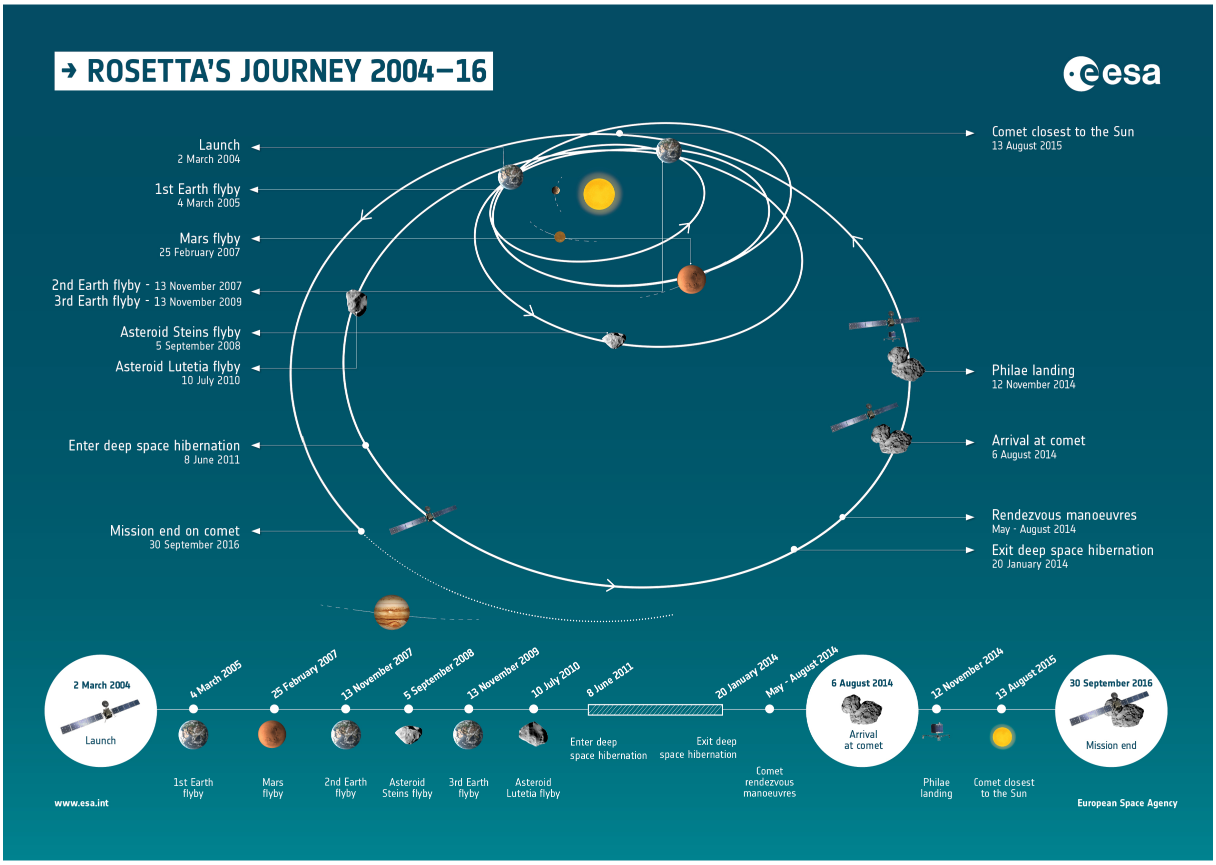

Figure 3.2: Rosetta's trajectory from Earth to 67P/C-G, with fly-bys of the Earth, Mars, the asteroid Stein and Lutetia. Credit: NASA/ESA.

The trajectory from the take off until the crash on the comet is shown in Figure 3.2. The trajectory of Rosetta was designed to optimize the energy consumption. The spacecraft used multiple gravitational assists during the travel. It first used the assist of the Earth in 2005, then the assist of Mars in 2007 to get closer to the Earth again. Rosetta flew by asteroid (2867) Šteins and used for the last time the gravitational assistance of the Earth in 2009. One year later, the spacecraft flew by a second asteroid: (21) Lutetia. Figure 3.3 shows pictures of both asteroids taken by the OSISIS camera on-board Rosetta.

The spacecraft was put on a hibernation mode in June 2011 for the last part of the travel far from the Sun where the illumination of the solar panels was insufficient to provide enough power to operate the mission. Rosetta successfully woke up after 31 months of hibernation in space. The rendez-vous with 67P/C-G occurred in August 2014 after several months of manoeuvres to approach the comet. Rosetta discovered the rough surface of the bilobate comet, which complicated the selection of the landing site for Philae. The J site was finally chosen, and named Agilkia. On 12th November, Philae was dropped by Rosetta.

Unfortunately, Philae landed but did not succeed in attaching itself to the surface and bounced a few times on the hard surface of the nucleus. Out of control, the lander ended its course somewhere on the surface just below the equator, to the East of the initial selected site. The set of data recorded during the descent was successfully sent to the

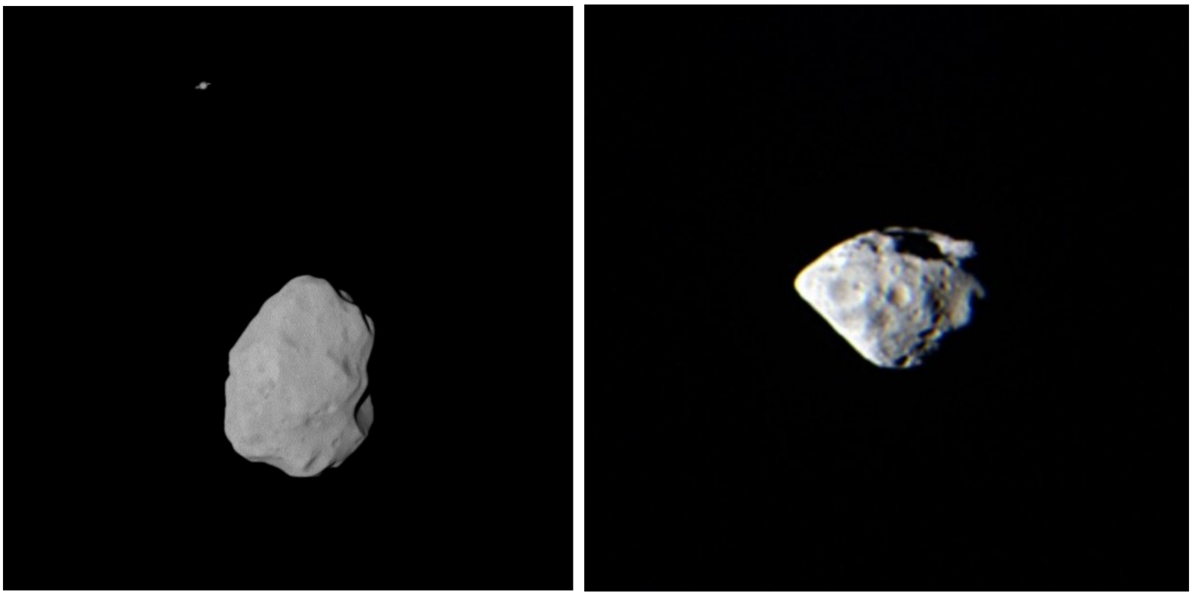

Figure 3.3: Left: View at 100 km from the surface of asteroid (21) Lutetia with, in the background, Saturn. Right: view at 800 km from asteroid (2867) Šteins. Pictured by OSIRIS. Credits: ESA/Rosetta/MPS for OSIRIS Team.

spacecraft. In a site with poor illumination, Philae functionned for a few days making most of the measurements that were programmed during its main science mission. Then it shut down because of a lack of power. Tentatives to communicate with Philae later on were unsuccessful. In total, 60 hours of data have been sent before the batteries ran out of energy. The spacecraft attempted to communicate with the lost lander a few times during the mission. Philae was finally found on a picture of OSIRIS (shown in Figure 3.4) less than a month before the end of the mission, and revealed that it landed on its side, in the darkness of a cliff in the Abydos site at the Hatmehit-Bastet boundary, unable to charge its batteries for further science.

The end of mission was initially planned for 2015, it was then extended until September 2016.

On 30 September 2016, Rosetta made its last move to end up on the surface of the comet, not far from Philae's landing site. During the descent, some instruments kept recording data, in particular OSIRIS, the camera, which continued to take pictures. The last picture of Rosetta (shown in Figure 3.5) was taken at an altitude of about 20 meters, before the final impact in the Ma'at region.

3.5 Overview of the main scientific results

Rosetta has been a highly successful mission with important scientific results. We describe in this section the main results concerning the cometary nucleus and the coma's composition and evolution, which are of major interest for the studies of this work made with ROSINA.

The Rosetta mission first achieved to characterize the properties of the cometary nucleus. The period of the body is of about 12.4 hours, slighty changing with the loss of

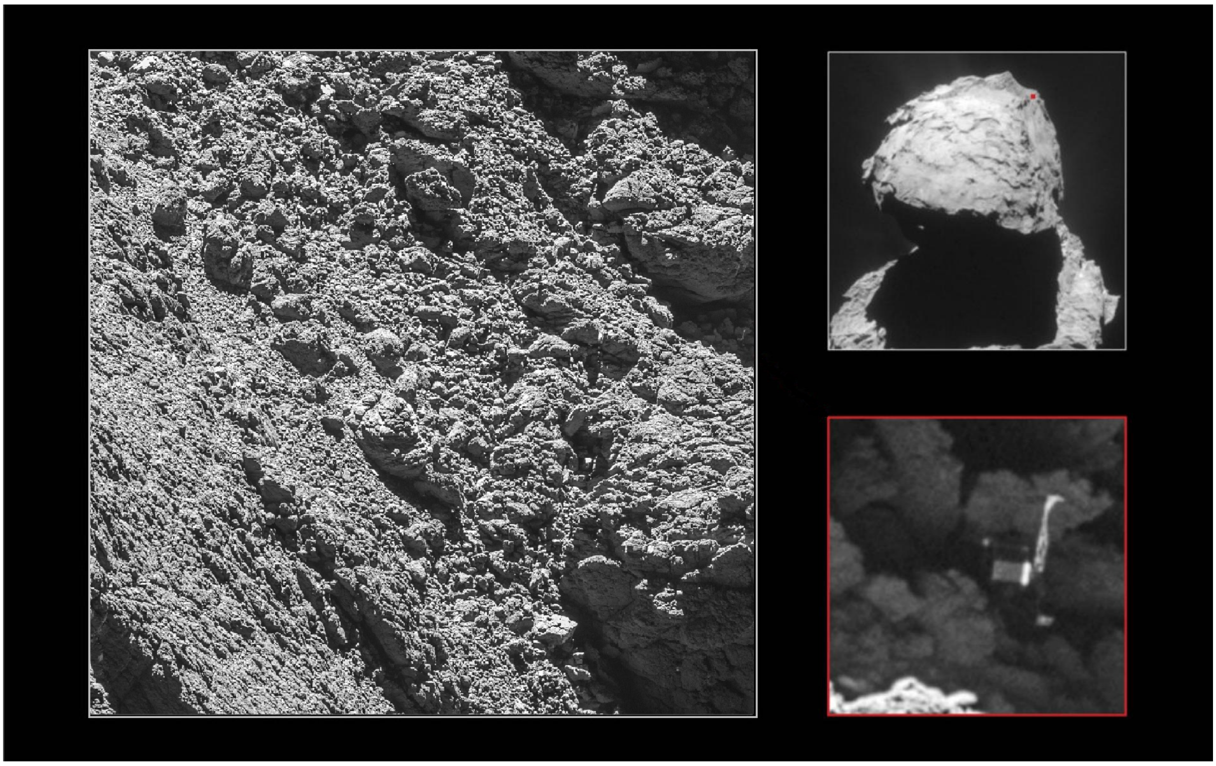

Figure 3.4: Left: Picture taken by OSIRIS on the 2 September 2016 at 2.7 km from the surface, which allowed to identify Philae less than month before the end of the mission. The image scale is 5 cm/pixels and Philae's size is ∼ 1 m. *Would the reader be able to find Philae?* → Find the solution at the end of the document. Right: The location of Philae on the nucleus and a zoom on the lander wedged into a crack.

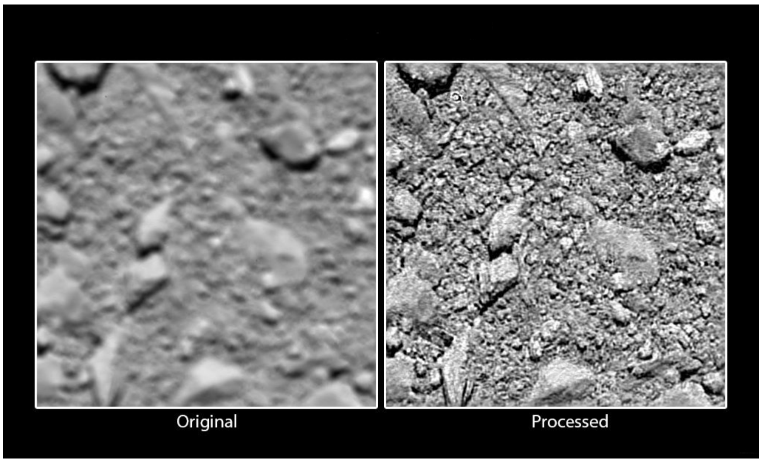

Figure 3.5: Last picture of the Rosetta mission, taken by OSIRIS from an altitude of 24.7 ± 1.5 m. Credit: ESA/Rosetta/MPS for OSIRIS Team.

mass of the comet at each orbit (Keller et al., 2015a). Its mass at the beginning of the mission was estimated to be 9.982 ± 3 x 10^9 kg with a bulk density of 533 ± 6 kg/m^3 for a volume of 18.7 ± 0.3 km^3 (Pätzold et al., 2016). Jorda et al. (2016) described a body constituted of a big lobe -later called *the body*- of 4.10 km x 3.52 km x 1.63 km, and a small lobe -later called *the head*- of 2.50 km x 2.14 km x 1.64 km. The junction of the two parts has been named *the neck*.

The OSIRIS camera took highly detailed pictures of the shape and surface topography of the nucleus. It revealed an impressive bilobate object with a complex topography, see Figure 3.6. The camera revealed a highly rugged surface of the illuminated nucleus (the northern hemisphere and equator at the beginning of the mission), as described in Sierks et al. (2015). The comet's surface has been separated in regions defined by their morphogeological appearance, with the use of names of Egyptian deities (Thomas et al., 2015b; El-Maarry et al., 2015), see Figure 3.7. They also observed the dominant activity from the neck region, with the constant apparition of jets, in particular from Hapi, Hathor, Anuket and Aten (Lara et al., 2015). The northern hemisphere is also characterised by some smooth areas, probably composed of dust particles (Thomas et al., 2015a). The southern hemisphere remained in the shadow until May 2015. Once illuminated, the OSIRIS camera was able to observe the surface and detailed topography dominated by outcrops of consolidated material (Lee et al., 2017). The southern hemisphere appeared flatter than the northern hemisphere, with an erosion rate three times higher due to the intense summer endured close to the Sun (Keller et al., 2015b). It also shows 3 times more large boulders on its surface (Pajola et al., 2016). The morphology of the surface indicates complex material transport processes (Keller et al., 2017). The active zones, such as the neck region, which are related to cliffs and pits – possibly due to sink-hole collapse – were mapped and discussed by Vincent et al. (2015, 2016). Massironi et al. (2015) identified a difference in the stratification of the small and the big lobe, constraining the process of comet formation. They suggested that the bilobate shape is the result of a low velocity collision between two independent bodies.

The instruments onboard Philae worked during the $\sim$ 7 hours descent, the first touchdown in the targeted site Agilkia, the following multiple touchdowns and the final landing site Abydos. The albedo of Algikia has been estimated at 6.7% by OSIRIS, slighly higher than the albedo of the nucleus, estimated at $6.5 \pm 0.2\%$ (La Forgia et al., 2015; Fornasier et al., 2015), while Abydos's albedo is 3-5 % (Lucchetti et al., 2016). The surface at Algikia presented a soft granular surface of $\sim$ 20 cm possibly covering a harder subsurface (Biele et al., 2015). CIVA collected images during the touchdowns and landing. The Abydos site has a complex fractured surface (Bibring et al., 2015). Ptolemy reported the detection of CHO-bearing organics compounds in a near surface analysis. The radar CONSERT probed the upper part of the head and revealed an homogeneous material (at a scale of tens of meters) (Kofman et al., 2015). They measured an average permittivity of 1.27, which suggested a volumetric dust/ice ratio of 0.2-2.6, a high porosity of 75 to 85 % and a change of local properties (dielectric constant) with depth (Ciarletti et al., 2015). ROMAP revealed that the nucleus has no intrinsic magnetic field (Auster et al., 2015).

The nucleus surface was observed covered by a dark material, with a very low reflectance and no ice-patch in the northern hemisphere (Capaccioni et al., 2015). The spectrophotometric study of the nucleus did not reveal clear differences between the two lobes. The VIRTIS (Visible and InfraRed Thermal Imaging Spectrometer) team detailed the dynamics of 67P/C-G surface and the loss of a dust layer due to increased water sublimation during the approach to the Sun (Filacchione et al., 2016). They also revealed a cyclic pattern, which modified the activity and water ice production rate on the surface

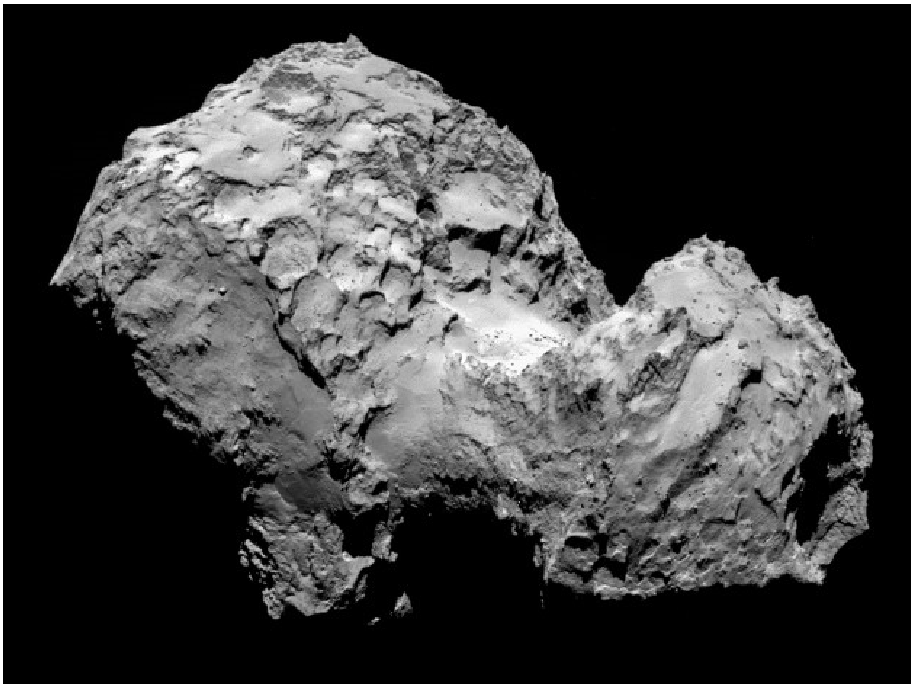

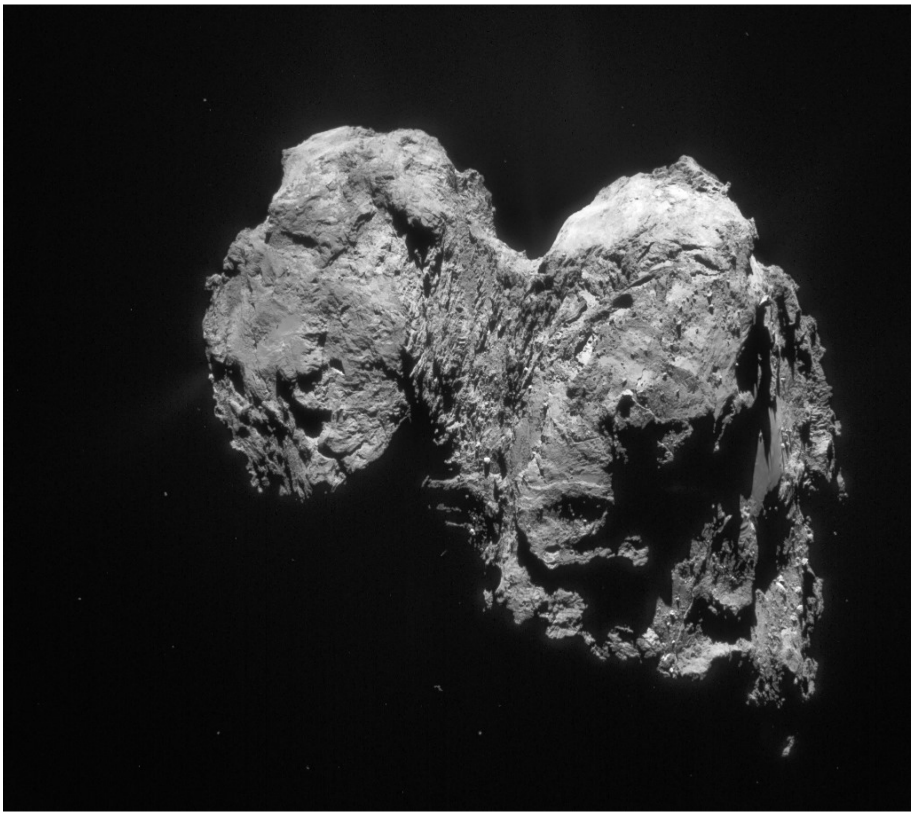

Figure 3.6: Pictures of the bilobate comet $67P$/Churyumov-Gerasimenko taken during the Rosetta mission, on the 3rd August 2014 (upper picture) and 28 January 2016 (lower picture). Credits: ESA/Rosetta/MPS and /NAVCAM.

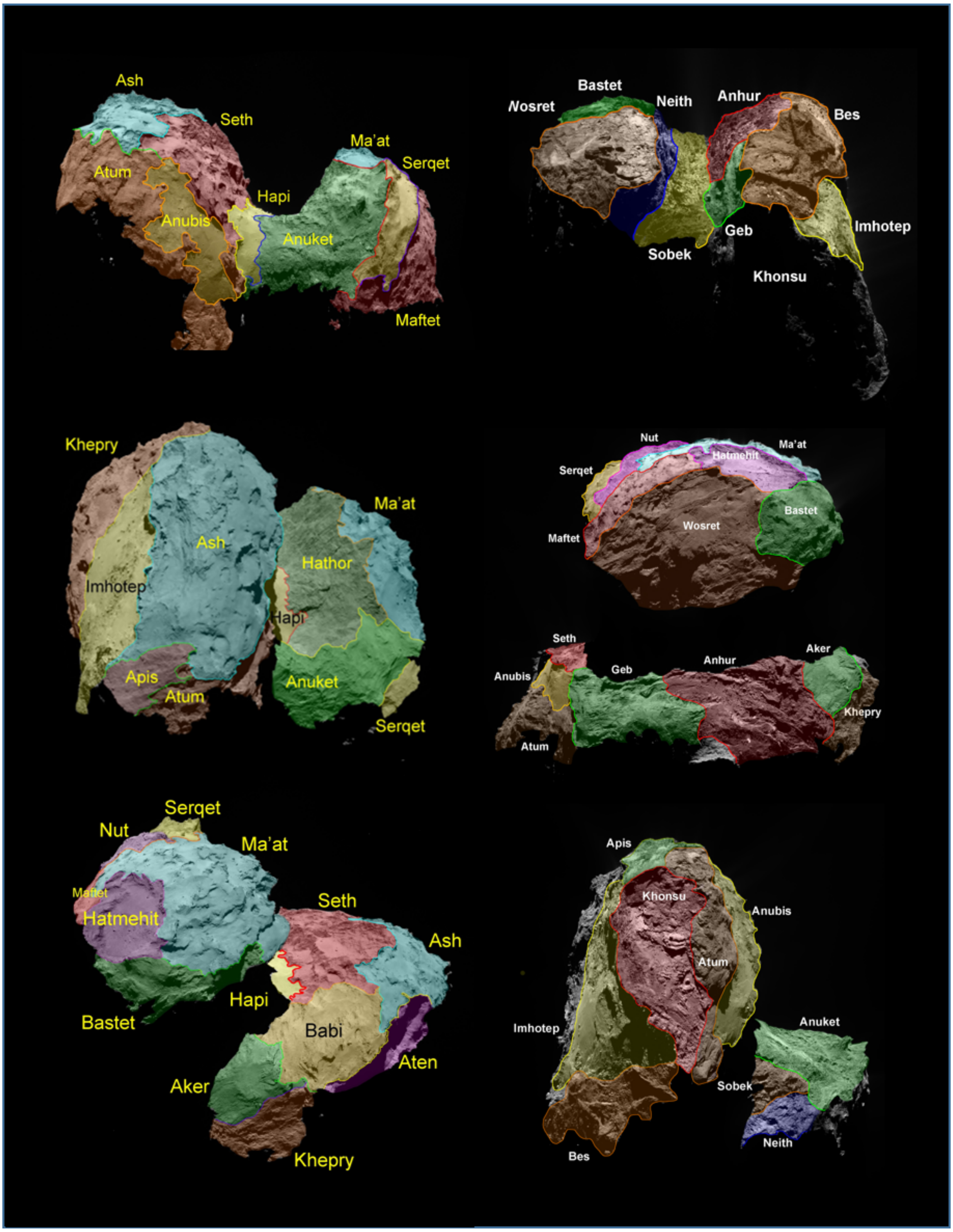

Figure 3.7: The regions boundaries and names of 67P/C-G's northern hemisphere (left side) and southern hemisphere (right side). Credits: ESA/Rosetta/MPS for OSIRIS Team.

of the comet (De Sanctis et al., 2015). Tens of water ice patches have been observed to date (De Sanctis et al., 2015; Barucci et al., 2016), and one patch of carbon dioxide was identified on the surface, in the Anhur region (Filacchione et al., 2016). MIRO observations showed temperature profiles of the near surface following the seasonal and diurnal variations (Gulkis et al., 2015). The highly porous nucleus leads to a very low thermal inertia in a range of 10-50 $J.K^{-1}m^{-2}s^{-0.5}$.

The composition and isotopic ratios of the coma were studied by the spectrometers on-board the spacecraft. Altwegg et al. (2015) analysed the D/H (deuterium/hydrogen) ratio, measured by ROSINA. The obtained value of $5.3 \pm 0.7 \cdot 10^{-4}$ is three times more important than the D/H ratio of terrestrial oceans. This result excludes the hypothesis that Earth's water was provided by 67P/C-G-like comets. The D/H of 67P/C-G is notably different from all the other known D/H ratios measured on comets, which means that the Jupiter family comets have diverse origins. Balsiger et al. (2015) reported the detection of argon and its isotopic ratios, confirming that major volatiles on Earth were not brought by 67P/C-G like comets either. Bieler et al. (2015) revealed the detection of large amounts (4%) of free oxygen molecules in the gas. The high volatility and high chemical reactivity of O_2, and the absence of strong variations in O_2/H_2 ratio over several months, suggested an inclusion of O_2 in the ices during the formation of the nucleus. This conclusion is not consistent with the actual Solar System formation models. They proposed two hypothesis: the O_2 molecules were formed by grain surface reactions and would have been incorporated unaltered into cometary material, or gaseous O_2 was incorporated into H_2O ice in the proto-planetary disk, which required a rapid cooling (typically a drop in temperature occurring after the heating induced by an accretion burst onto the star), from more than 100 K to less than 30 K, making the trapping in water ice possible. ALICE confirmed the detection of molecular oxygen but measured a O_2/H_2O ratio in abundance at 11-68 %, with median value at 25% (Keeney et al., 2017), which is considerably larger than the $3.8 \pm 0.85\%$ detected by ROSINA.

Calmonte et al. (2016) reported the detection of sulfur-bearing species, with in particular the presence of the very volatile molecules S_2 at heliocentric distances larger than 3 AU. They investigated the link between cometary material and the ISM. Their hypothesis is that the sulfur species were processed in the protosolar cloud and were incorporated as ices in the cometary material. Their observations appeared inconsistent with the clathrate hydrates trapping process. Xenon isotopes were investigated by Marty et al. (2017) who suggest that comets contributed to Earth's atmosphere. ROSINA also recorded the first detection of amino acid (glycine) and phosphorus (Altwegg et al., 2016) that are primary constituents of life blocks. Le Roy et al. (2015) presented an inventory of the molecules found in the coma. Considered as the most abundant form of nitrogen in the protosolar nebula, molecular nitrogen (N_2) has been found for the first time in a comet Rubin et al. (2015a). N_2 is formed through condensation or trapping in ice in the protosolar nebula at very low temperatures (< 30 K). The N_2/CO ratio appeared to be lower than the protosolar value, which brings another constraint on the formation of the comet. The diversity of the molecules detected by ROSINA are illustrated in Figure 3.8 by the *ROSINA zoo*, which associates each type of molecules with an animal according to a common characteristic.

A strong chemical heterogeneity was revealed in the illuminated northern hemisphere of the coma based on the DFMS data analysis by Hässig et al. (2015) (see also our

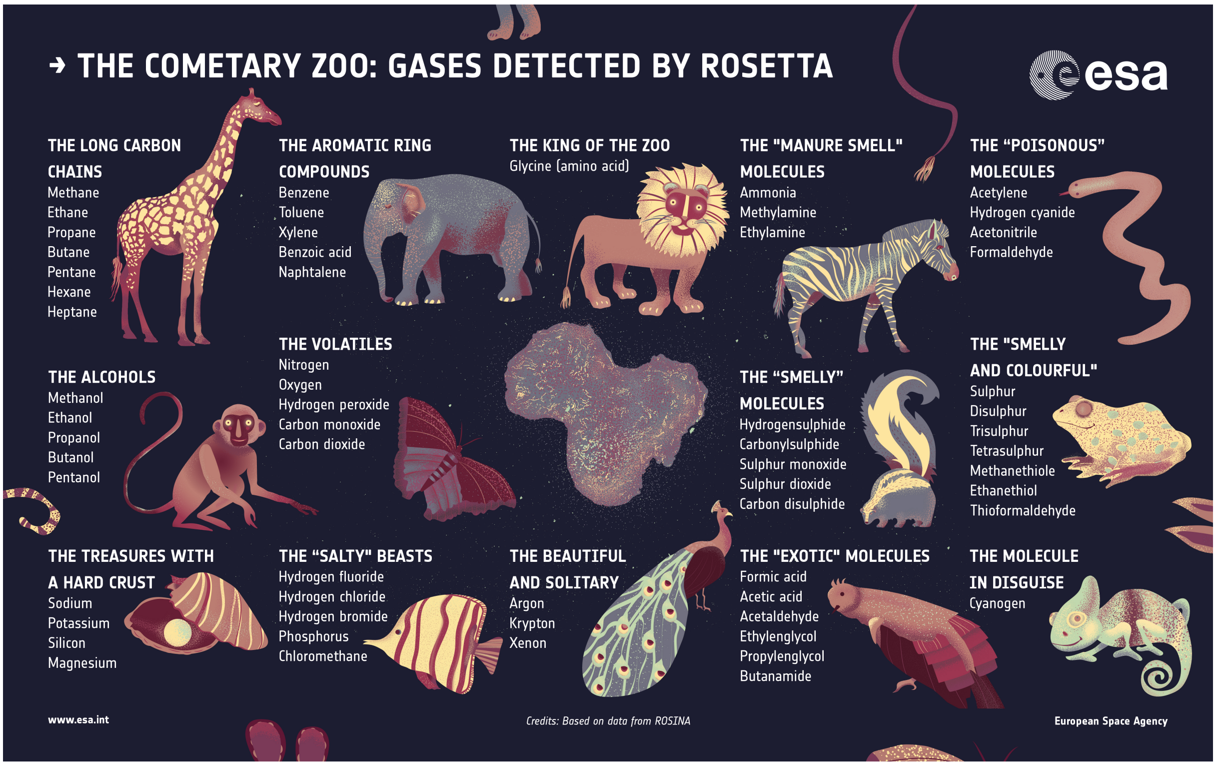

Figure 3.8: The ROSINA zoo illustrates the diversity of the molecules detected in the coma of 67P/C-G by ROSINA/DFMS. Credits: ESA.

work in Part III). These authors studied H_2O, CO_2, and CO variations in the coma in the early mission and found diurnal and latitudinal variations of H_2O with a more homogeneous behaviour of CO_2 and CO, which probably originated from layers deeper inside the comet. The rotational axis is tilted by 52 degrees with respect to the orbital plane of the comet, which induces a strong seasonal effect, further detailed in Section 6.1.2. Luspay-Kuti et al. (2015) demonstrated that minor species density variations are correlated with major species H_2O or CO_2 while CH_4 showed a different pattern. The change of outgassing pattern during the second equinox in March 2016 was described in Gasc et al. (2017a), questioning the correlation of minor species with the sublimation of pure ices- water ice and CO_2 ices. Moreover, the ultraviolet imaging spectrometer called ALICE, with measurements of near-nucleus atomic hydrogen and oxygen emissions, revealed an unexpected influence of electrons, rather than photons, on the break up of molecules (Feldman et al., 2015).

The spectrometer VIRTIS studied the composition of the surface of the comet, rich in organics and very poor in detectable ices (Capaccioni et al., 2015). Water and carbon dioxide spatial distributions have been investigated by Bockelée-Morvan et al. (2015) and by Migliorini et al. (2016) with VIRTIS data. They described a water production originating from the illuminated areas, in particular above the neck. They suggested that CO_2 sublimated below the diurnal skin depth, while detection of CO_2 was observed in illuminated and non illuminated regions. They observed two water active regions, Aten-Babi and Seth-Hapi, and high detections of CO_2 from the head and the southern hemisphere.

Hansen et al. (2016) compared the water production measured by DFMS, MIRO, VIRTIS-H, VIRTIS-M and RPC-ICA. They found the maximum of outgassing seen occurred 18 to 22 days after perihelion with a water production of $3.5 \pm 0.5 \times 10^{28}$ molecules/s. Given the total production rate from the comet and its density, it is expected that the comet sheds about one meter of material per orbit (Bertaux, 2015).

This list of results is a brief summary of the main results of the Rosetta mission, oriented towards the analysis of the 67P/C-G coma's volatiles (see Boehnhardt et al. (2017) and Taylor et al. (2017) for more complete summaries). Adding the measurements of Philae to the two years study of Rosetta, the mission provided a global study of the nucleus and the coma of the comet 67P/C-G, collecting a huge amount of results compared with the previous cometary missions. Nevertheless, some questions remain unsolved and highly discussed. Among others, we cite the internal structure of the nucleus, the dust/ice ratio and the form of water ice allowing the trapping of minor species. The goal of this present work was to analyse in details the volatiles's species temporal and spatial distribution of the coma of 67P/C-G over the entire Rosetta mission (based on ROSINA/RTOF data), and to provide a comparison with models to constrain the internal structure of the comet.

The reader may found a more detailed and illustrated review about comets and cometary space missions in Lequeux and Encrenaz (2015) and Levasseur-Regourd and Borg (2018).

Part II

Description of the experiment and data analysis

Chapter 4

The ROSINA experiment

This thesis concerns the analysis of the 67P/C-G coma based on the data of RTOF, the time-of-flight mass spectrometer of the ROSINA experiment. In this chapter, we thus give a description of the ROSINA experiment, with its three instruments (see Section 4.1) and its scientific objectives and performances (see Section 4.2), we then introduce the mass spectrometry principle (see Section 4.3) and detail the three instruments of the experiment, in particular the Reflectron-type Time-Of-Flight mass spectrometer RTOF (see Section 4.4 and 4.5).

4.1 General presentation

The Rosetta Orbiter Spectrometer for Ion and Neutral Analysis (ROSINA) is a very high capability experiment lead by the University of Bern, with the participation of the Southwest Institute of San Antonio (Texas, USA), the Centre d'Etudes Spatiales des Rayonnements of Toulouse (today Institut de Recherche en Astrophysique et Planétologie), the Max-Planck-Institut für Aeronomie of Katlenburg-Lindau (Germany), the Technical University of Braunschweig (Germany) and the University of Giessen (Germany). The initial Principal Investigator is Pr. Hans Balsiger and the actual is Pr. Kathrin Altwegg. The Institut de Recherche en Astrophysique et Planétologie participated in the HV power supplies of the RTOF mass spectrometer (Co-Investigator Pr. Henri Rème), with the support of the Centre National d'Etudes Spatiales (CNES).

The intended performances of the experiment required the combination of three instruments: the Double Focusing Mass Spectrometer (DFMS, see Section 4.4.1), the COmet Pressure Sensor (COPS, see Section 4.4.2) and the Reflectron-type Time-Of-Flight mass spectrometer (RTOF, see Section 4.5). RTOF and DFMS are two complementary mass spectrometers which analyse the composition of neutrals and ions, while COPS monitors the density and velocity of neutrals in the coma. The instruments are located at three different positions on the spacecraft, as seen in Figure 3.1 and are controlled by a Data Processing Unit (DPU).

ROSINA has been a very successful experiment, with the unprecedented analysis of a comet's coma over more than 2 years. It gave important results by analysing the cometary activity along its orbit, witnessing the change of behaviour of the gas composition and density around the nucleus during the equinoxes and perihelion, and by finding many molecules in the coma, previously known or not (see Section 3.5). The composition of the coma is indeed of high interest in cometary science. It gives indications on the composition of the nucleus and eventually constrains the comet's formation conditions in terms of temperature and pressure. ROSINA has also been involved in the study of dust and plasma, even if we will focus on neutral gas detection in this manuscript.

4.2 Science objectives and performance

The scientific objectives of the ROSINA experiment are the in situ analysis of the coma's constitutive gases. Combining the performance of the three instruments, ROSINA has a large mass range[1] (1 u/e to 300 u/e), a high mass resolution[2] ($m/\Delta m > 3000$), a dynamic range[3] of 10^{10} and a sensitivity[4] $>10^{-5}$ A/mbar. The detailed description of ROSINA is given in Balsiger et al. (2007). The two mass spectrometers were conceived to determine the molecular, elemental and isotopic composition of the gases and the pressure sensor to determine the total density, temperature and bulk velocity. The science objectives and measurements requirements are reported in Table 4.1.

4.3 Mass spectrometry

Mass spectrometry is a technique for gas composition analysis by identifying the ratio (of ionised atom and molecule) mass per charge (m/q). Different types of mass spectrometers exist and all require three elements: an ion source to ionise the entering molecules, a mass analyser to separate the ionised atoms and molecules according to their mass/charge ratio, and a detector to collect the ionised particles and convert the current into a digital signal. As the cometary molecules are broken by the ionisation process, it is necessary to know the exact fragmentation pattern of the molecules in order to identify the gas composition.

The ROSINA's spectrometers use two different methods of mass spectrometry to give complementary results. As the RTOF mass spectrometer is the main subject of this work,

---

[1] With u, the unified atomic mass unit and e, the elementary charge

[2] The mass resolution is the ability to separate the peaks of two ions with slightly different masses in the spectra. It is given by the ratio $m/\Delta m$ taken at the peak's Full Width at Half Maximum (FWHM).

[3] The dynamic range is the ratio between the highest and the lowest peak intensity.

[4] The sensitivity is expressed in A/mbar, which corresponds to 0.2 counts/s if density is in cm^{-3}.

Scientific objectives	**Associated critical measurements**	**Measurement requirements**
Determine elemental abundances in the gas	Separate CO from N_2	Mass resolution $<$ 2500 at 1% of the peak height at mass 28 amu
Determine molecular composition of volatiles	Measure and separate heavy hydrocarbons	Mass range 1 to $>$ 300 amu with a resolution of 300 at 1%; sensitivity $>$ 10^{-3} A/mbar
Determine isotopic composition of volatiles	Separate ^{12}CH and ^{13}C. Measure HDO DCN and other deuterated neutrals and ions	Mass resolution$>$ 3000 at 1%, absolute accuracy 10%
Study the development of the cometary activity	Measure the composition between 3.5 AU and perihelion	Mass range 1 to$>$ 300 amu, dynamic range 10^8
Study of the coma chemistry ant test existing models	Measure ions and molecules in the mass range 1-300 amu, their velocity and temperature	Mass range for ions and neutrals 1 to $>$ 300 amu, dynamic range 10^8, sensitivity $>$ 10^{-3} A/mbar
Study of the gas dynamics and the interaction with the dust	Measurement of the bulk velocity and temperature of the gas	Bulk velocity corresponding to E=0.02 eV ± 10%, temperature = 0.01 eV ± 20%
Characterisation of the nucleus	Characterisation of outbursts and jets of limited angular extent	2 degrees narrow field of view, time resolution = 1 min
Characterisation of asteroids	Detect asteroid exosphere or determine upper limit	Extreme sensitivity for H_2O, CO and CO_2.

Table 4.1: Scientific objectives, critical measurements and measurement requirements of the ROSINA experiment (Balsiger et al., 2007).

we focus our description on the principle of its method of mass analysis: the time-of-flight mass spectrometry.

4.3.1 Time-of-flight mass spectrometry

Time-Of-Flight (TOF) mass spectrometers are able to recognize the nature of an ion thanks to the time needed to move through the instrument, based on the following principle: for a similar energy, a light particle will reach the detector faster than a heavier one. Such a technique gives a spectrum of the complete mass range at each measurement and does not require mass scanning. A first linear TOF mass spectrometer was introduced by Wiley and McLaren (1955). A schematic representation of the principle is shown in Figure 4.1, with a resulting typical TOF spectrum. Mass spectrometers contain three sections: (1) the ionisation region, where the incident atoms and molecules are ionised (typically by electron impact ionisation), (2) the acceleration region, which accelerates the newly charged ions thanks to an electric potential difference, and sends them through (3) a field free drift region where the ions have a constant velocity before finally reaching the detector.

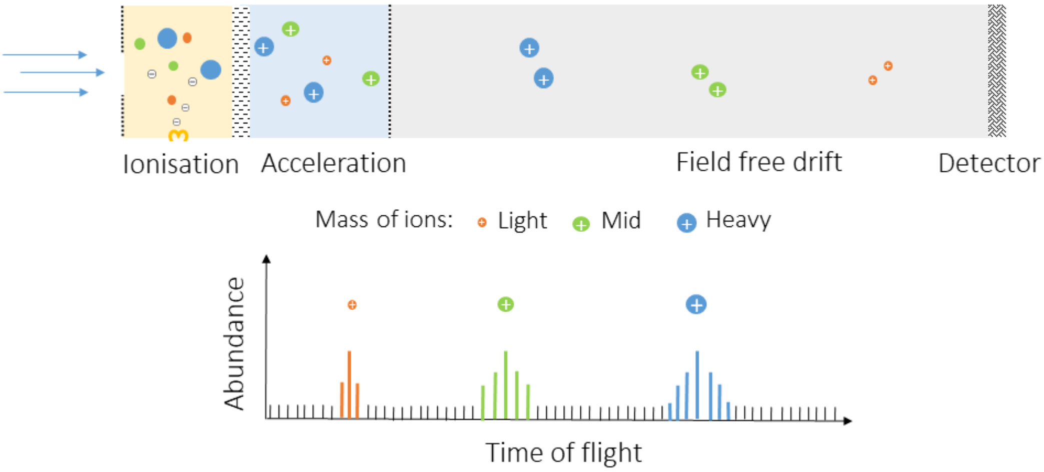

Figure 4.1: Sketch of a linear Time-Of-Flight mass spectrometer. The atoms and molecules are first ionised. All ions receive the same kinetic energy. They are separated by their masses in the acceleration region, sent in a field free drift region before they finally reach a detector. The lighter ions (with the smaller mass/ratio) travel faster and are the first detected. Lower figure: a corresponding typical TOF spectrum, in abundance versus time-of-flight. The resolution decreases with the mass, leading to broader peaks for the heavier masses.

An ion of charge q that travels through a difference of potential U gains an energy qU (4.1). The main idea of a TOF mass spectrometer is to give the same energy to all ions so that their speed v only depends on their mass m (4.2).

$$qU = \frac{1}{2}mv^2 \tag{4.1}$$

$$v = \sqrt{\frac{2qU}{m}} \tag{4.2}$$

The ions with a small mass-per-charge ratio will move faster and reach the detector before the ions with a higher mass-per-charge ratio. In this ideal case, the ions with the same mass-per-charge ratio which start at the same time should arrive together at the detector after a time t defined as the length path L divided by the speed v (4.3). Indeed, the time of flight of each ion is proportional to the square root of the mass of the species.

$$t = L\sqrt{\frac{m}{2qU}} \tag{4.3}$$

Linear TOF mass spectrometers are relatively simple instruments, easy to construct and commonly used. However, the performance are limited by three effects which induce a broadening of the peaks in the spectra and thus decrease the mass resolution:

- The spatial distribution. Two ions of the same mass/charge can receive a slightly different amount of energy as they are not exactly located at the same distance from the extraction grid, as shown in Figure 4.2 (a).
- The kinetic energy distribution is the time delay due to the initial direction of motion of the ions, as shown in Figure 4.2 (b). Two ions at the same distance from the grid can have different initial velocity vectors. One will eventually need to turn around before travelling through the grid.
- The temporal distribution is due to ionisation which occurs during the extraction pulse. An ion produced at the end of the pull pulse will be delayed compared to the ion extracted at the beginning of the pulse. Nevertheless, the highly negative charge of the grid during the pulse repels the electron beam and stops the ionisation of the molecules in the ion source.

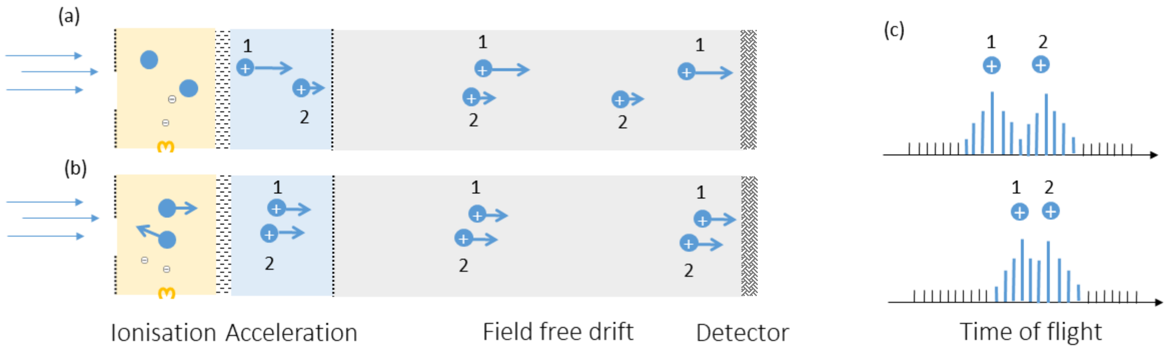

Figure 4.2: Sketch of the time spread due to spatial distribution (a) and kinetic energy distribution (b). The ions with same m/q have slightly different speeds and the mass resolution decreases, leading to a broadening (and eventually overlap) of the peaks (c).

The introduction of an electrostatic ion mirror or reflectron was developed by Mamyrin et al. (1973) to compensate the errors due to the spatial distribution and the kinetic energy

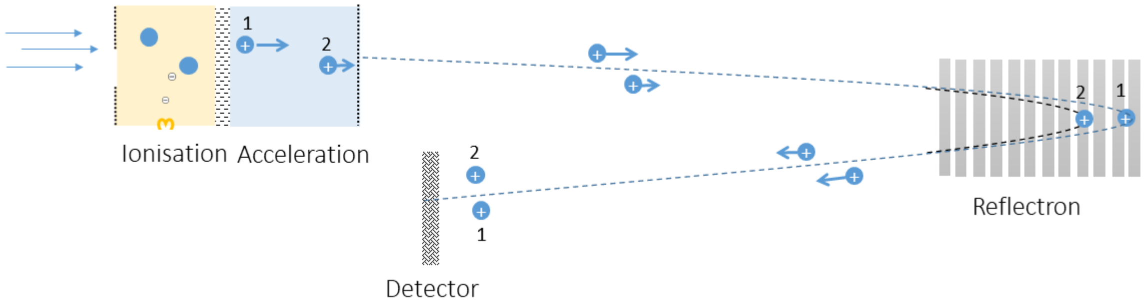

Figure 4.3: Sketch of a Time-Of-Flight mass spectrometer equipped with a reflectron. The introduction of a reflectron compensates for the spatial and kinetic energy distributions by synchronising the ions in time, which increases the mass resolution.

distribution. The reflectron consists in a uniform electrostatic field able to decelerate the ions and reverse their direction. The detector is now placed on the same side as the ion source. Firstly, this added electromagnetic element increases the time resolution by doubling the flight path of the ions, without increasing the size of the instrument (critical parameter for space science). Secondly, as shown in Figure 4.3, two ions (1 and 2) with same m/q but different locations will get different kinetic energies and will therefore penetrate more or less deeply in the reflectron; the ion with the smaller velocity (2) will turn around earlier and will be focused at the same time as the other one when reaching the detector. In this way, both kinetic energy and spatial distributions are compensated. RTOF is a time-of-flight mass spectrometer equipped with a reflectron, as described in details in Section 4.5.

4.4 Description of the ROSINA instruments

We now describe the three instruments of the ROSINA experiment. A general overview of DFMS, RTOF and COPS is given, with a more detailed description for the RTOF mass spectrometer's principle, components and operating modes.

4.4.1 The Double Focusing Mass Spectrometer

DFMS was designed to measure the composition of the cometary neutral gas as well as cometary ions (Balsiger et al., 2007). It has a high mass resolution of $m/\Delta m = 3000$ at 1% level, capable to resolve CO from N_2 and ^{13}C from ^{12}CH, and a high sensitivity of 10^{-5} A/mbar, with a mass range of 12-150 amu. DFMS is a mass spectrometer of 63 × 63 × 26 cm for a mass of 16.2 kg and is shown in Figure 4.4. It has two different viewing directions with different fields of view (FOV) of $20^\circ \times 20^\circ$ and $2^\circ \times 2^\circ$ and requires 19 W during nominal operations.

It has two operating modes: the gas mode and the ion mode. The gas is first ionized in the instrument by electron impact. The mass analyser is a combination of a 90 degrees deflection electrostatic analyzer and a 60 degrees deflection magnetic analyser. A mass scan is achieved mass-by-mass by varying the sensor potentials. The integration time per mass is 20 seconds, leading to a lower temporal resolution for each species than for RTOF (e.g. about 40 minutes for H_2O).

4.4.2 The COmet Pressure Sensor

COPS was a reference point for the instruments aboard Rosetta; it gives a measure of the comet activity. It was used to alert the instruments in case of critically high pressures and to normalise the DFMS and RTOF data. For safety reasons, the spectrometers must be switched off at 10^{-7} mbar while COPS can be operated up to 10^{-5} mbar. The instrument measures 26 × 26 × 17 cm for a mass of 1.6 kg and requires 3 W during nominal operations.

The COPS instrument consists of two separate sensors, i.e. the Nude Gauge (NG) and the Ram Gauge (RG). In Figure 4.4, a picture of COPS is shown, where the horizontal gauge is the NG and the vertical gauge is the RG. They are both based on the extractor gauge developed by Redhead (1966). On the spacecraft, the nude gauge is parallel to the solar panels and the ram gauge is perpendicular to the instrument platform (i.e. it points most of the time towards the comet).

The NG measures the total ambient neutral pressure and number density (with no separation between the species). It measures pressures from 4×10^{-11} mbar to 10^{-5} mbar. It is composed of two filaments (one used and one back-up), two nested cylindrical grids (the outer grid at -12 V and the inner grid at 180 V), a base plate, a reflector and an ion collector. The entering gas is ionised by electrons emitted by one filament. The ionised atoms and molecules are collected by a cathode (ion collector) located under the base plate. The cathode is in the center of an hemispherical reflector, which increases the current. The total neutral density is proportional to the measured current.

The RG measures the ram pressure of the expanding cometary atmosphere. As seen in Section 4.4, the vertical raw gauge is terminated by a sloted equilibium sphere. Inside, the configuration of the ionisation volume is similar to the NG, with an anode grid at 180 V, a base plate, and with an ion collector in the center of a hemispherical reflector. A plane electron emitter replaces the filament between the grid and the gauge, facing an electron repeller. The cometary gas enters through a 6 mm hole at the spherical extremity of the gauge, and multiple reflections cause a compression of the gas. The ions are attracted in the node grid and accelerated to the base plane and the reflector.

COPS densities are used to convert DFMS and RTOF data in units of densities. The pressure and density are linked by the perfect gas equation $P = nkT$, where P is the pressure in Pascal, n the density number of gas particles per m^{-3}, k the Boltzman constant $1.38 \times 10^{-23}\mathrm{J\ K}^{-1}$ and T the temperature in K. The gauges were calibrated with N_2 gas, as it is the easiest to use in laboratory conditions at 20 °C. As COPS does not distinguish between the different species present in the gas, a correction factor β_{tot} is calculated based on the relative abundance species measured by DFMS or RTOF, and will be developed in the next chapter.

4.5 The Reflectron-type Time-Of-Flight mass spectrometer

The instrument has dimensions of 114 × 38 × 24 cm, weighs 14.7 kg and requires 24 W during nominal operations. A picture of RTOF is shown in Figure 4.5. It has a field of view of 10° × 40° and is characterised by a large mass range, a high sensitivity, and a high temporal resolution. RTOF mass resolution is $m/\Delta m = 500$ at 50% level. It is able

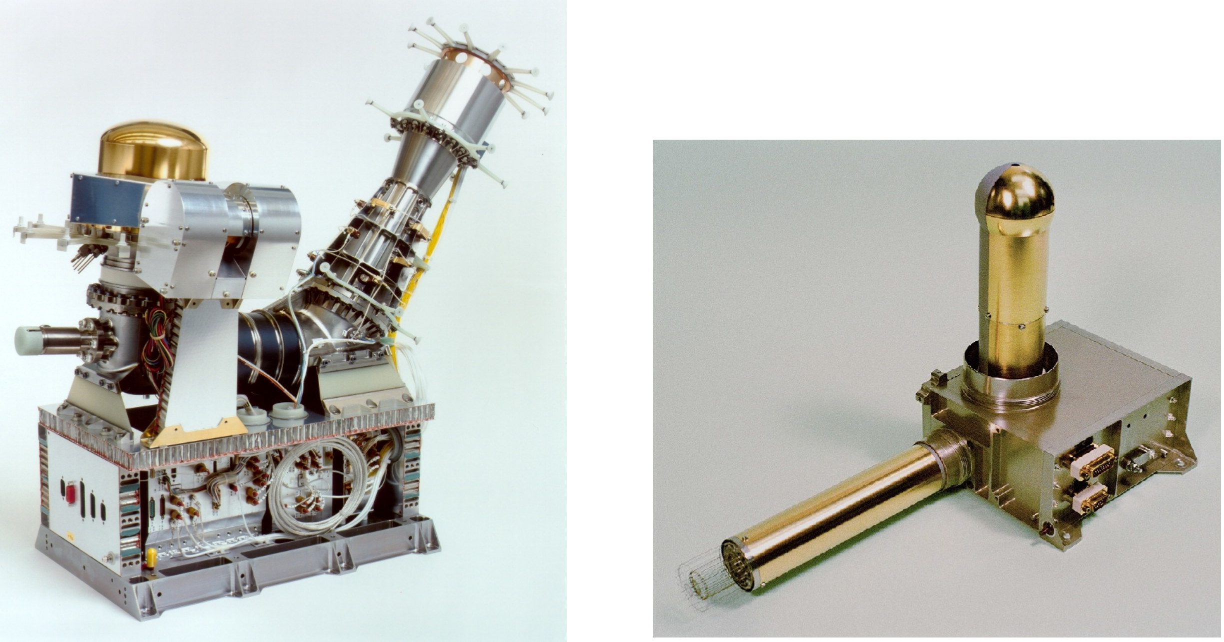

Figure 4.4: Picture of ROSINA/DFMS (left), an instrument of 63 × 63 × 26 cm for a mass of 16.2 kg. Picture of ROSINA/COPS (right), an instrument of 26 × 26 × 17 cm for a mass of 1.6. Credits: University of Bern.

to detect ions and molecules from 1 amu/e (Hydrogen) to 300 amu/e (organic molecules) in the nominal case. Depending on the modes of RTOF, the temporal resolution is 200 seconds or 400 seconds. A detailed description of the RTOF mass spectrometer is given in Scherer et al. (2006) and Balsiger et al. (2007).

4.5.1 Instrument description

RTOF is a Time-Of-Flight (TOF) mass spectrometer as described in Section 4.3.1. In addition to the main components of a simple linear TOF mass spectrometer, RTOF possesses an integrated reflectron and a hard mirror, which increases the mass range and the resolution by elongating the flight path of the molecules in a fixed length instrument. The use of a reflectron also compensates the energy dispersion due to spatial and kinetic energy distribution in an ions pack. Two spectrometers are functional in the RTOF structure. In fact, it can be operated in two different configurations using two distinct channels. The two spectrometers share the same reflectron and hard mirror, but have their own ion source, detector and acquisition system. The instrument can be calibrated in flight thanks to a gas calibration unit. A schematic of the instrument is given in Figure 4.6.

Ion sources

The two ions sources inside RTOF are the electron impact storage source or Storage Source (SS) and the orthogonal extraction ion source or Orthogonal Source (OS).

The Storage Source is optimised to sample the neutral gas, while the Orthogonal Source is capable of analysing cometary ions as well as neutral gas atoms. The first step

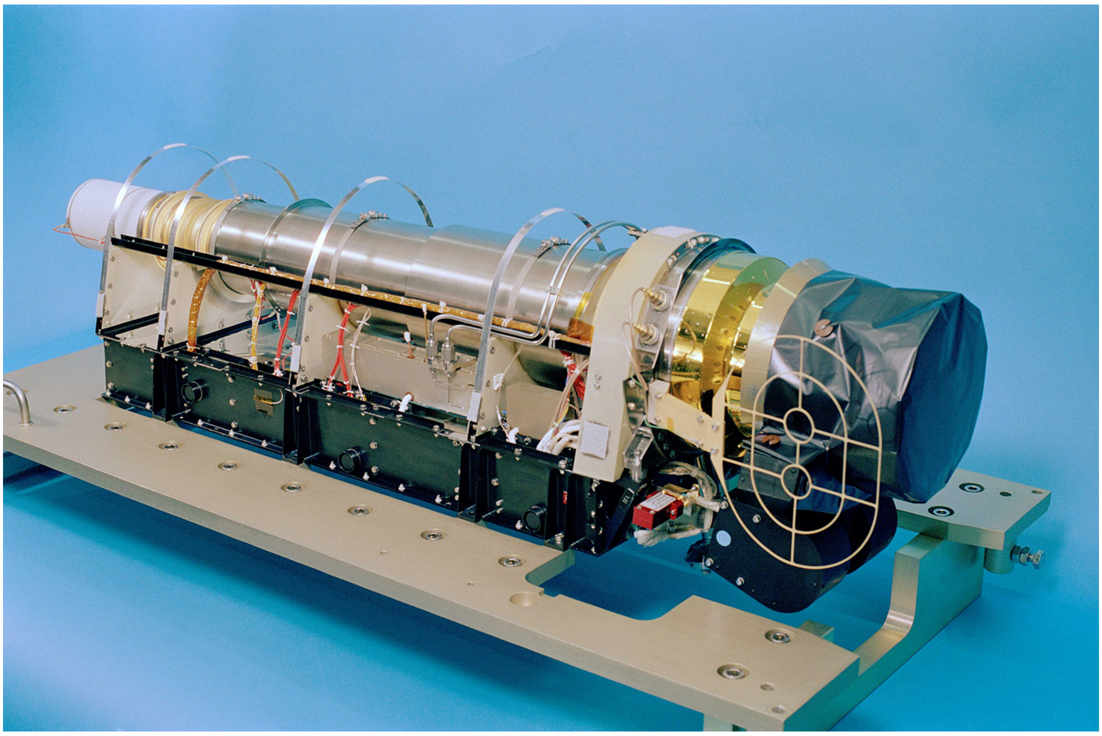

Figure 4.5: Picture of ROSINA/RTOF, an instrument of 114 × 38 × 24 cm for a mass of 14.7 kg. Credits: University of Bern.

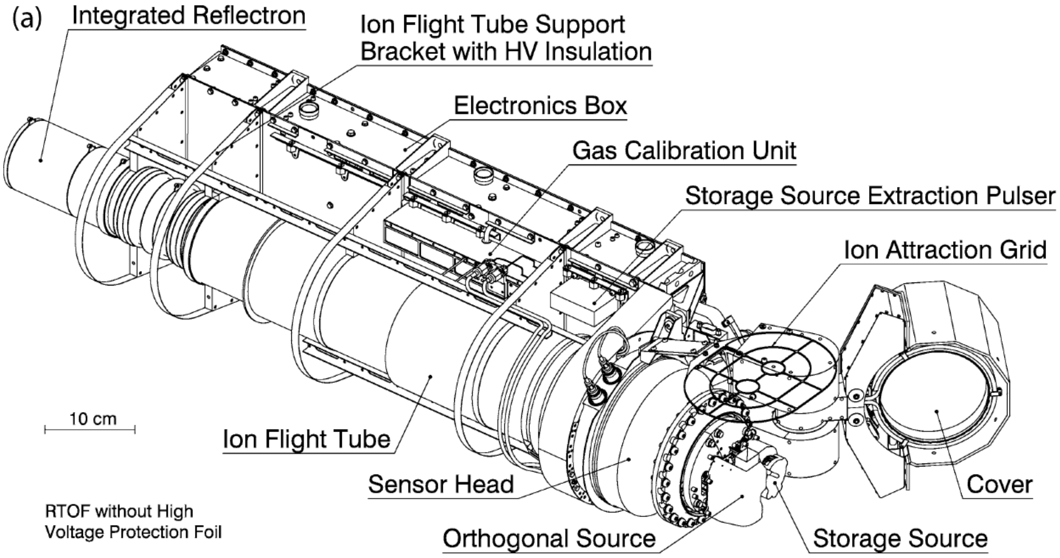

Figure 4.6: Schematic of the RTOF mass spectrometer (Balsiger et al., 2007).

is the ionisation of the entering neutral gas by one of the ion sources. Each ion source has two tungsten filaments (for redundancy reasons) able to ionise the neutrals by electron impact ionisation process. The process consists in heating a filament to create an electron

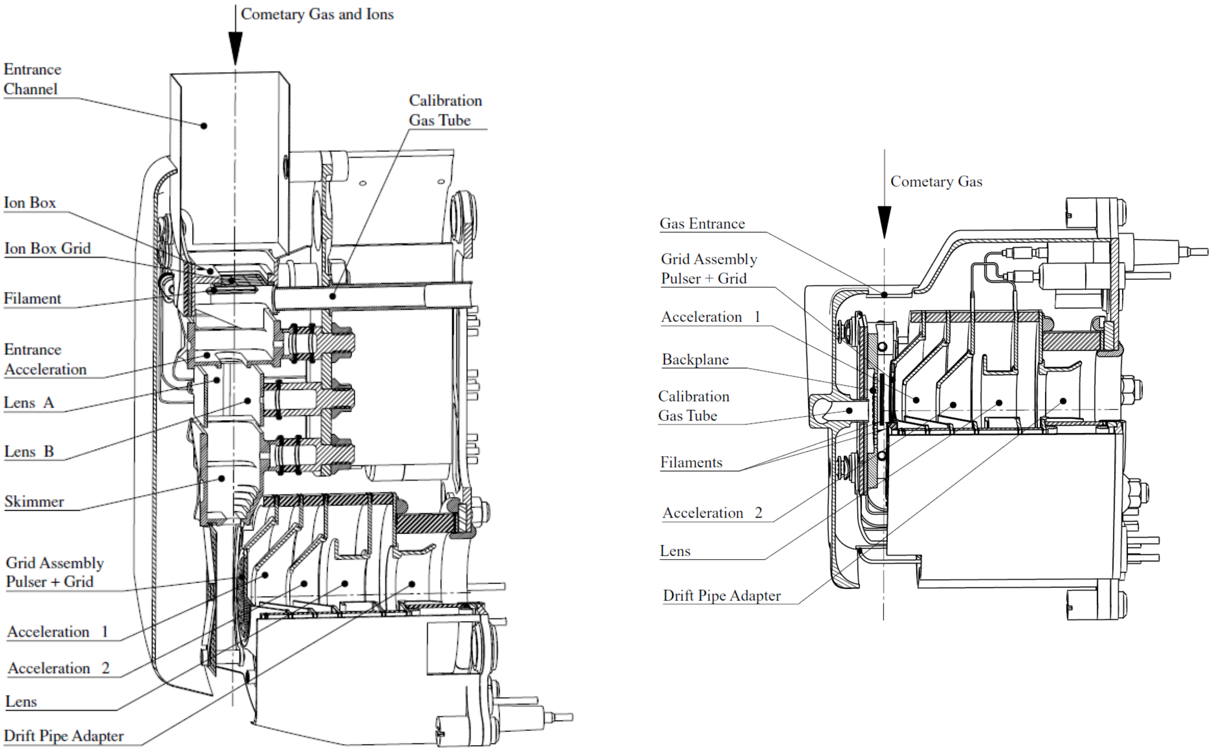

Figure 4.7: Schematics of the two RTOF's ion sources: Orthogonal Source (left) and Storage Source (right). From Balsiger et al. (2007).

beam with a typical energy of 70 eV. The energy of the electron is given by the potential difference between the filament and the ionisation regions. The acceleration region is located between the grid and the drift tube, and consists of three electrodes (Acceleration 1, Acceleration 2 and Source Lens) shown in Figure 4.7.

The bombardment of electrons will perturb the electron cloud of the neutral atoms or molecules, extract one (or more) electron(s) and lead to a fragmentation, depending on the electron beam energy. The SS channel stores the produced ions between a backplane and the extraction grid, until the pulse. The positively charged grid keeps the ions in the ionisation region between two pulses. It becomes negative for a 100th of nanoseconds (*pull pulse*) to extract the ions in the acceleration region.

Reflectron and hard mirror

The reflectron is located at the end of a field free drift tube. The ions lose two-thirds of their kinetic energy in a part called retarding region, then arrive in the repelling region from where they are sent back in the tube until they reach the detector (simple-reflection mode). An integrated lens is located just before the reflectron in the tube. By changing the voltage applied on the lens, one can change the orientation of the ion beam. In triple-reflection mode, the particles are repelled at the reflectron to reach a hard mirror (located on the ion sources' side of the tube) which sends them back again into the reflectron, and then through the drift tube where they finally reach the detector. Simple and triple-reflection modes are illustrated in Figure 4.8. The elongation of the flight path results in an increase of the mass resolution.

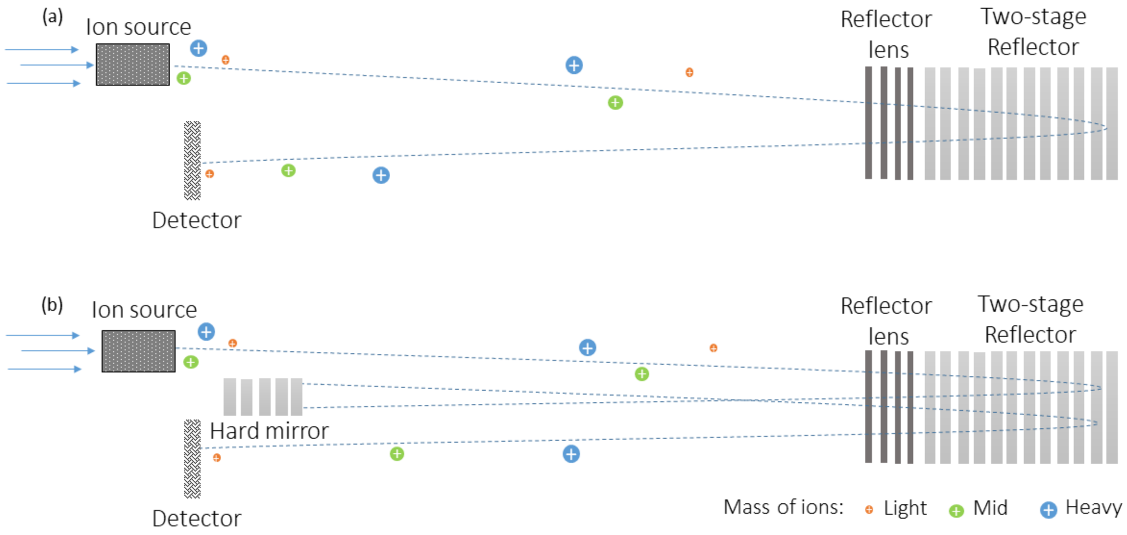

Figure 4.8: Sketch of simple-reflection mode (a) and triple reflection modes (b). The elongation of the path induced by the triple reflection modes increases the mass resolution.

Gas Calibration Unit

A Gas Calibration Unit (GCU) contains a well calibrated gas mixture. The gas is released in the sources to calibrate the instrument. To cover a large range of mass, the mixture contains 1/3 of helium, 1/3 of carbon dioxide and 1/3 of krypton. helium is the lightest noble gas with a mass m = 4.002 u, inert and not found in comet which avoids contamination; CO_2 is a molecule with a mass m = 43.99 u and with a well known fragmentation pattern visible in the center of the spectrum; and Kr, a heavy noble gas with a mass m = 83.91 u with several known abundant isotopes.

4.5.2 Principle

A cover protects the instrument and can be opened in different positions, from completely opened (position 1) to closed (position 20), in case of high activity or the presence of dust. The cometary gas is ionised by electron impact ionisation in one of the ion sources. The newly charged particles are extracted towards the drift tube by an extraction grid. In simple-reflection mode, the particles go through the 83 cm long drift tube, are deviated back by the reflectron located at the end of the tube, and finally reach the detector. In triple-reflection mode, the particle are repelled at the reflectron to reach a hard mirror which sends them back again into the reflectron to go through the drift tube and finally reach the detector.

4.5.3 Operating modes

The instrument can be operated in science mode, using either the OS channel or the SS channel as well as in calibration mode (GCU for OS and for SS). Considering the limitations of the data rate and the compression of the data by the DPU, both OS and

SS channels are almost never used at the same time.

There are three different filament emissions: low emission (LE) at 20 μA, medium emission (ME) at 100 μA and high emission (HE) at 200 μA; and three different frequencies for the extraction: 2 kHz, 5 kHz or 10 kHz. The detection of heavy masses requires more time, therefore the frequency of 10 kHz allows detection until maximal masses of 120 u/e, the frequency of 5 kHz allows the detection of masses until 350 u/e and the frequency of 2 kHz reaches very heavy mass until 1200 u/e.

4.5.4 In flight performance limitations

In September 2004, discharges occurred in the 9 kV high voltage converter, leading to instabilities of the instrument and to an important reduction of the highest voltage applicable. A quick switch on and switch off of the HV power supply has been found as a solution to apply a 2 kV voltage and avoid discharges. This regulation was applied on either the OS source lens, or the SS source lens or the hard mirror electronic. From this solution, the triple-mode reflection could not be used for both OS and SS simultaneously, as the hard mirror can not be implied in the reflection if used for the regulation. Nevertheless, the triple-reflection mode has not been used during the mission. The intensity of the peaks has been degraded by the reduced highest voltage achievable (2 kV instead of 9 kV) and the speed of ions. As the peaks in the triple-reflection mode would have been even smaller than in simple-reflection mode, the optimisation campaign focused on the simple-reflection modes.

An important part of this thesis consists in the optimisation of the degraded performances through a detailed analysis of the spectra, as explained in the next part.

Chapter 5

Data analysis of RTOF spectra

The calibration and data analysis/interpretation of the RTOF spectra, with the help of the PI team (University of Bern), stands for the major part of my thesis work. We detail in this chapter the different steps of the data analysis, as schematised in Figure 5.1: the RTOF raw spectra corrections (see Section 5.1), the mass calibration and integration of the peaks (see Section 5.2), and finally the conversion in volatiles density (see Section 5.3).

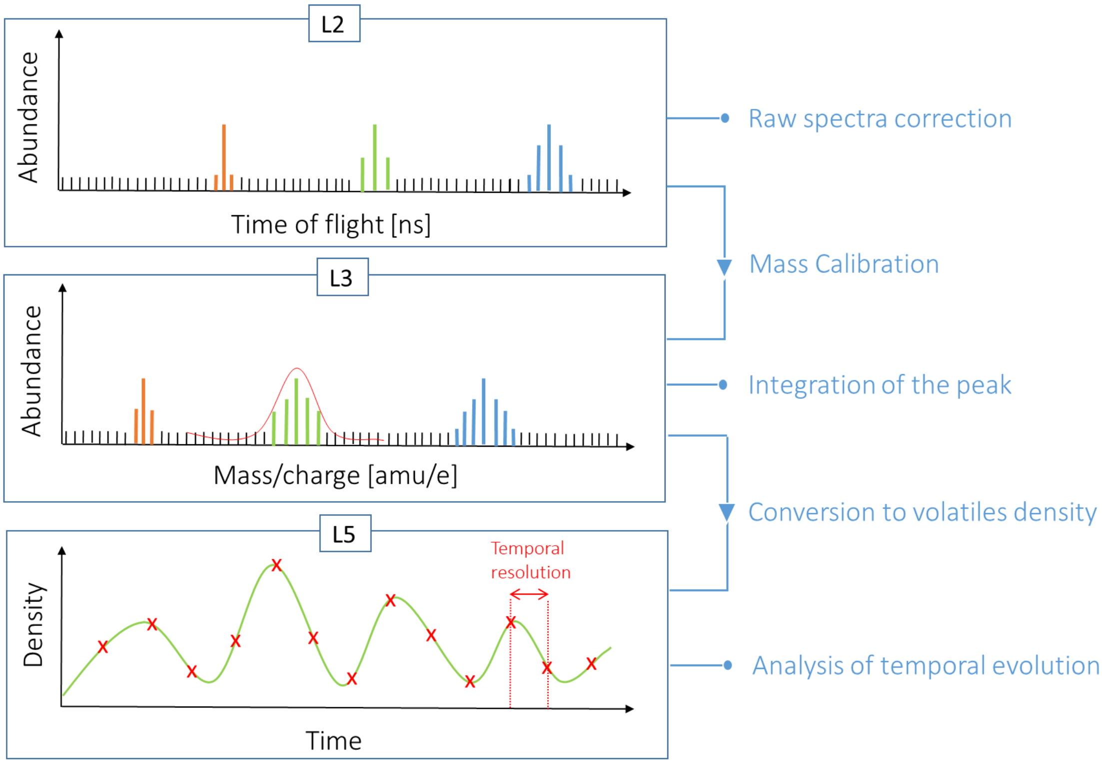

Figure 5.1: Schematic of the data analysis: L2 are the raw RTOF spectra, L3 are the mass calibrated spectra and L5 are the temporal evolutions for species density (note that there are no L4 spectra for RTOF).

5.1 RTOF raw spectra

The raw data from RTOF provide abundances (in arbitrary unit) versus time-of-flight, identified as Level 2 (L2) spectra. They associate a number of detected events to each bin of 1.65 nanoseconds time-of-flight. The instrument either operated in OS mode, using the orthogonal extraction ion source channel, or in SS mode, using the electron impact storage ion source. Periodically, a few spectra were recorded using the GCU mode to calibrate the science spectra regularly.

The modes SS M0521 and OS M0523, as well as their corresponding GCU mode SS M0181 and OS M0183 have been the most used during the mission. This work will concern exclusively those four operational modes. These modes correspond to an extraction frequency of 10 kHz, a filament emission of 200 μA and acquisition time of 200 s. RTOF recorded spectra in different modes, including SS M0522 and OS M0524, the corresponding modes of M0521 and M0523 with an acquisition time of 400 seconds.

5.1.1 Acquisition

In each channel, the signal is amplified by dedicated Micro Channel Plates (MCP) and processed by data acquisition boards. In OS mode, a Time to Digital Converter (TDC) converts the signal in a number of *events*. It counts one event each time a threshold level is reached, assuming that only one ion reaches the detector at a given time. In SS mode, multiple ions are expected to arrive at the same time due to the storage. Analog to Digital Converters (ADC) convert the signal into a numerical value. It analyses the intensity of the current to deduce the number of ions reaching the detector. They allow to detect the presence of multiple particles in the acquisition time. ADC are not used in OS mode, as the detection of ions were expected to be low, in which case the TDC and ADC are redundant.

5.1.2 ADC Correction

There are sixteen ADCs with singular responses, producing an ADC pattern, which needs to be corrected in the RTOF SS spectra. With this correction, the SS spectra show a higher signal to noise ratio and a smaller dispersion. One example of ADC pattern is shown in Figure 5.2 (left) as well as the same part of the spectra after ADC correction (right).

5.1.3 Baseline

One important feature in the RTOF spectra is the high level of the baseline, i.e. the level of counts between the peaks. In addition, variations of the baseline through the mission have been observed, from approximately 10 to 10^4 in SS mode and from 10 to 100 in OS mode. The signal can be hidden if the level of noise is too important, and the area under the peaks can appear smaller. The variations of the baseline have been linked with the solar array angle variation, suggesting that the baseline level was dependent on the solar radiation.

The optimisation campaign was lead by A. Jäckel and S. Gasc (University of Bern). They tentatively improved the signal to noise ratio by reducing the noise level. Different

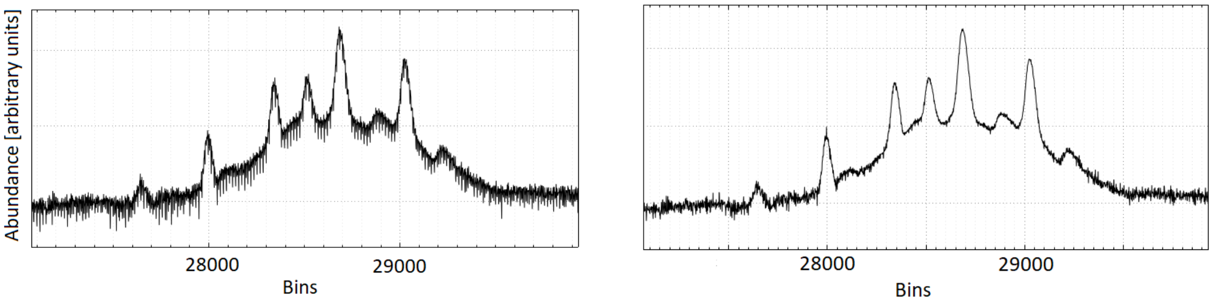

Figure 5.2: Denoising of the ADC pattern. Zoom on a SS spectrum before (left) and after (right) ADC correction.

solutions were tried to improve the quality of the spectra such as protecting the entries of the sources from stray light by modifying the cover position from 1 to 14, try weaker filament emission and change the threshold value of detection (THD).

Another feature was seen in some spectra: one or more vertical shifts in the baseline level (*byte-shift*) were present and have been corrected spectrum by spectrum.

5.1.4 Electronic noise and other non desirable peaks

The spectrum cleanout also concerns the identification of peaks that are not real compounds and do not originate from the comet. The determination of those peaks was investigated by S. Gasc who found out that a large series of peaks appears periodically spaced in the spectra and have the same shape (thin FWHM) regardless of their time of flight. The peaks do not move with the changes in voltages, which confirms that they are not due to impacting molecules and are probably linked to the reading electronics. This series of peaks is called *electronic noise* and shown in Figure 5.3. These peaks are cleaned out from the final spectra.

In addition, four notable peaks sometimes appear at the masses 12, 15.9, 17 and 19 in SS modes and have to be studied with caution. As they slightly change location with the variations of applied voltages, they are suspected to be real compounds but their origin are still being discussed.

5.2 RTOF L3 spectra

5.2.1 Mass calibration

The analysis and interpretation of the data require the conversion of L2 data into physical units, called level 3 (L3) data. A mass scaling is needed to convert the L2 spectra (abundance versus time-of-flight) into L3 spectra which gives abundance [ions/s] versus mass/charge ratio [u/e].

To get the mass of an ion from its time-of-flight, one has to choose N reference elements (typically 3 or more) of theoretical masses m_i and time-of-flight t_i to determine the parameters C and t_0 defined as in equations 5.1 and 5.2.

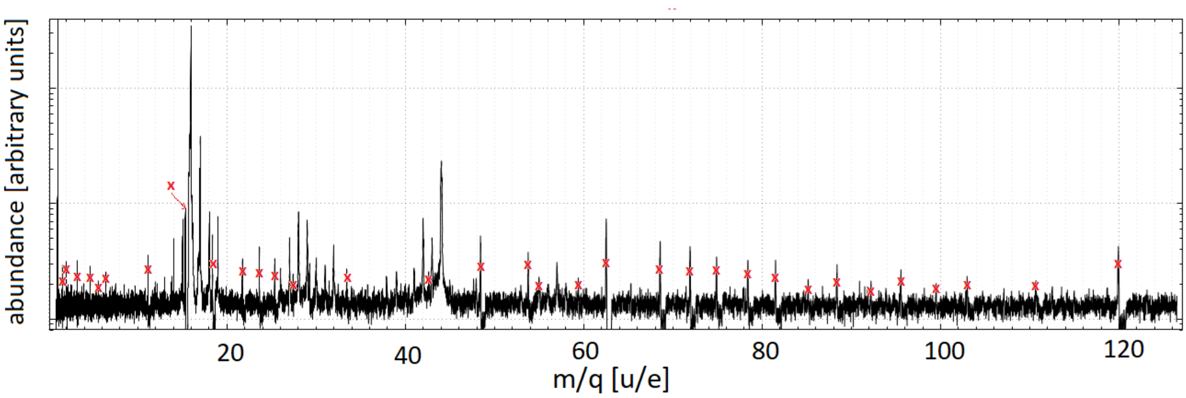

Figure 5.3: Electronic peaks (indicated with red crosses) in a SS spectrum. Credits: S. Gasc.

$$C = \frac{N\sum_{i=1}^{N} t_i^2 - (\sum_{i=1}^{N} t_i)^2}{N\sum_{i=1}^{N}(\sqrt{m_i} t_i) - \sum_{i=1}^{N}\sqrt{m_i}\sum_{i=1}^{N} t_i} \tag{5.1}$$

$$t_o = \frac{\sum_{i=1}^{N}(\sqrt{m_i} t_i)\sum_{i=1}^{N} t_i - \sum_{i=1}^{N}\sqrt{m_i}\sum_{i=1}^{N} t_i^2}{N\sum_{i=1}^{N}(\sqrt{m_i} t_i) - \sum_{i=1}^{N}\sqrt{m_i}\sum_{i=1}^{N} t_i} \tag{5.2}$$

For the calculated values of C and t_0, the delay t between two pulses leads to the mass m of the particle:

$$m = (\frac{t - t_o}{C})^2 \tag{5.3}$$

The mass calibration is helped by the Gas Calibration Unit described in Section 4.5.1. In GCU mode, instead of analysing cometary gas, RTOF analyses the well-know mixture of the unit. In the GCU spectra, the helium, carbon dioxide and krypton peaks are the chosen reference masses t_0. The peak fitting is based on a pseudo-Voigt function [1], which takes background, baseline, and electronic noise into account.

We reported the time-of-flight of four reference peaks identified in GCU spectra: He, CO, CO_2 and ^{84}Kr, in SS mode (Table 5.1) and in OS mode (Table 5.2). Those chosen elements' masses and positions allow to determine C and t_0 thanks to the relation 5.1 and 5.2. With those two examples, we obtained C = 3127.18 and t_0 = 27.11 for the OS mode and C = 3056.27 and t_0 = 28.64 for SS mode. They allow to scale the entire L2 spectra into L3 spectra, as shown in Figure 5.4. Those values are not constant, they slightly varied and GCU modes have been used few times a week in order to have precise mass calibrations.

Species	Mass (amu/e)	Deviation (ppm)	TOF (ns)
He	4.002	-221	6283.7
CO	27.994	108	16572
CO_2	43.989	55	20767.4
^{84}Kr	83.91	-55	28673.8

Table 5.1: Time-of-flight (TOF) of four reference peaks in a GCU SS mode, with the deviation between the theoretical masses and the masses calculated with the C and t_0 obtained values.

Specie	Mass (amu/e)	Deviation (ppm)	TOF (ns)
He	4.002	83	6142.5
CO	27.994	-10	16199.4
CO_2	43.989	11	20299.1
^{84}Kr	83.91	4	28024.93

Table 5.2: Time-of-flight (TOF) of four reference peaks in a GCU OS mode, with the deviation between the theoretical masses and the masses calculated with the C and t_0 obtained values.

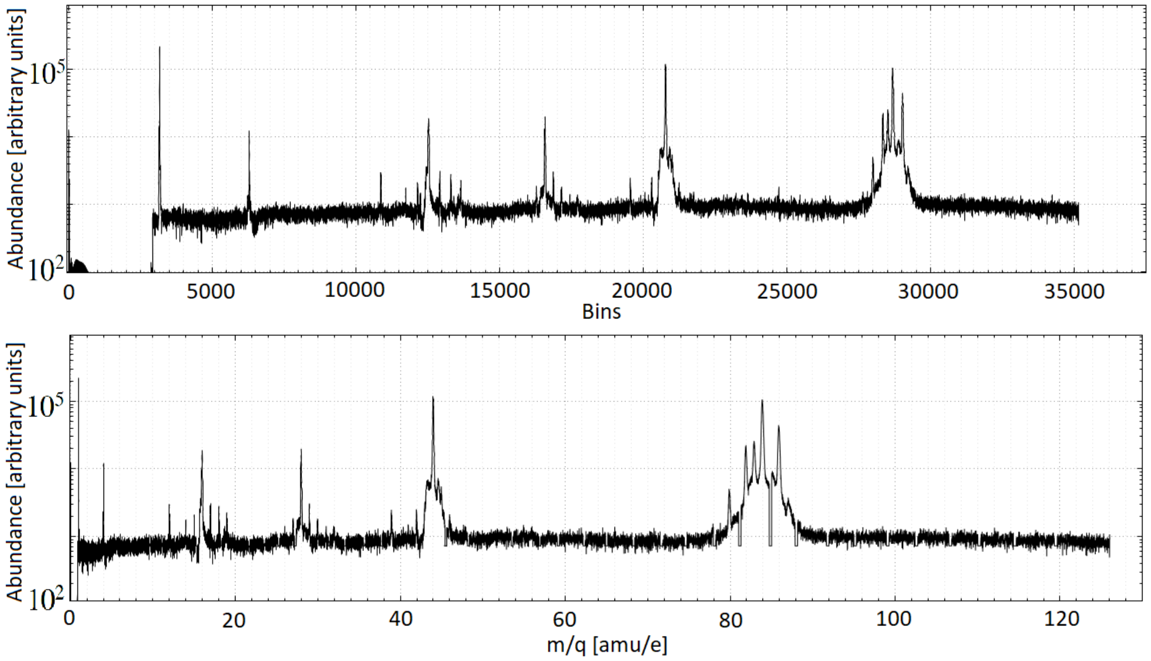

Figure 5.4: Mass scale of a level 2 GCU spectrum (upper figure) to a level 3 spectrum (lower figure) and electronic peaks correction.

Using the GCU spectra recorded in flight, we calculated the value C and t_0 over the whole mission and achieved the mass calibration of 104 592 spectra: 82 256 SS spectra

---

[1] Approximation of the Voigt function, which is a convolution of a Lorentzian and a Gaussian. The pseudo-Voigt approximation uses a linear combination instead of a convolution

and 22 336 OS spectra.

5.2.2 Abundance of volatiles

The peak fitting method has been applied to obtain the L3 spectra, as shown in Figure 5.5 for the peaks of cometary water, carbon oxide and carbon dioxide. The areas under the peaks give the number of ions reaching the detector in 200 s or 400 s depending on the mode.

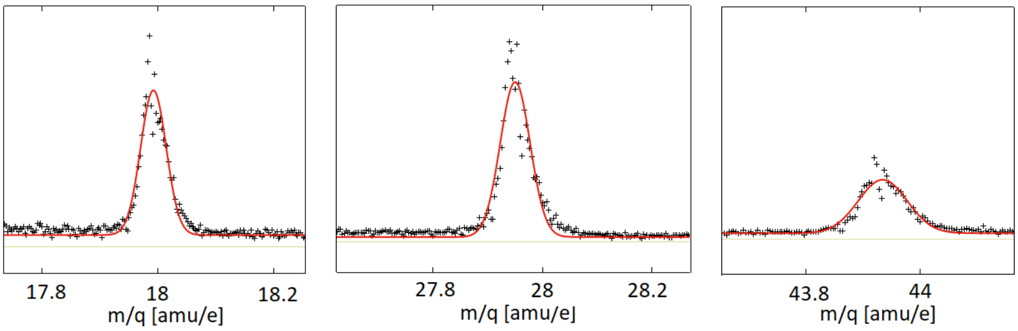

Figure 5.5: Zoom of a L3 RTOF spectra: peaks of H_2O, CO and CO2 with the pseudo-Voigt function's fitting in red. The fitting appeared to be a non-convincing method of quantification, and was substituted by a numerical integration.

However, the peak shape is not perfect and not always symmetrical through the numerous optimisations. Thus, if the pseudo-Voigt function gives satisfying fitting for the calibration (as only the position of the maximum is needed), the fitting is not the best solution for the determination of the abundance of species. A numerical integration approach more closely approximates the total abundance of a species than the theoretical area under the peak. The integration sums the number of counts in an area defined by 3 σ (i.e. about 99% of the counts) around the center of the peak.

Mass scaling, peak fitting and integration were performed with the Spectra Analyser software (see Figure 5.6 developed and provided by S. Gasc (University of Bern). I wrote a user tutorial and helped in the development of the software by testing and improving the different versions.

5.3 Conversion to volatiles density

To convert the abundances (ions/s) into densities, one needs to derive the relative abundances, to take into account the specific sensitivity and fragmentation pattern of each species and modes, and then to scale the results to the COPS total densities (Gasc et al., 2017b). We detail in the next sections the fragmentation ratios and sensitivities for the three molecules H_2O, CO_2 and CO and the COPS calibration.

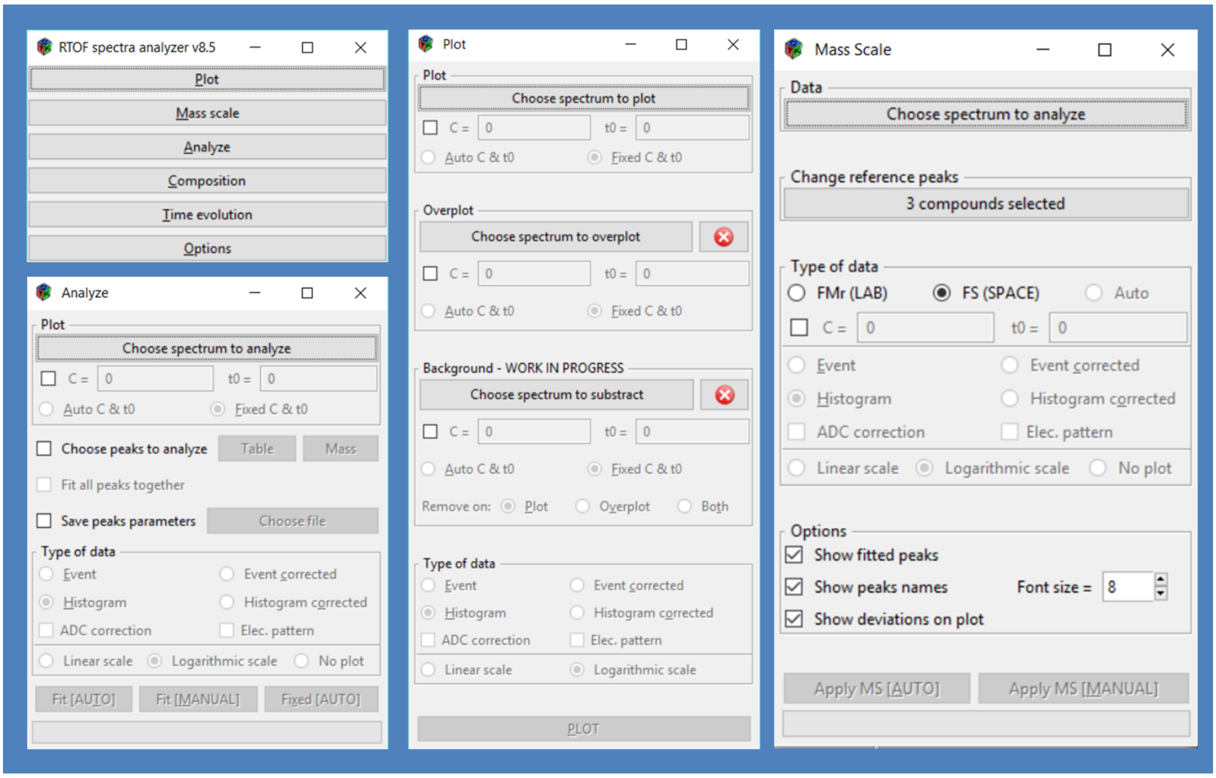

Figure 5.6: Main interfaces of the RTOF spectra analyser software (version 8.5), developed by S. Gasc and tested in Toulouse.

5.3.1 Fragmentation

The fragmentation patterns allow for the identification of the species, while the sensitivity values (see 5.3.2) give the quantification. Inside the ion source, the electrons ionise the entering molecules by disturbing their electronic cloud, which can eventually lead to a fragmentation of the molecules. The fragment corresponding to the initial ionised molecule is the *parent* and the other fragments are called the *daughters*.

We focus our work on the most abundant species of the coma, H_2O, CO and CO_2. The first electron impact ionises those molecules into respectively H_2O^+, CO^+ and CO_2^+. These three parent molecules' fragmentations are described below:

$$H_2O + e^- \longrightarrow H_2O^+, H_2O^{++}, OH^+, H^+, O^+ \tag{5.4}$$

$$CO + e^- \longrightarrow CO^+, C^+, O^+ \tag{5.5}$$

$$CO_2 + e^- \longrightarrow CO_2^+, CO_2^{++}, CO^+, C^+, O^+ \tag{5.6}$$

The fragmentation ratios are defined by the abundance of each daughter relative to the abundance of the parent. Tables 5.3, 5.4 and 5.5 respectively list the ion fragments of H_2O^+, CO^+ and CO_2^+, their masses and the relative fragmentation ratios calibrated for RTOF SS mode and OS mode. The species' masses are taken from the Handbook of Chemistry and Physics database while the relative fragmentation ratios have been obtained by comparing the intensity of parent and daughter's peaks during calibration tests on the ground with the RTOF model in the laboratory. C and O correspond to the most abundant isotopes of C (i.e. ^{12}C) and O (i.e. ^{16}O) respectively.

Ion	**Mass**	**f(SS) in %**	**f(OS) in %**
H^+	1.0073	13.02±0.91	6.80± 13.34
H_2^+	2.0151	0.80±0.30	0.09±0.08
O^+	15.9944	1.34±0.82	1.15±0.06
OH^+	17.0022	23.34±1.03	23.73±0.42
H_2O^+	18.0100	100.0±2.7	100.0±0.8

Table 5.3: Masses of the H_2O ionisation fragments and the relative fragmentation to H_2O^+ for SS modes and OS modes.

Ion	**Mass**	**f(SS) in %**	**f(OS) in %**
C^+	11.9995	3.31±0.57	0.77±0.02
O^+	15.9944	0.46±0.15	0.08±0.04
CO^+	27.9944	100.0±5.1	100.0±1.4

Table 5.4: Masses of the CO ionisation fragments and the relative fragmentation to CO^+ for SS modes and OS modes.

Ion	**Mass**	**f(SS) in %**	**f(OS) in %**
C^+	11.9995	0.44±0.02	1.20±0.10
O^+	15.9944	10.45±0.24	5.07±0.22
CO_2^{++}	21.9944	0.25±0.07	0.75±0.05
CO^+	27.9944	9.73±0.25	3.86±0.21
CO_2^+	43.9893	100±2.5	100±2.2

Table 5.5: Masses of the CO_2 ionisation fragments and the relative fragmentation to CO_2^+ for SS modes and OS modes.

5.3.2 Sensitivity

The sensitivity is defined as the ratio of the current I_i produced by the detected ion over the emission current of the filament I_{em} and the gas density n_i, see equation 5.7:

$$S_i = \frac{I_i}{I_{em} n_i} \tag{5.7}$$

Specie	**S**$_{SS}$ $[cm^3]$	**S**$_{OS}$ $[cm^3]$
H_2O	$3.35{\pm}0.14{\times}10^{-23}$	$5.73{\pm}0{,}66{\times}10^{-21}$
CO	$9.03{\pm}0{,}8{\times}10^{-23}$	$5.03{\pm}0{,}58{\times}10^{-21}$
CO_2	$1.40{\pm}0.28{\times}10^{-23}$	$6.84{\pm}0.69{\times}10^{-21}$

Table 5.6: Sensitivity values for the OS and SS modes of RTOF.

The species have different sensitivities S_i as their ionisation cross sections are different. In particular, the sensitivities for H_2O, CO and CO_2 have been calibrated in laboratory by measuring the ion currents at different pressures and by computing the slope I_i/n_i.

5.3.3 COPS calibration

To calibrate the COPS Nude Gauge pressures, we removed the background density (1.2×10^6 cm^{-3} which corresponds to 5×10^{-11} mbar at 293 Kelvin) from the NG pressure. Then, we multiply by a correction factor β_{total} (as seen in Section 4.4.2) to scale the COPS neutral density to the sensitivity of different gas species using relative abundances.

$$n_{COPS} = \frac{P_{NG} - P_{background}}{k_b \cdot T} \cdot \beta_{tot} \tag{5.8}$$

The correction factor β_{tot} is calculated with the specific correction factors for the main species β_{H_2O}, β_{CO} and β_{CO_2}, and their relative abundances ($r_{CO} = CO/H_2O$ and $r_{CO_2} = CO_2/H_2O$).

$$\beta_{total} = \frac{1 + r_{CO} + r_{CO_2}}{\frac{1}{\beta_{H_2O}} + \frac{r_{CO}}{\beta_{CO}} + \frac{r_{CO_2}}{\beta_{CO_2}}} \tag{5.9}$$

The correction factor for the measurement of the Granville-Phillips Ion Gauge are $\beta_{H_2O} = 0.893$, $\beta_{CO} = 0.952$ and $\beta_{CO_2} = 0.704$, as measured from Granville (2007), with errors of 4% to 6%.

The CO_2/H_2O and CO/H_2O ratios depend on the abundances c_i (precisely the number of detections within 200 or 400 s), the sensitivities S_i, and the fragmentation ratios $f_{i \to j}$, where i is the parent and j one of the fragments. They are expressed as in equations 5.10 and 5.11 (where the contribution of CO_2 in the CO detection is removed). The contribution of other eventual parent's molecules are neglected in those equations, as the bulk composition is expected to be dominated by these three volatiles. The contribution of O_2, which appeared surprisingly high in the coma of 67P/C-G, is thus not taken into account in this calibration. Unfortunately, the sensitivity of the molecule O_2, required to convert the abundances into densities, has not been calibrated in laboratory. A first approach to determine the sensitivity and estimated the O_2 density is proposed in Section 8.4.

$$r_{CO_2} = \frac{c_{CO_2}}{c_{H_2O}} \cdot \frac{S_{H_2O}}{S_{CO_2}} \cdot \frac{f_{H_2O \to H_2O}}{f_{CO_2 \to CO_2}} \tag{5.10}$$

$$r_{CO} = \frac{c_{CO}}{c_{H_2O}} . \frac{S_{H_2O}}{S_{CO}} \cdot \frac{f_{H_2O \to H_2O}}{f_{CO \to CO}} - r_{CO_2} \cdot f_{CO_2 \to CO} \tag{5.11}$$

Finally, densities of H_2O, CO_2 and CO are calculated thanks to the equations 5.12, 5.13 and 5.14. The resolution of one minute of COPS densities allows to calculate the RTOF densities, whose resolution is lower. Note that the same method is used for the calibration of DFMS' spectra, with different numerical values.

$$n_{H_2O} = \frac{n_{COPS}}{\left(\frac{1}{\beta_{H_2O}} + \frac{r_{CO}}{\beta_{CO}} + \frac{r_{CO_2}}{\beta_{CO_2}}\right)} \tag{5.12}$$

$$n_{CO_2} = r_{CO_2} \cdot n_{H_2O} \tag{5.13}$$

$$n_{CO} = r_{CO} \cdot n_{H_2O} \tag{5.14}$$

Part III

The heterogeneous coma of 67P/C-G seen by ROSINA

This part is dedicated to the characterization of 67P/C-G's coma using the ROSINA data and numerical simulations. In chapter 6, we describe the RTOF dataset used in our study, as well as the important orbitography parameters which will help the interpretation of the data. The chapter 7 presents the dynamics of the three main volatiles as seen by ROSINA/RTOF through the whole Rosetta mission. The chapter 8 investigates the spatial distribution of the volatiles and highlights the strong seasonal effects experienced by 67P/C-G. The chapter 9 will present the observations from the ROSINA/DFMS's point of view and presents the correlation between the two spectrometers. Finally, the chapter 10 shows a comparison between the RTOF data and a 3D DSMC model adjusted on the DFMS' measurements.

Chapter 6

Description of the datasets

As RTOF was on-board the Rosetta spacecraft, which evolved around the rotating active nucleus and escorted it along its travel around the Sun, the knowledge of the orbitography parameters is of first importance to interpret the RTOF data. The evolution of the orbitography parameters during the Rosetta mission is detailed in this chapter (see Section 6.1), as well as the description of the RTOF dataset recorded during the whole mission (see Section 6.2).

6.1 Orbitography parameters

6.1.1 Sub-spacecraft point coordinates

The geographical origin of the outgassing is an essential parameter to understand the coma's observations. Thus, we define the coordinate of the sub-spacecraft point (SSC), i.e. the geographic location of the spacecraft with respect to the nucleus, in the comet's fixed frame, which corresponds to the point on the comet located exactly under the spacecraft.

The geographical coordinates of the comet have been defined as represented in Figure 6.1. The equator of the nucleus is the plane perpendicular to the rotational axis. It corresponds to the latitude zero and separates the northern hemisphere from the southern hemisphere. The point of latitude 0 and longitude 0 is the extremity of the small lobe. The corresponding two-dimensional maps projections shown in the figure are the standard way to describe the geometry of the comet in this work. The center of the small lobe is the center of the 2D map (point of latitude 0 and longitude 0) and the big lobe area is located at the borders of the maps.

6.1.2 67P/C-G's orbit

The evolution of the coma's outgassing directly depends on the orbit of the comet (Snodgrass et al., 2017). Firstly, the heliocentric distance will drive the global intensity of the nucleus' heating, and secondly, since the rotational axis of 67P/C-G is tilted by 52° (Sierks et al., 2015), the nucleus experiences strong seasonal variations along its orbit.

Rosetta reached the comet in August 2014. 67P/C-G experienced a first equinox on 10 May 2015 at a heliocentric distance of 1.67 AU, reached its perihelion on 13 August

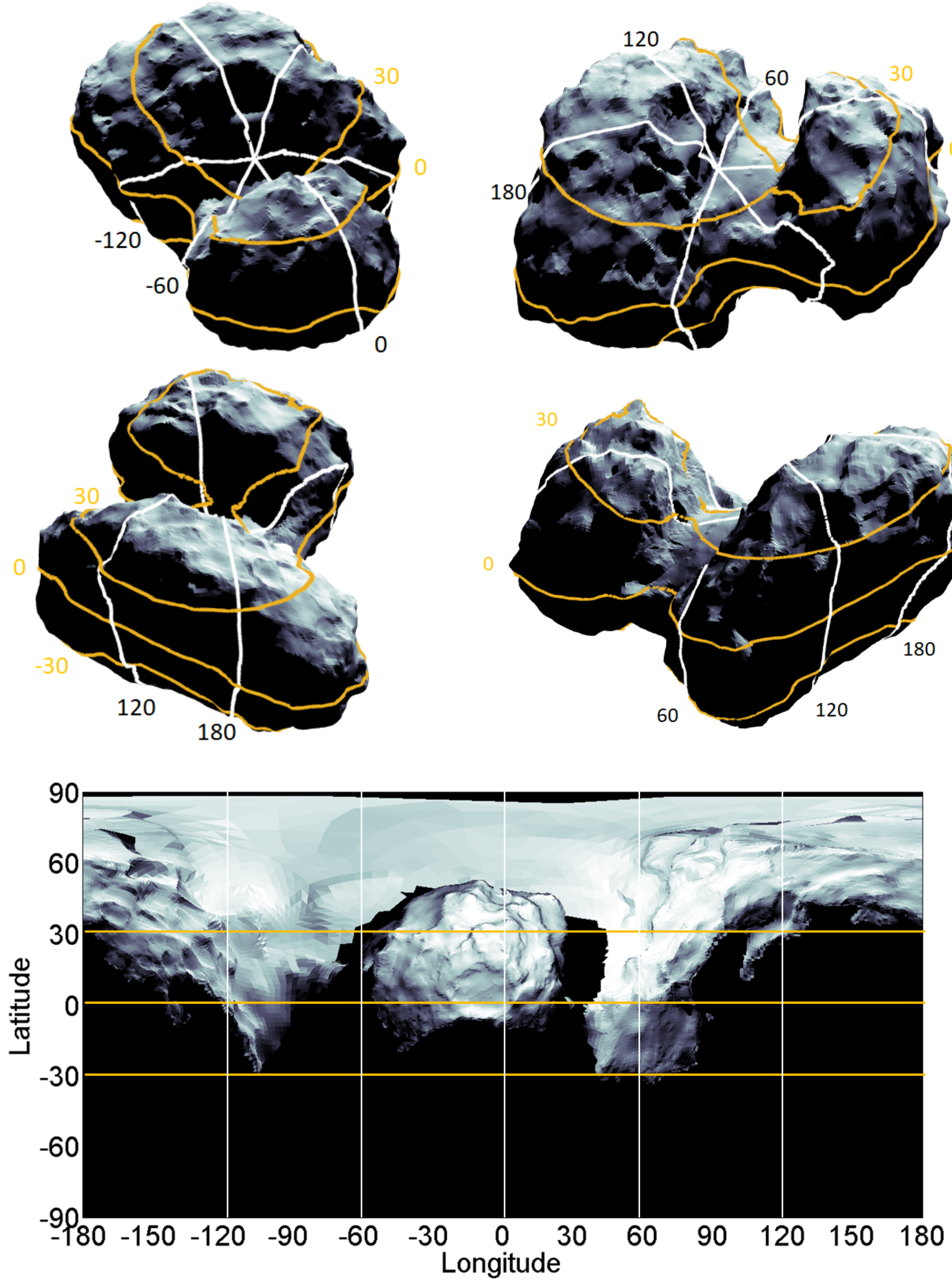

Figure 6.1: Four top panels: Sub-spacecraft latitude (orange lines) and longitude (white lines). Bottom: 2D map representation of the comet 67P/C-G.

2015, at its closest distance from the Sun, 1.24 AU. The second equinox occurred on 21 March 2016 at 2.63 AU. Rosetta studied the comet until a distance of 3.28 AU from the Sun and landed on the surface on 30 September 2016. The positions of the comet at those four important dates are represented in Figure 6.2.

The variation of heliocentric distance and of sub-solar latitude in the comet-fixed frame are shown in Figure 6.3. The Rosetta spacecraft reached the comet during the inbound part of its orbit, when the northern hemisphere was illuminated by the Sun. The sub-solar latitude then declined to reach the equator line at the 1st equinox. The

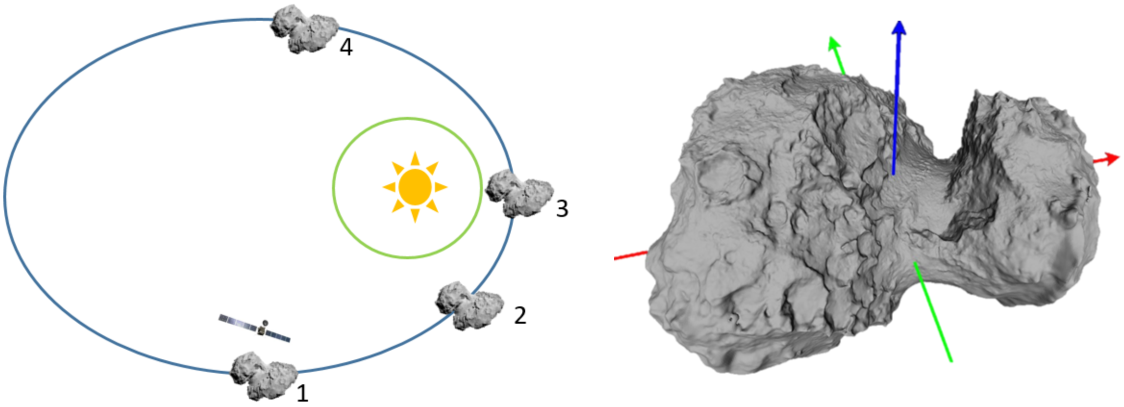

Figure 6.2: Left panel: orbit of 67P/C-G (in blue), with the rendez-vous with Rosetta in August 2014 (1), the first equinox on 10 May 2015 (2), perihelion on 13 August 2015 (3) and the second equinox on 21 March 2016 (4). The Earth's orbit is shown in green. Right: Shape of 67P/C-G with its equatorial axis (x axis in red and y axis in green) and its rotation axis (in blue), tilted by 52°. The orbit of 67P/C-G has an inclination of 7° with respect to the ecliptic plane. Credits: ESA/Rosetta/MPS for OSIRIS Team.

southern hemisphere was then illuminated for a few months around perihelion time. It experienced a shorter but stronger summer than the northern hemisphere, as the comet was approaching closer to the Sun and passed the perihelion. Thanks to the extension of the mission, Rosetta continued its study of the comet in the outbound part of its orbit. After the 2nd equinox, the position of the sub-solar vector went back to positive latitudes, meaning that the northern hemisphere was illuminated.

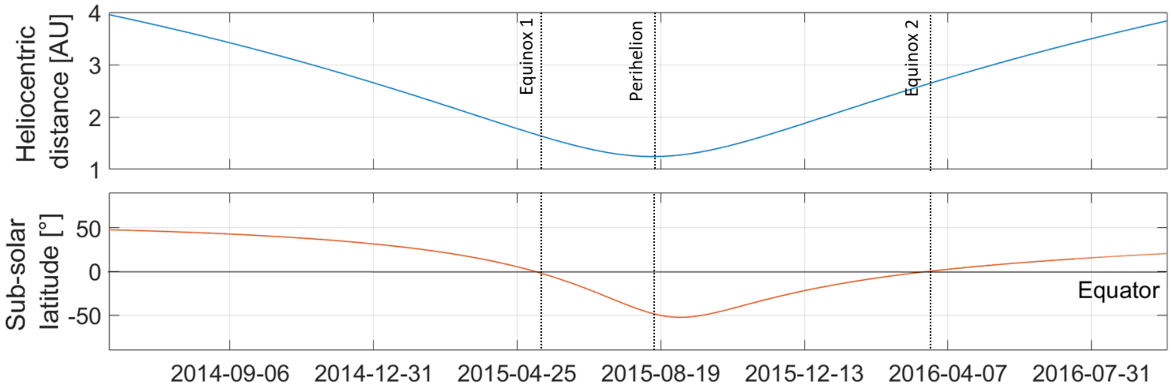

Figure 6.3: Upper panel: heliocentric distance. Lower panel: latitude of the position of the Sun in the comet fixed frame.

6.1.3 Spacecraft to comet distance

During the mission, the spacecraft to comet distance varied, from a few kilometers (except for the last manoeuvers which brought Rosetta on the surface of the nucleus) to approximately 1500 km.

Rosetta successfully woke up on 20 January 2014 after the hibernation phase. The science and engineering teams started the commissioning of all the instruments and RTOF was switched on in April 2014. Between May and August, the spacecraft operated a series of approach maneuvers and arrived near the comet's nucleus. The distance between the spacecraft and the comet is shown for the whole mission in Figure 6.4, as well as the phase angle variation, i.e. the angle between the Sun-comet and the comet-spacecraft vectors, which varies from 0° (Sun-spacecraft-comet aligned) to 180° (Sun-comet-spacecraft aligned). An important milestone of the mission was the landing of Philae on 12 November 2014, which brought the spacecraft to a distance of 16 km from the nucleus' surface. In February and March 2015, the spacecraft operated a series of flybys and collected data at short distances from the nucleus (with a notable approach at 6 km on Valentine's day). The navigation of the spacecraft was done thanks to the information provided by star trackers. The increase in density of gas and dust lead to severe star tracker issues, as they confused moving dust particles with fixed stars. On 28 March 2015, the spacecraft even had to enter safe mode after a loss of signal due to the unability of the star track-

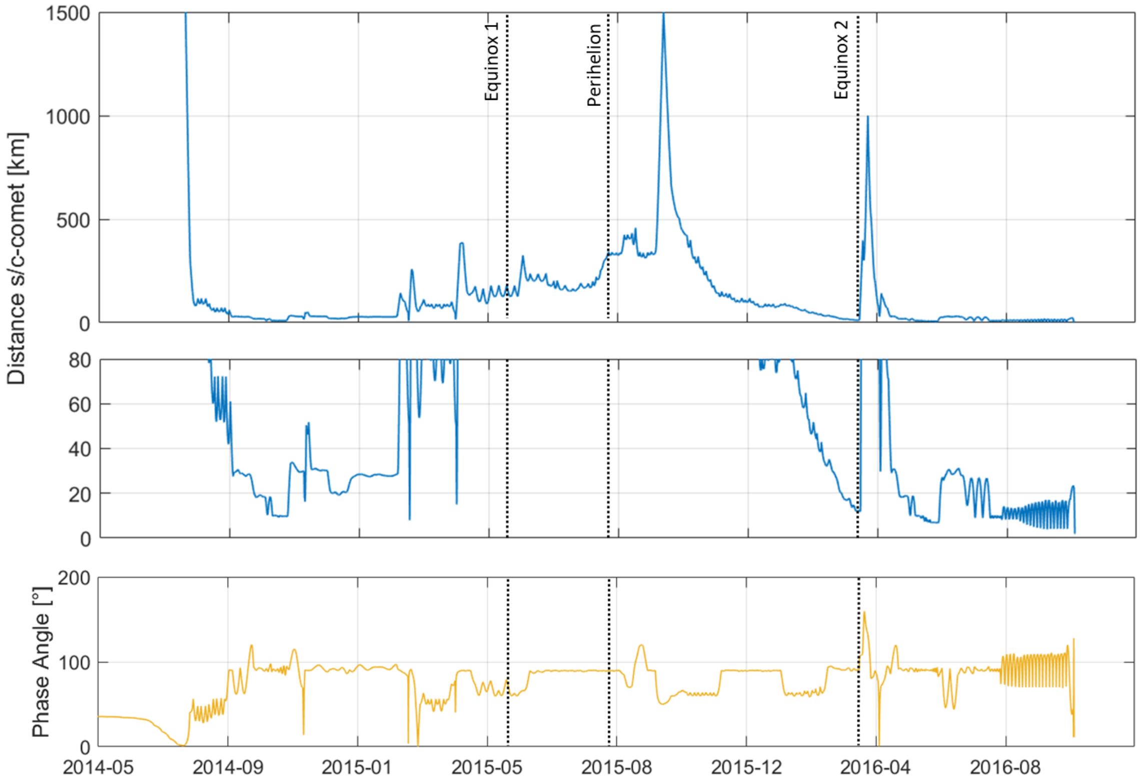

Figure 6.4: Variation of the distance between the spacecraft and the comet during the mission (upper panel), zoom on the closer distances (middle panel), and variation of the phase angle (lower panel).

ers to determine the spacecraft's position: the safe mode consisted in switching off the instruments and getting away from the nucleus, up to a distance of more than 200 km. The safety operation again distanced the spacecraft to 400 km from the surface, before it quickly came back around 140 km.

Fearing strong outgassing of the nucleus, long periods at short cometo-centric distances were avoided. In particular, Rosetta stayed at large distances from the nucleus while approaching the Sun and particularly during perihelion, where an important increase of the cometary activity was expected and measured. Just after perihelion, the biggest excursion of the mission brought Rosetta to a distance of 1500 km on 13 September 2015, to have the opportunity to study the coma at a large scale, as well as the global solar wind interaction with the comet. Rosetta went on another far excursion in March-April 2016. The final approach started in August 2016, until the spacecraft was controlled to impact the surface of the comet on 30 September 2016.

6.1.4 Nadir off-pointing

The nadir off-pointing is the angle between the nadir direction and the line of view of the spacecraft. Variations of the nadir off-pointing are due to unavoidable spacecraft maneuvers that are necessary for navigation purposes or requested by other scanning instruments, such as ALICE or VIRTIS. We therefore applied a data filtering to ignore the detections when the amplitude of a slew exceeds 5°, considering that the instruments were not pointing to the comet anymore. Seen from a distance of 60 km, the comet has a diameter of about 5°.

6.2 RTOF dataset

RTOF did not record data continuously during the mission. Nevertheless, a total number of 104 592 spectra has been collected. The recorded types of spectra are summarised in Figure 6.5, where the blank areas report the gaps in RTOF recording, the blue lines are the SS modes spectra, and the green and red lines are the OS modes spectra. RTOF switched between the OS and SS modes throughout the mission to record the best possible quality spectra.

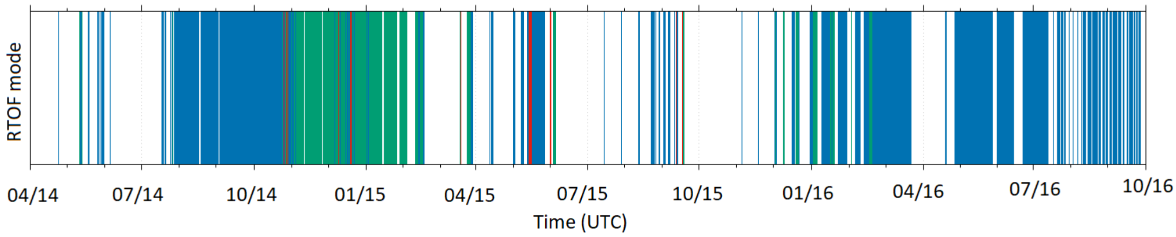

Figure 6.5: SS neutrals (blue), OS neutrals (green) and OS ions (red) operation modes through the whole mission. Credit: S. Gasc.

RTOF was not operational at large distances (in particular during excursions, see Figure 6.4), where the density was too weak for a detection of the molecules. At the beginning, RTOF was off during each wheel-off-loading (WOL [1]) but consecutive turn-off and turn-on lead to an important outgassing of the instrument lasting a few hours after switch on. Indeed, off phases correspond to a low temperature phase which attracts dirt that later outgasses when the instrument is switched on. The decision was taken to keep RTOF ON during the WOL. RTOF remained OFF during the orbit control manoeuvers which required a thruster firing and which would have contaminated the instrument.

Spectra were acquired in SS mode from July 2014 until the end of November 2014 approximately. The OS modes were then used until mid-February 2015. The spectra from OS and SS appeared significantly different, as the OS spectra showed very few and weak peaks while the SS spectra showed unexplained peaks.

In May 2015, RTOF endured the death of filament 1 in the SS ion source. The spare filament 2 was used afterwards. Few months of operations were needed to optimise the instrument with caution for the new filament. The SS modes were optimised at the end of 2015 and were mostly used until the end of the mission.

In the 104 592 RTOF spectra, 82 256 were recorded in SS modes and 22 336 in OS modes. In the next part, we provide an analysis of the 78 439 spectra recorded in the SS mode M0521 and the 7 447 spectra in the OS mode M0523.

---

[1] Pointing control manoeuvers which required the ignition of the thrusters

Chapter 7

Global dynamics of the main volatiles

In this chapter, we analyse the main volatiles variations derived from the entire RTOF data set. The temporal variations observed by Rosetta are induced by the combination of different parameters, mostly the distance to the comet (see Section 7.1), the spatial variations (related to either illumination or longitude/latitude), and the distance to the Sun that plays a role in long timescales. We investigate the influence of those parameters. First, we present an analysis of the density power law related to the comet-spacecraft distance (see Section 7.1). Then we will study the diurnal variations (periodicities which depend on the rotation of the comet) observed in the RTOF data (see Section 7.2). Finally, we present a global study of the whole mission's dataset to highlight the influence of the heliocentric distance and of the solar illumination on the comet's activity (see Section 7.3). We show the evolution of the coma's density and composition along its orbit and, in particular, strong seasonal variations.

7.1 Dependence on the comet-spacecraft distance

The spacecraft distance to the comet varied along the mission, covering a large range of distances. The spectrometer has been able to analyse the coma at different altitudes and experienced the decrease of density as the Rosetta spacecraft moved away from the nucleus.

The simplest description of the density distribution of a coma (see Section 2.1.3) assumes a constant velocity outflow of particles escaping radially the surface of a spherical body, without any collisions or destruction, and describes a density distribution decreasing as a $1/\mathrm{r}^2$ power law at short distances to the nucleus. Festou (1981) showed that a low activity comet has a collisional sphere very close to the surface of the nucleus, which is the case of 67P/C-G whose coma is thus expected to follow this $1/\mathrm{r}^2$ density distribution.

Those assumptions are not verified by our case study, nevertheless the global trend was checked. We used the COPS pressure measurements to analyse the dependence between the ROSINA molecule density detections and the distance to the comet's nucleus. To reduce the influence of all the other parameters, we chose a time period with a large variation of the distance over a short time period to limit the variation in density. After the 14th February 2015's fly-by of the nucleus, the altitude increased from 8 to 242 km in only 3 days, which led to a power-law statistical fit with a slope in between -1.8 and -1.9, as shows in Figure 7.1.

This power law approximation was also confirmed by Hässig et al. (2015). Hereafter, we use the $1/r^2$ power law to extrapolate the density $n(r)$ measured at a given distance r to an arbitrary fixed distance r_i (e.g. $r_i = 10$ km).

$$n(r_i) = n(r).(\frac{r}{r_i})^2 \tag{7.1}$$

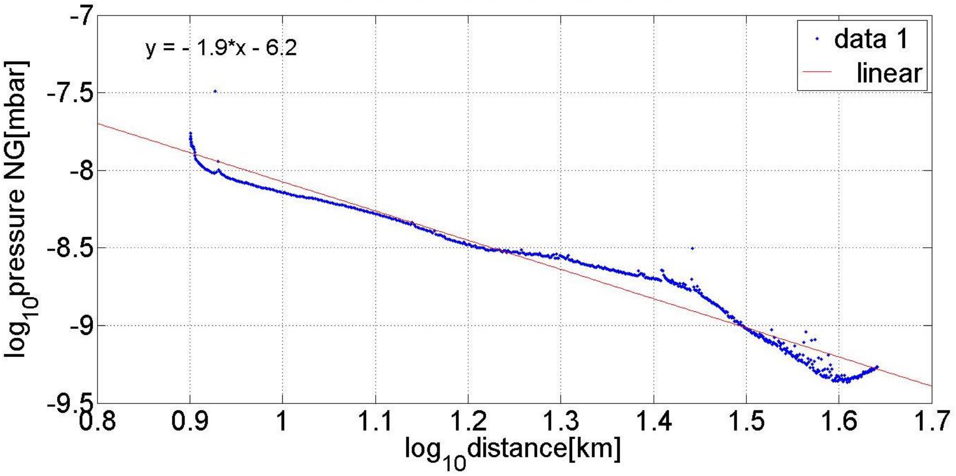

Figure 7.1: Dependence between the COPS pressure and the altitude of the spacecraft after the 14th February 2015's fly-by.

7.2 Diurnal variation

The coma development is the consequence of the solar illumination which heats the nucleus and allows the sublimation of the gas. Thus, the maxima of densities are expected to originate from the illuminated parts of the nucleus. Indeed, RTOF detections present a clear and strong diurnal variation. In Figure 7.2, we observe the diurnal variations (related to the rotation period of the comet) during a few days in October 2014. The northern hemisphere was well illuminated during this period and this led to enhanced sublimation, as clearly observed in the variations of H_2O densities.

We also measured high frequency variations in the detection of volatiles. For one comet rotation, we observe two minima (1 and 3 on upper panel in Figure 7.2) and two maxima (2 and 4) directly correlated with the geometrical asymmetry of 67P/C-G. These periodic variations are linked to the geometry of the nucleus. For a sub-spacecraft point (SSC) longitude 90°, the spacecraft sees a large illuminated area. Since the rotation period of 67P/C-G was about 12.4 hours at that time in the mission, this induces a half-diurnal variation for coma measurements with high detections each time the spacecraft is above the neck in the northern hemisphere, i.e. approximately every 6.2 hours.

The CO_2 and CO observations showed more complex density variations with detections in both hemispheres and less clear asymmetries. As the water sublimation occurs close to the surface, where variations of illumination are important due to the complex shape of the nucleus, the outgassing appears more scattered than the CO_2 and CO sublimation which occurs in deeper layers where the outgassing is expected to be more continuous.

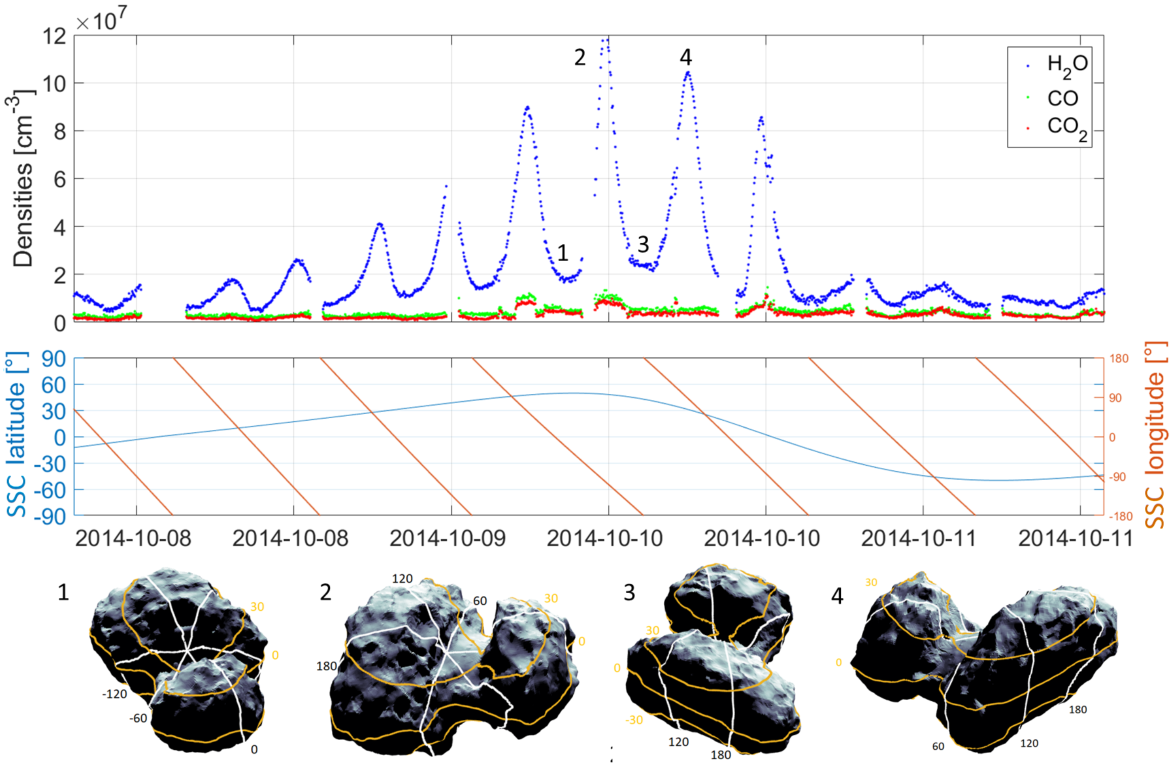

Figure 7.2: Diurnal variation of main volatiles. Upper panel: densities of H_2O, CO and CO_2 from 8 October to 11 October 2014. Middle panel: sub-spacecraft point longitude and latitude variations during the same period. Low panel: views of the comet from the spacecraft at specific times marked as 1, 2, 3 and 4 on the upper panel. Figure modified from Hoang et al. (2017).

To highlight periodic signals on a statistical basis and confirm the presence of strong periodicities of about 6 and 12 hours, we applied a Lomb-Scargle periodogram to H_2O data. The Lomb-Scargle periodogram (or least-squares spectra analysis) is an algorithm to identify the periodicity in an uneven dataset, based on a least squares fit of sinusoids. Lomb-Scargle periodograms applied to CO_2 and CO data showed a more homogeneous behaviour with a smaller 12 hours periodicity than H_2O, as we can also see through the analysis of short time periods, following the results of Hässig et al. (2015). The Lomb-Scargle periodograms for H_2O and CO_2 are shown in Figure 7.3.

This behaviour of the main volatiles is in agreement with the common assumption that CO_2 and CO originate from deeper layers than H_2O and are therefore less sensitive to change in solar illumination (De Sanctis et al., 2010; Prialnik et al., 2004). The diurnal and orbital skin depth of 67P/C-G are, respectively, about a few centimeters and a few meters (Huebner et al., 2006). A possible interpretation is the following: H_2O originates from the shallow subsurface (the first centimeters below the surface), which is very sensitive to diurnal temperature variations, while CO_2 and CO sublimate from deeper layers inside the comet. These deeper layers are rather influenced by a seasonal effect due to obliquity, in agreement with thermodynamic models of the cometary subsurface (Huebner et al., 2006; De Sanctis et al., 2010), and laboratory experiment like KOSI, which simulated the cometary processes (Grün et al., 1989).

A similar behaviour was detected by the Deep Impact spacecraft at comet 103P/Hartley 2, where the water release was mostly originating from the illuminated part of the nucleus (A'Hearn et al., 2011). Like 67P/C-G, 103P/Hartley 2 has a bilobate nucleus, with two lobes of different sizes connected by a neck which presents a smoother surface than the lobes. Comet 103P/Hartley 2 revealed surprising observations, as the small nucleus appeared very active with an outgassing driven by jets of CO_2. A large amount of icy grains and dust chunks, partly responsible for H_2O outgassing, were actually lifted by those jets, and not driven by the sublimation of H_2O ices. Clear surface heteorogeneities were observed: the two lobes, in particular the extremity of the small lobe, presented bright jets of CO_2 and an outgassing enriched in organic compounds, while the neck released large amounts of H_2O, with a little CO_2. One hypothesis to explain this difference in outgassing is the redeposition of dust and icy grains originating from the extremities of the lobes in the neck area. The two lobes also showed different CO_2/H_2O ratios, with a factor two higher in the smaller lobe.

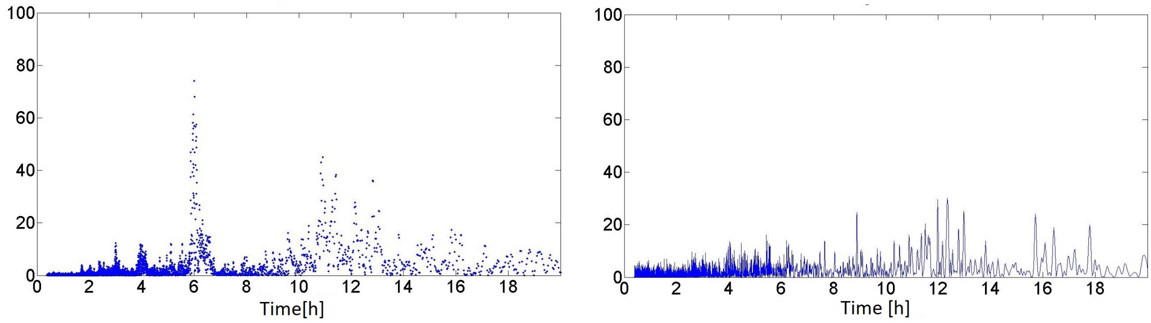

Figure 7.3: Lomb-scargle periodogram of H_2O (left), with strong periodicities at 6 and 12 hours, and of CO_2 (right), with a more homogeneous behaviour and a main periodicity of 12 hours.

The influence of the solar illumination is also visible in Figure 7.4, which shows the total density from COPS, as well as the H_2O, CO_2, and CO densities from RTOF during the approach as a function of the local time (0/24 hours is midnight, 12 is noon) at the time of the measurements. This confirms that the solar illumination is the main variability source as the maximum of all densities corresponds to noon time on the comet. The study of the influence of the phase angle also shows the same behaviour, as expected, with a decrease in densities as phase angle increases. We may note that CO appears less influenced than H_2O and CO_2 by the local time, with a variation amplitude that is only half as large. This seems again in agreement with both the high volatility of CO (whose sublimation temperature is low, see 2.1.2) and the assumption that CO layers are located deeper than the H_2O and CO_2 ones due to a lower sublimation temperature. The local time variations obtained do not allow us to conclude anything about a clear asymmetry between morning and afternoon, confirming the low thermal inertia previously observed at comets (estimated < 30 J K^{-1} m^{-2} $s^{-0.5}$ for Hartley 2 and < 50 J K^{-1} m^{-2} $s^{-0.5}$ for Tempel 1), and more recently at 67P/C-G ($\sim$ 10 to 50 J K^{-1} m^{-2} $s^{-0.5}$) (Lisse et al., 2009; Davidsson et al., 2013; Groussin et al., 2013; Gulkis et al., 2015).

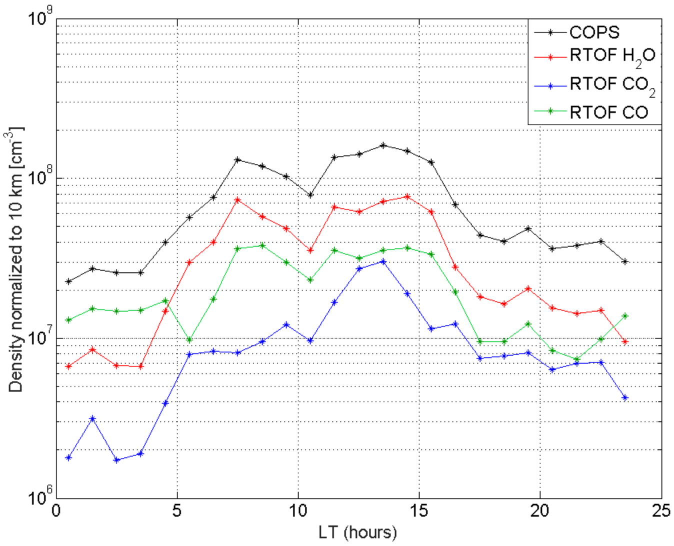

Figure 7.4: Total density from COPS, as well as the H_2O, CO_2, and CO densities from RTOF during the approach as a function of the local time. Densities were normalised at a constant 10 km altitude.

7.3 Evolution of the activity with the heliocentric distance

The full mission data set shows the evolution of the outgassing of the nucleus during the escort phase as a function of the heliocentric distance. The data set starts during the inbound part of the comet's orbit around the Sun ($\sim$ 3.4 AU), at a cometo-centric distance of about 50 kilometers, which is a reasonable distance to study the coma composition, and ends in the outbound part until a heliocentric distance of 3.28 AU.

Figure 7.5 shows the three main volatiles' densities seen by RTOF from September 2014 until September 2016 together with some orbitography parameters: the latitude of the sub-spacecraft point, the cometocentric distance, and the heliocentric distance through the whole mission. The densities are multiplied by the distance to the comet to remove the influence of the cometocentric distance (that strongly varied during the mission). The entire dataset is shown by the points in blue (H_2O), red (CO_2) and green (CO). We also show the data averaged over two rotations of the comet (coloured lines) to filter the diurnal variations in order to highlight the large-scale variability of the coma.

7.3.1 Global pattern

The activity of the nucleus strongly depends on the distance to the Sun. The rendez-vous occured in August 2014, at a heliocentric distance of 540 $\cdot 10^6$ kilometers, when the comet's activity was weak, then the activity increased during the inbound part of the orbit. The global evolution of the main volatiles' density shows the expected increase of the outgassing during the pre-perihelion period and decrease after perihelion. When the comet approaches the Sun, the heating of the nucleus causes an increase in the sublimation of ices (followed by the dust release as well). At perihelion, the nucleus's heating reaches

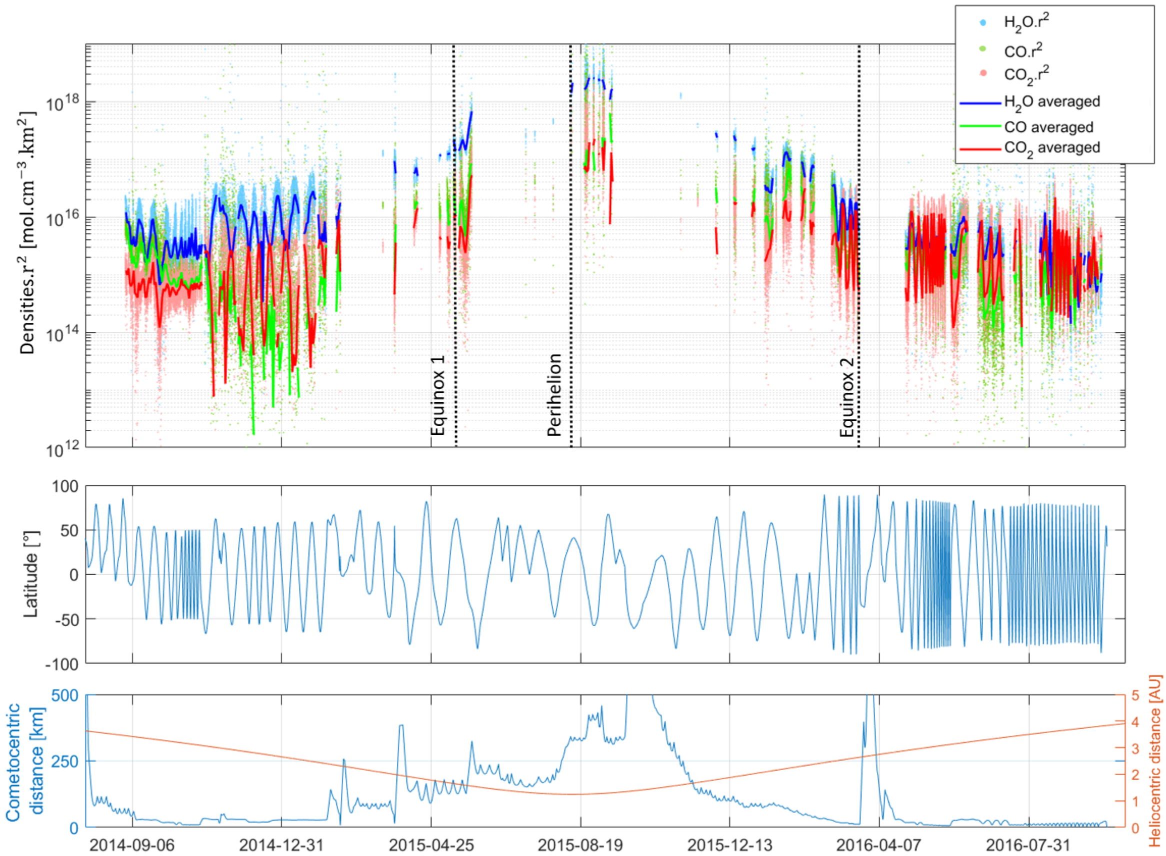

Figure 7.5: Upper panel: temporal evolution of H_2O, CO_2 and CO densities corrected for distance effect, seen by the RTOF spectrometer over the Rosetta mission. Coloured lines are averaged over two comet rotations. Middle panel: latitude of the sub-spacecraft point in the 67P/C-G fixed frame. Lower panel: variation of the heliocentric distance (red) and the distance between Rosetta and 67P/C-G (blue). RTOF data are missing during excursions of the spacecraft. First equinox occurred on 2015/05/10 at 1.67 AU, perihelion on 2015/08/13 at 1.24 AU, and second equinox on 2016/03/21 at 2.63 AU. From Hoang et al., 2018 (to be submitted).

its maximum intensity, leading to a maximum outgassing rate. A similar behaviour has been observed with other comets, see for exemple the evolution of the outgassing of Hale-Bopp in Biver et al. (1997).

Surprisingly, as described by Hansen et al. (2016), we however observe an unexpected decrease of H_2O while the heliocentric distance is decreasing, during the approach period. Meanwhile CO and CO_2 densities follow the same trend. This unexpected decrease will be discussed further in Section 7.4.1, where a scenario will be proposed.

Overall, one can observe that water is the major contributor to the gas composition of the coma, except during the last months of the mission. The contribution of carbon monoxide and carbon dioxide became in particular more important during the last months.

7.3.2 Deriving the outgassing rate

The total outgassing was not directly measured by the in-situ ROSINA data, indeed, the instrument did not continuously measure gas fluxes from all over the nucleus but it did from a specific location. Nevertheless, COPS pressures allow the analysis of the evolution of the activity of 67P/C-G, with the assumption of the radial distribution in r^{-2} to remove the influence of the distance to nucleus.

In Figure 7.6, we show the estimated outgassing as a function of the heliocentric distance from September 2014 until March 2015 and compare it with the activity predicted by ground-based measurements of the luminosity of the comet by Snodgrass et al. (2013). We plot the direct estimate (dark blue), as well as the sliding average (red). We also derived an estimate (green) where we tried to remove the potential bias of some probed regions of the comet being more active than others, using the following procedure: we mapped the COPS (normalised at 10 km) densities on 2D longitude/latitude maps with 5 degrees resolution cells every 15 days (see later such maps in Section 8.3), kept only the cells common to all periods, and calculated the overall median value. We thus observe that the evolution of outgassing of the nucleus approaching the Sun measured by COPS is very close to the global prediction and therefore well describes the expected increase of activity of the comet.

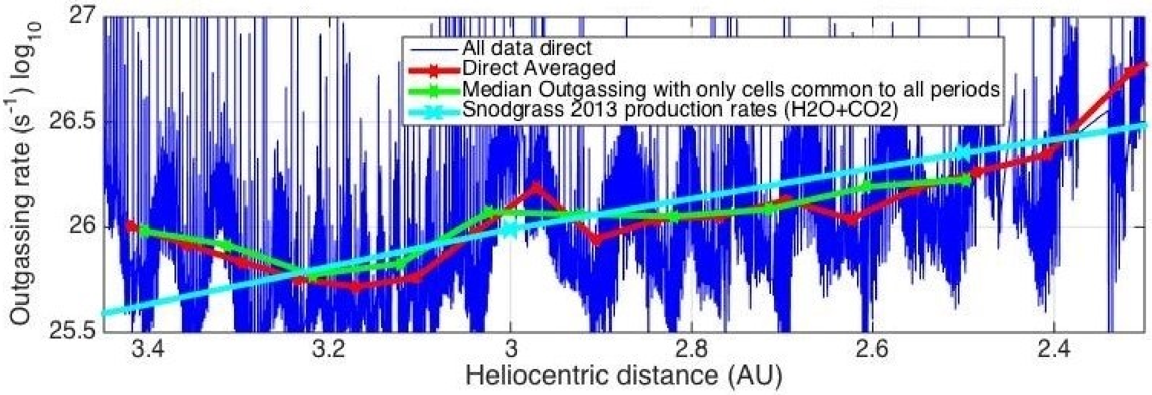

Figure 7.6: Outgassing rate from COPS and prediction of activity from Snodgrass et al. (2013).

However, the measurements by COPS also strongly depend on other orbitography parameters, such as the phase angle, the nadir off-pointing and the sub-spacecraft point. Therefore, a model of coma which reproduces the in-situ ROSINA data is needed to calculate the outgassing at all locations and at all times. Such a work is proposed in Hansen et al. (2016), who developed an empirical model for the water outgassing based on the Direct Simulation Monte Carlo (DSMC) model by Fougere et al. (2016) (detailed in Chapter 10). They performed a multi-instrument analysis of the water production rate as a function of the heliocentric distance. They compared the empirical coma model with Rosetta instruments: ROSINA/DFMS, VIRTIS-H, VIRTIS-M, RPC-ICA and MIRO, from June 2014 and May 2016. As shown in Figure 7.7, they observed a good agreement between the different instruments, even though their measurements may sometimes be difficult to compare (VIRTIS, for example, observes the coma near the nucleus by integration over lines of sight). They reported a maximum of water outgassing about 18 to 22 days after perihelion at $3.5 \pm 0.5 \times 10^{28}$ molecules/s^{-1}. The fitting curve presents a steeper slope after the maximum.

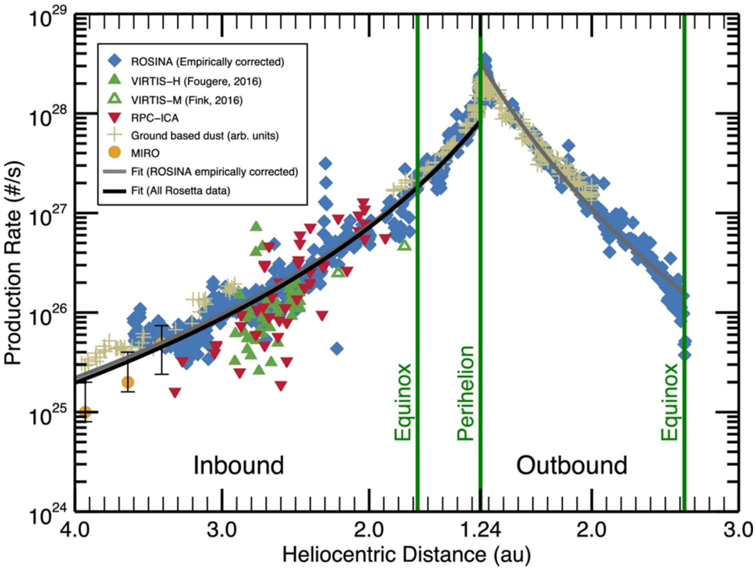

Figure 7.7: Water production rate as a function of the heliocentric distance (Hansen et al., 2016), from different instruments onboard Rosetta (ROSINA, VIRTIS, RPC-ICA and MIRO), as well as the estimated dust production rate. The maximum of water outgassing occured 18 - 22 days after perihelion.

Similarly, we observed a delay between the maximum of outgassing and perihelion in the RTOF dataset. Maxima of outgassing reached 10^{19} cm^{-3} for H_2O and CO and 2.10^{18} molecules/cm^{-3} for CO_2 around 24th August, i.e. eleven days after perihelion. This is due to the heat wave propagation delay from the surface of the nucleus to the deeper layers, where the ices are located. Therefore, the maximum of sublimation occurs slightly after the closest approach to the Sun.

Numerous observations of comets show the same behaviour: the maximum of brightness (directly linked to the outgassing) is often shifted with respect to perihelion (see Ferrín (2010); Festou et al. (1990)). Snodgrass et al. (2016) reported the activity of 67P/C-G around perihelion as observed from Earth, they observed a peak of activity about two weeks after perihelion.

7.4 Seasonal variations

67P/C-G experiences seasons, due to its rotation axis tilted by 52°. The two hemispheres of the nucleus have completely different illumination conditions through one orbit. The northern hemisphere is illuminated for years, while the nucleus is far from the Sun and the solar heating is soft. Around the first equinox, the southern hemisphere gets out of the shadow for less than a year but receives a stronger heating, because the nucleus is closer to the Sun, around perihelion.

To study the seasonal variations of the coma's densities, we distinguish five periods of time to study the evolution of the coma through the mission. They are referred to in the text as the approach, the pre-equinox 1, the pre-equinox 2 or post-perihelion, the post-equinox 2 and the end of mission, as shown in Figure 7.8 and detailed in Table 7.1. The paucity of RTOF data during the six months after perihelion makes the interpretation of the data during this period more difficult.

	Period start	Period end	Heliocentric distance (AU)
Approach	2014-09-01	2014-10-30	from 3.45 to 3.05
Pre-equinox 1	2014-11-01	2015-02-15	from 3.05 to 2.3
Pre-equinox 2	2015-12-01	2016-02-15	from 1.8 to 2.4
Post-equinox 2	2016-03-01	2016-06-01	from 2.5 to 3.1
End of mission	2016-07-10	2016-09-30	from 3.4 to 3.88

Table 7.1: Beginnings and ends of the five time periods studied, with the corresponding heliocentric distances.

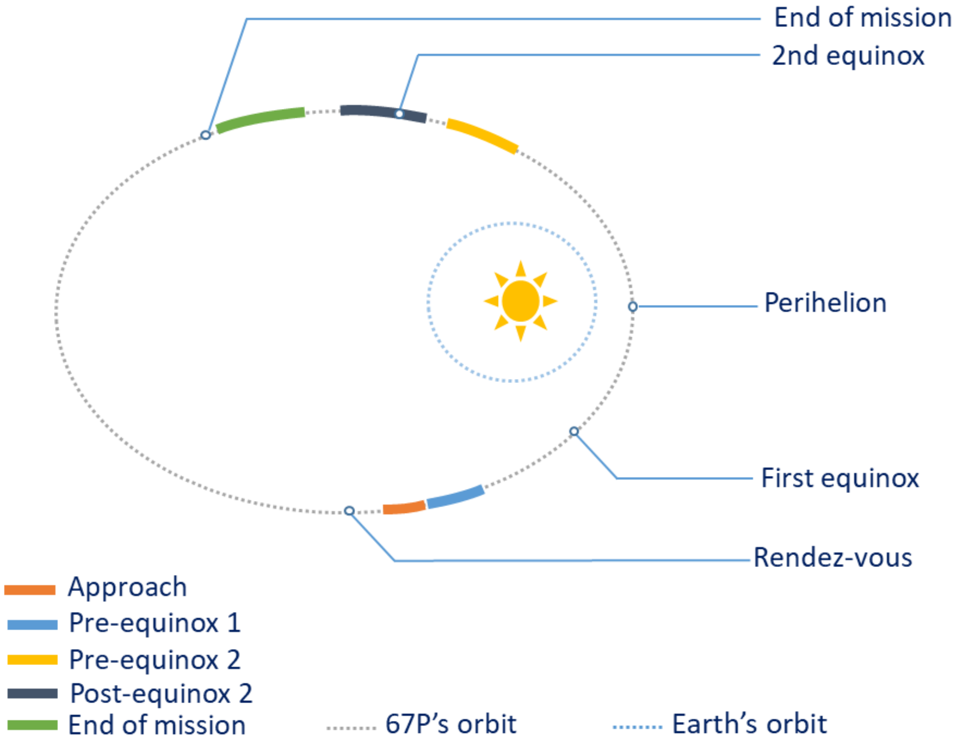

Figure 7.8: Illustration of 67P/C-G and Earth's orbits with the position of the comet at the equinoxes and perihelion, and during the five periods described in Table 7.1.

7.4.1 Approach

The first period started on the 1st September 2014 and ended on the 30th October 2014. It corresponds to the first two months of RTOF data measurements at short distance from the nucleus, as the spacecraft approached it from 80 km down to 9 km during this period. Interpretation of the main volatiles density for the approach, pre-equinox 1 and pre-equinox 2 are also found in Hoang et al. (2017).

The main volatiles densities seen by RTOF are reported in Figure 7.9. The first panel shows the global periodic pattern discussed above with a clear and strong diurnal variation at the comet rotation period. Beyond the diurnal variation, it appears clearly that H_2O densities followed closely the variation of the sub-spacecraft point latitude. The northern hemisphere was well illuminated during this period and this led to an enhanced sublimation for positive latitude regions. During this period, water was the most abundant volatile, followed by CO then CO_2. In the first half of the period, contribution of CO_2 was very small, and increased in the second half to become as important as CO. We observe the previously described dependence with the distance to the surface: as Rosetta came closer to the comet, the ROSINA instruments recorded a progressive increase of density with a maximum around 2.10^8 cm^{-3} when the spacecraft reached 8 km.

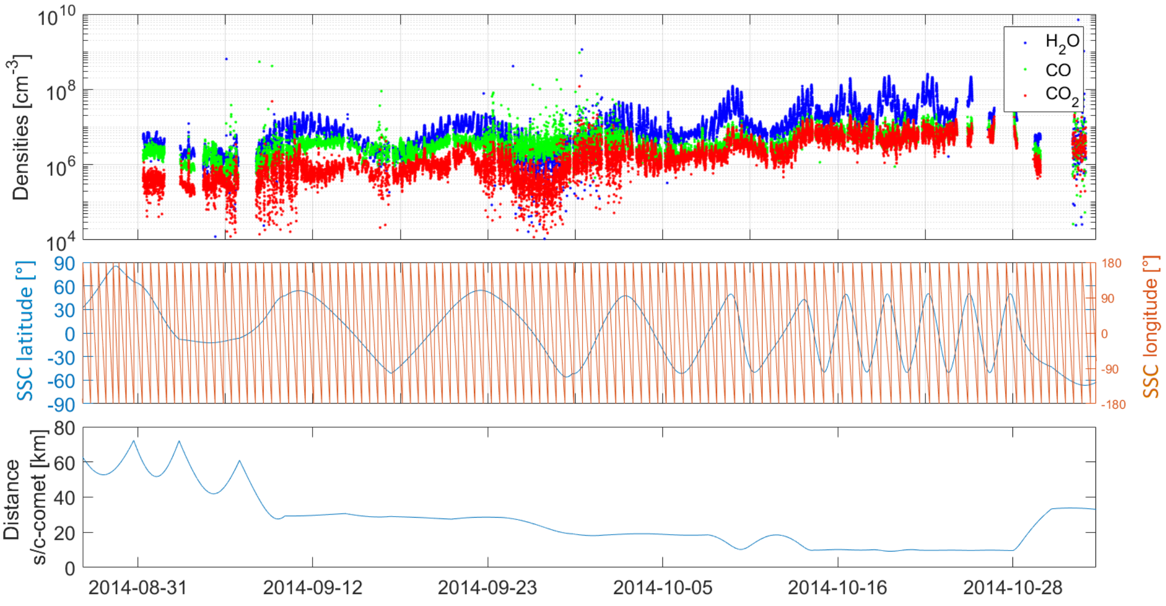

Figure 7.9: Densities of the main volatiles during the approach time period.

7.4.2 Pre-equinox 1

Except during the manoeuvers required for Philae's landing, which brought the spacecraft to 16 km then back to 50 km from the comet's nucleus, the spacecraft remained at a distance of 30 km during the second time period.

H_2O remained the first contributor in the total density of the coma. Except during the first 15 days of November 2014, when the density of H_2O accurately followed the variation of the sub-spacecraft latitude, with the maxima of outgassing for the positive latitude. As those latitudes correspond to the illuminated northern hemisphere at the time, we observe that the intensity of H_2O outgassing followed well the illumination.

CO and CO_2 showed a completely different behaviour during this time period. The largest CO_2 and CO densities correspond to negative latitudes (southern hemisphere). The variations of both volatiles were anti-correlated with the SSC latitude, meaning they were detected from the less-illuminated area. As ices sublimate at different temperatures, the detection of CO and CO_2 probably originates from parts of the comet which have reached a temperature higher than their sublimation temperature (around 70 K for CO and around 150 K for CO_2 from Huebner et al. (2006)). The southern hemisphere may have kept heat from the previous perihelion. This hypothesis could maybe explain how a part of the nucleus reaches those temperatures while still unilluminated in the shadow.

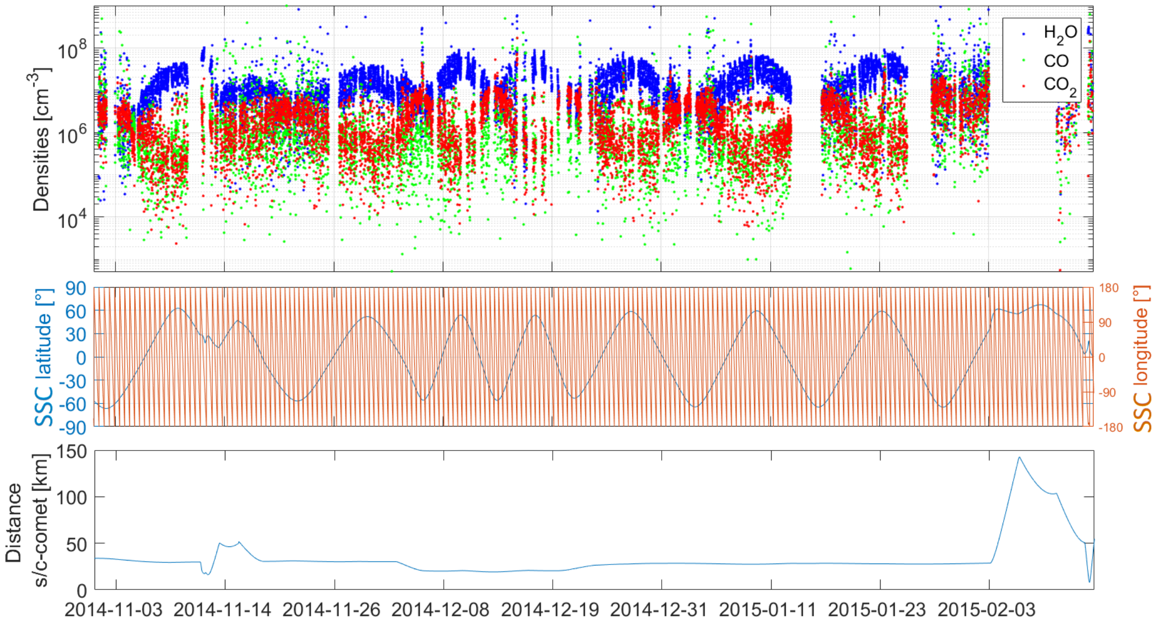

Figure 7.10: Densities of the main volatiles during the pre-equinox 1 time period.

67P/C-G arrived at a heliocentric distance of 2.4 AU at the end of this period. The crossing of the water ice line occurring at about 2.6 AU, the global activity was expected to significantly increase afterwards.

7.4.3 Pre-equinox 2

The pre-equinox 2 time period started in December 2015, i.e. four months after perihelion and five months before the first equinox. The spacecraft was far from the nucleus, at a distance larger than 100 km, and slowly approached to stand at 35 km at the end of the period. RTOF switched between SS and OS modes regularly during this period. We studied 6300 SS spectra to plot the evolution of H_2O, CO, and CO_2 in the upper panel of Figure 7.11. As the data were recorded non continuously, the correlations between the variability and the orbitography parameters are more difficult to see.

In this third period, CO and CO_2 variations followed the H_2O variations and seemed to be concentrated in the southern hemisphere. The total density variation also appears to be anti-correlated with the SSC latitude. As 67P/C-G passed the inbound equinox (May 2015), the illumination crossed the equator and moved to the southern hemisphere. After the equinox, the maximum of sublimation originated from negative latitudes.

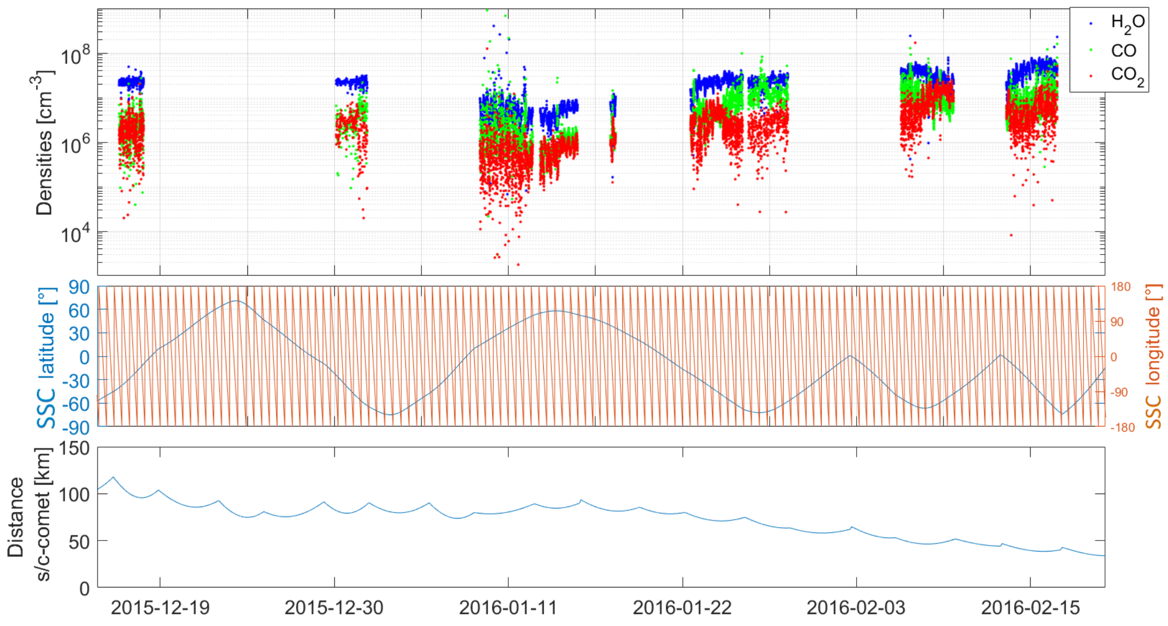

Figure 7.11: Densities of the main volatiles during the pre-equinox 2 time period

7.4.4 Post-equinox 2

In this 4th period of time, RTOF recorded data almost continuously during two months – from end of February until end of March 2016 and from end of April until end of May 2015 – shown separately in Figure 7.12.

At close distances from the nucleus, RTOF observed very clear variations of the main volatiles's densities, with a strong anti-correlation of all three volatiles with the SSC latitude.

If water was the first contributor since the beginning of the mission, CO_2 and CO densities now increased in the global composition of the coma. We observe this evolution by comparing the left panel (right before equinox 2) and the right panel (right after). The evolution of the ratios through the whole mission will be discussed in Section 7.5.

At the end of this period, the comet was at a heliocentric distance of about 3 AU, getting beyond the water ice line, so that the measurements of H_2O were expected to highly decrease.

7.4.5 End of mission

The last time period stands for the two last months of the mission – from the end of July 2016 until the end of September 2016. The spacecraft performed approach manoeuvers and the distance to the nucleus varied a lot during this period. Plus, RTOF recorded

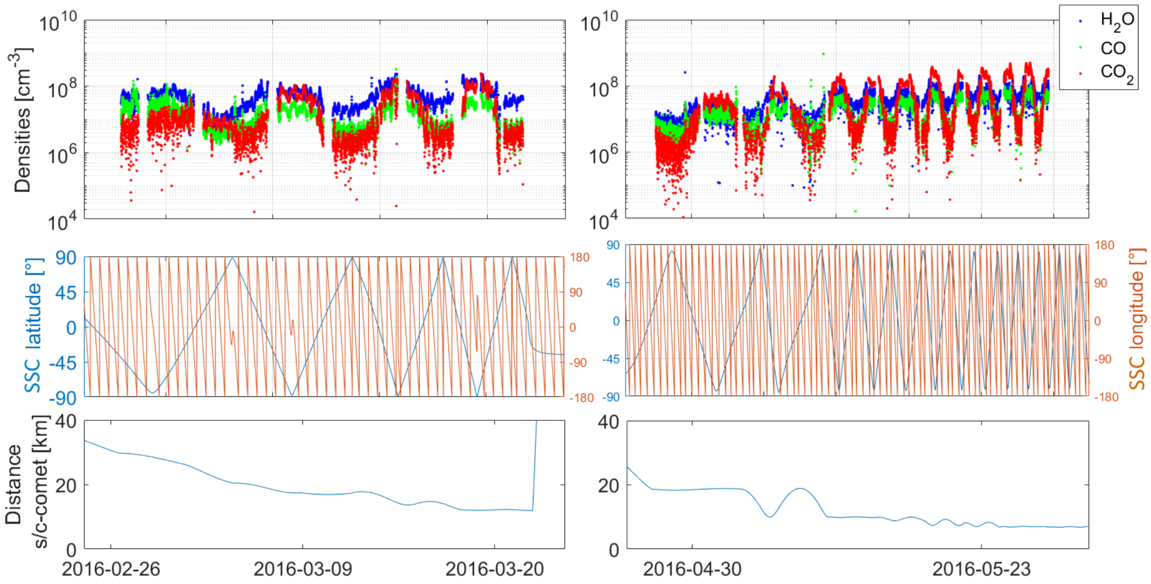

Figure 7.12: Densities of the main volatiles during the post-equinox 2 time period.

spectra sporadically during the whole period, making the behaviour of the main volatiles not easy to analyse.

A zoom on the very last days of the RTOF dataset (from 21 to 26 September 2016) is visible in Figure 7.13. We observe the different behaviours of the three main volatiles at close distance from the nucleus. During 2016, water detection slowly decreased as the comet moved away from the Sun. Towards the end of the mission, H_2O values are mainly below the value of CO_2 and CO, except for some points with sub-spacecraft point latitudes above 30°. The water density (blue points) appears more scattered at low density values, around 3.10^6 cm^{-3} on average.

Comparing the variation with the sub-spacecraft point latitude given in the lower panel, we see that CO_2 and CO are anti-correlated with the latitude variation. They are mostly detected in the coma when the spacecraft flies over the southern hemisphere while the H_2O variations are affected neither by the latitude nor by the longitude. CO density variations seem to follow closely the CO_2 density but with smaller amplitude, which is in agreement with a deeper location of CO ices. Nevertheless, the correlation of CO detections with water ice or carbon dioxide ice is complex. The middle upper panel shows very well the change of coma composition when the line of sight of the instrument points towards the southern hemisphere rather than the northern hemisphere of the nucleus. However, during this time period, the northern hemisphere was illuminated and we confirm the detection of carbon dioxide and carbon monoxide from both illuminated and non illuminated areas. Overall the CO and CO_2 densities are larger over the southern hemisphere and the equator, with more CO_2 than CO in the southern hemisphere but less in the northern hemisphere.

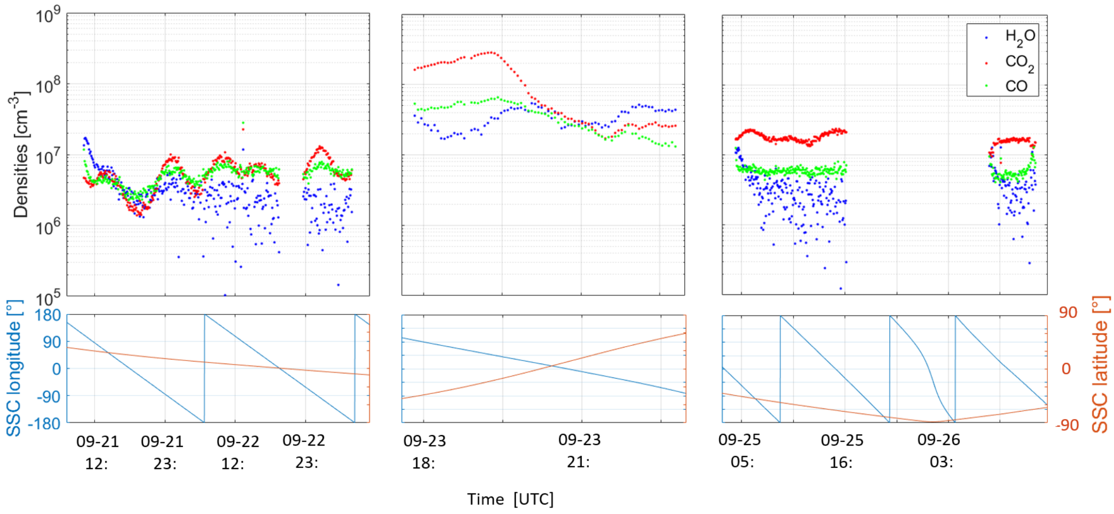

Figure 7.13: Densities of the main volatiles (zoom on the last days of the mission).

7.5 Evolution of density ratios

The variability of absolute density values of a specific species may hide several biases related to the orbitography. Thus, analysing density ratios between the species is important and may reveal interesting behaviors.

In figure 7.14, we show the CO/H_2O and CO_2/H_2O density ratios derived from RTOF spectra. During the approach, the variations of the ratios are synchronised but the CO/H_2O decreases while CO_2/H_2O increases slowly and both reach a similar value in October 2014. We then observed huge variations for both ratios, with higher density values for CO_2 on average. In the intermittent set of data of 2015 around perihelion, the CO/H_2O ratio is dominant. Around the second equinox, moving beyond the ice line, the ratios of CO_2 and CO versus H_2O globally increased, they both exceeded 5 and CO_2/H_2O even reached 25 in September 2016.

The sub-spacecraft point latitude is shown in the lower panel and the correlation with the ratios variation can be studied. Before the 1st equinox and after the 2nd equinox, the high density ratios are mainly located in the southern hemisphere, confirming the strong hemispherical asymmetry of CO and CO_2 during the mission. The variations of the ratios are mainly driven by the variations of the water density in the coma. Nevertheless, we observed larger variations of the CO_2/H_2O ratio than for CO/H_2O, suggesting a stronger CO_2 composition heterogeneity.

Figure 7.15 shows the CO_2/H_2O density ratio as a function of H_2O density from RTOF, which can be compared with the same ratio (as a function of column density) as seen by the Visible InfraRed Thermal Imaging Spectrometer (VIRTIS) during the exact same period, i.e. from 24 November 2014 to 24 January 2015. Both instruments used different techniques of measurements, RTOF measured in situ densities while VIRTIS derived column of density from remote sensing spectroscopy. Nevertheless, the results are similar with a clear anti-correlation between the CO_2/H_2O ratio and H_2O density or column density – in agreement with the previous conclusions on the pre-equinox 1 – down

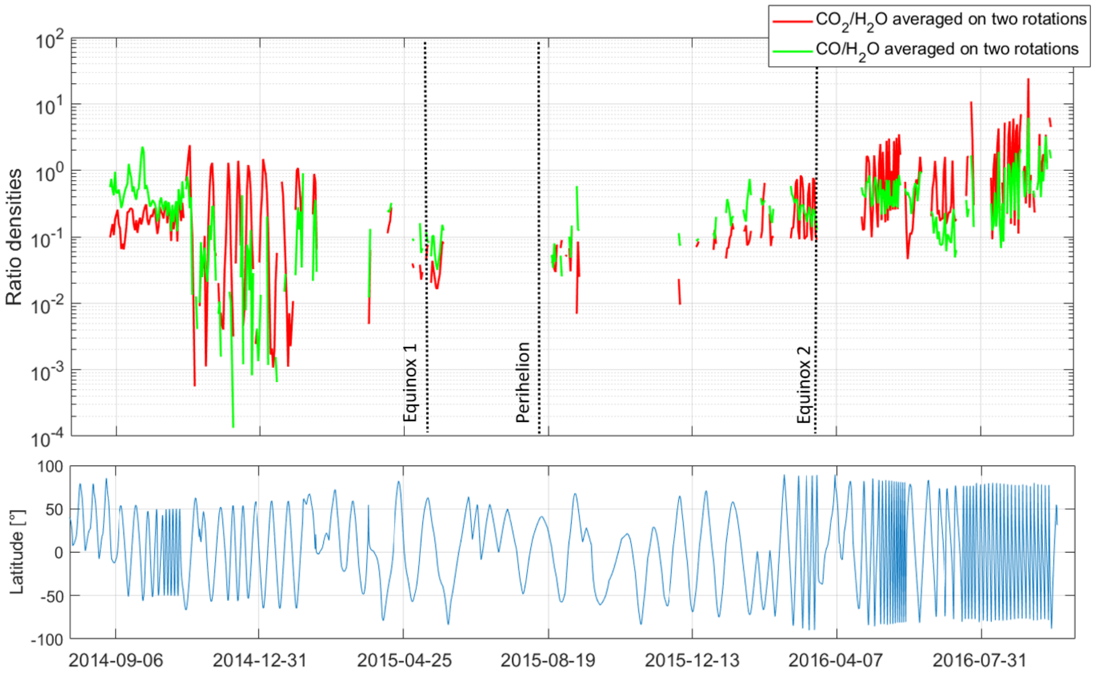

Figure 7.14: Upper panel: time evolution of CO/H_2O and CO_2/H_2O average density ratios for the entire mission, starting in September 2014 and ending in September 2016. Lower panel: variation of the sub-spacecraft point's latitude in degrees.

to a minimum value of 0.01-0.02 in the northern hemisphere. We also observe some CO_2 coming from both illuminated and non-illuminated parts of the nucleus, as mentioned by Bockelée-Morvan et al. (2015) .

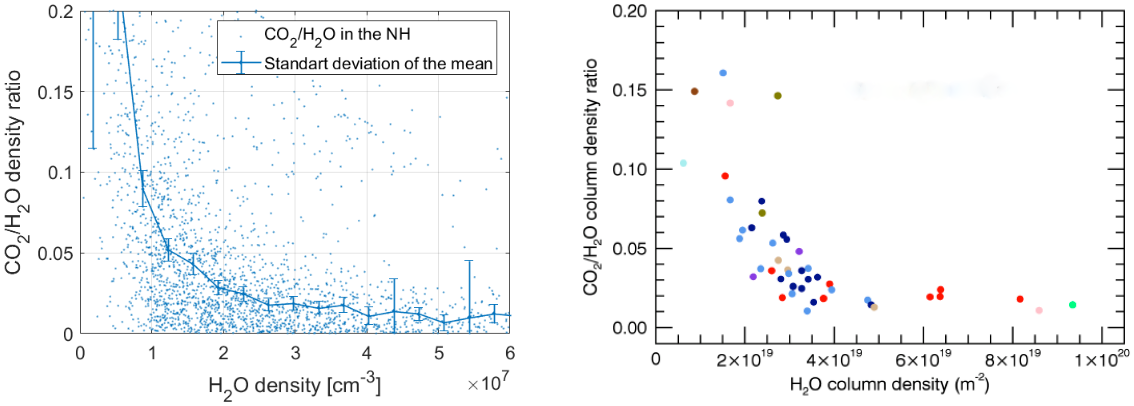

Figure 7.15: CO_2/H_2O density ratio from RTOF as a function of H_2O density from 24 November 2014 to 24 January 2015 (left). This figure is compared with the similar analysis in Fig. 11 published in Bockelée-Morvan et al. (2015) (right), where the colors indicated the observed regions.

The analysis of the ratios over the mission revealed the importance of the illumination in the density measurements, with the clear change in relative ratios to water when crossing the ice line. The variations of CO and CO_2 appeared more complex and are not fully explained by the illumination. To investigate the influence of the spatial variations of outgassing over the nucleus and eventually reveal active regions, we produced 2D maps of density for the three volatiles, in Chapter 8. A comparison with the measurements with other instruments, such as ROSINA/DFMS, and with a model of coma allow to analyse to what extent the instruments provide a consistent picture of the coma that is reproduced by the dominant physical processes included in a coma model (see Chapter 10).

Chapter 8

Spatial variation of the main volatiles

This chapter is dedicated to the study of the spatial variations, which allows to understand the influence of the complex shape of 67P/C-G and investigate heterogeneities on the surface or potentially inside the nucleus. A two-dimensional projection described in the first section will help compare the spatial heterogeneities later discussed. In a second section, we describe an illumination model developed to investigate the correlation between illumination and outgassing and present the maps of average illumination for the five studied period defined in Section 7.4. In a third section, we present maps of density of the three main volatiles seen by RTOF as well as the maps seen by DFMS for the five periods. We analyse the evolution of the spatial heterogeneities through the mission and the difference between the maps of both instruments. In particular, we describe the dichotomy between the two hemispheres during the mission and the difference between the lobes seen by RTOF at the end of the chapter.

8.1 The geographical coordinate system

Understanding the geographical variability of the comet outgassing needs the use of a geographical coordinate system centered on the comet. The Rosetta team defined a coordinate system based on the rotation axis of the comet 67P/C-G, leading to a system of longitude and latitude defined as follows. The latitude zero is the equatorial plane of the comet, separating the northern and the southern hemisphere. The center of the map, i.e. the point of latitude 0 and longitude 0, is the extremity of the small lobe. The big lobe area (Imhotep region) is located at the borders of the maps (+ or − 180 degrees).

Based on OSIRIS pictures, El-Maarry et al. (2015) mapped the nucleus surface in regions according to their morphology and/or structural boundaries. The morphology of the regions are, among others, consolidated (ex: Anuket), fractured (Maftet), smooth (ex: Hapi), dust covered (ex: Ash), brittle/weakly consolidated (ex: Seth), with large depressions (ex: Aten), etc. The various different features observed on the surface seem to indicate an heterogeneity of composition and physical parameters over the nucleus.

The correspondence between the morphological regions introduced by El-Maarry et al. (2015) and this 2D mapping is shown in Figure 8.1. Hereafter, 2D longitude/latitude maps are used to visualise the geographical heterogeneities of the coma and link them with surface and sub-surface heterogeneities.

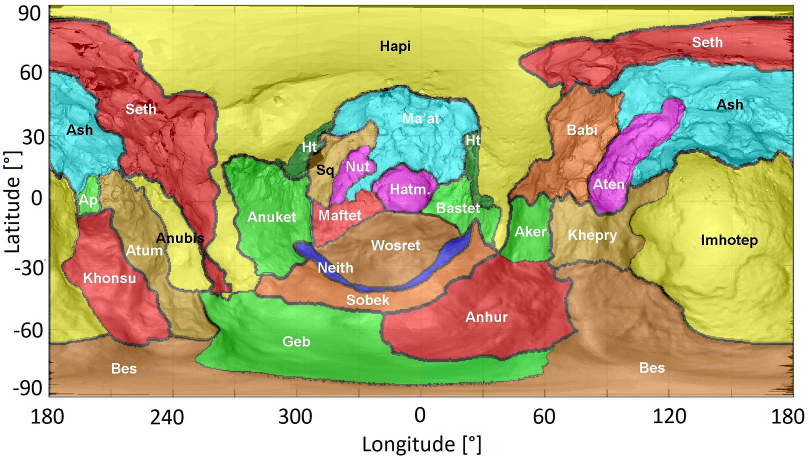

Figure 8.1: Two-dimensional longitude/latitude representation of the morphological regions of 67P/C-G as defined in El-Maarry et al. (2015). Credit: OSIRIS Team.

8.2 Illumination model

To study the correlation between solar illumination and outgassing, we produced maps of illumination for 67P/C-G, based on an illumination code developed for a shape model with 10 000 facets (SHAP5, provided by ESA) by D. Toublanc and A. Beth. A version of this code is available online in the virtual observatory for planetary science called VESPA (http://www.europlanet-vespa.eu/).

One can observe in Figure 8.2 the maps of illumination for each of the 5 periods defined and discussed earlier in Section 7.4. The heliocentric distance and sub-solar latitude are shown in the left column in Figure 8.2 while the maps of surface illumination appear in the right column. The illumination is averaged over one rotation period with mean latitude conditions appropriate to each period considered. The normalised intensity of the colour (maximum in red, minimum in blue) at every illuminated facet is given by the cosine of the angle between the normal to the surface and the direction to the Sun.

During the approach and the pre-equinox 1 periods, the Sun illuminates mainly the northern hemisphere. The illumination maps of the two periods are almost identical with the illuminated regions in the northern (summer) hemisphere, being mostly the Set, Ash, Ma'at, and Hapi regions, extending towards slightly lower latitudes closer to equator for the pre-equinox 1 period. The Imhotep region starts to be illuminated here. The summer in the southern hemisphere is visible in the third time period. After perihelion, the southern (summer) hemisphere became strongly illuminated, except just below the head of the comet (Sobek region) which remained in shadow. During the post-equinox 2, the illuminated region were the latitudes close to the equator. At the end of the mission, the summer was back in the northern hemisphere, somehow similar to pre-equinox 1 illumination conditions.

The variation of the sub-solar point latitude is well visible on the map, with a strong seasonal evolution. In addition, the complex shape of 67P/C-G's nucleus induces a heterogeneous illumination, in particular around the neck and the lobes. These areas undergo a

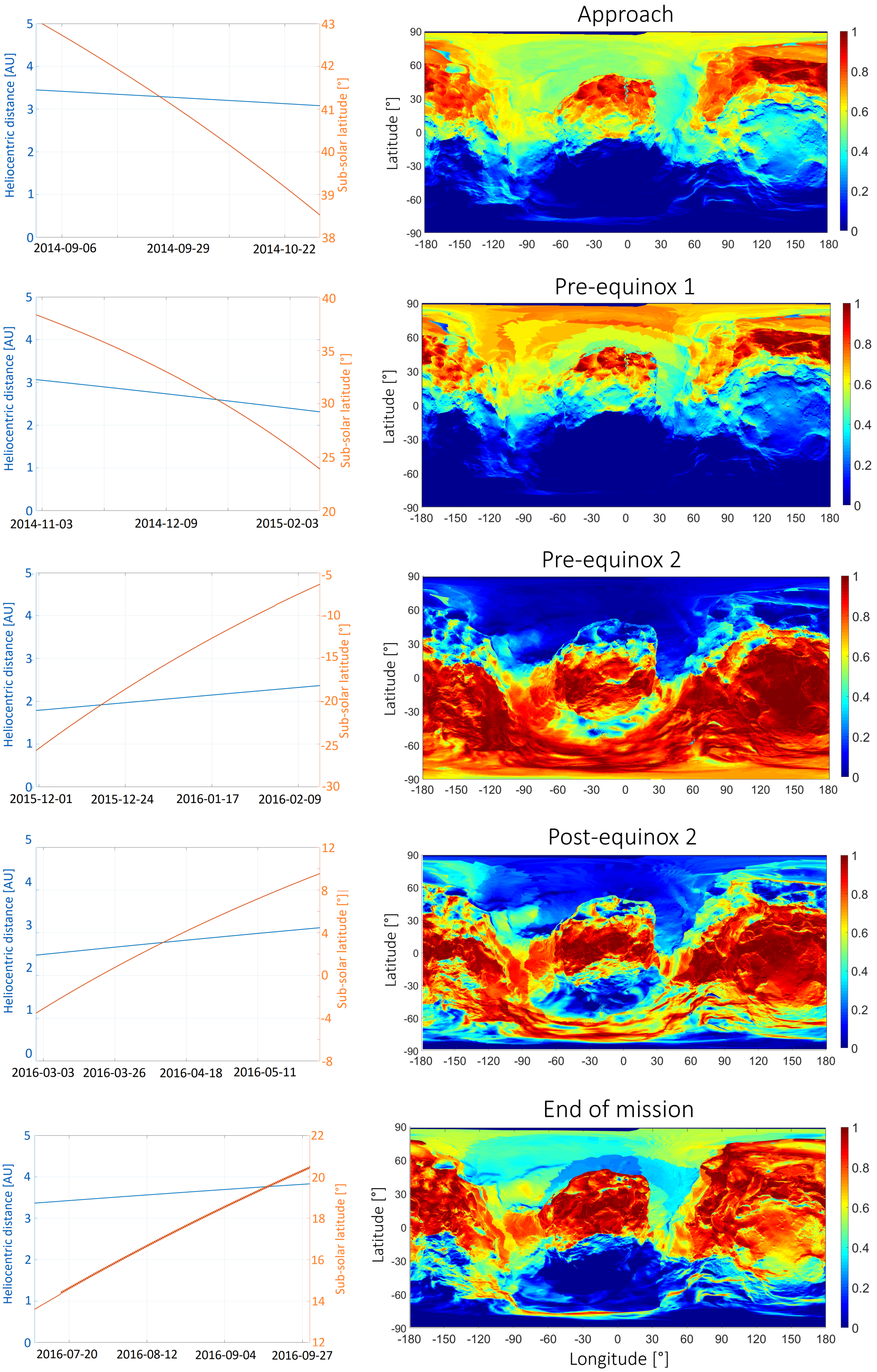

Figure 8.2: Left: variation of the heliocentric distance and sub-solar point latitude for the five studied periods. Right: 2D longitude/latitude maps of average illumination during the five periods.

.

thermal gradient which plays an important role in the activity of the comet. The neck, for example, is a concave area and experienced the fastest temperature changes. Alí-Lagoa et al. (2015) showed that the early activity of the comet originated from the high rate of thermal cracking due to the rapid change of temperature.

8.3 Density maps through the mission

To investigate the spatial heterogeneities at the surface of the comet, we created density maps using the density values of the three main volatiles measured by RTOF.

To do so, we normalised all the densities from RTOF and DFMS to the expected densities at the surface of the nucleus. Assuming that the comet is a point source with no significant loss process at small distances, we used a $1/r^2$ variation to estimate the normalised densities (see previous Section 7.1). In addition, we removed all the data corresponding to a nadir off-pointing angle larger than five degrees due to the uncertainties in the origin of the detected molecules. Their origin is assumed to be given by the sub-spacecraft latitude and longitude at the moment of the detection. This assumption allows us to project the measurements detected in the coma onto the comet surface. Nevertheless, this simplifying assumption will give us a global trend of the spatial distribution of the densities, but does not allow to study details.

For a more detailed analysis, a complex modelling of gas propagation would be required, taking into account the fact that, on one hand, the detected molecules originate from the irregularly shaped nucleus with a solid angle of about 60 degrees, and that for most of the mission, on the other hand, the whole comet was visible in the field of view of RTOF. Such a global coma model will be discussed later in Chapter 10.

8.3.1 Description of the maps

The resolution of the RTOF density maps is 5 × 5 degrees square and has been chosen as the best compromise between the temporal and spatial resolution of the spectrometer. Each studied period lasts a few months and they provide together a good coverage of the whole nucleus' surface, with more than five detections per facet. Since most of the facets have been in the field of view of RTOF several times, we represent the median value on each facet. Facets with less than 5 data points are coloured in white. Topography lines are overplotted on the maps in white based on the 3D shape model SHAP5, provided by ESA/Rosetta/MPS for OSIRIS team.

These maps are shown in the six lower panels in Figures 8.3 and 8.4, showing the RTOF densities of H_2O, CO_2 and CO during the five studied periods (approach/pre-equinox 1/pre-equinox 2/post-equinox 2/end of mission). All the maps are colored following the logarithmic colorbar shown on the extreme right of the figure.

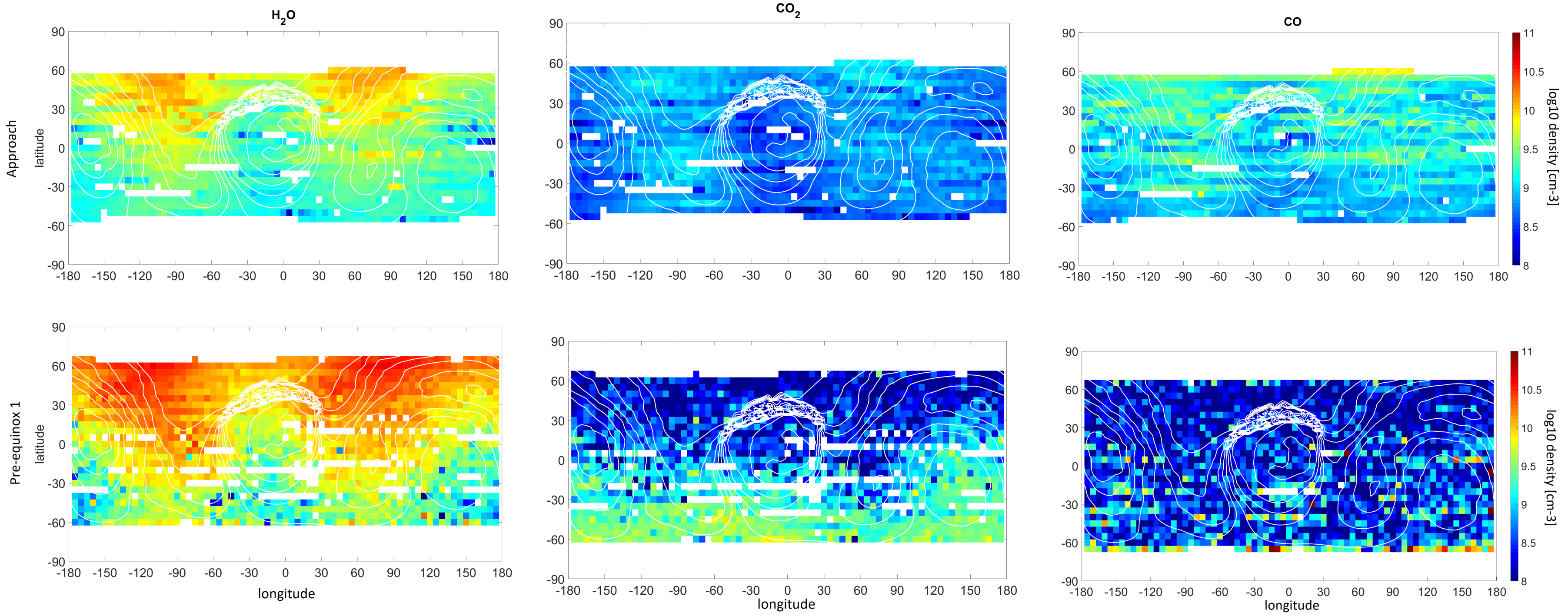

Figure 8.3: Spatial heterogeneities of the coma for the approach (top) and pre-equinox 1 time period (bottom), for H_2O (left), CO_2 (middle) and CO (right) densities.

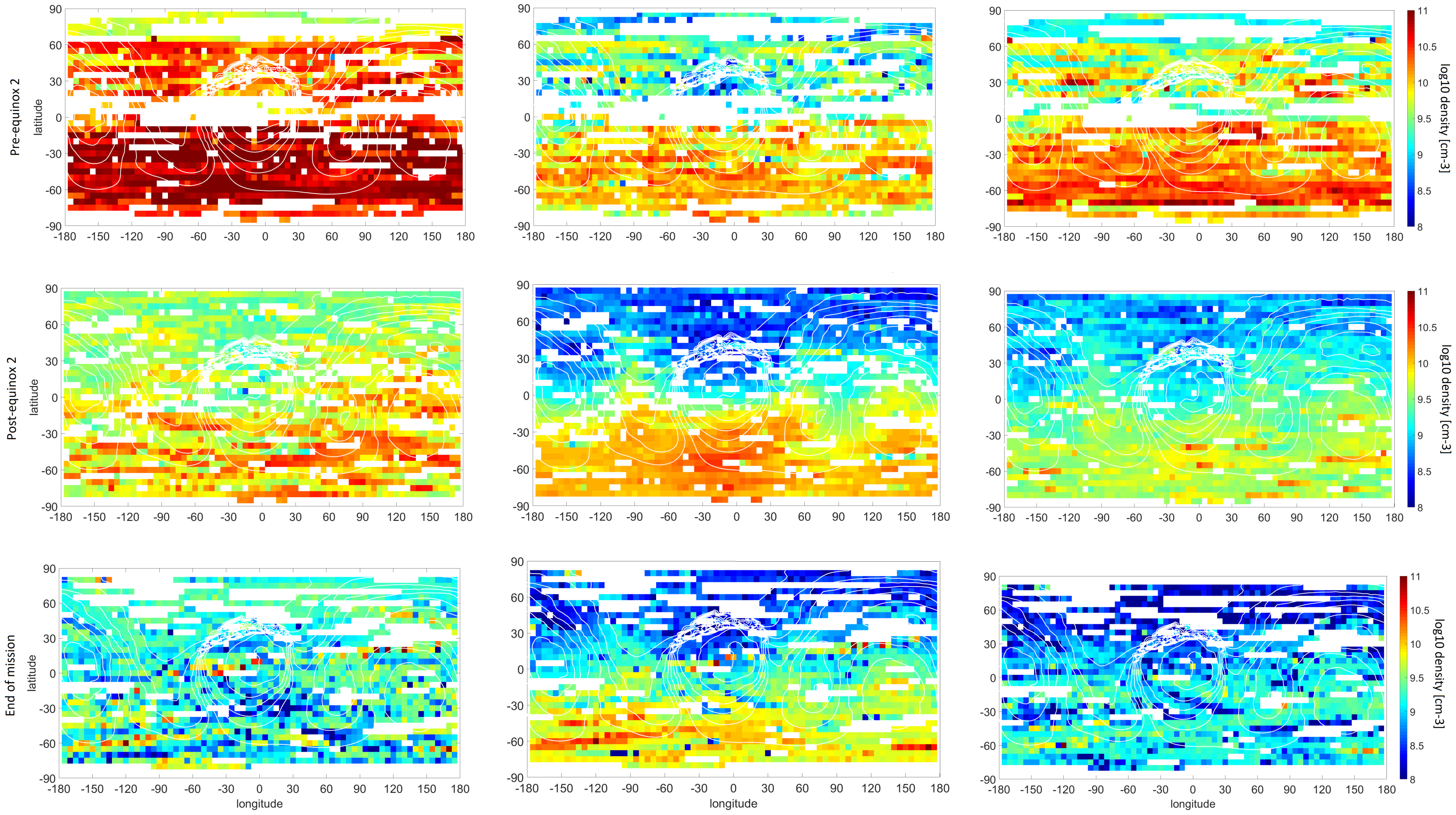

Figure 8.4: Spatial heterogeneities of the coma for pre-equinox 2 (top), post-equinox 2 (middle) and end of mission (bottom) time period, for H_2O (left), CO_2 (middle) and CO (right) densities.

8.3.2 Analysis of the density maps

Maps of water

The H_2O outgassing appeared, as expected, dominant compared to CO_2 and CO in the cometary gas during the whole mission, except at the end, after crossing the ice line. The five periods present detections of H_2O almost all over the surface, this is partly due to the nadir approximation associating RTOF detections with SSC coordinates. Overall, we observe a good correlation between the outgassing pattern and the illumination map. The influence of the solar illumination is clearly responsible for the H_2O ejection behaviour with a strong correlation between illuminated and active regions except for the small lobe of the comet. The approach and pre-equinox 1 reveal an obvious and coherent inhomogeneous production. The production was very localized in the northern summer hemisphere around the neck zone (Hapi region) with a maximum at the highest latitudes, where RTOF sometimes detected hundreds of counts per second. The illuminated neck zone thus appears responsible for the most important outgassing of water, as previously observed by several instruments, like MIRO, DFMS and OSIRIS (Biver et al., 2015; Hässig et al., 2015; Vincent et al., 2015). According to the first two maps, H_2O essentially originates from the Babi, Hapi, and Seth regions. From approach to pre-equinox 1, the average density increased in the northern and in the southern hemisphere, from an average value of 3×10^9 cm^{-3} to an average of 9×10^9 cm^{-3} and shifted slowly to the equator, together with the illumination pattern.

The third map acquired ten months later, shows the heterogeneities of the coma after perihelion with an important increase of the main volatiles' outgassing. Between the second and the third periods, the comet crossed the ice line and the detection of H_2O reached up to 10^{13} cm^{-3}. Close to perihelion, we observa a southern hemisphere largely more productive due to the summer illumination. H_2O was predominant in the northern hemisphere before perihelion and was expected to be detected in the southern hemisphere after equinox in early May 2015, as shown and confirmed in the H_2O map. After second equinox, the nucleus activity declined as it moved away from the Sun. The Sun illuminated again the northern hemisphere but sublimation in the southern hemisphere remained important. Nevertheless, we detected water all over the surface. At the end of the mission, we observed the lowest density for water, with a mean density over the surface of 2×10^9 cm^{-3}. The northern hemisphere, which was illuminated during this period, was slightly more active than the southern hemisphere regarding water. The H_2O outgassing pattern moved slowly from the south to the north and the heating over all the surface seemed to be still efficient enough to sublimate water. During the last months of the mission, water kept being detected above the limit of detection from all regions of the comet.

Maps of carbon dioxide

The spatial maps of CO_2 present a completely different behaviour. The first map (approach period) shows that CO_2 detections were less abundant and more homogeneous than water detections. The densest CO_2 outgassing were observed above both hemispheres, mostly above the neck region and above regions close to the head (Anubis, Anuket) or to the body (Babi, Aker, Khepri) as well as from the Imhotep region.

During the second period (pre-equinox 1), the CO_2 densities increased and appeared more localised. Most of the detections were made in the southern hemisphere (essentially below 30 degrees latitude south, except for the Imhotep large source region). This hemisphere was the less illuminated part of the comet during the studied period. Thus, this depletion does not follow the illumination conditions of the nucleus. From the first to the second time period, CO_2 sublimation clearly increased in the southern hemisphere. The southern hemisphere is, on average, seven times more active than the northern hemisphere during this second time period.

After perihelion, there is a global maximum of carbon dioxide detection in our instrument, originating from all the nucleus but with higher density detections in the southern hemisphere, by a factor of 5. The source regions are not clear, with the largest sources located below the head of the comet and below the Imhotep region. After the second equinox and until the end of the mission, the same source of carbon dioxide is active, with a strong north-south dichotomy. The CO_2 outgassing came mainly from the south (Sobek region) and the equator, but was also detected in the north, in Hapi and on the big lobe up to 30 deg latitude. The temperature became considerably colder while the comet moved away from the Sun and the sublimation rate slowly decreased.

Maps of carbon monoxide

At the beginning of the mission, CO was detected mostly from the illuminated part of the nucleus, like H_2O and CO_2, with density values larger than CO_2 by a factor 4 (CO_2 average density of $5{\times}10^8$ cm^{-3} and CO average density of $2{\times}10^9$ cm^{-3}). During the second time period, the CO density strongly decreased and was practically at the limit of detection in the spectra. However, activity from the south was two times higher than in the north. This transition can be linked to the similar behaviour of CO_2 at the same time: CO_2 detections surprisingly disappeared in the northern hemisphere and appeared strongest in the south during the winter.

CO became again more abundant than CO_2 after perihelion, where it was detected from all the surface in higher density. It then decreased slowly to become the third contributor by the end of the mission. In the fourth period (post-equinox 2), the dichotomy observed in CO_2 detections is less clear in CO. CO detections are higher than CO_2 detections in the northern hemisphere, but lower in the southern hemisphere and at the equator (in particular the neck and big lobe). From the post-equinox 2 to the end of the mission, sublimation of CO and CO_2 decreased in the northern hemisphere, which was the illuminated part of the comet at the time. Overall, the regions which released CO molecules correlate well with the regions releasing CO_2 for all the studied periods.

8.3.3 Interpretation of the observations

While H_2O represents the first contributor of the gas activity during most of the mission, the CO_2 and CO outgassing contributions overall increased in the last months and CO_2 became dominant after the second equinox.

Water sublimation is spatially well correlated with the illumination, as coherent with VIRTIS, which observed patches of water ice on the surface, appearing and disappearing in a cycle following the illumination conditions (De Sanctis et al., 2015). During the summer in the northern hemisphere, the water outgassing of the whole nucleus increased with a maximum located around the neck of the comet. After perihelion until the end of mission, the whole surface was still sublimating H_2O but the total outgassing decreased as the comet moved away from the Sun. The comparison of the situation before the first equinox and after the second shows a completely different spatial distribution. The illumination conditions and heliocentric distances are comparable but as the thermal inertia of the upper surface of the nucleus is very low (10-50 $JK^{-1}m^{-2}s^{-0.5}$ measured in Gulkis et al. (2015)), the heat may remain longer in the interior and the sublimation of H_2O (and other volatiles as well) can be prolonged.

The behaviour of CO and CO_2 is more complex. CO and CO_2 sublimation do not follow the illumination like H_2O. At the beginning of the mission, unexpected depletions of CO_2 and CO in the northern hemisphere were observed. An explanation has been brought by Keller et al. (2017) based on OSIRIS observations. The absence of detections in the northern hemisphere, though illuminated, could be explained by a back fall of dust originating from the southern hemisphere when active at the previous perihelion, that would insulate the northern hemisphere. This would result in a layer of solid materials containing water which has been depleted in more volatile species like CO or CO_2, due to their lower sublimation temperature (Keller et al., 2017). This could be responsible for the overall dichotomy seen between the northern and the southern hemisphere which appears clearly in the density maps.

The complex variations of ratios in Figure 7.14 is simplified by splitting the set of data according to the hemisphere. Figure 8.5 shows CO_2/H_2O and CO/H_2O ratios for the entire mission, for the sub-spacecraft point latitudes higher than 30 degrees (northern hemisphere) and lower than -30 degrees (southern hemisphere). In the northern hemisphere, the CO/H_2O ratio is higher than the CO_2/H_2O for almost all the mission, while the southern hemisphere ratios variations are more complex. We notice that CO spatial maps are in general more homogeneous, in agreement with the fact that CO molecules are highly volatile, the first layer containing CO should be located deeper, typically expected to be at 100 meters deep based on simple nucleus models (Prialnik, 2004), and its detection should depend less on the diurnal or seasonal variations.

In the northern hemisphere, CO and CO_2 have a cyclic outgassing behaviour: medium sublimation at the approach, very low sublimation at the pre-equinox 1, highest sublimation at the pre-equinox 2, medium sublimation at the post-equinox 2, low sublimation at the end of mission. The highest sublimation appears at the end of summer in the southern hemisphere. Two scenarii can be proposed to explain this observation:

- The northern near-surface nucleus could be structured as follows: first a dust layer containing water ice, then a layer of pure water ice, and finally CO and CO_2 located underneath. Far from the Sun, the temperature at the subsurface is at first high enough to sublimate CO and CO_2 but not H_2O. Approaching the Sun, the temperature then rises at the surface, allowing the sublimation of the water ice contained in the dust, but since the temperature drops rapidly with depth, the temperature is too low to sublimate the pure water ice layer, allowing CO and CO_2 located underneath to be sublimated (approach period). At lower heliocentric distances, the temperature in the interior then increases until it is sufficient to induce the sublimation of the pure water ice layer. This process consumes a large part of the available energy and the CO and CO_2 fluxes drop in the northern hemisphere (pre-equinox 1 period) until perihelion, where the heat wave reaches again the CO and CO_2.

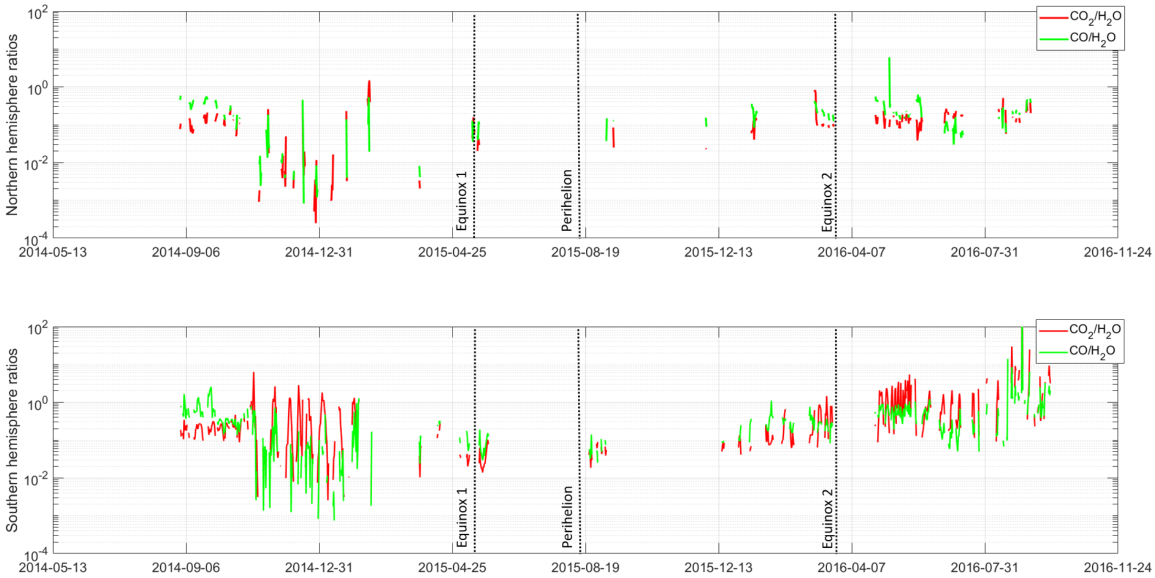

Figure 8.5: Time evolution of CO/H_2O and CO_2/H_2O density ratios for the entire mission for the northern hemisphere (upper panel) and the southern hemisphere (lower panel).

- The cyclic outgassing behaviour of CO and CO_2 in the northern hemisphere could be otherwise explained by the presence of CO and CO_2 included in the wet dust layer. The dust material is ejected from the southern hemisphere, were CO and CO_2 may be close to the surface (in particular CO_2, cf. the CO_2 ice patches discussed by Filacchione et al. (2016)). The ejected dust containing water could also have carried CO and CO_2 if the species have been previously trapped. These ice species would thus be sublimated and depleted during the approach and pre-equinox 1 periods, leading to the observed CO and CO_2 flux decrease until the sublimation of the deeper layers dominated before perihelion. This hypothesis requires the ejection of large dust particles capable of retaining CO and CO_2 molecules until the redeposition in the northern hemisphere. Nevertheless, dust particles are not expected to be large enough, as estimated in Keller et al. (2017), thus this scenario appears less probable.

In the southern hemisphere, CO_2 and CO are sublimated from almost the whole hemisphere from the end of 2014 until the end of the mission, without particular correlations with water detections. The active zones sublimating CO seem to overlap the zones sublimating CO_2 in the RTOF data set.

8.3.4 Difference between the two lobes

Two main assumptions can explain the bilobated shaped of 67P/C-G: 1) the nucleus was formed by two distinct objects, or 2) the neck region has been strongly eroded by a localised outgassing. Schwartz et al. (2018) showed through numerical simulations that bilobated and elongated comets like 67P/C-G may have been formed in a collisional disruption of a larger body. The low density and cross section of the neck of 67P/C-G nucleus suggested a low velocity collision (de Niem et al., 2018). Massironi et al. (2015) also observed two independent stratified envelopes over the big lobe and the small lobe. They therefore concluded that the shape is the result of a low velocity accretion of two distinct bodies.

We investigated an eventual difference in composition of near-surface layer between the two lobes, by studying the ratios of CO_2/H_2O and CO/H_2O. We defined two areas of 20 degrees of latitude and 30 degrees of longitude, centered on (0,0) over the small lobe and centered on (145,0) over the big lobe. In Figure 8.6, we show the ratio CO_2/H_2O as a function of H_2O density for the big lobe and the small lobe (upper panel) and the same analysis for the CO/H_2O ratio. Besides these species are ejected from the upper layers after significant erosion, and may not be good indicators of different initial compositions of the two lobes.

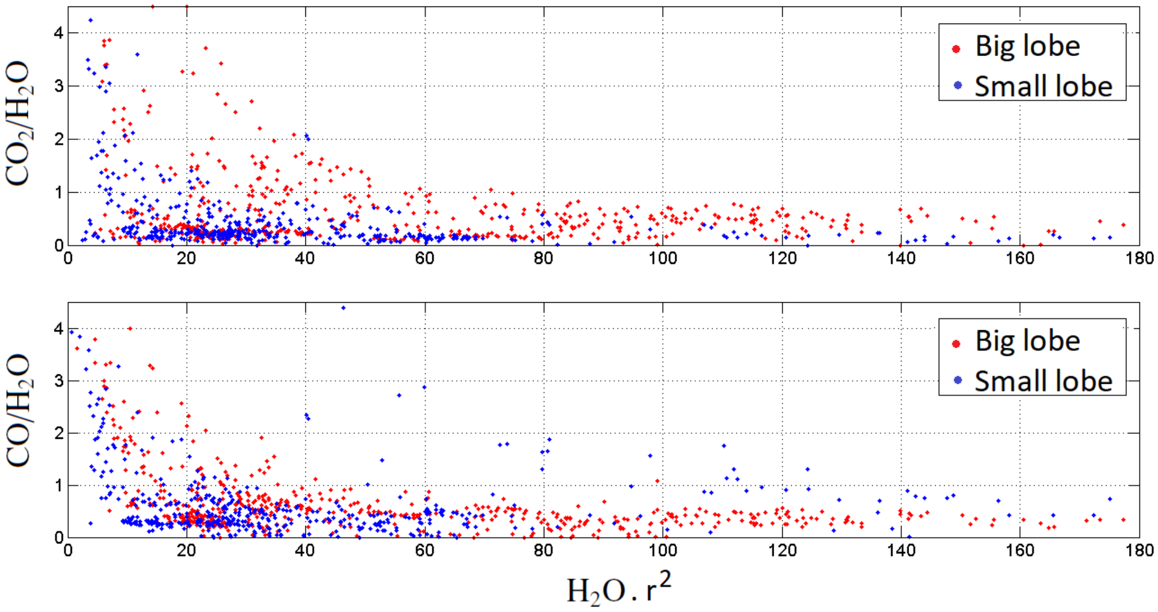

Figure 8.6: Study of the difference between the two lobes. CO_2/H_2O (top) and CO/H_2O (bottom) as a function of H_2O density (top) for the big lobe and the small lobe.

From the entire set of data, we calculated the following median ratios: $CO_2/H_2O = 0.19$; $CO/H_2O = 0.32$ for the small lobe, and $CO_2/H_2O = 0.32$; $CO/H_2O = 0.38$ for the big lobe, with standard deviations from 0.6 to 1. This shows that the ratio CO/H_2O is practically identical between the two lobes, while there is a difference for the CO_2/H_2O ratio. However, we can hardly conclude on a different lobe composition for CO_2 due to the large dispersion of the data and also due to strong hemispherical asymmetries and complex dynamics of the coma measurements.

8.4 Detection of molecular oxygen

In a typical RTOF spectrum where the instrumental effects have been removed (as shown in Chapter II), one can observe numerous peaks. In addition to the three largest peaks H_2O, CO_2 and CO, RTOF was able to detect minor peaks like a peak at mass 32, which corresponds, amongs others molecules, to O_2.

The detection of abundant O_2 in the coma of 67P/C-G stands for a major result of the Rosetta mission. If O is the third most abundant species in the universe, the O_2 molecules are highly chemically reactive and easily broken apart. Therefore, their detection in comets rises questions about their formation and their survival, and helps to constrain the models of the formation of the Solar System. Different processes may explain the presence of O_2 molecules in the coma:

- they may have been produced through radiolysis and trapped in clathrates during the comet formation (Mousis et al., 2016),
- they may be formed before the formation of the comet, in the ice mantle on dust grains in the protosolar nebula (Taquet et al., 2017),
- they may be created via dismutation of H_2O_2 ($2\ H_2O_2 \rightarrow 2\ H_2O + O_2$) (Dulieu et al., 2017).
- Yao and Giapis (2017) reported the formation of O_2 through a collision between an energetic H_2O^+ and an oxidised surface, which produced O_2^- (after dissociation) and finally formed O_2 (after photo-detachment). However, (Heritier et al., 2018) claimed that this mechanism may indeed happen on cometary surfaces but cannot explained the large amounts of O_2 found on 67P/C-G.

Bieler et al. (2015) revealed the first in situ detection of O_2 in comets, measured by ROSINA/DFMS. They surprisingly detected large amounts of O_2 with values in the range 1% - 10% from September 2014 to March 2015 and a mean value of 3.8% for the O_2/H_2O ratio. This made O_2 the fourth most abundant species in the coma of 67P/C-G. The analysis of the DFMS data reveals detections of O_2/H_2O, independent from the heliocentric distance. They thus concluded the O_2 measured in the coma was incorporated during the formation of the comet. Rubin et al. (2015b) afterwards detected O_2 in the spectra of comet 1P/Halley after reanalysing the Giotto data, with a mean value of $3.7 \pm 1.7\%$ for the ratio O_2/H_2O. As 67P/C-G is a Jupiter family comet and 1P/Halley is a Oort cloud comet, this may indicate that high abundances of O_2 are present in comets of all types.

Keeney et al. (2017), with the measurements of the ALICE spectrometer, measured a O_2/H_2O ratio ranging from 11% to 68%, with a mean value of 25%, which is considerably higher than the relative abundance detected with DFMS. The comparison between both values is complex due to the different types of measurements: indeed, ALICE measured column densities along a line of sight while DFMS recorded in-situ data.

With RTOF, we bring a third point of view to the characterisation of O_2 in the coma of 67P/C-G, with a higher temporal resolution.

8.4.1 Method

If we clearly measured a peak at mass 32, the study of O_2 in the RTOF spectra has to be made with caution. Considering its mass resolution, RTOF is not able to distinguish between different species with close m/q ratios. Among the molecules detected in the comet's coma, three of them contribute to the peak at mass 32: molecular oxygen (31.999 amu/e), sulfur (32.065 amu/e) and methanol (32.042 amu/e).

The excellent mass resolution of DFMS allows to resolve the contribution of the different species with a mass/charge close to 32. Figure 8.7 (from Bieler et al. (2015)) shows typical DFMS spectra around mass/charge 32, with the clear detections of S, O_2 and CH_3OH.

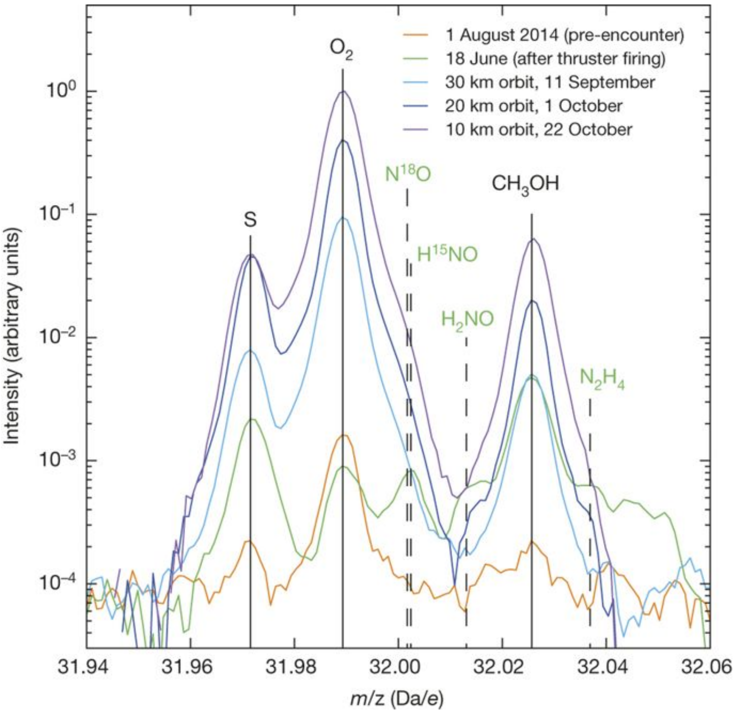

Figure 8.7: DFMS spectra acquired at 5 different time periods, showing the most abundant species detected at mass 32 over the mission (Bieler et al., 2015).

The analysis of O_2 can be helped by the identification of the parent molecules. RTOF recorded a full spectrum at each measurement, thus it measured at the same time parent and daughter's molecules. For example, the detection of sulfur is mainly due to the dissociation of the molecule H_2S, therefore, the presence of S in our peak at mass 32 should go hand in hand with a peak at mass 34. A second help comes from the DFMS dataset. During the mission, those three compounds were not measured by DFMS all the time, therefore periods were identified where sulfur and methanol were negligible, allowing us to deduce that the peak at mass 32 is mainly due to the detection of O_2.

Studied period

To identify a suitable period, we observed the evolution of abundance of O_2, CH_3OH and S detected by DFMS over the mission, visible in Figure 8.8. One good period to study

O_2 with RTOF turned out to be the approach period, where we have high abundances at mass 32 and where the relative amounts of CH_3OH and S measured by DFMS are small. Nevertheless, we observe that their abundances are not zero and will contribute to the peak detected at mass 32.

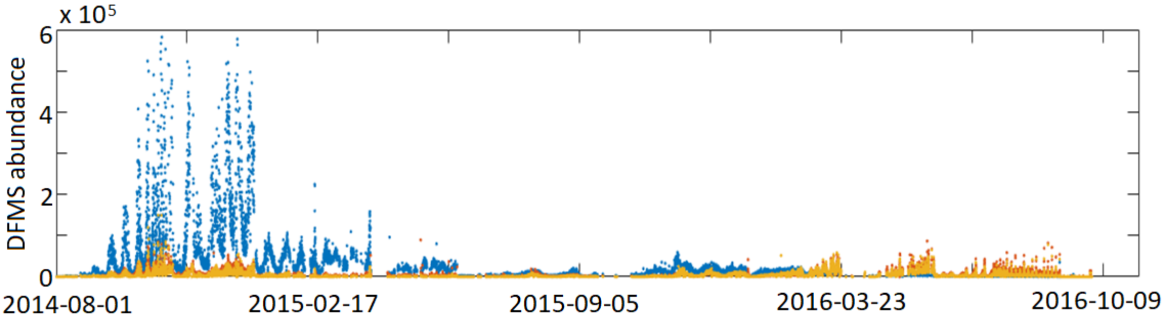

Figure 8.8: Abundances of O_2 (blue), CH_3OH (yellow) and S (orange) detected by DFMS through the whole mission.

Sensitivity

Another important point about the studied O_2 concerns RTOF and DFMS performance: the sensitivity value for O_2 has not been determined in laboratory, thus there exists an uncertainty in the exact quantification of O_2. To estimate the sensitivity, we used the correlation between sensitivity and ionization cross-sections described in Gasc et al. (2017b). Figure 8.9 from Gasc et al. (2017b) shows the linear trend between the sensitivity and cross sections of different species (taken from Kim et al. (2005); Szmytkowski et al. (1996)).

Tables 8.1 and 8.2 report the estimated sensitivity from the correlation, for H_2O, CO_2, CO, O_2, S and CH_3OH. From the comparison between the estimated values and the calibrated values available for H_2O, CO_2 and CO, we observe that the method is not perfect (in particular the estimation of H_2O sensitivity for the SS mode) but allows a first estimation on the densities of the non-calibrated species.

	Cross section [Å^2]	Est. sensitivity [cm^3]	Cal. sensitivity [cm^3]
H_2O	2.27×10^{-16}	8.27×10^{-23}	3.35×10^{-23}
CO_2	3.50×10^{-16}	1.28×10^{-22}	1.40×10^{-22}
CO	2.51×10^{-16}	9.15×10^{-23}	9.00×10^{-23}
O_2	2.40×10^{-16}	8.88×10^{-23}	not calibrated
S	4.40×10^{-16}	1.60×10^{-22}	not calibrated
CH_3OH	4.80×10^{-16}	1.75×10^{-22}	not calibrated

Table 8.1: Cross section of species, with the estimated sensitivity and the calibrated sensitivity for mode SS 521.

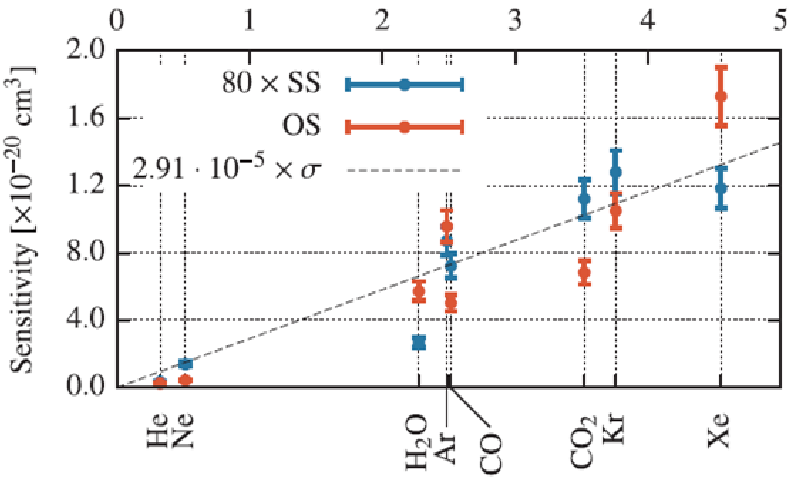

Figure 8.9: Sensitivities versus ionization cross section [$\times$ 10^{-16}] cm^2 for RTOF SS and OS modes (Gasc et al., 2017b).

	Cross section [Å^2]	Est. sensitivity [cm^3]	Cal. sensitivity [cm^3]
H_2O	2.27×10^{-16}	6.62×10^{-21}	5.73×10^{-21}
CO_2	3.52×10^{-16}	1.00×10^{-20}	6.82×10^{-21}
CO	2.51×10^{-16}	7.30×10^{-21}	5.00×10^{-21}
O_2	2.40×10^{-16}	7.10×10^{-21}	not calibrated
S	4.40×10^{-16}	1.28×10^{-20}	not calibrated
CH_3OH	4.80×10^{-16}	1.39×10^{-20}	not calibrated

Table 8.2: Cross section of species, with the estimated sensitivity and the calibrated sensitivity for mode OS 523.

8.4.2 Analysis

We studied the temporal evolution of the estimated O_2 over the approach period. Figure 8.10 shows the H_2O and O_2 densities measured by RTOF (upper panel) and by DFMS (lower panel). We observe a large dispersion of RTOF measurements, partially due to a greater time resolution. The average of O_2 outgassing globally followed H_2O.

We observed that the correlation with H_2O is less strong in RTOF detections than with DFMS (Bieler et al., 2015), and obtained a correlation coefficient of 0.42 between both species.

In our RTOF measurements, we found a mean value of O_2/H_2O ratio of 8.7% and a median value of 4.9%, which is within the 1 - 10% measured by DFMS with a median value slightly higher in the RTOF detection. The values are clearly lower than the ones derived from ALICE measurements.

We also present the spatial variation of O_2 during the approach period (Figure 8.11). The projection of the RTOF measurements on a latitude/longitude map revealed a heterogeneous distribution for O_2, as observed previously in the main volatile's density maps. The sublimation of O_2 appears very well correlated with illumination. The maxima of outgassing are in the northern hemisphere, around latitude 60° (no available data beyond) and the neck.

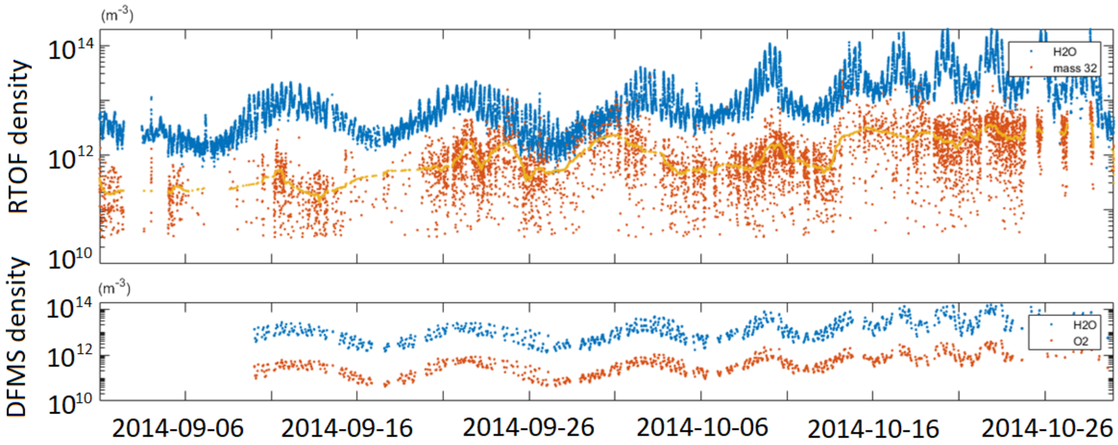

Figure 8.10: Temporal evolution of H_2O (blue) and O_2 (orange, with a moving average in yellow) densities from RTOF (upper panel) and DFMS (lower panel) over the approach period.

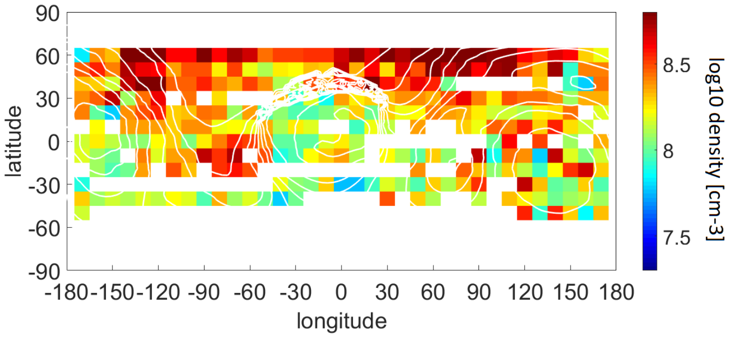

Figure 8.11: Map of O_2 density in molecules/cm^3 averaged over the approach time period.

Despite the degraded quality of RTOF spectra and its mass resolution, our method proposes a first analysis of the O_2 detections in the RTOF spectra. The analysis of a spectrum depleted in S and CH_3OH allows to observe the spatial distribution of O_2 at the beginning of the mission.

The work on molecular oxygen detected by RTOF has been done as a part of the internship of Helene Gourlaouen in our RTOF team in Toulouse.

Chapter 9

Comparison with DFMS

This chapter provides a comparison of the RTOF main volatiles densities with the densities measured by ROSINA/DFMS. In a first section, we investigate the correlation between the densities derived from the two spectrometers, which have their own sensitivity, and temporal resolution (see Section 9.1). We then compare the observations of density ratios of the two different spectrometers and of the spatial heterogeneities (see Section 9.2).

9.1 Cross correlation RTOF vs DFMS

ROSINA's package includes three different instruments. The comparison of their measurements represents a chance to validate the detection and to combine the high performance of the instruments. As described in Chapter 5, the COPS densities are used to normalise the densities of the two spectrometers.

We present in Figure 9.1 the cross correlation between the RTOF and DFMS temporal variations for H_2O, CO_2 and CO. We observe a linear trend for the three species which demonstrates the good global agreement between the derived densities from the two instruments. However, a notable dispersion appears in the cross correlations, especially for the low densities.

We quantified this effect by analysing the variation of a correlation factor for different maximum values of densities in RTOF. As visible in Figure 9.2, which shows the detections during the approach period, the correlation clearly increases for densities higher than 10^6 molecules/cm^3. As the sensitivity of DFMS (approximatively 10^{-19} cm^3 for H_2O) is higher than the sensitivity of RTOF (approximatively 10^{-23} cm^3 for H_2O in SS mode), this gives us a threshold of detections to increase the confidence in the RTOF measurements.

Another important difference stands between the detections of the two spectrometers. RTOF records a full spectrum every 200 seconds, while DFMS scans one mass range at a time, covering the full range from 13 amu/e to more than 130 amu/e in about 40 minutes (depending on the mode), counterbalanced by a better mass resolution. DFMS therefore has a lower temporal resolution compared with RTOF.

In Figure 9.3, we show the detailed data recorded during six days, after the second equinox, for the three ROSINA instruments. The excellent temporal resolution of RTOF is visible in the upper panel of Figure 9.3. In the second panel, the DFMS densities for the three volatiles are given for the same time. To adapt their measurements to the recordings of RTOF, the derived densities were time-interpolated and time-shifted to the

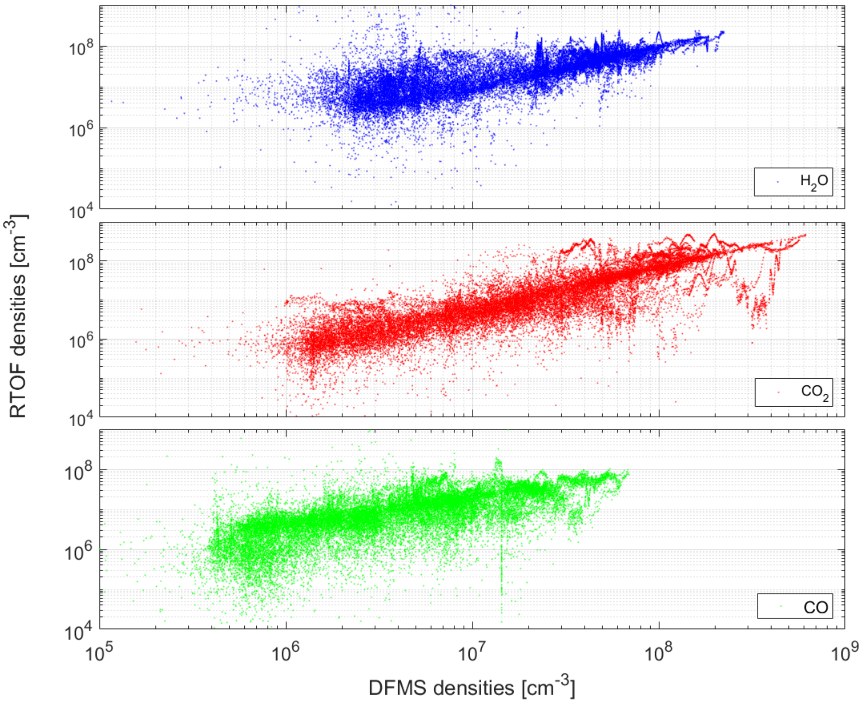

Figure 9.1: Cross correlation between RTOF and DFMS for H_2O (upper panel), CO_2 (middle panel) and CO (lower panel).

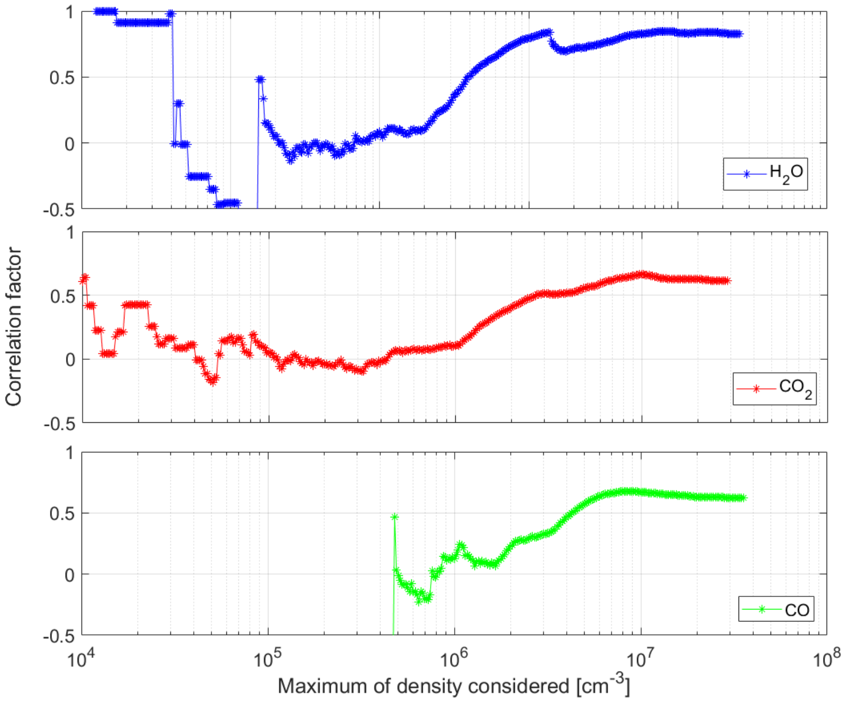

Figure 9.2: Correlation factor between the DFMS and RTOF measurements, for H_2O (upper panel), CO_2 (middle panel) and CO (lower panel).

.

time of water's measurements, i.e. about every 40 minutes. We thus note that DFMS does not measure the different species at the same time, while RTOF does, which makes the RTOF density ratios particularly interesting to understand the temporal variability of the volatiles. The difference of temporal resolution can be seen in the set of data of the two spectrometers: DFMS recorded much less data per species. The variations of the COPS pressures are also shown in the third panel. The pressure sensor provides global gas detections, which are close to the sum of the detections of the three main volatiles, as COPS does not distinguish the different volatiles.

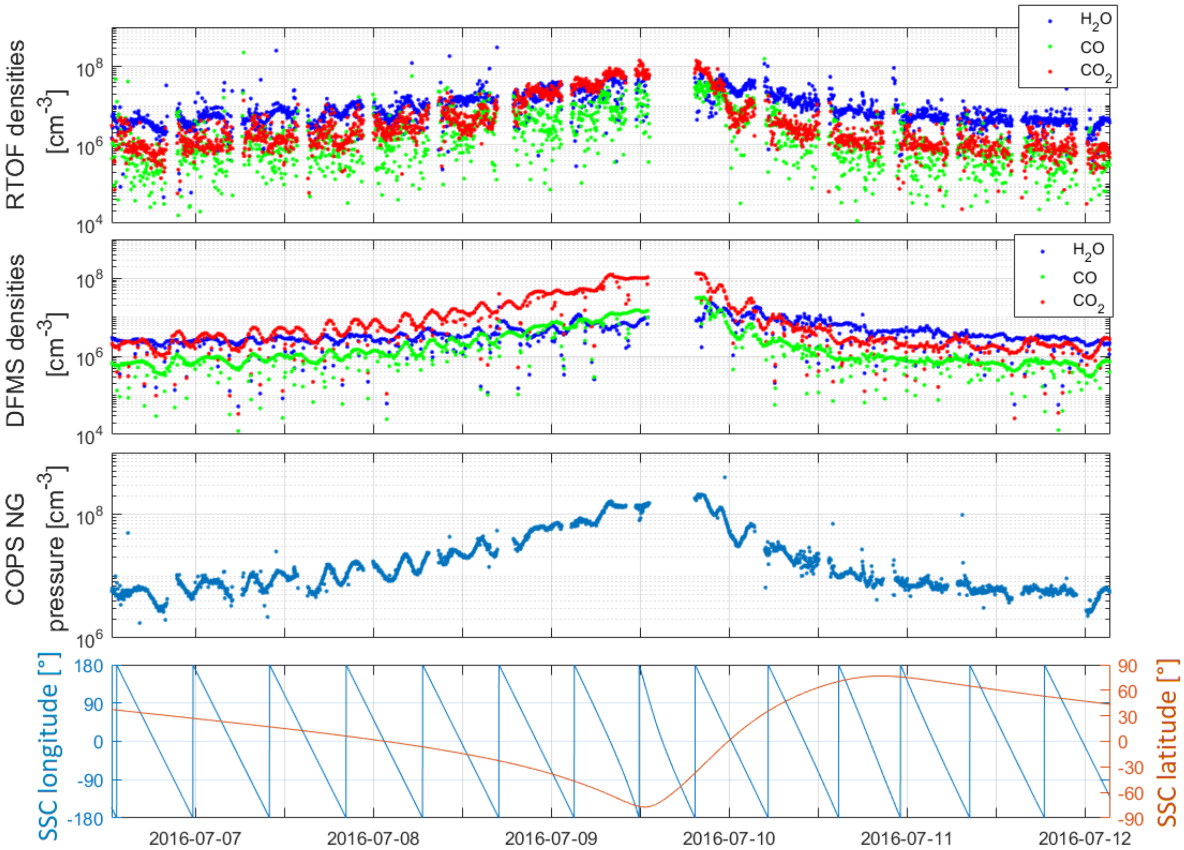

Figure 9.3: Temporal evolution of the main volatiles's densities after outbound equinox (first panel), DFMS corresponding densities (second panel), COPS nude gauge total densities (third panel) and sub-spacecraft point latitude and longitude (fourth panel).

During that period, the three volatiles were strongly correlated, suggesting very similar source emission regions. The anti-correlation with the sub-spacecraft latitude (lower panel) indicates that the ice sublimation mostly occurs in the southern hemisphere. The comparison reveals that the instruments are globally in good agreement with each other. The diurnal variation seen in RTOF and DFMS data is well confirmed by COPS. Nevertheless, as observed in this example, the datasets are not identical and DFMS detections sometimes do not match the RTOF data. We already cited the difference in sensitivity and temporal resolution, which induce an important diffusion in the RTOF measurements, and we observe that the relative abundances measured by the two spectrometers can be very different. In this example, the water outgassing is underestimated by DFMS, it appears lower than in the RTOF panel in particular around the maximum, the CO_2

detections are overestimated, and the CO detections are slightly overestimated. If some differences arise in the detailed individual variations of the species, the evolution of ratios reveal overall a good agreement between the spectrometers. As an example, in Figure 9.4, we provide the temporal variations of CO/H_2O and CO_2/H_2O ratios from RTOF and DFMS, with the variation of the SSC latitude. The correlation between the RTOF and DFMS ratios is very good, despite a significant dispersion of the RTOF values already discussed, partially due to the higher time resolution of RTOF.

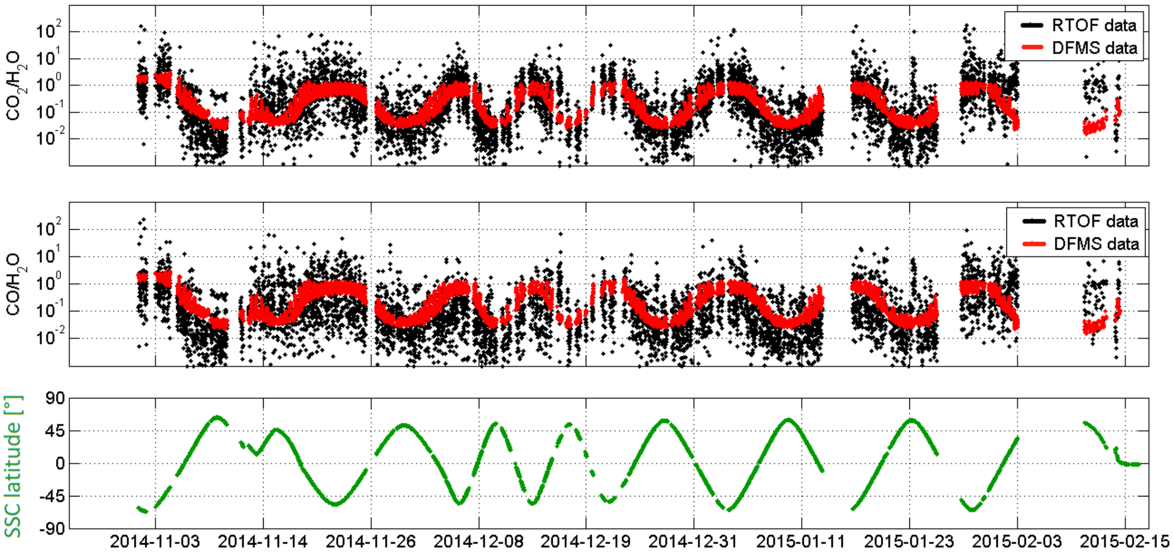

Figure 9.4: CO_2/H_2O (upper panel) and CO/H_2O (middle panel) ratios from RTOF and DFMS during pre-equinox 1, with the variation of the SSC latitude (lower panel).

9.2 DFMS density maps

The motivation to analyse the density maps as seen by DFMS is to confirm the observations made previously with RTOF. Once confirmed, the detailed maps seen by RTOF bring a finer precision in time, and in localisation.

We present here the density maps for the three volatiles, as described in Section 8.3, seen by DFMS. Figures 9.5 and 9.6 show the densities of H_2O, CO_2 and CO for the five periods given in Table 7.1. A resolution of 10 × 10 degrees square has been chosen due to the lower temporal resolution of the instrument.

The DFMS maps overall show the same global behaviour for the three volatiles, even if the resolution of the DFMS maps is lower than the RTOF maps, and even if they therefore do not study the coma at the exact same time for each species.

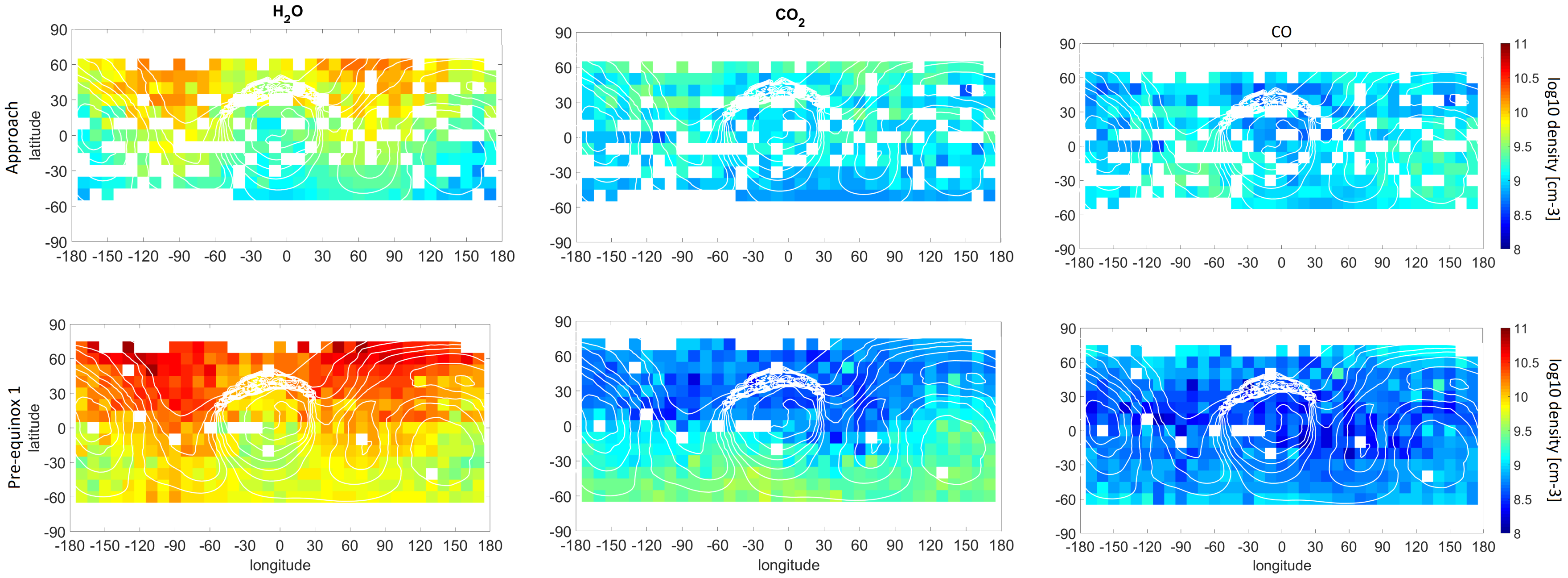

Figure 9.5: Spatial heterogeneities of the coma for the approach (top) and pre-equinox 1 (bottom) time periods, for H_2O (left), CO_2 (middle) and CO (right) densities, measured by DFMS.

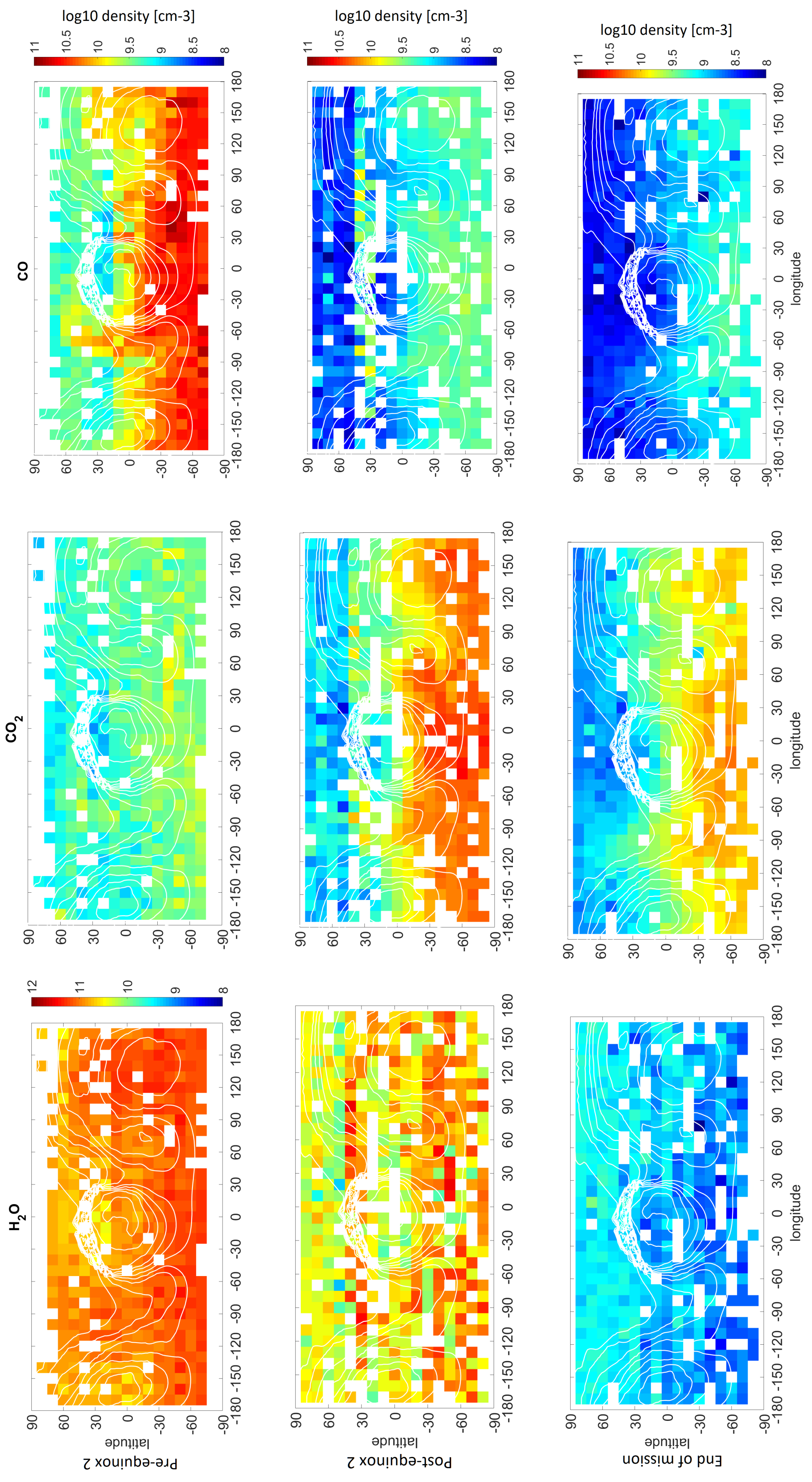

Figure 9.6: Spatial heterogeneities of the coma for pre-equinox 2 (top), post-equinox 2 (middle) and end of mission (bottom) time periods, for H_2O (left), CO_2 (middle) and CO (right) densities, measured by DFMS.

However, some differences are found with the density maps seen by RTOF:

- For the approach period, CO detections from DFMS are observed all over the surface, like in the RTOF map, but show a maximum in the southern hemisphere while the RTOF data show a maximum around 60 degrees of latitude. The data do not allow us to provide conclusions on the regions below -60° latitude. Also, CO_2 densities are higher in the DFMS maps during the approach.
- For the pre-equinox 1 period, the maps are in good agreement, with a weak activity of CO seen by both spectrometers, slightly higher in the DFMS map.
- The water's map from DFMS shows detections up to 10^{13} cm^{-3} while RTOF detections only reach 10^{12} cm^{-3}. Plus, the CO_2 detections appear lower in the DFMS map during the pre-equinox 2.
- In the fourth period, DFMS overestimated the CO_2 detections and underestimated the CO detections compared to RTOF.

To visualise more precisely the differences and investigate the ratios above specific regions of 67P/C-G (beyond the comparisons between the hemispheres previously discussed), maps of ratios have been studied. For exemple, Figure 9.7 provides the CO_2/H_2O and CO/H_2O ratios during pre-equinox 1 from both RTOF and DFMS.

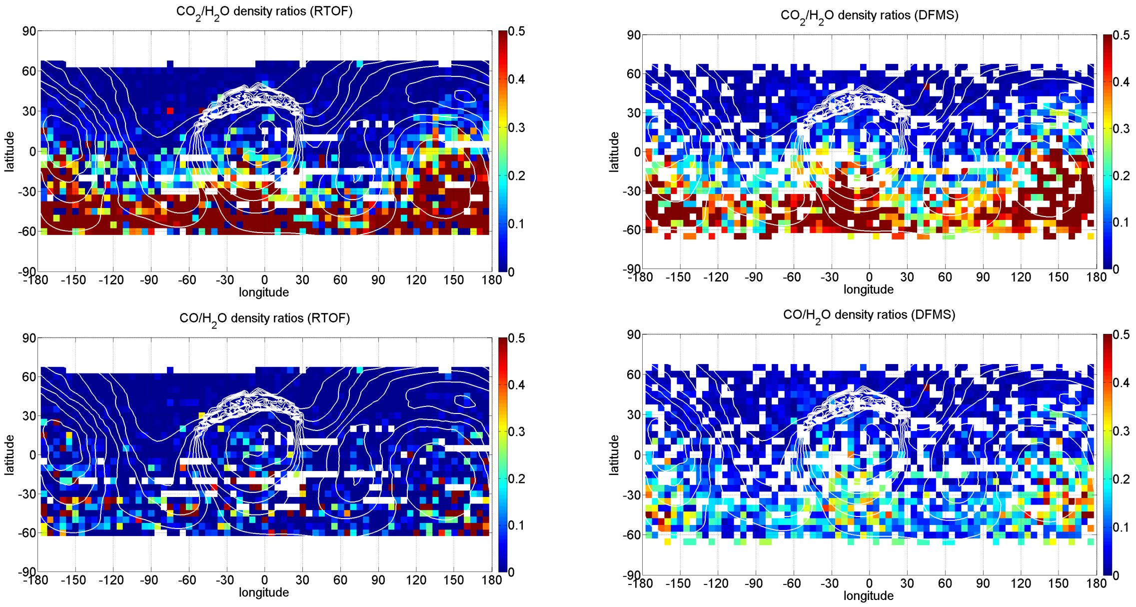

Figure 9.7: Two-dimensional maps of CO_2/H_2O (upper panels) and CO/H_2O (lower panels) density ratios based on RTOF (left) and DFMS (right) data for the pre-equinox 1 period.

The two spectrometers produce very similar maps for both CO and CO_2 ratios with a much larger number of points per cell (factor 7) for RTOF owing to the very different time resolution between the instruments. Maps of CO/H_2O show that DFMS overestimates the CO density compared to RTOF. Overall, the highest ratios seen by both instruments were very localised in the southern hemisphere. More precisely, the CO/H_2O ratio was highest (larger than 0.3-0.4) in the Imhotep, Khonsu, Wosret, Neith, and Sobek regions, whereas the CO_2/H_2O was highest (larger than 0.5) in the same regions as CO/H_2O but also in the whole latitude band [-60° -30°] (with parts of the Anhur, Bes, Atum, and Geb regions). The CO/H_2O ratio appeared both overall more homogeneous and with the highest detections more confined to the southern parts of the head and body of the comet, whereas CO_2 was strongly confined to and spread over the southern hemisphere. These observations are in agreement with the previous conclusions on the density maps of both species and the illumination conditions.

Both sets of maps are in very good agreement over the studied periods in term of spatial variations.

Despite the fact that the maps are not exactly identical, the DFMS dataset agrees with the important observations made with the RTOF dataset, both in terms of intensity values and spatial variations. H_2O outgassing maxima followed the illumination, high detections are localised around the neck region in the inbound part of the orbit, covered the entire surface after perihelion, and strongly decreased after crossing the ice line. As well, the DFMS maps show the dichotomy between the southern and the northern hemisphere observed by RTOF (Hoang et al., 2017) and also lead to the conclusion that a dust layer is covering the northern hemisphere (Keller et al., 2017). Similarly, the cyclic behaviour of CO and CO_2 in the northern hemisphere (Hoang et al., 2018, to be submitted) is confirmed clearly in the DFMS maps and needs to be explained.

Chapter 10

Comparison with a numerical model of the coma

The ROSINA in situ measurements allow to characterise one location of the coma at each time. To describe the entire coma of 67P/C-G and its evolution along its orbit, a complex modeling of the coma is needed. In this chapter, we describe the DSMC model (developped at the University of Michigan by the team of Mike Combi), which simulates the coma of 67P/C-G, and compare its results with RTOF measurements. The model is able to derive fluxes up to 400 km from the surface using the shape and the illumination conditions. The model also includes a heterogeneous activity surface distribution as boundary conditions, based on DFMS observations.

10.1 DSMC model

A Direct Simulation Monte-Carlo (DSMC) model was developed at the University of Michigan by the team lead by Mike Combi, and is detailed in Bieler et al. (2015). The DSMC model discussed in this work is a 3D DSMC approach using the Adaptive Mesh Particle Simulator (AMPS) code described in Tenishev et al. (2008).

Using the thermophysical model from Davidsson and Gutiérrez (2005), the model estimates the surface temperature on each facet from a triangulation of the shape SHAP5.1 (provided by OSIRIS team), according to the local illumination and, taking into account the self-shadowing of the nucleus. It then reproduces the collisions and trajectories of the particles, as well as the physical processes, like photo-dissociation and radiative cooling (Tenishev et al., 2008), from the surface to the spacecraft. This allows to simulate the atmosphere of 67P/C-G up to 400 km, linking the surface conditions to the in situ reference data recorded by ROSINA.

The DSMC model was successfully compared with both COPS and DFMS data by Bieler et al. (2015) and Fougere et al. (2016). Bieler et al. (2015) made the assumption that the solar illumination was the main driver of the outgassing. They were able to reproduce the main features measured by COPS from August to December 2014. Later, Fougere et al. (2016) constrained the model thanks to the ROSINA data. As ROSINA observed a dichotomy between the northern hemisphere and the southern hemisphere (Hässig et al., 2015; Hoang et al., 2017), Fougere et al. (2016) derived two heterogeneous activity maps for H_2O and CO_2, based on spherical harmonics and used them as inner boundary conditions for the 3D DSMC coma model.

The activity distributions are shown on the left of Figure 10.1. Note that the 2D maps are shifted of 90 degrees in longitude compared to the maps previously shown in this work. The computed surface heterogeneities contain a dominant source of H_2O in the Hapi region and dominant sources of CO_2 in the south of the Imhotep region and above Khonsu region. They coupled the activity distribution and the local illumination to simulate the density recorded by ROSINA. An example of simulation of H_2O density in the coma is shown on the right of Figure 10.1.

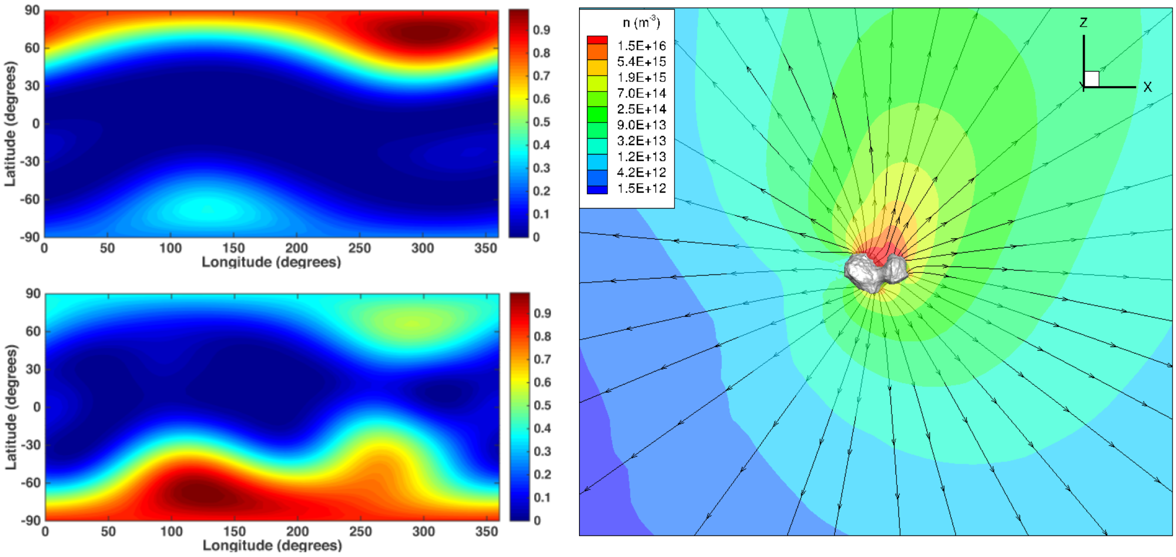

Figure 10.1: 2D maps of the H_2O (top left) and CO_2 (bottom left) modeled activity distribution at the surface of the nucleus described with a 25-term spherical harmonic expansion. Simulation of density (n) and streamlines for 23 December 2014 at 12:00:00 UT (Fougere et al., 2016) (right).

From the DSMC output, the densities are extracted every hour at the location of the spacecraft to allow a direct comparison between the model prediction and the in situ ROSINA data. Figure 10.2 from Fougere et al. (2016) show the densities of H_2O and CO_2 measured by DFMS from August 2014 to June 2015 and the DSMC outputs. They observed that the model reproduces well the seasonal variation over ten months, and even the diurnal variation.

Thus, the activity distributions which localise H_2O maxima outgassing around the neck and CO_2 in the south of the big lobe allow to fit the spectrometer's measurements.

10.2 Comparison with RTOF density

We compared for the first time the RTOF measurements with the output of the DSMC model. We investigated the reproduction of the seasonal and diurnal variation. Our study concerns the H_2O and CO_2 densities, the only species computed by the model at the time of the work.

First of all, the activity distribution maps shown in Figure 10.1 have been modeled from observations made between 4th August 2014 and 2nd June 2015 (including approach

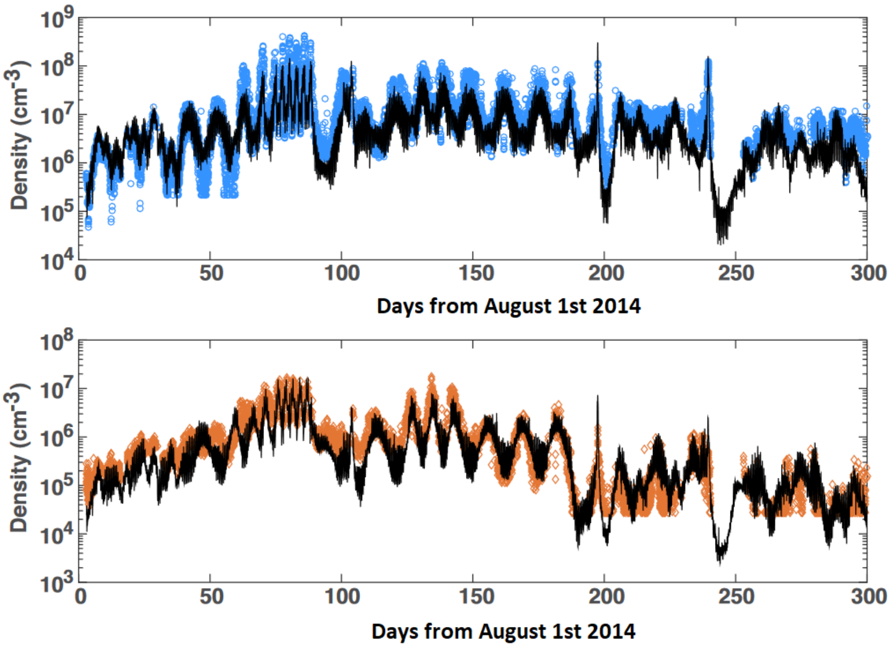

Figure 10.2: Density measured by DFMS (H_2O in blue and CO_2 in orange) and the DSMC density extracted at the location of spacecraft (in black) (Fougere et al., 2016).

and pre-equinox 1 periods). Thus, we compare those two maps and the corresponding density maps obtained from the RTOF measurements (see Section 8.3). Like in the computed activity maps, the pre-equinox 1 maps (see Figure 8.3) show a strongly different behaviour for the two species: H_2O mainly originating from the northern hemisphere and CO_2 mainly originating from the southern hemisphere. Also, the approach period shows detections of CO_2 in the northern hemisphere, on the neck region. Thus, the global localisation of active areas on the modeled maps is in good agreement with the observation made by RTOF during those periods, with the active region (North, mainly Hapi for H_2O; and South, mainly Imhotep and Khonsu for CO_2). However, a notable difference is the size of the active zones, which appears much larger in the RTOF maps, probably due to the approximation of a nadir off-pointing origin of the molecules.

The diurnal variations over nine days are shown in Figure 10.3. We observe that the global trend is reproduced by the DSMC model, but notice some important differences. In particular, the model underestimates the minima of densities for H_2O, while the CO_2 computed values are close to the detected values but are clearly not similar.

The seasonal evolution is studied in Figure 10.4 for the combined approach and pre-equinox 1 periods. The H_2O and CO_2 densities from the DSMC model are shown in black, and the in situ data of RTOF are visible in blue (H_2O densities) and red (CO_2 densities). The comparison with the RTOF dataset shows that the model can correctly reproduce the global trends measured in situ by RTOF. Nevertheless, RTOF data show an important dispersion compared to the model outputs, in particular for CO_2.

A more detailed analysis reveals that the DSMC model reproduces well the RTOF H_2O and CO_2 variations during the pre-equinox 1 but less during the approach. In Figure 10.5, we show the ratio CO_2/H_2O of density computed by the DSMC model and measured by RTOF for the two periods, approach and pre-equinox 1, as a function of

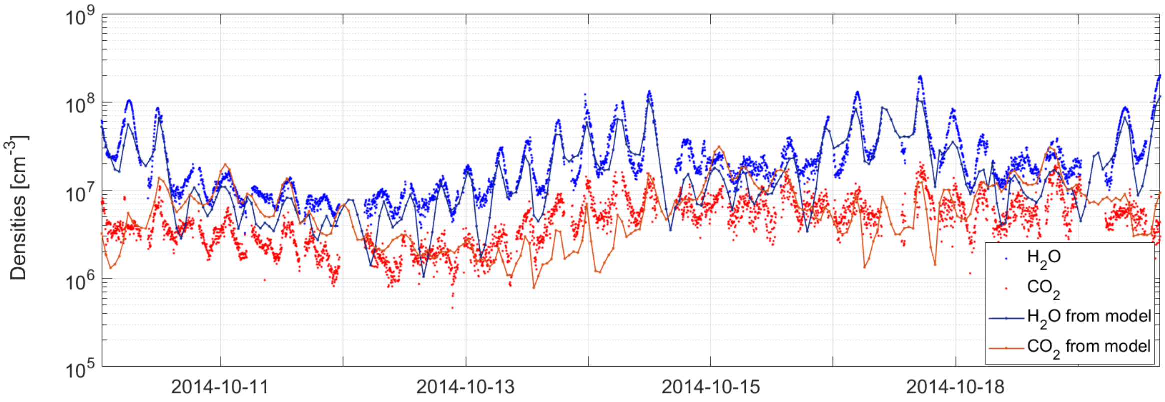

Figure 10.3: Diurnal variations of the H_2O and CO_2 densities: comparison between RTOF measurements and the results from the DSMC model.

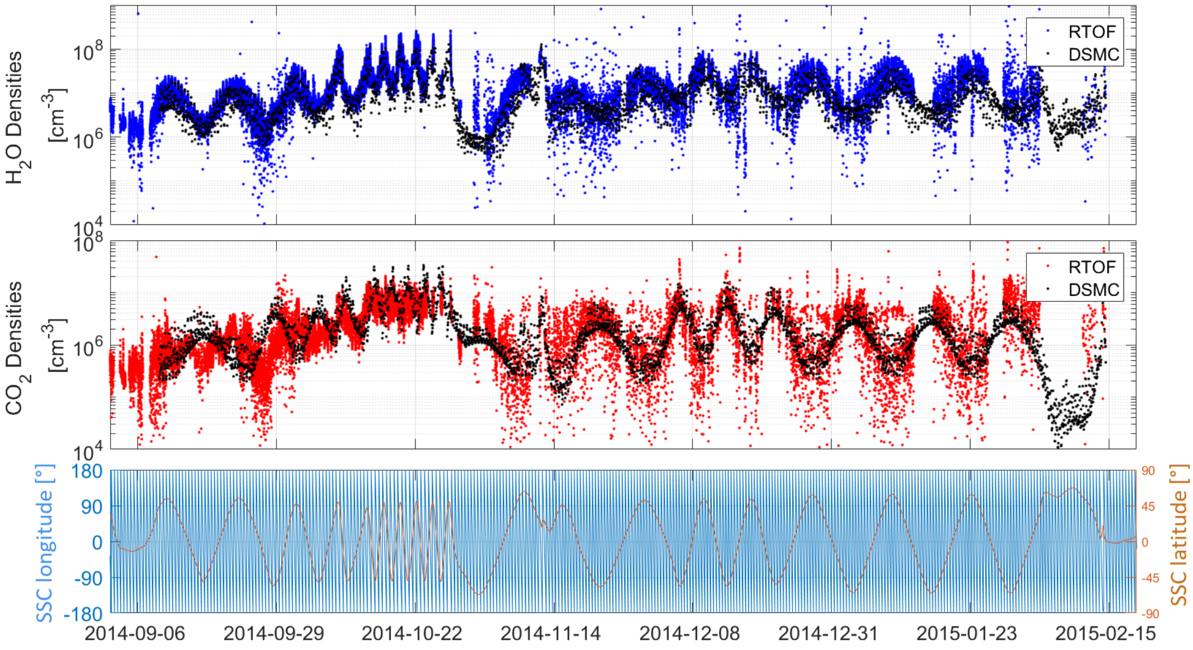

Figure 10.4: Comparison between the in situ data from RTOF and the data from the DSMC model for H_2O (upper panel) and CO_2 (middle panel). Lower panel: sub-spacecraft (SSC) longitude and latitude.

latitude. The DSMC model clearly underestimates/overestimates the CO_2 density in the northern/southern hemisphere. The data are less correlated during approach since the DSMC model considers a strongly active region in the southern hemisphere: the model needs large periods of time to retrieve activity maps, and CO_2 active areas may be unstable (Filacchione et al., 2016), with a CO_2 outgassing confined to the southern hemisphere mostly after the approach period (see our maps in Figure 8.3). For pre-equinox 1, the ratio between the DSMC model and RTOF H_2O and CO_2 is stable around 1, corresponding to a good agreement for both species: the DSMC derived activity map considers a strong CO_2 outgassing from the South as observed by ROSINA/RTOF.

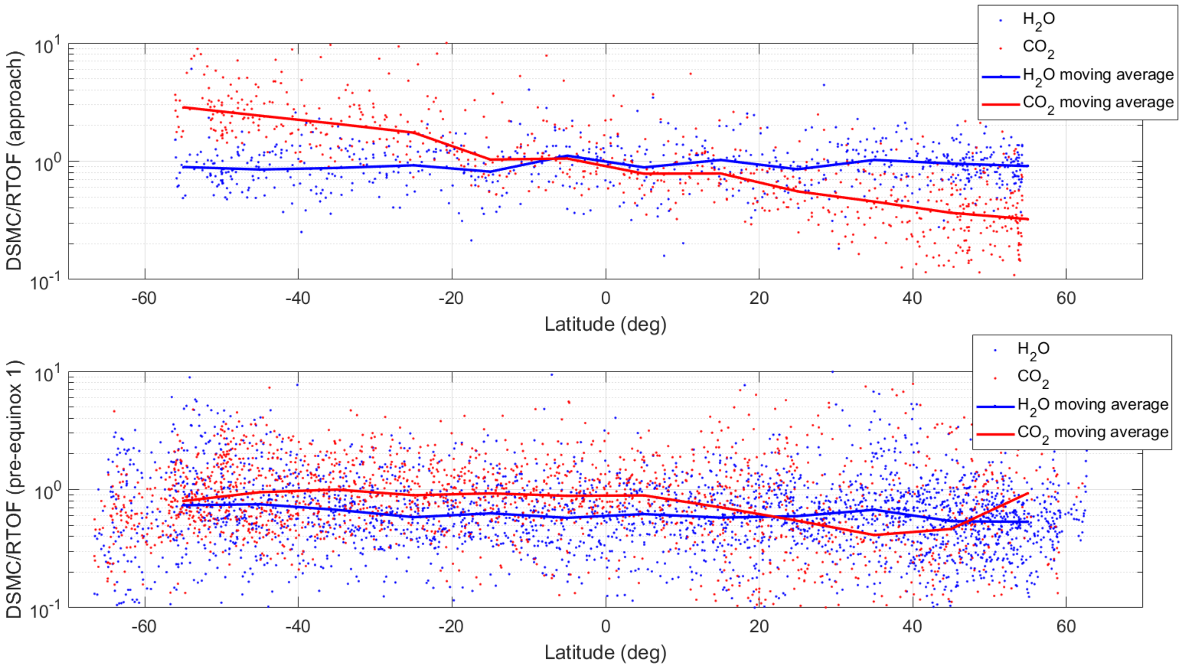

Figure 10.5: DSMC/RTOF ratio for H_2O and CO_2 for the approach (upper panel) and pre-equinox 1 (lower panel), with their corresponding sliding average (solid lines).

10.3 Global comparison between ROSINA and the DSMC model

We used the pre-equinox 1 period to directly compare all three ROSINA instrument's measurements and DSMC model's results. In Figure 10.6, we show the temporal variation of H_2O, in red, and CO_2, in blue, measured by RTOF (first panel), DFMS (second panel) – and for the total gas density – COPS (third panel). The fourth panel of Figure 10.6 shows the H_2O and CO_2 densities derived from the DSMC model. Variations of the phase-angle and nadir off-pointing are given in the fifth panel.

Beyond the diurnal and seasonal variations discussed previously, the composition and dynamics of the coma as measured by ROSINA and reproduced by the DFMS model also depend on parameters such as the phase angle and nadir off-pointing. The phase angle was mostly constant near 90°, except at two times (start and end of period pre-equinox 1) when it dropped significantly, leading to enhanced densities as expected (for a solar driven outgassing). As the DSMC method couples the illumination of the comet with an activity distribution constrained by the DFMS observations, both sets of data are in very good agreement, as shown by panel 4. In particular, the anti-correlation between the variations of the two species are well reproduced by the DSMC model during this period.

The comparison with the RTOF dataset, for H_2O and CO_2 during the periods studied in this work, reveals a globally good correlation, with some notable difference, as the model did not reproduce the details. Nevertheless, the model is able to simulate the outgassing of H_2O and CO_2 in three dimensions and their evolution over time. The correlation of the model and the main volatiles' behaviour seen with ROSINA indicates that the activity over the nucleus is strongly heterogeneous, since the model needs, in addition to the solar illumination, the use of heterogeneous surface activity maps for both H_2O and CO_2 species.

However, if the DSMC model overall reproduces the ROSINA observations, one needs to understand the origin of the heterogeneous activity at the surface of the comet. The illumination alone cannot explain the coma observations, thus we need to identify the nucleus conditions leading the surface heterogeneities that are, arbitrarily assumed by the DSMC model. For this reason, it is necessary to use a nucleus model to investigate the physical processes taking place inside the comet, which lead to these complex coma observations.

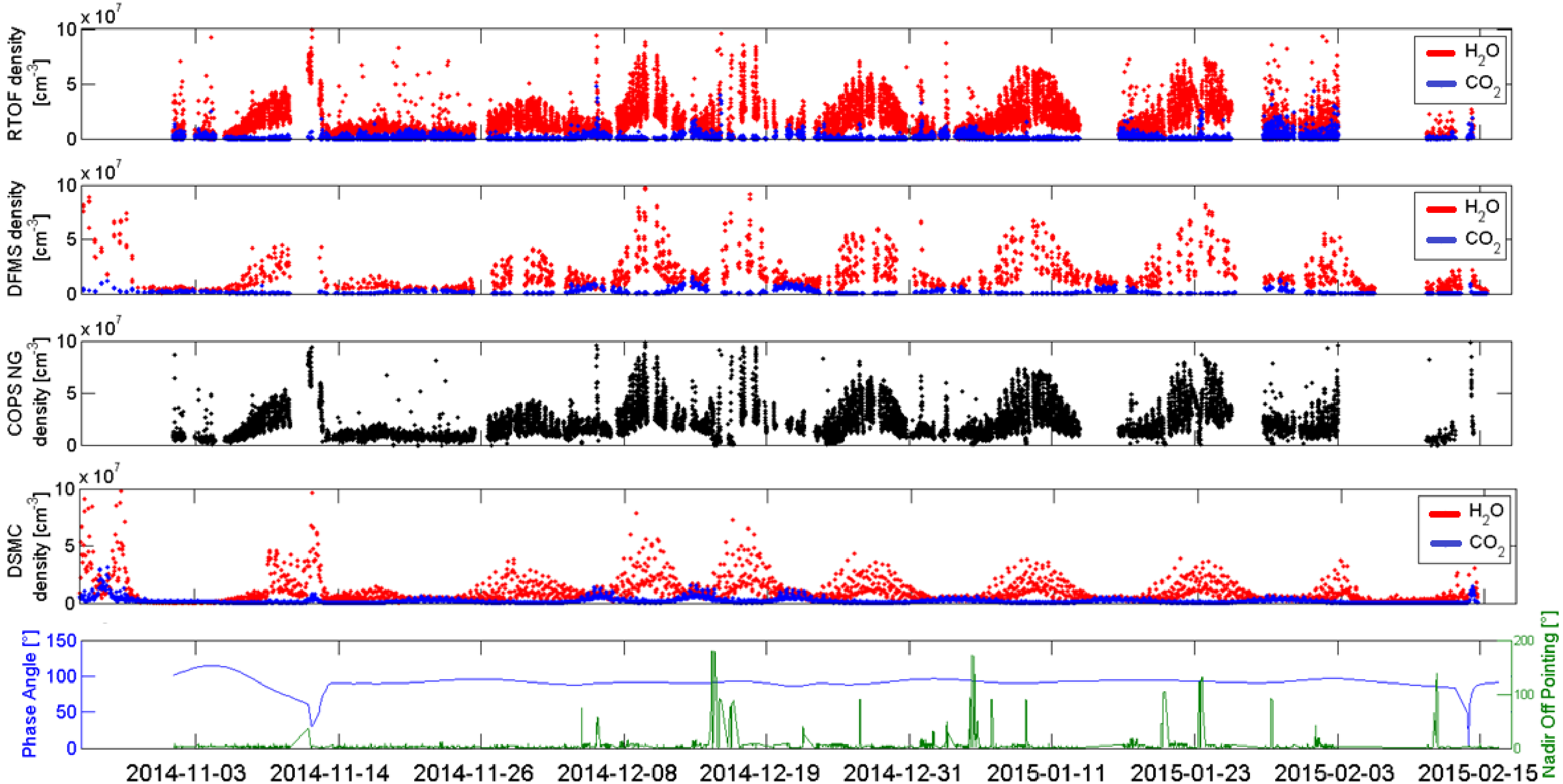

Figure 10.6: Temporal evolution of H_2O and CO_2 densities measured by RTOF (upper panel) and DFMS (second panel) during pre-equinox 1. Third panel: COPS nude gauge total densities. Fourth panel: H_2O and CO_2 densities derived from the DSMC model. Lower panel: phase-angle variations in blue and nadir off-pointing angle variations in green. From Hoang et al. (2017).

Part IV

Simulating the nucleus to constrain properties

Chapter 11

The thermo-physical model

This chapter presents a thermo-physical model applied for the case of 67P/C-G to interpret the data measured by RTOF and other instruments and to constrain properties of the nucleus. The physics of the model is described in Section 11.1, and some previous works based on the model are summarised in Section 11.2. Orbital parameters and typical values for the physical parameters, constrained by the measurements of the Rosetta's instruments, are given in Section 11.3.

11.1 Description of the model

The model is a quasi 3D thermo-physical model for simulating the evolution and the differentiation of an icy body, developed at the Istituto di Astrofiscica e Planetologia Spaziali (INAF-IAPS) in Roma and described in details in Lasue et al. (2008) and De Sanctis et al. (2010). The model is in fact a one dimensional model that can be applied on a facet of a shape model of a real or ideal body, assuming very low thermal inertia (no lateral heat transfer). The nucleus is initially a homogeneous mixture of dust particles and ices, where the water ice is probably initially in an amorphous form (see Section 2.2.1). The dust particles are embedded in a porous matrix of water ice and other minor species, like carbon dioxide and carbon monoxide. Species are possibly trapped in the amorphous ice and released during the crystallisation (transition from amorphous to crystalline ice). The model simulates the solar radiation reaching vertically the surface and calculates the temperature at the surface by taking into account the sublimation of ices (on the surface and below the surface), heat conduction in the interior and the re-emitted energy in the infrared. The heat wave propagation in the interior leads to different processes, as described in section 2.2.2: sublimation of ices, advection by gases, amorphous to crystalline transition, recondensation, heat and mass transfer. Over time, as the more volatile species are sublimated, the initially homogeneous nucleus presents a layering delimited by the sublimation front of the different species. This evolution may happen until the comet loses all its volatiles. This is what may have happened to inactive objects in cometary orbits such as 3200 Phaethon (Lupishko et al., 2000; Jewitt and Li, 2010).

The numerical computation solves the coupled equations of heat transfer (equation 11.1) and gas diffusion (described by the mass conservation's equation 11.2) assuming a number of physical parameters discussed further in Section 11.3 :

$$\rho c\frac{\partial T}{\partial t} = \nabla(\kappa.\nabla T) + Q_{H_2O} + Q_{CO_2} + Q_{CO} + Q_{tr} \tag{11.1}$$

where ρ is the density, c the specific heat, T the temperature, t the time, κ the thermal conductivity, Q_i the energy transfer due to sublimation and re-condensation of species i and Q_{tr} is the energy released at the amorphous to crystalline ice transition.

$$\frac{\partial \rho}{\partial t} = -\nabla\phi + Q_{gas} \tag{11.2}$$

where ϕ is the flux and Q_{gas} is the gas source term.

From 11.1, the penetration of the heat wave depends on the properties of the material (described by ρ, c and κ). The surface of the nucleus experiences the highest variations of temperature, which decreases exponentially with the depth. The depth where the amplitude of the heat wave is attenuated by a factor 1/e is the thermal skin depth, and is defined in relation 11.3:

$$D = \sqrt{\frac{\kappa P_{rot}}{\pi\rho c}} \tag{11.3}$$

where P_{rot} is the rotation period of the comet (to obtain the diurnal skin depth) or the revolution period of the comet (to obtain the orbital skin depth).

At the surface, the sublimation leads to gas and dust flows which cause an erosion of the surface and the formation of a dust mantle. A dust mantle appears when large dust particles accumulate at the surface, with a thickness that evolves freely as a function of time. The accumulation of dust grains on the surface leads to the formation of a crust which reduces the local activity and may extinguish it. The model allows different size distributions for dust particles and two different types (typically for silicate and organics). For each size distribution, a critical radius determines if the aggregate will either blow off ($r < r_c$) or redeposit ($r > r_c$) on the surface. The critical radius is calculated by comparing the three applied forces, i.e. the gravity, the drag, and the centrifugal force, as in equation 11.4.

$$r_c = \frac{3}{4}\frac{\sum \phi_g v_g}{\rho_{dust}[g\frac{m_n}{r_n^2} - r_n\omega^2 cos^2\theta]} \tag{11.4}$$

where r_c is the critical radius, ϕ_g the gas fluxes derived from equation 11.2, v_g the gas velocities, ρ_{dust} the dust density, $g\frac{m_n}{r_n^2}$ the gravitational force (m_n and r_n are respectively the mass and the radius of the nucleus) and $r_n\omega^2 cos^2\theta$ the centrifugal force at latitude θ.

The solar input energy arriving at the surface is spent in three processes: re-emission in the infrared, eventual sublimation of ices if present on the surface and propagation in the interior. The temperature on the surface is calculated from the balance between the solar input and those three processes. The boundary conditions are determined by conditions of temperature in the deep interior and a condition of pressure at the surface. The variations of temperature T are considered negligible at large depth (see equation 11.5) and the pressure P at the surface is the saturation pressure P_{sat} for a surface of ice, which equals zero if no ice is present (see equation 11.6).

$$\frac{\partial T}{\partial z} = 0 \tag{11.5}$$

$$P = Psat(t) \tag{11.6}$$

The regime of diffusion in the porous material depends on the ratio between the diameter of the pores and the size of the particles. This ratio is by definition an adimensional number called Knudsen number. The Knudsen regime occurs when the mean free path of the molecules is about the size of the pores; viscous or transition regimes are defined by a mean free path larger/smaller than the diameter of the pores, which affects the number of collisions of the gas molecules on the wall.

The thermal conductivity of the refractory components is described as in Gundlach and Blum (2012). They describe a model for packed spherical grains. Inside a porous material, the heat is transported either through the solid material, by radiation inside the pores, or by gas diffusion, as shown in Figure 11.1. Gundlach and Blum (2012) describe the total thermal conductivity by combining those different processes, as in relation 11.7. $\kappa_{Solid}(r,T)$ is the thermal conductivity through the solid material (with r the radius of the particles), it accounts for the efficiency of the heat exchange between the particle, strongly dependent on their radius and their surface of contact; $\kappa_{Rad}(T,\Lambda(r))$ is the heat conductivity of the radiative transport, which treats the radiation as a photon gas, where $\Lambda(r)$ is the mean free path of the photons; and κ_{Gas} the thermal conductivity due to gas diffusion. The final expression takes into account the conductivities of the different ices.

$$\kappa(r,T,\Lambda(r)) = \kappa_{Solid}(r,T) + \kappa_{Rad}(T,\Lambda(r)) + \kappa_{Gas} \tag{11.7}$$

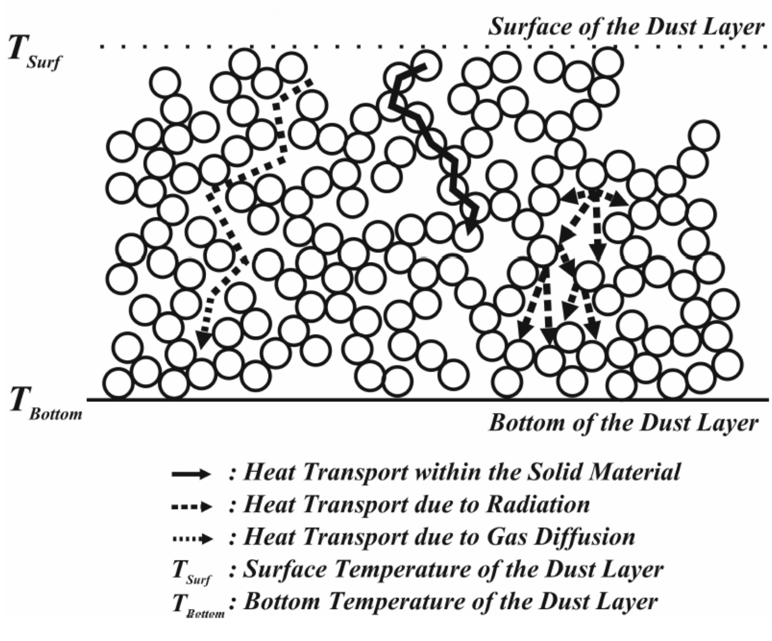

Figure 11.1: Schematic of a porous dust layer, with the three paths of heat transport represented by arrows, from Gundlach and Blum (2012). The layer is composed of dust aggregates made of micrometer-sized particle aggregates.

11.1.1 Description of the algorithm

The interior of the nucleus is simulated by a grid of 300 layers whose thickness increases toward the center. The thickness of the first 260 layers is one centimeter, then increases to meters and tens of meters going inward. The equations mentioned above are solved for each layer at a typical time step of 20 - 40 seconds. Thus, at each time step, the amount of ice sublimated and recondensated is calculated for each layer. If the amount of material in a layer is lower than a given value, the layer is added to the layer immediately below: a new layer with a new temperature, thickness and composition is generated. For the surface layer, we evaluate, in addition, the quantity of dust particles which remains on the surface. The ejection of dust reduces the thickness of the layer, and corresponds to the erosion of the surface.

11.2 Previous studies

Lasue et al. (2008) computed the model to compare the results for different shapes of nuclei (spherical, spherical with depression, spheroid) and different obliquities. They observed that a non-spherical nucleus leads to a higher production rate with a stronger erosion. They also observed the eventual formation of a dust layer far from the Sun and an asymmetry with respect to perihelion for H_2O, CO_2 and CO. De Sanctis et al. (2010) applied the model to the approximated shape of 67P/C-G, based on ground-based observations that revealed a non spherical shape nucleus. They observed that both dust mantling and activity strongly depend on the shape and the obliquity of the object. Capria et al. (2017) applied the model to the case of 67P/C-G, with the real shape model and illumination geometry on two locations of the big lobes. The computations showed that the activity remains in the first few tens of centimeters, which is consistent with the orbital skin depth of about 1 meter determined by Gulkis et al. (2015). The model has been adapted for different icy bodies (for example: comet P/2004 A1 (Loneos) in Capria et al. (2009) and main belt comets in Capria et al. (2012)). Our aim was thus to apply the model to 67P/C-G and compare its results with the ROSINA coma measurements.

11.3 Application of the model

We computed the model for the shape, orbit and illumination conditions of 67P/C-G and the physical parameters constrained by an unprecedented amount of measurements collected by the Rosetta mission. The illumination conditions are derived from SPICE kernels applied to the shape model of 67P/C-G provided by ESA.

11.3.1 Orbital parameters

Precedent works, cited above, simulated six types of orbits, with the three last based on the two known encounters with Jupiter which strongly changed the orbital parameters of the comet, in 1923 and 1959 (Maquet, 2015). The encounter of 1959 reduced the semi-major axis from 4.3 AU to 3.5 AU and increased the eccentricity from 0.38 to 0.63. Nevertheless, we expect those previous orbits to play a negligible role due to the peculiar shape and the low thermal conductivity. Thus, our computations use only one orbit at

25 AU to arrive at the present orbit with a less homogeneous temperature close to the surface to keep the code stable. The actual orbit has a period of 6.44 years, a semi-major axis of 3.5 AU and an eccentricity of 0.64 (Kelley et al., 2008; Davidsson and Gutiérrez, 2005). The closest distance to the Sun (at perihelion) is 1.24 AU and the aphelion is at 5.68 AU. 67P/C-G has a rotation period of about 12.4 hours which slightly changes with the nucleus' activity and an obliquity of 52° (Lamy et al., 2007; Mottola et al., 2014; Keller et al., 2015a).

11.3.2 Physical parameters

The evolution and differentiation of the nucleus depends on a series of parameters which describe the initial conditions of the comet material. Some of them are known since the Rosetta mission and are listed in Table 11.1.

Parameter	Value	Reference
Mass of the nucleus	9.982 ± 3.10^9 kg	Pätzold et al. (2016)
Bulk density	533 ± 6 kg.m^{-3}	Pätzold et al. (2016)
Porosity	0.75 ± 0.05	Sierks et al. (2015)
Albedo	0.06	Capaccioni et al. (2015)
Emissivity	0.94	Capaccioni et al. (2015)
Thermal conductivity	10^{-3} W K^{-1} m^{-1}	Spohn et al. (2015)
Thermal inertia [1]	10 - 30 JK^{-1}m^{-2}s$^{-\frac{1}{2}}$	Schloerb et al. (2015)
Dust/ice ratio	4-6 (GIADA), 0.4 to 2.6 (CONSERT), 6 (GIADA)	Rotundi et al. (2015); Kofman et al. (2015); Fulle et al. (2016)
Dust particles	fluffy aggregates from 0.2 to 2.5 mm (density < 1 kg.m^{-3}) and compact particles from 0.03 to 1 mm (density $\sim 10^3$ kg.m^{-3})	Fulle et al. (2015)

Table 11.1: Physical parameters constrained by the Rosetta's instruments, with references.

A dichotomy has been revealed between the two hemispheres: OSIRIS observed a granular material covering partly the northern hemisphere, while the surface of the southern hemisphere appeared more eroded (Keller et al., 2015b, 2017). This dichotomy is the result of very different conditions of heating endured by the two hemispheres. The water erosion averaged over one orbit is shown in Figure 11.2. Keller et al. (2015b) estimated an erosion per orbit of 70 cm to 3 m, while Bertaux (2015) estimated a loss of a 1.0 ± 0.5 m thick layer per orbit from observations of the activity during previous perihelion passages.

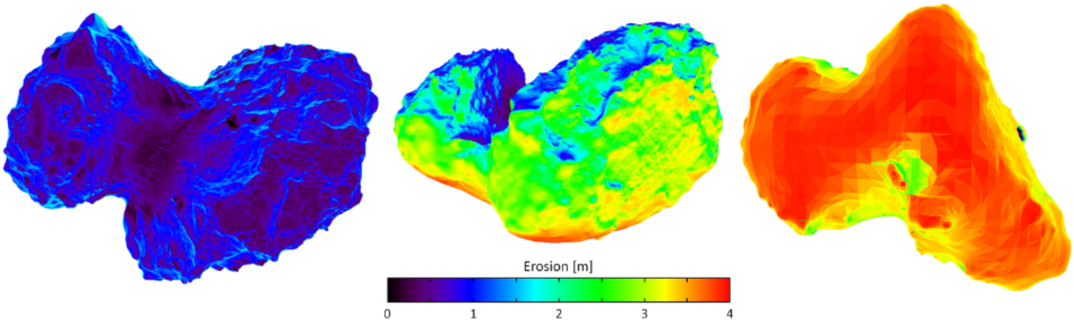

Figure 11.2: Northern view, with the neck (left), equatorial view (middle) and southern view (right) of the water erosion averaged over one orbit (Keller et al., 2015b). The erosion is drastically different between the northern and the southern hemisphere, indeed the northern hemisphere experienced a long and soft summer while the southern hemisphere is strongly heated by the solar illumination at close distance to the Sun.

Some important parameters are still unconstrained, and the simulations described in the following chapters concentrate on those ones: the relative percentage of the different ices in the pristine homogeneous material and the existence of amorphous ice and trapped gases.

11.3.3 Computed locations and description of the cases

We selected 24 locations over the surface of the nucleus: as the calculations take weeks, it was not possible to run for many facets of the comet. We indicated in Figure 11.3 the positions of the locations in a 2D map with the regions defined in El-Maarry et al. (2015) and listed the coordinates and the regions of the locations in Table 11.2.

We reported in Table 11.3 a list of initial parameters used in six different computations. To simulate the OSIRIS observations of a relatively thick layer of dust deposited on the northern hemisphere, the locations with positive latitudes allow the growth of a dust layer on the surface of the nucleus (dust 0, dust 1 or dust 2), while the locations in the southern hemisphere and at the equator do not allow the apparition of a dust mantle. These have been computed with the set of parameters ice 0, ice 1 and ice 2. In all computations, the dust/ice ratio is 4, the initial temperature is 30 K (compatible with amorphous ice), the dust distribution size range is 10^{-6} - 10^{-2} m with an average dust density of 10^3 kg.m^{-3}, the initial pores radius at 0.0001 m with a maximum size fixed at 0.05 m.

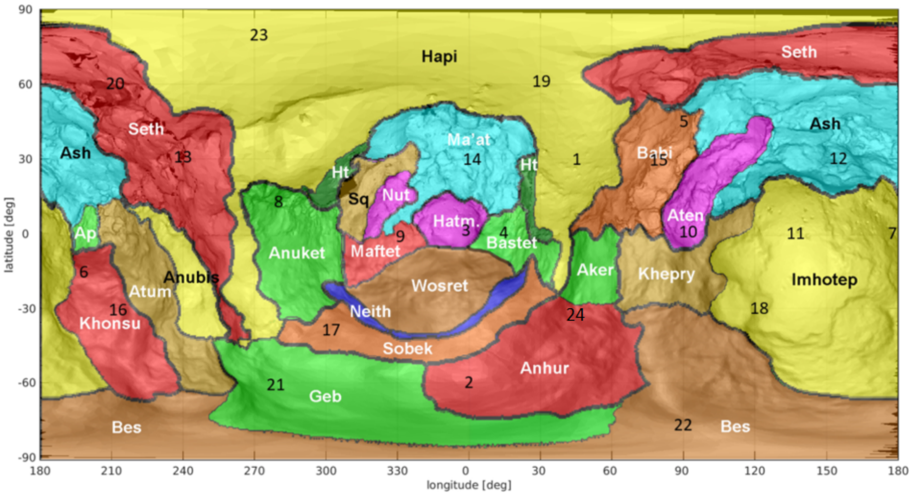

Figure 11.3: 2D latitude-longitude map of 67P/C-G with the regions (El-Maarry et al., 2015) and the position of the 24 points studied in this work.

	Latitude	Longitude	Region
1	30	45	Hapi
2	-60	0	Anhur
3	0	0	Hatm
4	0	15	Bastet
5	45	90	Babi
6	-20	195	Khonsu
7	0	180	Imhotep
8	15	-70 (or 290)	Anuket
9	0	-30 (or 330)	Maflet
10	0	90	Aten
11	0	145	Imhotep
12	30	150	Ash
13	30	-120 (or 240)	Seth
14	30	0	Ma'at
15	30	75	Aten
16	-30	-150 (or 210)	Khonsu
17	-40	-60 (or 300)	Sobek
18	-30	120	Imhotep
19	60	30	Hapi
20	60	-150 (or 210)	Seth
21	-60	-80 (or 280)	Geb
22	-80	90	Bes
23	80	-90 (or 270)	Hapi
24	-30	45	Anhur

Table 11.2: Coordinates of the 24 chosen locations indicated in Figure 11.3, and related morphological regions as defined in El-Maarry et al. (2015).

	dust 0	ice 0	dust 1	ice 1	dust 2	ice 2
CO_2/H_2O	0.02	0.02	0.02	0.02	0.02	0.02
CO/H_2O	0.02	0.02	0.002	0.002	0.005	0.005
Initial dust mantle thickness (m)	0	0	0	0	0.07	0
Trapped gas in amorphous ice	CO	CO	none	none	none	none
Growth of dust mantle	possible	none	possible	none	possible	none

Table 11.3: Set of initial parameters of the six computations: dust 0, dust 1 and dust 2 have been applied on the northern locations, and ice 0, ice 1 and ice 2 on the equator and the southern locations.

Chapter 12

Analysis of the nucleus model results

In this chapter, we study the results of the computations based on the parameters described in the previous chapter. In particular, we analyse the evolution of the temperature of the surface and the near-surface layers at two different heliocentric distances in Section 12.1. Then, in Section 12.2, we study the evolution of the internal structure, from a homogeneous nucleus to a stratified structure, by plotting the depth of H_2O, CO_2 and CO's sublimation fronts, and the front of crystallisation of the amorphous ice as a function of time. In Section 12.3, we analyse the variations of the fluxes for the three species and try to link them with the temperature at different depths. In Section 12.4, we observe the effect of the dust layer thickness and the presence of CO trapped in the amorphous ice on the fluxes of the volatiles and infer their consequences for the interpretation of RTOF measurements. Finally, we study the evolution of the production rate in the inbound part of 67P/C-G's orbit.

12.1 Evolution of the surface and interior's temperature

We study here the diurnal and seasonal variations of temperature at the surface and at different depths: 1 cm, 5 cm, 10 cm and 20 cm. The diurnal skin depth and orbital skin depth of 67P/C-G have been estimated respectively of about 1 - 2 cm and about 1 m from MIRO measurements (Gulkis et al., 2015). The obliquity of the nucleus' rotation axis and its complex shape induced large changes on the illumination conditions. Over a revolution, the two hemispheres experience very different solar heating conditions: the summer in the northern hemisphere stands for years and is low in temperature, as the comet is far from the Sun, while the southern hemisphere gets illuminated only during 10 months but suffers a strong heating as the nucleus is close to the Sun.

Figures 12.1 and 12.2 show the variations of temperature of the surface and of the near-surface interior of the nucleus, for nine locations over the surface: 3 in the North (points 12, 19 and 23 in Table 11.2), 3 at the equator (points 3, 7 and 10) and 3 in the South (points 2, 17 and 18). Figure 12.1 presents the temperature variations over two rotations at the beginning of September 2014, at a heliocentric distance of 3.4 AU, while Figure 12.2 follows the same variations at the beginning of April 2015, at a heliocentric distance of 1.9 AU.

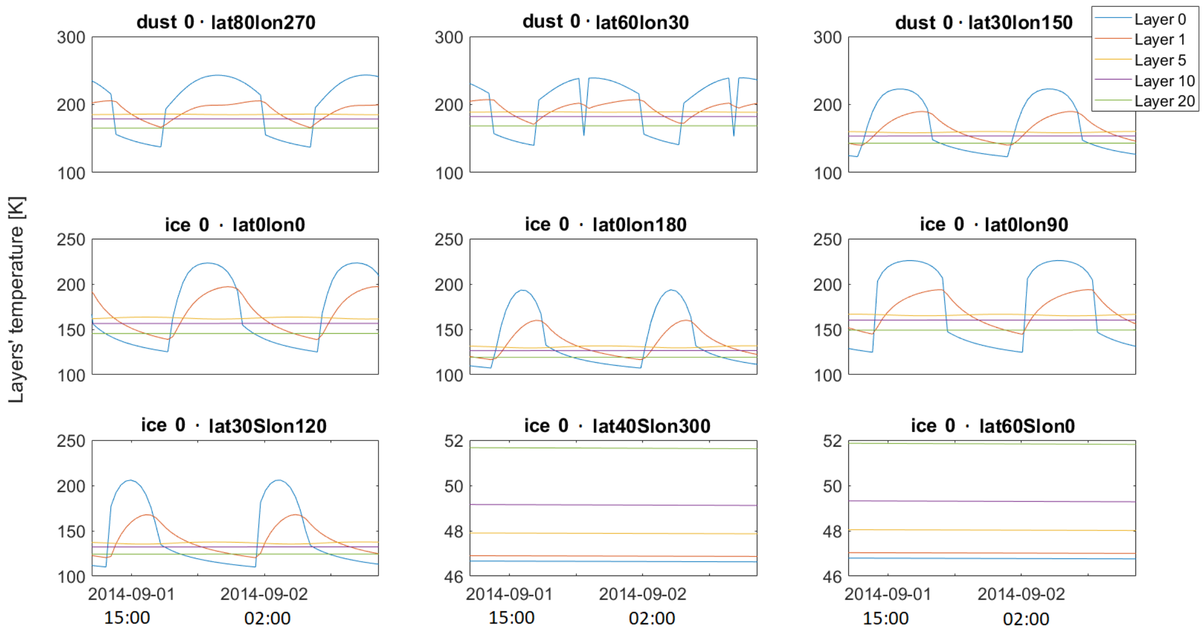

Figure 12.1: Evolution of the temperature of the different depths for nine chosen locations, over two rotations at a heliocentric distance of 3.4 AU. The locations in the northern hemisphere (first line) are computed with the case dust 0 and the locations at the equator (second line) and in the southern hemisphere (third line) with the case ice 0. Layer 0 represents the surface, layer 1 is at a depth of 1 cm, layer 5 is at 5 cm, layer 10 is at 10 cm and layer 20 is at 20 cm.

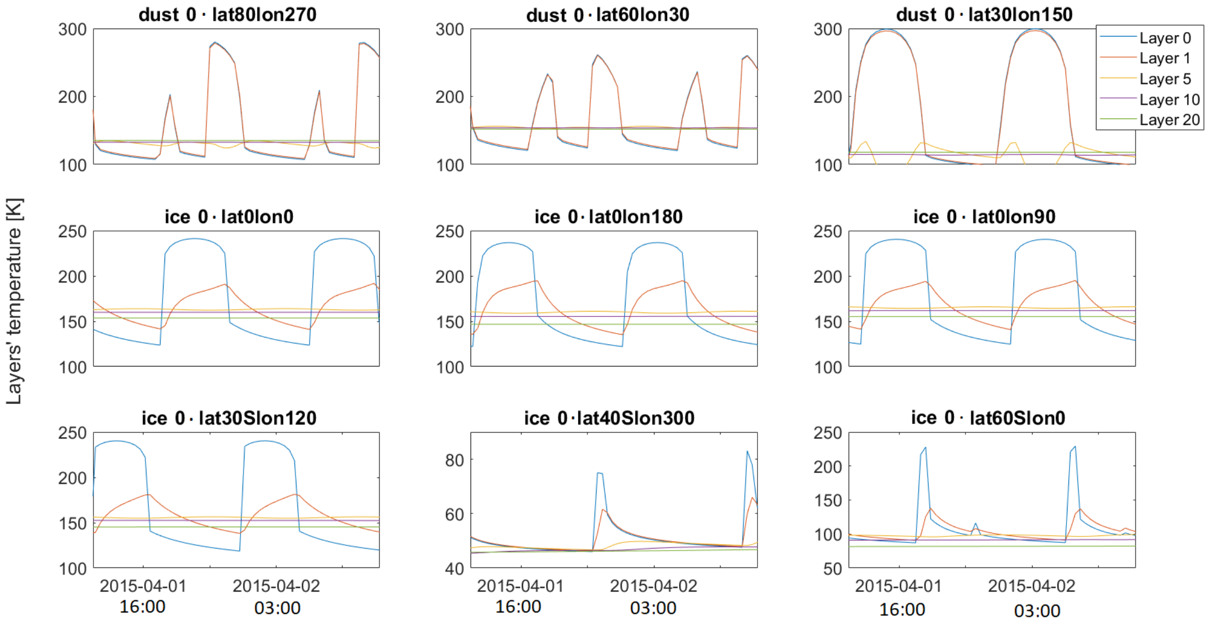

Figure 12.2: Evolution of the temperature of the different depths for nine chosen locations, over two rotations at a heliocentric distance of 1.9 AU.

For the illuminated locations (latitude $>$ 40 degrees), we observe the variation of temperature which corresponds to the heating due to the solar illumination. In particular, the temperature of the depths within the diurnal skin depth, i.e. layer 0 (surface) and layer 1 (1 cm), shows strong diurnal variations. The solar illumination heats up the surface (blue line) during the day and we observe a clear increase of the temperature, which then decreases during the night. During the cooling, the temperature at the surface and at 1 cm drops even under the temperature of the interior, which mainly depends on the value fixed as initial parameter. We observe very small variations at 5 cm, but underneath, the temperature is practically not affected by the variation of the illumination conditions on the surface. The temperature under 10 cm is constant, but the temperatures are not the same on the different studied locations. In the analysis of the temperature of the interior, the illumination is not the only parameter of influence. For latitudes of -40 degrees and below (southern hemisphere), the points are not illuminated and show no variation in the temperature. The interior of the comet is warmer than the surface, due to the low thermal inertia of the comet and the solar heating during the previous perihelion passage. The temperatures increase of a few degrees with depth reaching up to 50 K at 20 cm depth.

We also observe the propagation of the heat wave into deeper layers. The maximum of temperature at 1 cm (red line) under the surface is slightly delayed compared to the temperature curve of the surface, this delay is expected because of the thermal inertia. The variations of the temperature at 1 cm under the surface are smaller than the variations of the temperature at the surface, nevertheless, they show an amplitude of about 50 K. The small variations at 5 cm (yellow line) show a maximum almost in phase opposition with the surface increase of temperature, i.e. during the night.

In this example, the solar illumination heated the northern hemisphere and the equator, thus we observe a large difference of temperature over the nucleus' surface. The northern and equator locations experienced the highest temperature, in agreement with observations, with maxima of surface temperature in the north between 230 K and 250 K while the southern points had a surface temperature below 50 K. However, all the locations present a different pattern, even the points with the same latitude. They endure different conditions of illumination and shadowing due to the non-spherical shape of the comet, as illustrated by three different patterns on Figure 12.3. On the left of this Figure, we show an example of a clear day and night variation of temperature for a point which is never in the shadow. On the middle panel, we show an example of bimodal peaks. As the nucleus is not spherical and presents cavities, cliffs and so on, the temperature sometimes decreases during the day time due to shadowing by the structures on the comet itself. In the third example, the points are non illuminated most of the time over the rotation but are very briefly illuminated twice, thus we observe peaks of temperature following those quick illuminations. This is what happened at Philae's landing site where illumination was scarce.

The temperature of the nucleus' interior changes as the nucleus approaches the Sun. At a heliocentric distance of 1.9 AU (Figure 12.2), we observe different behaviours for the temperature of the different depths. In the northern hemisphere, the temperature at larger depths progressively decreased while the temperature at the surface and at the depth of 1 cm increased and now present the same temperature reaching 300 K. Clear bimodal peaks are seen on the two northern points. The pattern observed at a depth of 5 cm for the point 12 (lat 30, lon 150) is an effect of the sublimation of deeper layers (typically CO_2).

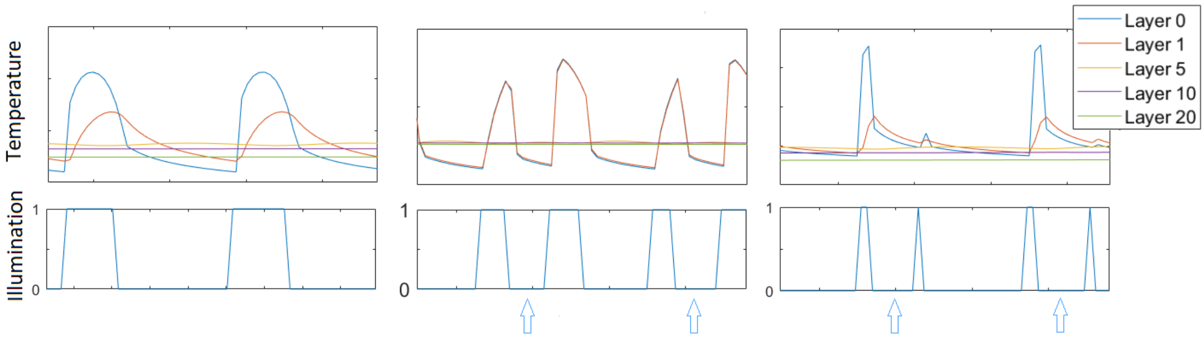

Figure 12.3: Three typical patterns of evolution of the temperature (top) with their specific illumination conditions (bottom). Shadowing is indicated by blue arrows. The point 18 at 3.4 AU (left panel) is located in the big lobe, it experience clear day and night illumination, without self-shadowing, the point 16 at 1.9 AU (middle panel) is located between the neck and the small lobe, it experienced a shadowing due the concavity of the neck, and the point 2 at 1.9 AU (right panel) is on the southern part of the small lobe, and is very few illuminated.)

In the southern hemisphere, the heat wave reached larger depths compared with the case at 3.4 AU from the Sun, with the three points in the South being warmer in Figure 12.2 compared to Figure 12.1. The activity started slightly before the equinox for the points of latitude -40 and -60 degrees as the solar illumination reached those areas for the first time of the orbit.

12.2 Evolution of the stratification

At the beginning of the computation, the nucleus is homogeneous and all the water is in amorphous ice state. The homogeneous nucleus evolves into a stratified structure, as the heat wave propagates inward and leads to the sublimation of the volatiles. We observe now the evolution of the stratification on three locations over the nucleus: one point in the northern hemisphere (location 14 in the Table 11.2), one point at the equator (location 0) and one point in the southern hemisphere (location 2). The three points were computed with the same case dust 1 - ice 1, i.e. dust 1 for northern point (left), and ice 1 for the equator (middle) and the southern point (right). The main parameters for this case are $CO_2/H_2O = 0.02$ and $CO/H_2O = 0.002$ and no initial dust layer. Figure 12.4 shows the evolution of the position of the surface, the first depth with H_2O ice, the first depth with CO_2 ice, the first depth with CO and the transition front between amorphous and crystalline ice from a distance of 3.6 AU to 1.7 AU. The upper panel shows a $\sim$ 60 meters thickness below the surface, the middle panel shows a zoom on the $\sim$ 3 first meters and the lower panels show a zoom on the $\sim$ 30 cm below the surface.

For the northern location, we observe the growth of a dust mantle (between the surface (blue line) and the layer with H_2O ice (red line). Note that the step function is due to the calculation method of the thickness of the layer in the computations. The dust mantle appears around 3.3 AU, which reaches a thickness of 6 cm at the end of the run. The erosion of the surface is very small, 0.05 cm. The sublimation front of CO remains constant at a depth of 52 m under the surface. The sublimation front of CO_2 sinks from a depth of 30 cm at 3.6 AU to a depth of 40 cm at 1.7 AU, as well as the crystallisation front of amorphous ice, which sinks from 70 cm to 1.2 m.

The equator's point shows a very similar evolution of the interior's structure. The important difference is that the computation ice 1 does not allow the apparition of a dust mantle. Thus, the water sublimation front is at the surface and we see a total erosion of 6.5 cm at the end of the run, an order of magnitude larger than the point at the north.

The point in the southern hemisphere is shown on the right of Figure 12.4. Like for the other point, the depth of CO is located deep (52 m) inside the nucleus, while the other fronts are very close to the surface. The southern hemisphere stayed in the shadow during the first months of the computation. We observe the beginning of the activity on this point around 2.1 AU from the Sun. As a consequence, the crystallisation front of amorphous ice dropped quickly from a depth of 2 cm to 18 cm at the end of the computation. The depth with CO_2 starts to sink at 1.7 AU; at this distance, we observe a small erosion of 0.4 cm.

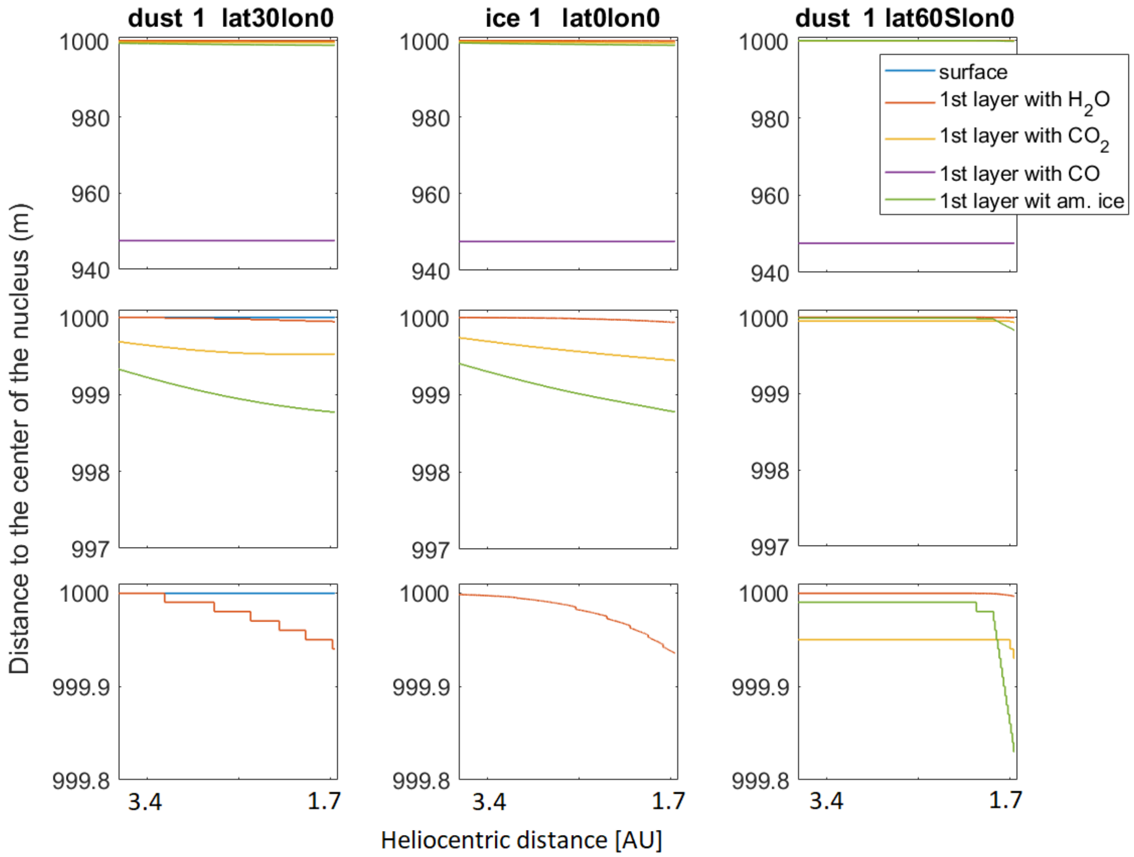

Figure 12.4: Evolution of the stratification for three locations: in the northern hemisphere (left), at the equator (middle) and in the southern hemisphere (right). The second and the third lines are zooms of the first line.

This analysis of the stratification gives an idea of the evolution of the near-surface of different locations over the nucleus. The position of the fronts clearly varies with heliocentric distance and the illumination conditions, and will induce an evolution of the outgassing. The three studied locations experienced very different illumination conditions, which induce a different heating and affect the structure of ∼ 1 meter under the surface. As the heat wave propagation lead to the crystallisation of the amorphous ice and the CO_2 sublimated faster than H_2O, we observed the drop of the transition front and the CO_2 sublimation front. The northern and equator locations present a progressive evolution of the near-surface structure, while the southern hemisphere structure present a strong change, when illuminated around the equinox. At the end of the run, i.e close to the equinox and at 1.7 AU from the Sun, the northern hemisphere is covered by a dust mantle, the equator suffered the strongest erosion and the southern hemisphere is not strongly affected by the heating yet.

12.3 Evolution of the fluxes

The evolution of the thermal conditions over the nucleus and the induced layering of the nucleus structure trigger the outgassing of volatiles. We study in this section the fluxes of H_2O, CO_2 and CO and their evolution. The fluxes computed by the model are normalised for a surface of 1 m^2. Figure 12.5 shows the evolution of the gas fluxes for the three volatiles during 5 days at 3.4 AU (upper panel) and 5 days at 1.9 AU (lower panel) for the point 15 (lat 30°, lon 75°) in the northern hemisphere. The case used the initial parameters dust 1, i.e. $CO_2/H_2O = 0.02$ and $CO/H_2O = 0.002$, without an initial dust mantle or trapped gas.

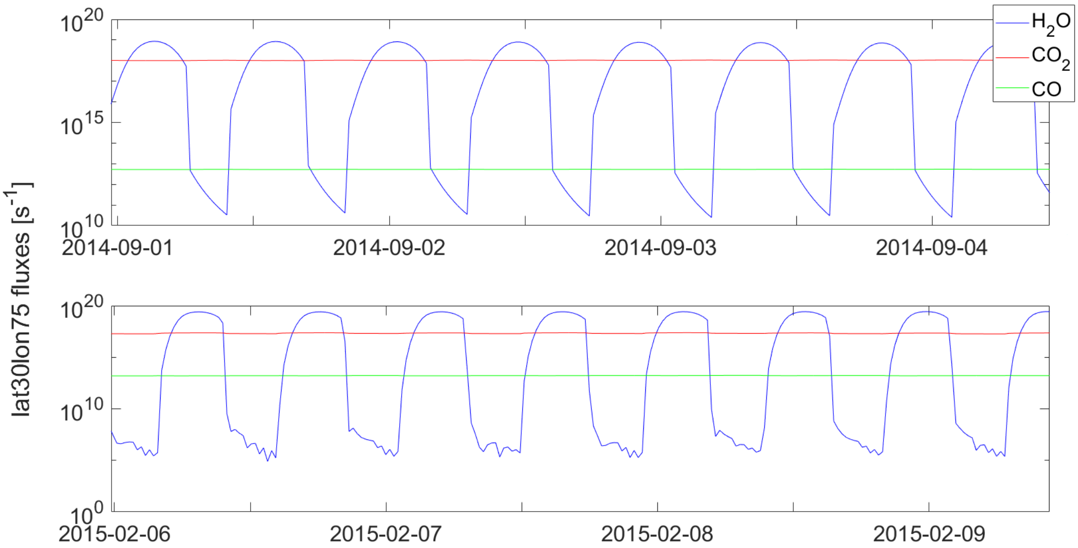

Figure 12.5: Evolution of the H_2O, CO_2 and CO outgassing for the point 15 of latitude 30 and longitude 75 during 5 days at 3.4 AU (upper panel) and 5 days at 2.3 AU (lower panel) in case dust 1.

At 3.4 AU (upper panel), we observe diurnal variations of the H_2O outgassing from $3{\times}10^{11}$ s^{-1}/m^2 (much lower than CO and CO_2) in the night to 10^{19} s^{-1}/m^2 in the day. The fluxes of CO_2 and CO are constant, respectively around 10^{18} s^{-1}/m^2 and $5{\times}10^{12}$ s^{-1}/m^2. We observe some changes at 2.3 AU (lower panel): H_2O fluxes are surprisingly lower during the night, with fluxes of only 10^5 s^{-1}/m^2, and slightly higher during the day ($2.4{\times}10^{19}$ s^{-1}/m^2). We observe again little variations (a bit larger than at 3.4 AU) in the

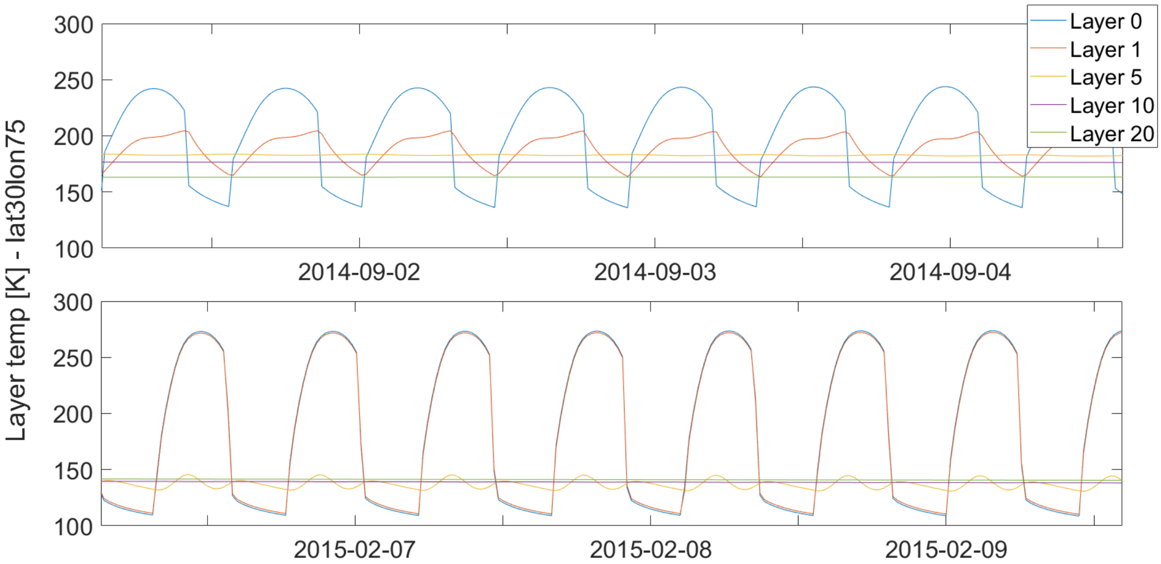

Figure 12.6: Temperatures at different depths for the point of latitude 30 and longitude 75 during 5 days at 3.4 AU (upper panel) and 5 days at 2.3 AU (lower panel) in case dust 1.

outgassing of CO_2, which decreased to 2×10^{17} s^{-1}/m^2. CO fluxes increase and remain constant at 1.5×10^{13} s^{-1}/m^2.

To understand the difference of fluxes at those two different positions of the orbit, we investigate the temperature at the depth of the sublimation front of the volatiles. From 3.4 to 2.3 AU, the water ice is at the surface and is progressively covered by a layer of dust with an erosion of the surface of 0.05 cm, the CO_2 front sinks from 30 cm to 50 cm, and the CO front remains at 52 m. The corresponding evolution of temperatures at the surface, under 1 cm, under 5 cm, under 10 cm and under 20 cm are shown in Figure 12.6. The surface temperature varies from 140 to 245 K at 3.4 AU, in correlation with VIRTIS, which measured surface temperature from 180 (limit of temperature measurable with VIRTIS) to 250 K at 3 AU (Capaccioni et al., 2015). From 3.4 to 2.3 AU, we note an increase of the maximum temperature of the surface during the daytime from 245 K to 270 K and a reduced minimum temperature during the night time, from 140 K to 110 K, much lower than water sublimation temperature. Those changes explain the evolution of the H_2O fluxes's behaviour, with a decrease at night despite approaching closer to the Sun. The presence of a dust mantle at 2.3 AU in the northern hemisphere actually reduces the H_2O fluxes during the night. Indeed, a similar study for points at the equator (computed with ice 1, i.e. without dust mantle) shows that the fluxes of water are higher during the day and during the night at 1.9 AU. The amplitude of the variation at 5 cm increased, due to the propagation of the heat wave. The temperature at 5 cm and below decreases from about 180 K to 140 K, which remains sufficient to sublimate CO_2 and CO. Under 10 cm, CO_2 and CO are located at a depth with no variation of temperature, thus their fluxes appear constant and unaffected by the change in illumination.

12.4 Effect of the dust layer and of the trapping conditions

Two assumptions will play a key role in the model: the dust mantle thickness (and geographical heterogeneities of the dust cover), and the trapping mechanism of minor species.

The OSIRIS camera observed a mantle of dust covering the northern hemisphere. It was estimated at $\sim$ 20 cm (Biele et al., 2015) on the Philae's landing site. A dust deposit estimated at about 1 meter resulted from the strong erosion of the southern hemisphere around perihelion (Hu et al., 2017). Keller et al. (2017) described a seasonal mass transfer, which originates from the strong erosion of the southern hemisphere and a redeposition as a granular material layer in the northern hemisphere. From our precedent observations, we analysed that the dust layer which naturally grows in the computation (only 6 cm thick at 1.7 AU) do not provide the thickness of dust observed in the northern hemisphere of 67P/C-G. Therefore, in our computations, we decided to vary to thickness of the initial dust layer on the surface of the northern hemisphere, and to maintain the southern hemisphere without any dust mantle.

If the observations indicate the presence of trapped species, the trapping mechanism is still debated, as minor species could be trapped either in amorphous ice (Bar-Nun et al., 1988), or in clathrate hydrates (Delsemme and Swings, 1952). Possible evidence for the presence of amorphous ice are the extremely low thermal conductivity (Kouchi et al., 1992), the enrichment of CO over N_2 (Notesco and Bar-Nun, 1996; Bar-Nun et al., 2007), the observed outbursts probably caused by the energy release during the phase transition (Prialnik and Bar-Nun, 1992; Jewitt, 2009; Agarwal et al., 2017). Luspay-Kuti et al. (2016) proposed however that the nucleus of 67P/C-G contains crystalline ice, clathrate, and other ices. They argued that the volatiles gases trapped in amorphous ice are released simultaneously, which does not seem to be the case for the minor species observed by ROSINA/DFMS. However, low pressure conditions required for the formation of clathrates are not in agreement with the actual models of cometary formation, thus we decided to include water completely in amorphous ice at the beginning, with the possibility of trapping species inside it.

To investigate the impact of the dust mantle thickness on volatiles sublimation and the trapping of CO in the amorphous ice, we ran three more cases for the point of latitude 30 and longitude 45. The set of parameters for the cases are given in Table 12.1.

	dust 1a	dust 1b	dust 1c
CO_2/H_2O	0.02	0.02	0.02
CO/H_2O	0.005	0.005	0.005
Initial dust mantle thickness(m)	0.2	0.1	0.1
Trapped gas in amorphous ice	none	none	CO

Table 12.1: Parameters of the runs dust 1a, dust 1b and dust 1c used to compute the point of latitude 30 and longitude 45.

12.4.1 Impact of the initial dust mantle thickness

We try to simulate the deposition of a dust layer on the surface of the northern hemisphere. We have shown that activity remains within 6 cm below the surface. Thus, we study the influence of imposing a dust mantle with different thicknesses : 0 m (case dust 1), 0.07 m (case dust 2), 0.1 m (case dust 1b) and 0.2 m (case dust 1a).

The stratigraphy for the three new cases are shown in Figure 12.7, where the dust mantle thickness is represented between the blue line (surface) and the red line (H_2O ice). The depth of CO is constant at 53 m (not visible), the depth with CO_2 drops by a few centimeters and the transition front between amorphous to crystalline ice drops by about one meter and the surface is eroded by 1.5 cm.

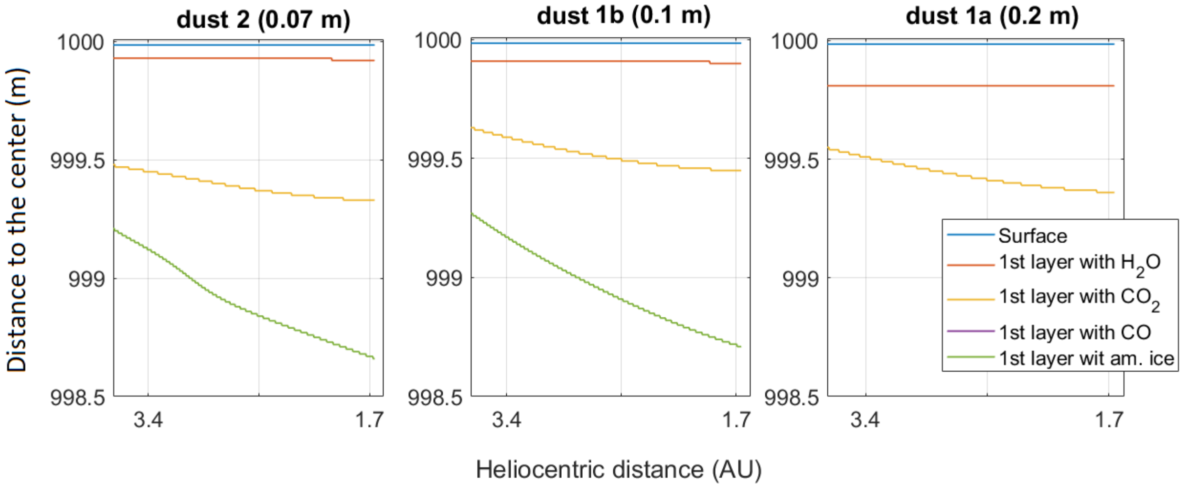

Figure 12.7: Effect of the initial dust layer on the stratification of the location 15 (latitude 30 and latitude 45). Left: case dust 2 (initial dust layer of 0.07 m). Middle: case dust 1b (0.1 m). Right: case dust 1a (0.2 m).

We compare the average fluxes of the point (lat30, lon45) for H_2O, CO_2 and CO in Figure 12.8 for the four different initial dust layers. The impact is very clear on the H_2O outgassing (upper panel). The increase of the mantle thickness reduces considerably the water average fluxes. The evolution of the fluxes with no initial dust mantle is not continuously increasing (shift in the blue curve), due to instabilities of the code, which changes the structure of the grid to take into account the loss of mass. The initial dust mantle of 0.2 m reduces the fluxes with no dust layer by one order of magnitude. The effect is very important at 3.4 AU with a reduction of 5.10^2 between the two cases. The difference is smaller at 1.9 AU. Comparing the mean fluxes over the computations, it appears that the mean outgassing increases exponentially with the thinness of the layer, at least for the four points of reference. The increase of the dust mantle thickness does not induce large changes in the outgassing of CO_2 and CO which will have important consequence on the interpretation of the RTOF maps (see Section 13.2.3).

12.4.2 Effect of the trapped CO on the averaged fluxes

The presence of trapped CO in the amorphous ice induces some sublimation of CO coming from a depth much closer to the surface around the water ice crystallisation front. Indeed,

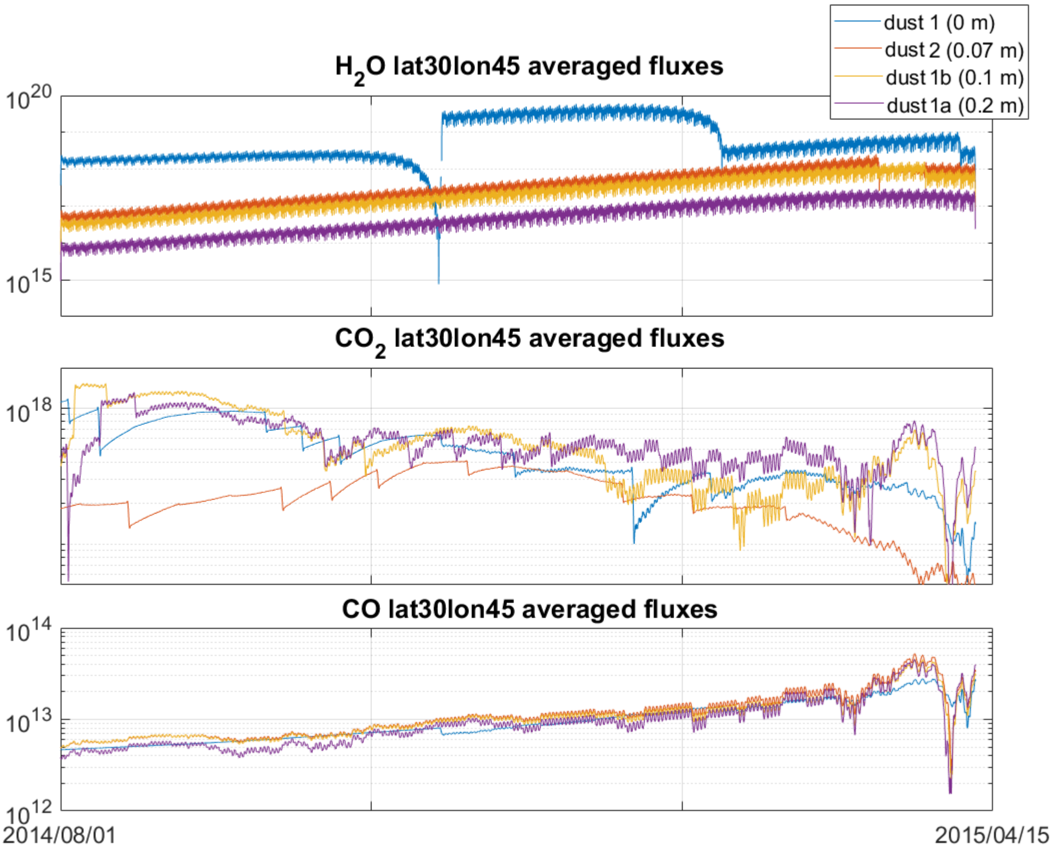

Figure 12.8: Evolution of fluxes from the point 15 (lat 30, lon 45), for H_2O (top), CO_2 (middle) and CO (bottom), in case dust 1 (initial dust layer of 0 m of thickness), case dust 2 (0.07 m), case dust 1b (0.1 m) and case dust 1a (0.2 m), from about 3.45 AU to 2.3 AU.

the sublimation front of CO is located deeper than the crystallisation front, due to the high volatility of CO.

We compare two runs of the point of latitude 30 and longitude 45 with the exact same set of parameters, including a dust layer of 10 cm, except for the absence (dust 1b) or the presence (dust 1c) of trapped CO gas. The effect on the outgassing is shown in Figure 12.9. For this studied point, we observe no large change in the fluxes of H_2O and CO_2 while the CO outgassing is 5 order of magnitude larger when CO is trapped in the amorphous ice.

The fluxes of CO are constant due to the depth of the crystallisation front, while the fluxes of H_2O and CO_2 show variations because they are located closer to the surface and are influenced by night-day and seasonal variations in the illumination. We note that some variations are not physical, but due to the computed grid which evolves to adjust the mass loss.

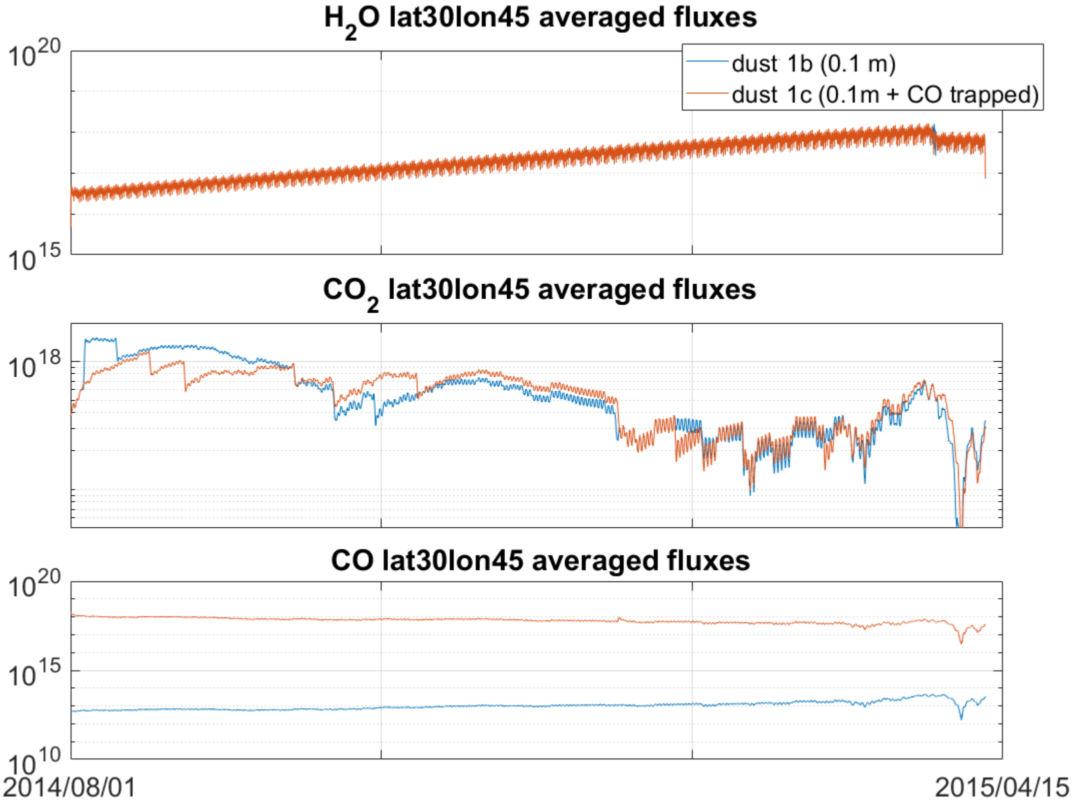

Figure 12.9: Evolution of fluxes from the point 15 (lat 30, lon 45), for H_2O (top), CO_2 (middle) and CO (bottom), in case dust 1b (no trapped CO) and case dust 1c (presence of trapped CO), from about 3.45 AU to 2.3 AU.

12.5 Analysis of the production rate

To estimate the total outgassing of the nucleus, we calculated the mean fluxes obtained at each time step for the 24 studied locations, then estimate the fluxes over the whole comet surface (48 474 m^2). We present the production rate of the nucleus in three different cases: dust 0 - ice 0 ($CO_2/H_2O = 0.02$ and $CO/H_2O = 0.02$, trapped CO, no initial dust layer), for the case dust 1 - ice 1 ($CO_2/H_2O = 0.02$ and $CO/H_2O = 0.002$, no trapped gas, no initial dust layer) and the case dust 2 - ice 2 ($CO_2/H_2O = 0.02$ and $CO/H_2O = 0.005$, no trapped gas, initial dust layer of 0.07 m in the northern hemisphere and at the equator), see Figure 12.10.

The water production rates are very similar in the cases dust 0 - ice 0 and dust 1 - ice 1, the two cases without an initial dust layer. In dust 2 - ice 2, the initial dust layer of 7 cm in the northern hemisphere reduces the fluxes by about one order of magnitude.

We observe very well the consequence of the trapped CO: in the first panel, we have large variations of the CO production rate while in the second and the third, the CO front is located at a constant depth (despite very different CO/H_2O ratios).

The behaviours of CO_2 and CO are very different due the initial ratio to H_2O. In the case dust 0 - ice 0 ($CO/H_2O = CO_2/H_2O = 0.02$ at the beginning) the outgassing of both volatiles increases while the nucleus is approaching the Sun with very important diurnal variations. In the case dust 1 - ice 1 ($CO/H_2O = 0.002$) and dust 2 - ice 2 ($CO/H_2O =$

0.0005), they present almost no variation. The decrease of the CO/H_2O ratio has a direct effect on the CO_2 outgassing. Indeed, the heating allows a larger sublimation of CO_2, as a smaller part of the available energy is consumed for the sublimation of CO, thus we observe an increase of the CO_2 outgassing.

The order of magnitude of production rate computed with the model is similar to the production rate derived from ROSINA/DFMS, with $\sim 10^{26}$ molecules/s at 3.5 AU and $\sim 10^{27}$ molecules/s at 2 AU (Hansen et al., 2016). This parameter will be compared to the RTOF observations in Section 13.1.

In conclusion, we have seen that the thermo-physical model allows to study the evolution of the internal structure, the condition of temperature at the surface and in the interior, the resulted surface fluxes at different locations over the surface and the evolution of the global production rates of the species H_2O, CO_2 and CO with the heliocentric distance. In particular, the outgassing is strongly influenced by the initial conditions such as the initial dust layer, the trapping of CO and the initial ratios. We thus aim at constraining these parameters with a detailed comparison between the model results and the RTOF measurements.

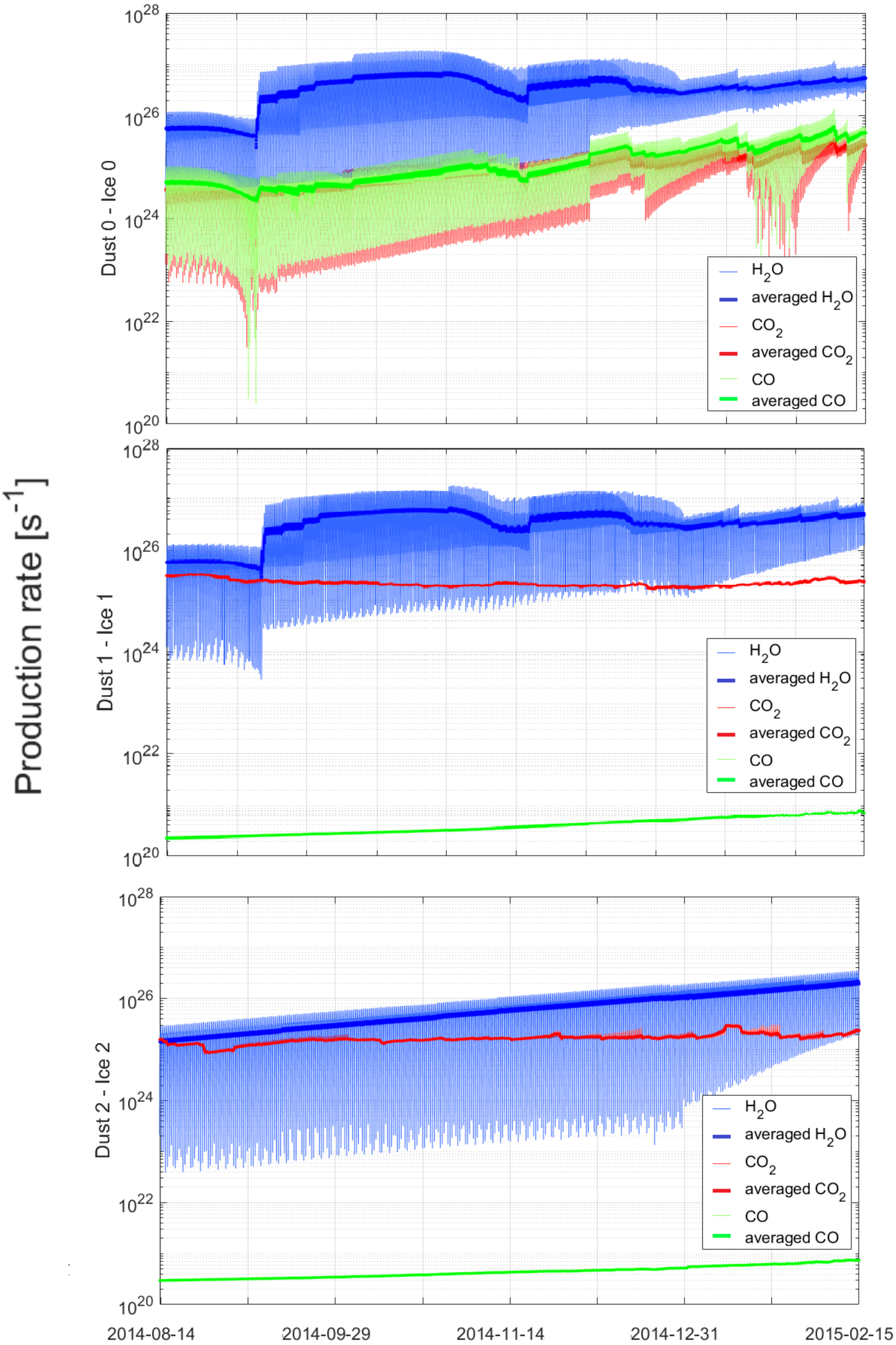

Figure 12.10: Comet gas production rate [s^{-1}] with the set of parameters dust 0 - ice 0 (top panel), dust 1 - ice 1 (second panel) and dust 2 - ice 2 (third panel) from about 3.45 AU to 2.3 AU.

Chapter 13

Comparison with fluxes derived from RTOF

In this chapter, we use the model results discussed in the previous chapter to try to find the best combination of input parameters to reproduce the coma RTOF measurements. In particular, the temporal and spatial variations observed by RTOF during the approach and pre-equinox 1, including the peculiar decrease of volatiles density measured during the approach, the observed north/south dichotomy and the depletion of CO_2 and CO in the northern hemisphere. As the thermo-physical model gives fluxes of sublimation on the surface, the comparison with the in-situ data is only possible using several assumptions to derive surface fluxes from RTOF. A model of gas expansion in the coma, such as the DSMC model, would be needed to provide a more accurate comparison. Such a coupling between the nucleus model and a DSMC model will be needed in the future, but a first comparison is provided in this part.

In Section 13.1, we use the RTOF densities to derive fluxes at the surface of the nucleus and compare the production rates of the main species with the model outputs. In Section 13.2, we describe our method of work for a detailed comparison: we run the computation for 24 locations and interpolate the results over the whole nucleus to visualise the spatial distribution. We then present and analyse the 3D and 2D maps of fluxes for H_2O, CO_2 and CO. We then deduce some interpretations to explain the observations in Section 13.3.

13.1 Global comparison with RTOF

13.1.1 Deriving surface production rates from RTOF

In order to convert the RTOF densities in fluxes, we need information concerning the ejection velocities. From the surface temperature T given by the model, the mean speed v of gas molecules of mass m is described by the speed distribution of a Maxwell -Boltzmann distribution (Huebner et al., 2006), as in the relation 13.1:

$$v = \sqrt{\frac{8kT}{\pi m}} \tag{13.1}$$

We analyse the computed surface temperature and compare the calculated velocities with the velocities measured by MIRO and COPS. As an example, from the temperature computed for August 2014, we observe that velocities in the northern hemisphere varied between 420 and 500 m/s, and in the southern hemisphere, between 325 and 370 m/s. From MIRO data, Gulkis et al. (2015) analysed the temperature of the subsurface at 1.6 mm and 0.5 mm and derived an ejection velocity between 550 and 750 m/s for water from the data collected from 7 until 9 August 2014 (velocities are measured from H_2O spectra and not from temperature). The corresponding analysis with the equation 13.1 gives a velocity from 385 to 425 m/s, which underestimates the MIRO measurements. This difference is most probably due to the approximation used to derive the velocities. The COPS measurements and derived gas velocities were studied in Tzou (2016): she compared the COPS derived velocities with the DSMC modeling from the 1st to 5th October 2014. The DSMC model takes into account the dynamics of particles but Bieler et al. (2015) showed that the cometary volatiles are accelerated. She computed a velocity range from 280 to 750 m/s for COPS compared to 300 to 500 m/s for the DSMC. Our model yields a velocity range from 390 to 435 m/s, which is in good agreement with COPS and DSMC ranges (note the large range values, indicating large uncertainties in this estimation).

From estimated ejection velocities, we convert RTOF densities into approximated production rate (allowing for a comparison with the model derived production rates) following the relation 13.2, using the assumption of a spherical body and an isotropic expansion in r^2 for a gas of density n and an ejection velocity v.

$$Q = v.n.4\pi r^2 \tag{13.2}$$

13.1.2 Comparison with RTOF global production rates

As an indication of the agreement between the computed and the RTOF derived production rate, we reported the median values for each volatile measured by RTOF and computed by the model in Table 13.1. We calculated the median of the production rate averaged over the 24 computed locations (shown in Figure 12.10), from 2014-08-14 to 2015-02-15 (including the approach and pre-equinox 1 time periods). We calculated the median production rates of RTOF derived from the densities of H_2O, CO_2 measured during the same periods.

	H_2O	CO_2	CO
RTOF	6.7×10^{25}	6.3×10^{24}	1.0×10^{25}
dust 0 - ice 0	2.4×10^{26}	6.4×10^{24}	7.7×10^{24}
dust 1 - ice 1	2.6×10^{26}	2.1×10^{25}	3.3×10^{20}
dust 2 - ice 2	5.6×10^{25}	1.6×10^{25}	4.5×10^{20}

Table 13.1: Median values of each species surface production rate from RTOF and from three cases of model computations: dust 0 - ice 0, dust 1 - ice 1 and dust 2 - ice 2 described in Table 11.3

.

An initial dust layer of 0.07 m (dust 2 - ice 2) reduces the mean water fluxes and provides the best prediction to the H_2O fluxes measured, while no initial dust layer (dust 0 - ice 0 and dust 1 - ice 1) slightly over-estimates the observations. The mean fluxes of

CO_2 are in best agreement with the observations when the initial ratios CO_2/H_2O and CO/H_2O are fixed at 0.02 (dust 0 - ice 0). It appears that the trapped CO (dust 0 - ice 0) is probably needed in the model to approach the RTOF observations for CO. It allows to obtain a comparable outgassing of CO_2 and CO ($\sim 10^{24}$-10^{25}). If the presence of amorphous ice is still an assumption in the composition of the cometary's nucleus, we bring an indirect observation of the presence of trapped CO in the amorphous ice.

This first analysis allows to globally compare the influence of parameters on the production rates and to get closer to the rates derived from RTOF. However, a more detailed comparison, proposed in the next section, requires the individual analysis of points over the nucleus to study the geographical heterogeneities eventually hidden by these global values, and better constrain the characteristics of the internal structure of the nucleus.

13.2 Comparison of the flux geographical maps

13.2.1 Visualisation and Interpolation

We compute the thermo-physical model on the 24 locations defined in Table 11.2 and interpolate the results to the entire surface of the nucleus. We used a method – a generalized Green's function for a spherical surface spline in tension – developed by Wessel and Bercovici (1998) which allows an interpolation for a not equidistantly sampled set of data, using two-dimensional splines to resampling the data to an equidistant grid. This method of gridding leads to unwanted oscillation between the points, thus they introduced a tension term to suppress this effect. An example of interpolation based on 24 locations on the surface of 67P/C-G shape (ESA) is shown on Figure 13.1.

We projected fluxes on 2D maps and on the 3D shape of 67P for the three complete runs dust 0 - ice 0, dust 1 - ice 1 and dust 2 - ice 2 (see Table 11.3 for their definition). We calculated the averaged H_2O, CO_2 and CO fluxes for each studied locations over the approach period and the pre-equinox period. The computed H_2O maps are visible in Figure 13.2 for the approach (6 left panels) and the pre-equinox period (6 right panels), CO_2 maps are shown in Figure 13.3 and CO maps in Figure 13.4.

13.2.2 Analysis of the model maps

We previously observed that the spatial variations globally follow the illumination conditions and that the intensity of the fluxes increases as the nucleus gets closer to the Sun.

On Figure 13.2, the three runs show a very active northern hemisphere in H_2O. We observe the consequence of the different illumination conditions between the approach and the pre-equinox 1 on the map on the right; the fluxes originating from the southern hemisphere became more important in all cases. There is no large difference in the spatial distribution of water between the runs dust 0 - ice 0 (first line) and dust 1 - ice 1 (second line). The case dust 2 - ice 2 shows that a 0.07 m thick layer of dust reduces clearly the outgassing of H_2O in the northern hemisphere and around the equator, so that the dichotomy between the hemispheres seen in the two first runs is reduced as well.

In Figure 13.3, the difference of spatial distribution for CO_2 between the approach and the pre-equinox 1 is well visible in all cases, with more detection in the southern

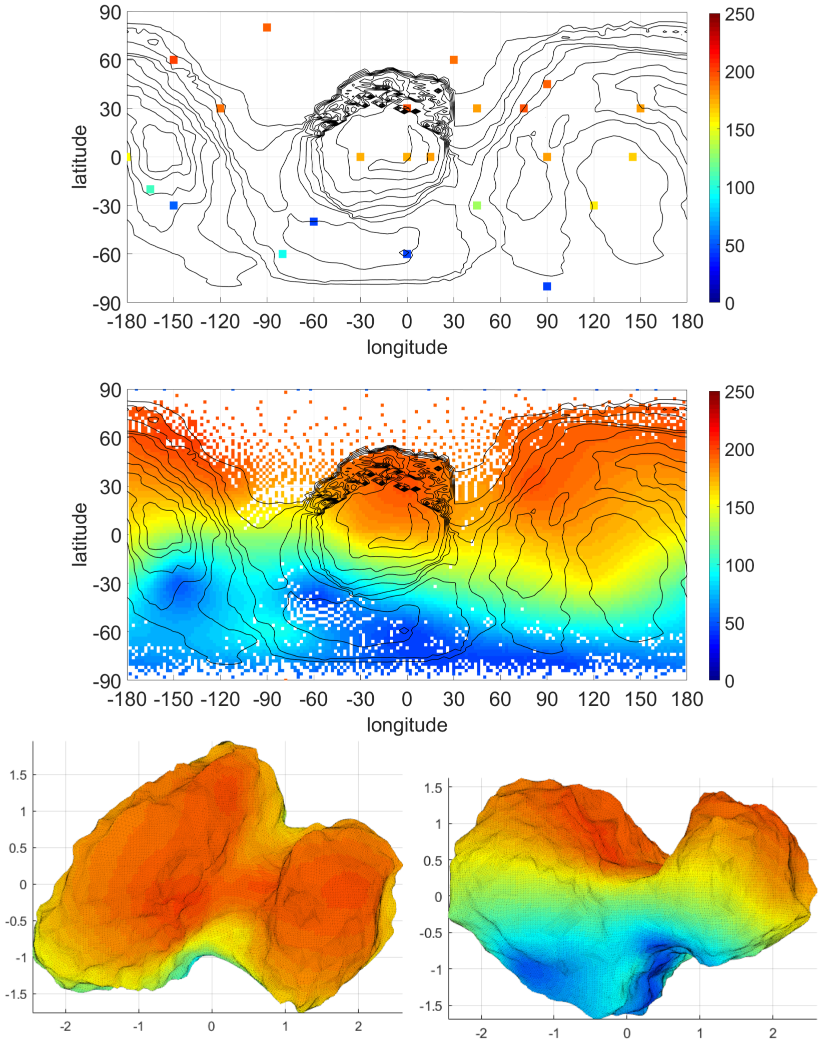

Figure 13.1: Example of interpolation using the Green's functions for splines in tension. Map of 24 studied locations (top left), 2D visualisation (top right), where the white facets are due to the non-convex shape of the nucleus, and projected on 3D shape (four bottom's figures) visualisation after interpolation over all the surface regions. In this example, colours represent the surface temperature of the nucleus around 3.3 au.

hemisphere, especially on the big lobe. The increase of the fluxes from 3 AU to 2 AU seen in the first case does not appear in the cases dust 1 - ice 1 (second line) and dust 2 - ice 2 (third line). The CO_2 fluxes appear clearly dependent on the initial CO/H_2O ratio. The second run ($CO/H_2 = 0.002$) and third run ($CO/H_2 = 0.005$) show fluxes higher than the first run (with $CO_2/H_2O = CO/H_2O = 0.02$) by an order of magnitude.

In Figure 13.4, the spatial evolution of CO fluxes obtained with the case dust 0 - ice 0 are very similar to the corresponding CO_2 maps, with larger values of fluxes, due to the presence of trapped CO in the amorphous ice and released at the transition to crystalline ice. The decrease of the initial CO/H_2O ratio strongly reduces the CO fluxes all over the nucleus, as shown on the maps of the second and third line.

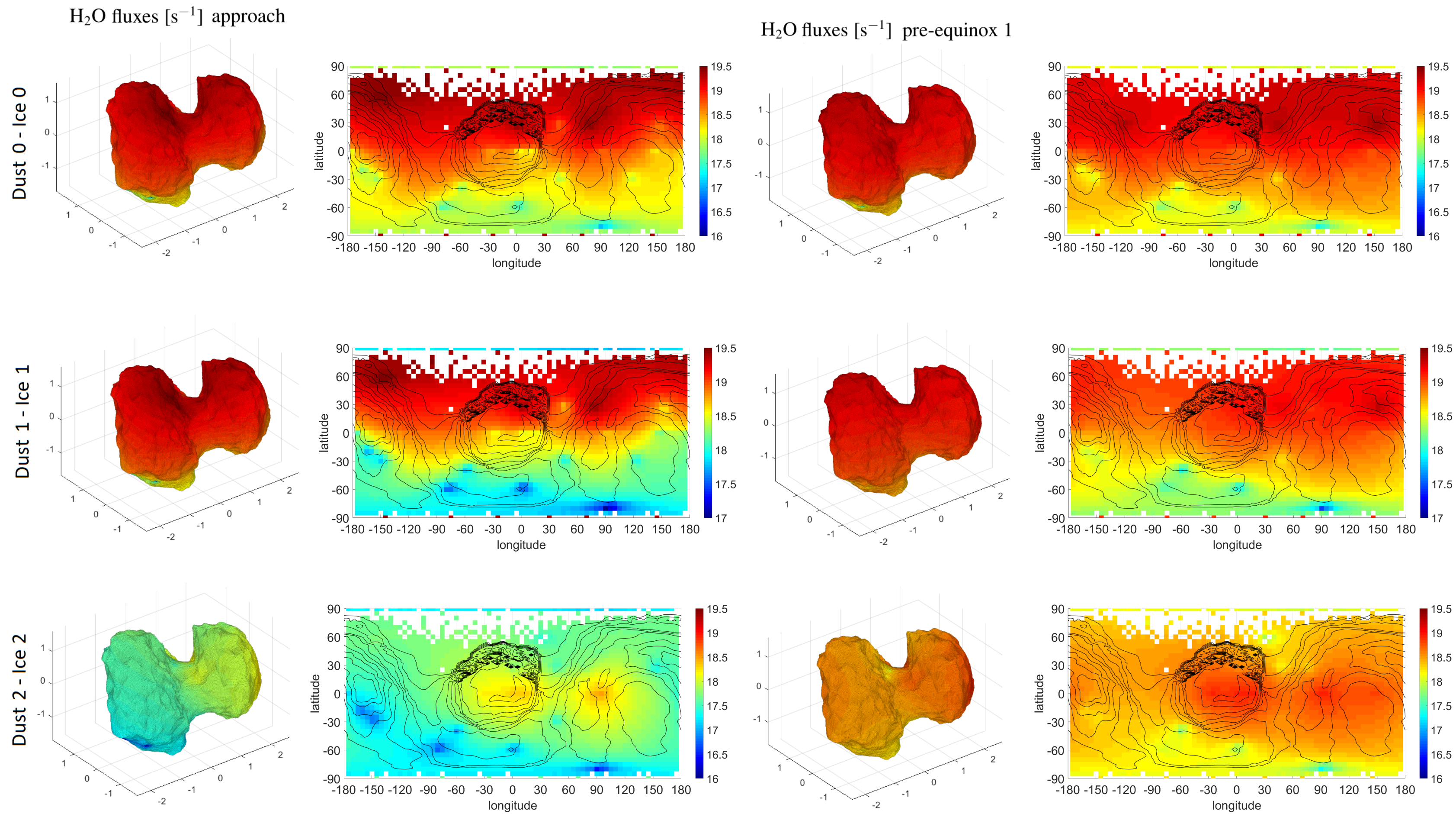

Figure 13.2: 3D and 2D representations of the H_2O averaged fluxes [s^{-1}] for the approach (six left panels) and the pre-equinox 1 (six right panels) periods with the three computations: dust 0 - ice 0 (first line), dust 1 - ice 1 (second line) and dust 2 - ice 2 (third line). The dust 0, dust 1 and dust 2 sets of parameters are used to computed the northern points and the ice 0, ice 1 and ice 2 sets of parameters are used for the equator and southern points.

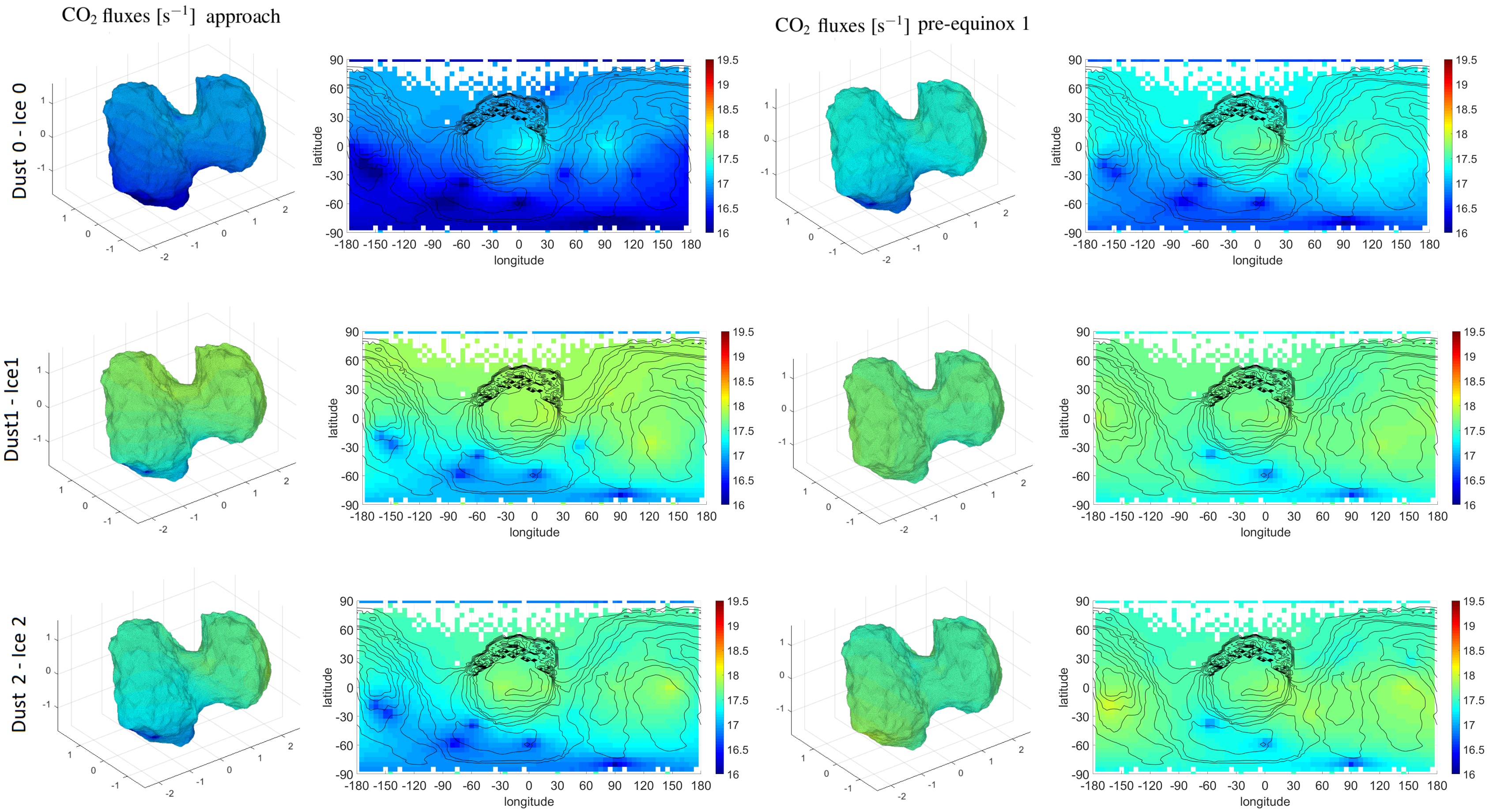

Figure 13.3: 3D and 2D representations of the CO$_2$ averaged fluxes [s^{-1}] for the approach (six left panels) and the pre-equinox 1 (six right panels) periods with the three computations: dust 0 - ice 0 (first line), dust 1 - ice 1 (second line) and dust 2 - ice 2 (third line). The dust 0, dust 1 and dust 2 sets of parameters are used to computed the northern points and the ice 0, ice 1 and ice 2 sets of parameters are used for the equator and southern points.

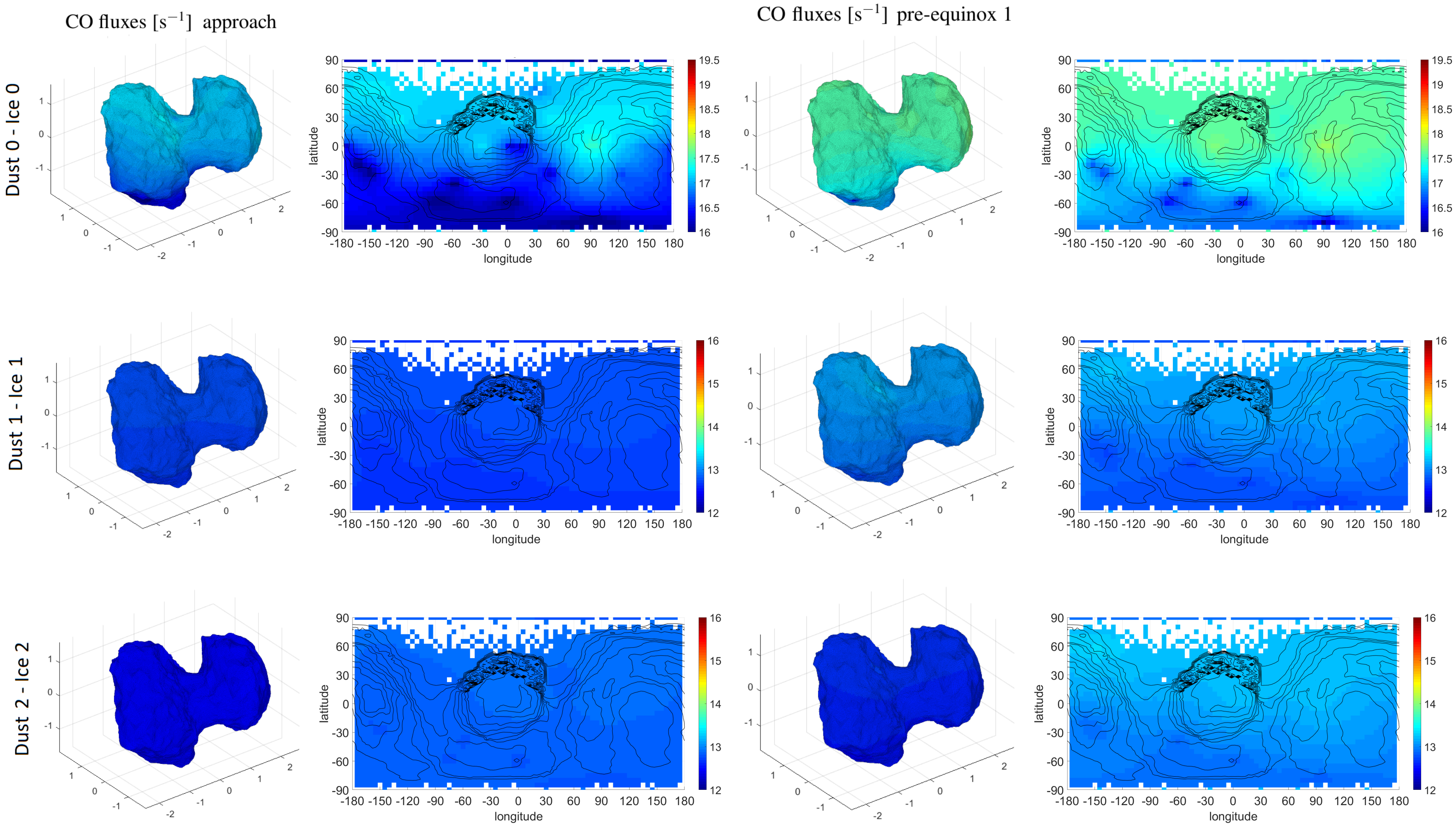

Figure 13.4: 3D and 2D representations of the CO averaged fluxes [s^{-1}] for the approach (six left panels) and the pre-equinox 1 (six right panels) periods with the three computations: dust 0 - ice 0 (first line), dust 1 - ice 1 (second line) and dust 2 - ice 2 (third line). The dust 0, dust 1 and dust 2 sets of parameters are used to computed the northern points and the ice 0, ice 1 and ice2 sets of parameters are used for the equator and southern points.

The difference in outgassing between the approach and the pre-equinox 1 is mainly due to difference of illumination condition, thus, to the surface and sub-surface heating. As described previously (see Section 8.2), the illumination condition slightly changed from approach to pre-equinox 1. The sub-solar point moved from around 41° latitude during the approach to around 30° during the pre-equinox 1. This change in the illumination conditions has a direct incidence on the surface temperature of the nucleus. Local changes in temperature may modify the outgassing for a species, especially if the surface or internal temperature is close to the sublimation temperature.

The maps of average surface temperature for the approach and the pre-equinox 1 have been studied and appeared globally similar, with some slight differences. We present the difference of temperature between the two periods in Figure 13.5. This representation indicates the areas which experienced a change of temperature, positive or negative. A clear example of the link between the activity and the variation in surface temperature is the following: the area of latitude -15°/-30° and longitude -175° experienced a strong increase of temperature, consequently this area presents a weak outgassing during approach (being in the shadow), and is getting more active during pre-equinox 1. The latitudes over 30 degrees remained globally constant while the northern extremity of the head lost a few degrees. The equator zone gained a few degrees which lead to an enhanced outgassing observed in all the maps. The southern hemisphere and the big lobe gained a few degrees with an increase of more than 20 K around the Khonsu region.

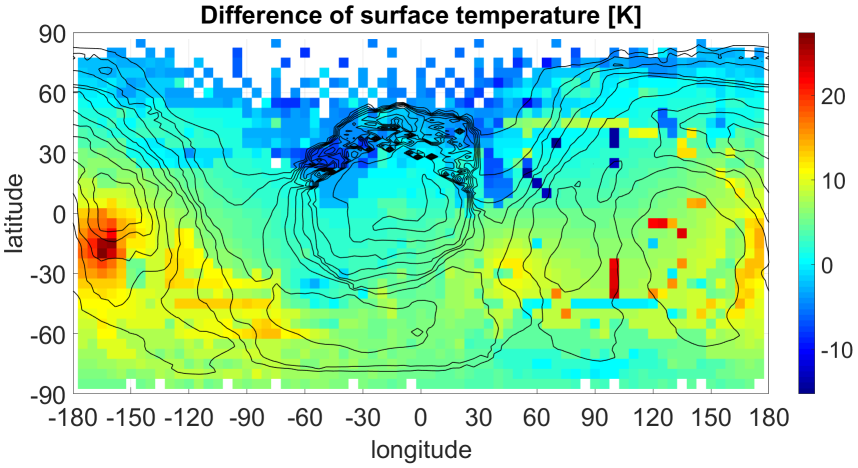

Figure 13.5: Map of the difference of average surface temperature between the approach and the pre-equinox 1 periods.

13.2.3 Comparison with the RTOF spatial variation

Figure 13.6 shows the flux maps derived from the RTOF densities for the approach (left) and the pre-equinox (right) periods, with modeled ejection velocities of 420 m/s for H_2O, 270 m/s for CO_2 and 330 m/s for CO. The estimation of the velocities and the approximation on the radial gas expansion do not allow for a very precise comparison with the modeled maps. Nevertheless, such a comparison brings first order constraints on the amount of ejected ices and the depth of their sublimation fronts, the dust layer thickness, and the trapped CO required to explain globally the temporal and spatial variations measured by RTOF.

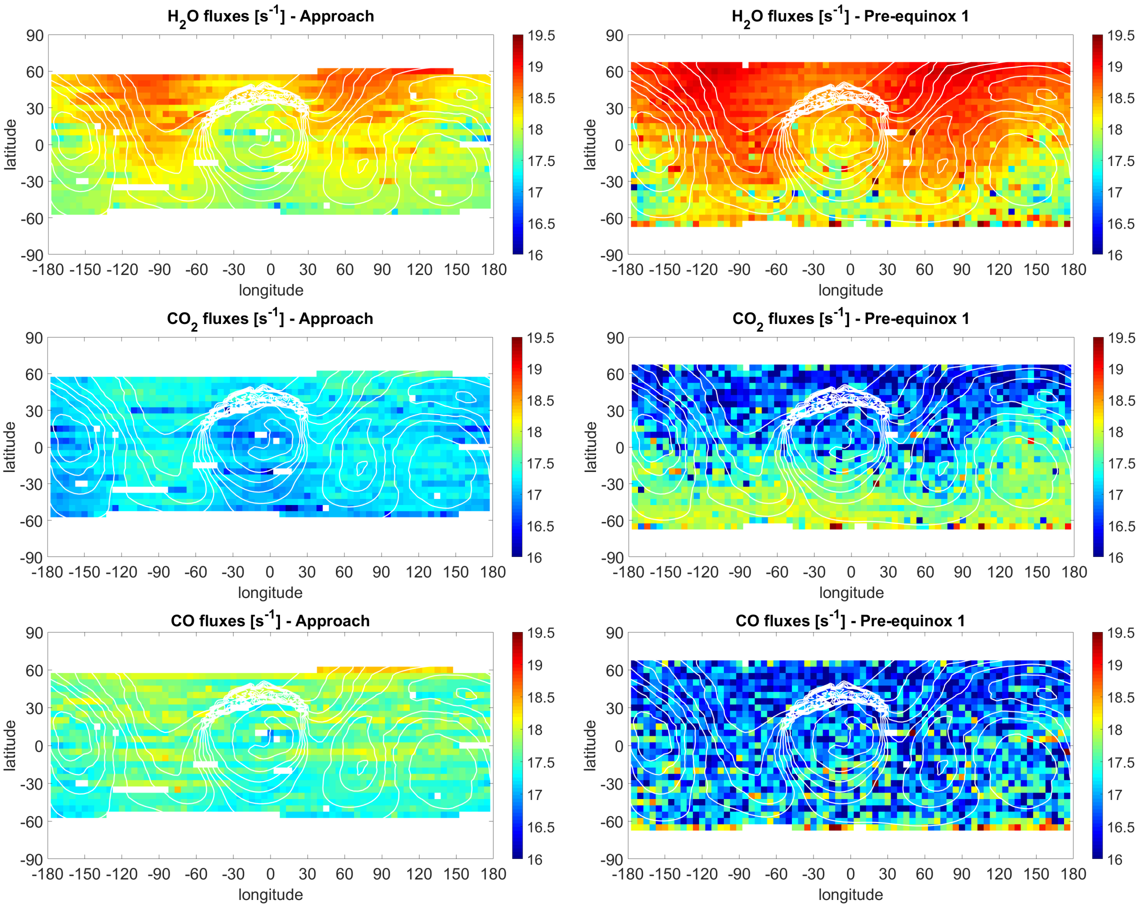

Figure 13.6: RTOF mean fluxes [s^{-1}] for the approach (left) and pre-equinox 1 (right) periods, for H_2O (top), CO_2 (middle) and CO (bottom).

The first computation (dust 0 - ice 0) had no initial dust layer but a thin dust layer naturally appeared in the end. It used an initial ratio of 0.02 for CO_2/H_2O and for CO/H_2O. The comparison with the RTOF fluxes maps show that this model over-estimates the water outgassing in the northern hemisphere but the location of the detections are well reproduced. Note that RTOF data at locations situated at latitudes larger than 60 degrees latitude are not available. As seen by RTOF, the fluxes of CO are larger than those of CO_2 and they originate from the same locations. Nevertheless, they are both underestimated by the model globally over the nucleus. For the pre-equinox 1, H_2O fluxes are quantitatively well evaluated by the computation. At the equator, the model predicts H_2O outgassing on the head and the big lobe while RTOF detected the maxima of H_2O mainly on the neck. This difference may be due to the fact that, during most of the mission, the whole comet was in the field of view of RTOF (i.e while pointing near the neck, RTOF measured also the contribution from both lobes). CO_2 and CO maps from the model are completely opposite to RTOF maps. The modeled fluxes are largely overestimated in the northern hemisphere and underestimated in the southern hemisphere.

The second computation (dust 1 - ice 1) starts with an initial CO/H_2O ratio of 0.002 and CO_2/H_2O of 0.02. For the approach time period, as the dust layer is still initiated at zero, the H_2O fluxes in the northern hemisphere were overestimated by the model. In this run, the detection of CO in the southern hemisphere was underestimated due to the low CO ratio. The decrease of the initial CO/H_2O ratio to 0.002 strongly decreases the CO outgassing, with values under $10^{12}s^{-1}$ all over the nucleus while fluxes derived from RTOF are over $10^{17}s^{-1}$. For the second time period, we observe the same behaviour as for the first computation. The outgassing of water vapor is indeed well estimated but the localisation of the maxima are not the ones seen by RTOF. Moreover, the dichotomy seen on RTOF CO_2 and CO maps are not observed in the modeled maps.

The third computation (dust 2 - ice 2) has an initial CO/H_2O ratio at 0.005 and CO_2/H_2O at 0.02, with an initial dust layer of 0.07 m. The addition of an initial dust mantle strongly reduces the H_2O outgassing and the water flux is now under-estimated for the approach and the pre-equinox 1. The modeled maps of CO_2 are very similar to the second computation, while CO modeled flux map remain under-estimated.

13.3 Discussion and perspectives

After completing an analysis of the RTOF data, and identifying active zones over the nucleus, based on the DSMC simulations, the different scenarii of nucleus modeling provide important elements to constrain the internal structure of the nucleus.

Keller et al. (2017) proposed that the strong erosion of the southern hemisphere ejected dust which then redeposited in a back fall and widely covered the northern hemisphere. This hypothesis is not reproducible by the quasi-3D model with the same initial set of parameters in both hemispheres. Therefore, we modeled the surface dichotomy by fixing an initial dust layer in the northern hemisphere, which simulates the back fall consequence. The comparison between model and RTOF maps brings several conclusions:

- A smaller CO/H_2O initial ratio increases considerably the CO_2/H_2O fluxes. The same heating leads to a higher sublimation of CO_2, as the available energy is less consumed by the sublimation of CO.
- Getting CO and CO_2 fluxes similar to RTOF appears impossible without trapped CO in the amorphous ice. Note that Kouchi and Yamamoto (1995) mentioned the possibility to have CO trapped in CO_2 ice, but experiments reveal no detection of gases from samples of CO_2 ices so far (from private conversation with Maria Teresa Capria, work of Murty S. Gudipati).
- H_2O and CO_2 fluxes are not largely affected by the presence of trapped CO.
- H_2O fluxes are not largely affected by the initial ratios of minor species.
- The dust mantle does not affect largely the CO_2 and CO fluxes but rapidly decreases the fluxes of H_2O
- An initial dust layer mantle of 0.07 m underestimates slightly the water fluxes but allows to better match the relative amount of CO_2 versus H_2O measured by RTOF.
- The decrease of the RTOF fluxes from the approach to pre-equinox 1 is not reproduced by the computations. This phenomenon is not well understood as the nucleus is approaching the Sun and the rest of the dataset globally increases when the nucleus is closer to the Sun.

- The dichotomy North-South that is clearly visible in the CO and CO_2 RTOF maps cannot be reproduced by any model scenario above. In particular, a dust layer of 7 cm in the North does not reduce significantly enough the CO and CO_2 fluxes, a much thicker layer would be needed, but this would almost extinguish the H_2O fluxes in the North.

The best computation appears to have an initial ratio of CO/H_2O smaller than that of CO_2/H_2O with the presence of trapped CO in the amorphous ice (initial value of about 0.02 for CO_2/H_2O and 0.005 for CO/H_2O), as well as the presence of an initial dust layer of about 0.07 m in the northern hemisphere.

Beyond the comparison of the gas fluxes, the model predicted surface temperatures of 140 to 245 K, comparable to the diurnal temperature of 180 to 250 K seen by VIRTIS at 3 AU (Capaccioni et al., 2015). The computed surface temperature gives ejection velocities in agreement with COPS measurements and DSMC simulations. MUPUS measured a dust layer of 10 to 20 cm on the Philae's landing site Abydos, in the Worset region, which is close to the values from 0.07 m to 0.2 m tried in our simulations (cf. Figure 12.7). Such an initial dust layer simulates effectively the terrain covered by dust reported by El-Maarry et al. (2015) in the northern hemisphere. The modeled erosion in the southern hemisphere is estimated at more than 20 cm per orbit in Capria et al. (2017) while Keller et al. (2015b) estimated an erosion of 70 cm to 3 m. We obtained a water production rate of about 2×10^{25} s^{-1} at 3.45 AU and 2×10^{26} s^{-1} at 2.3 AU, in good agreement with the production rate presented in Hansen et al. (2016), $\sim 4\times10^{25}$ s^{-1} at 3.45 AU and $\sim 3\times10^{26}$ s^{-1} (see Figure 7.7), who provided a multi-instruments study combining the results of ROSINA/DFMS, VIRTIS, RPC-ICA and MIRO.

Nevertheless, as mentioned previously, two observations are not reproduced by the studied computations of the model: 1) the north/south dichotomy and 2) the decrease of CO and CO_2 outgassing in the northern hemisphere between the approach and pre-equinox-1. The first observation will either require the use of different intrinsic ratios for the two hemispheres, which will be difficult to explain in terms of comet formation (all the more colliding bodies assumed to form the comet correspond to the lobes and not the hemispheres), or to force different depths of sublimation fronts for CO_2 and CO. One can also note that the history of the comet is not well known. Thus, the northern hemisphere might have been depleted during previous orbits. The second observation (already discussed in details in Section 8.3.3) requires either an amount of CO and CO_2 included in the dust back fall (but the estimated size of the dust particles is not large enough to explain this inclusion (Keller et al., 2017)), or the presence of a layer of pure water ice under the wet layer of dust.

We thus provided here a first order comparison between a thermo-physical model of the nucleus of 67P/C-G and RTOF observations. However, this work assumed important hypotheses, in particular that the RTOF measurements originated from the nadir. Additionally, the modeling of the nucleus' surface is complicated as the two hemispheres presented specificities, such as ice patches on the dust covered areas (Fornasier et al., 2016; Filacchione et al., 2016). Furthermore, the surface of the nucleus is not smooth but is covered by boulders of various sizes (Lee et al., 2017). Those specificities are not taken into account in this work, as we compute the same set of parameters for each hemisphere. Moreover, the fast activity events, such as outbursts, are not modeled and can lead to non continuous fluxes of volatiles and dust. In a further work, the nucleus modeling has to be coupled with a model of coma, such as the DSCM model, to simulate the transport of the particles and the collisions and take into account the induced modification of the velocity and the direction of the particles. More work also needs to be done in terms of direct comparison with the other Rosetta instruments (like VIRTIS and MIRO) to refine the single instrument based interpretations.

Conclusion and perspectives (English version)

The time-of-flight mass spectrometer RTOF, onboard the Rosetta' spacecraft, provided in-situ measurements of the coma of comet 67P/Churyumov-Gerasimenko from the rendezvous in August 2014 until the end of the mission in September 2016. The large amount of spectra recorded over two years of mission, allows a characterisation of the coma with a high temporal resolution at various heliocentric distances.

The coma composition of 67P/C-G appeared dominated by H_2O, followed by CO_2 and CO. The fourth more abundant volatiles in the coma surprisingly appeared to be O_2 (Bieler et al., 2015). ROSINA detected almost all the species known in cometary comae and discovered a few ones (Le Roy et al., 2015). The outgassing revealed strong heterogeneities for the three main volatiles Hässig et al. (2015); Bockelée-Morvan et al. (2015); Migliorini et al. (2016), as previously observed in the bilobate comet 103P/Hartley 2 (A'Hearn et al., 2011), which showed high detections of H_2O in the neck region, and active jets of CO_2 at the extremity of the lobes. On 67P/C-G, the neck region appeared to be very active with a large amount of dust jets, but jets were also observed originating from the lobes as the activity increased approaching the Sun (Sierks et al., 2015).

Our analysis of the coma of 67P/C-G revealed strong periodicities in time and spatial heterogeneities, for the three main volatiles H_2O, CO_2 and CO. We provided a high temporal resolution study of the diurnal and seasonal variations for the three species. We measured the evolution of the global outgassing of 67P/C-G with heliocentric distance, including an asymmetry with respect to perihelion, as observed in various comets (see for exemple Biver et al. (1997) for Hale-Bopp). We observed a maximum of outgassing occurring $\sim$24 days after perihelion. Hansen et al. (2016) observed a maximum of water production of $3.5 \pm 0.5 \times 10^{28}$ molecules/s 18 to 22 days after perihelion (when RTOF data are missing). If the coma composition appeared dominated by H_2O during most of the mission, we observed variations of the CO_2/H_2O and CO/H_2O ratios with an increasing contribution of CO_2 and CO in the total outgassing toward the end of the mission. The influence of different parameters, such as the distance between the spacecraft and the nucleus, the distance between the comet and Sun, the sub-spacecraft location and the nadir off-pointing angle, on the outgassing detected by ROSINA/RTOF was individually analysed and interpreted.

Spatial heterogeneities in terms of the three main volatiles were studied in details and were correlated with the illumination conditions (see Hoang et al. (2017) for the analysis of the first six months of the mission). We observed that the H_2O measurements followed essentially the illumination, while CO and CO_2 showed complex behaviours. The analysis of the coma composition revealed a dichotomy between the northern hemisphere and the southern hemisphere. Indeed, the two hemispheres experienced very different heating conditions: the northern hemisphere endures a long and soft illumination far from the Sun, while the southern hemisphere is shortly but strongly heated around perihelion, when the nucleus is close to the Sun. The southern hemisphere sublimated in particular more CO and CO_2 than the northern hemisphere. CO and CO_2 ices are probably very close to the surface in the South and easily sublimated when the temperature is high enough, which is in agreement with the observed strong erosion of the southern hemisphere between the equinoxes. Our observations (of CO_2 and, mostly, CO being more homogeneous than H_2O) are consistent with the assumption that CO_2 and CO originate from deeper layers than H_2O in the northern hemisphere.

In addition, a cyclic behaviour was observed in CO_2 and CO detections in the northern hemisphere (Hoang et al, to be submitted). Indeed, their outgassing was medium at the approach, very low before the 1ft equinox, high before the 2nd equinox , medium after the 2nd equinox 2 than low at the end of the mission. The depletion of CO_2 and CO early before the May 2015 equinox and after the March 2016 equinox, despite a surface and subsurface temperature large enough to sublimate them, suggests the presence of an icy dust layer covering the northern regions. The strong erosion of the southern hemisphere after the previous perihelion would have ejected dust particles, which then redeposited in the northern hemisphere (Keller et al., 2017), preventing the heat from reaching the CO_2 and CO rich layers. This icy dust layer mainly contains water transported by the dust particles, leading to strong water outgassing during the northern summer hemisphere. Nevertheless, the illumination conditions and the back fall of dust particles carrying water are not sufficient to explain the observed cyclic behaviour for CO and CO_2, which lead us to propose a new stratification scenario with a pure ice layer in between the icy dust layer and the underneath CO and CO_2 layers.

Our study provides the first global comparison between the data recorded by the three instruments of ROSINA: DFMS, RTOF, and COPS. The comparison between those in situ data reveals a very good correlation and increase our understanding of the global behaviour of the main volatiles. We also achieved a comparison with a Monte Carlo coma model (DSMC model, University of Michigan) which revealed a heterogeneous activity over the nucleus' surface, including a north-south dichotomy for H_2O and CO_2. From our work, we conclude that the sublimation of volatiles at the surface are directly impacted by the shape, attitude and orbit of the comet and the observed dynamic results from a complex combination of seasonal, diurnal, and heterogeneous surface activity effects.

To investigate those surface heterogeneities and understand their internal origin, we applied a quasi-3D thermo-physical nucleus modeling to the case of 67P/C-G to simulate the internal structure of the nucleus and its evolution with the heliocentric distance. We also analysed the variations of the surface and sub-surface temperatures, the resulting fluxes for the three main volatiles and the apparition of a dust layer on the surface of the nucleus. As the actual quasi-3D model cannot simulate the back fall of dust, we fixed an initial layer of dust (with various thicknesses) in the northern hemisphere. We studied the influence of this initial dust mantle, as well as the influence of different initial species ratios and the eventual presence of CO trapped in the amorphous ice. The analysis of the production rate with different initial dust mantles reveals that the thickness of the layer essentially affects H_2O outgassing and not much CO_2 and CO outgassing. The water production rate modeled with an initial dust layer of 7 cm ($\sim 2\times 10^{25}$ s^{-1} at 3.45 AU increasing to $\sim 2\times10^{26}$ s^{-1} at 2.3 AU) well fits the production rate estimated by RTOF and by others instruments aboard Rosetta reported in Hansen et al. (2016). However, the dichotomy observed in the outgassing between the two hemispheres is not reproduced by the studied cases. The 7 cm thick layer does not reduce significantly the outgassing of CO_2 and CO in the northern hemisphere to reproduce the depletions. A thicker layer is needed, but would then extinguish the water fluxes. The comparison with the observations showed that similar outgassing of CO are only obtained with the inclusion of trapped CO in the amorphous ice, which does not largely affect the outgassing of CO_2 and H_2O. The initial CO_2/H_2O and CO/H_2O ratios directly impact the species outgassing, with a higher CO_2 outgassing when the bulk composition initially contains less CO.

Finally, a comparison between the ROSINA detections during the mission with the outgassing rate derived from the nucleus model suggests the following conclusions: the CO species must be trapped in the amorphous ice since the comet formation, and differential intrinsic ratios or sublimation front depths must exist between the northern and southern hemispheres of the nucleus.

In a further work, the comparison between the model and RTOF has to be extended to the whole mission, in particular to highlight the seasonal evolution and the asymmetry with perihelion. Our comparison used important assumptions (e.g. detections originated from the nadir pointing direction), thus, coupling the nucleus model with a specific model for gas expansion, such as the DSMC model, is required to simulate the collisions and the complex trajectory of the molecules from the surface of the nucleus until the instrument. Constraining the properties of the 67P/C-G's nucleus also needs a further comparison with the other Rosetta instruments (MIRO, VIRTIS, ALICE, and ROSINA for the gas).

Conclusion et perspectives (french version)

À bord de la sonde Rosetta, le spectromètre de masse RTOF a étudié la coma de la comète 67P/Churyumov-Gerasimenko depuis le rendez-vous en août 2014 jusqu'à la fin de la mission en septembre 2016. Les spectres enregistrés durant les deux années de mission ont permis de caractériser la coma à différentes distances heliocentriques avec une excellente résolution temporelle.

L'étude du gaz cométaire a montré que sa composition était dominée par H_2O, suivi de CO_2 et de CO. Étonnamment, O_2 fut le quatrième volatile le plus abondant détecté dans la coma (Bieler et al., 2015). L'expérience ROSINA a permis de détecter quasiment toutes les espèces précédemment observées dans du gaz cométaire, et en a détecté de nouvelles (Le Roy et al., 2015). L'analyse des principaux volatiles a révélé de fortes hétérogénéités (Hässig et al., 2015; Bockelée-Morvan et al., 2015; Migliorini et al., 2016), comme observées sur la comète bilobée 103P/Harltey 2 (A'Hearn et al., 2011), pour laquelle de fortes abondances de H_2O avait été détectées dans la région reliant les lobes, alors que d'intenses jets de CO_2 provenaient des extremités des lobes. Sur 67P/C-G, une importante activité a été observée dans la région du cou, mais des jets de poussières ont également été observés au niveau des deux lobes lorsque l'activité s'est intensifiée à l'approche du Soleil (Sierks et al., 2015).

Notre analyse de la coma de 67P/C-G a révélé des périodicités en temps et des hétérogeneités spatiales, pour les trois volatiles H_2O, CO_2 and CO. Grâce à la haute résolution temporelle de RTOF, nous avons réalisé une étude fine des variations diurnes et saisonnières pour les trois espèces. Nous avons analysé l'évolution du dégazage global de 67P/C-G en fonction de la distance héliocentrique, et observé une asymétrie par rapport au périhélie, comme vu sur d'autres comètes, par exemple Hale-Bopp (Biver et al., 1997). Le maximum de dégazage est détecté $\sim$24 jours après le périhélie dans les mesures de RTOF. Hansen et al. (2016) ont observé un maximum de dégazage avec $3.5 \pm 0.5 \times 10^{28}$ molecules/s 18 à 22 jours après le périhélie, journées durant lesquelles RTOF n'a pas enregistré de données. Si le dégazage de H_2O a dominé la composition de la coma pendant la majorité de la mission, on a cependant observé une évolution des rapports CO_2/H_2O and CO/H_2O avec une augmentation de la contribution de CO_2 et CO dans le dégazage total à la fin de la mission. L'influence de différents paramètres sur le dégazage mesuré, comme la distance entre la sonde et le noyau, la distance héliocentrique, la position de la sonde dans le repère cométaire ou le nadir off-pointing, a été individuellement analysée et interprétée.

Les hétérogénéités spatiales observées pour les trois volatiles principaux ont été étudiées en détail et corrélées avec les conditions d'illumination du noyau (voir Hoang et al. (2017)

pour l'analyse des six premiers mois de la mission). Les détections d'H_2O sont apparues très bien corrélées avec l'illumination, alors que les détections de CO et CO_2 étaient plus complexes à expliquer. En effet, l'analyse de la composition de la coma a montré une dichotomie entre l'hémisphère nord et l'hémisphère sud. Pour cause, les deux hémisphères subissent des conditions de chauffage très différentes: l'hémisphère nord est illuminé durant une grande partie de l'orbite mais le chauffage est modéré, alors que l'hémisphère sud connait un été court mais très intense, car le noyau cométaire se trouve alors proche du Soleil. Les zones actives en CO_2 et CO sont apparues plus localisées dans l'hémisphère sud que dans l'hémiphère nord. Ces deux espèces sont probablement situées plus proche de la surface dans l'hémisphère sud et donc plus facilement sublimées lorsque la température atteint leur température de sublimation respective. Cette hypothèse est en adéquation avec la forte érosion de l'hémisphère sud, observée entre les équinoxes. Par ailleurs, nous avons observé des distributions spatiales plus homogènes pour CO_2 et CO que pour H_2O dans l'hémisphère nord, ce qui confirme que les couches contenant du CO_2 et du CO y sont situées plus en profondeur.

De plus, un comportement cyclique a été obervé pour CO_2 et CO dans l'hémisphère nord (Hoang et al, en cours de soumission). En effet, RTOF a enregisté des dégazages moyens durant l'approche, très faibles avant le 1er équinoxe, forts avant le 2nd équinoxe, moyens après et enfin faibles vers la fin de la mission dans l'hémisphère nord. Les déplétions observées avant le premier équinoxe de mai 2015 et après le second équinoxe de mars 2016, malgré une température de surface et sous-surface suffisante, suggèrent la présence d'une couche de poussière riche en eau recouvrant l'hémisphère nord. La forte érosion de l'hémisphère sud lors des précédents périhélies aurait éjecté de la poussière qui se serait ensuite déposée dans l'hémisphère nord, empêchant l'onde de chaleur d'atteindre les couches riches en CO_2 et CO. Cette couche de poussière contiendrait des molécules d'H_2O transportées par les particules de poussières, et qui sont ensuite largement détectèes dans la coma lorsque l'hémisphère nord est illuminé (Keller et al., 2017). Cependant, les conditions d'illumination et le dépôt d'une couche de poussière contenant de l'eau dans l'hémisphère nord n'expliquent pas le comportement cyclique observé pour CO_2 et CO. Nous proposons une nouvelle stratification du noyau avec une couche de glace d'eau pure entre la couche de poussière contenant de l'eau et les couches riches en CO and CO_2.

Nous avons réalisé pour la première fois une comparaison globale des données enregistrées par les trois instruments de ROSINA: DFMS, RTOF et COPS. Cette comparaison a montré une très bonne corrélation des données in situ et a amélioré notre compréhension du dégazage des volatiles principaux. Nous avons également réalisé une comparaison de nos observations avec les prédictions d'un modèle Monte Carlo de la coma (le modèle DSMC de l'Université du Michigan) qui a mis en évidence une activité hétérogène de la surface du noyau et a précisé la dichotomie nord-sud. En conclusion, notre étude révèle que la forme, l'attitude et l'orbite de 67P/C-G impactent fortement la sublimation des volatiles à la surface du noyau cométaire et que la dynamique observée est le résultat d'une combinaison complexe entre des effets saisoniers, diurnes et d'une activité de surface hétérogène.

Pour étudier ces hétérogénéités de surface, nous avons ensuite utilisé un modèle thermo-physique de noyau appliqué au cas de 67P/C-G pour simuler l'intérieur du noyau cométaire et son évolution en fonction de la distance héliocentrique. Nous avons également analysé les variations de température en surface et sous-surface, ainsi que les flux résultant pour les trois volatiles principaux et l'apparition d'une croûte de poussière à la surface du noyau. Comme le modèle actuel ne permet pas de simuler le dépôt sur l'hémisphère nord de particules de poussières provenant de l'hémisphère sud, nous avons fixé une couche de poussière initiale recouvrant l'hémisphère nord. Nous avons étudié l'influence de cette couche de poussière en utilisant différentes épaisseurs, et l'influence de différentes abondances relatives entre les espèces ainsi que la présence ou non de CO piégé dans la glace amorphe. L'analyse des taux de dégazages obtenus avec différentes couches de poussière initiale a montré que l'épaisseur de poussière affecte fortement le dégazage d'eau, mais très peu les dégazages de CO_2 et CO. Le taux de production de l'eau obtenu avec une couche de poussière initiale de 7 cm ($\sim 2\times10^{25}$ s^{-1} à 3.45 UA et $\sim 2\times10^{26}$ s^{-1} à 2.3 UA) reproduit très bien le dégazage estimé à partir des données RTOF et le dégazage enregistré par d'autres instruments de Rosetta, observé par Hansen et al. (2016). Cependant, la dichotomie nord-sud observée n'est pas reproduite par les différents cas étudiés. La couche de poussière de 7 cm ne permet pas de réduire suffisamment les dégazages de CO_2 et CO pour reproduire les déplétions de l'hémisphère nord. Une couche plus épaisse serait plus efficace mais éteindrait alors les flux d'eau qui sont eux largement observés. La comparaison avec les observations montrent que le dégazage de CO est obtenu, en premier ordre de grandeur, lorsque nous incluons du CO dans la glace amorphe, ce qui, par ailleurs, influence peu les dégazages de H_2O et CO_2. Les valeurs initiales choisies pour les rapports CO_2/H_2O and CO/H_2O impactent directement les dégazages obtenus, avec un dégazage plus important de CO_2 lorsque la composition du noyau contient moins de CO.

Finalement, la comparaison entre les observations de ROSINA et les taux de dégazage obtenus avec le modèle suggère que du CO est probablement inclus dans la glace amorphe depuis la formation du noyau comètaire, et que, entre l'hémisphère nord et l'hémisphère sud, les abondances relatives intrinsèques sont différentes ou que les front de sublimation sont situés à des profondeurs différentes.

En perspective, une comparaison entre le modèle de noyau et les données RTOF devrait être étendue à l'entièreté de la mission pour mettre en évidence, entre autres, les variations saisonnières et l'asymétrie avec le périhélie. Une importante amélioration de notre comparaison entre observations et modèle de noyau est à apporter par la simulation de la trajectoire des molécules entre la surface et l'instrument. En effet, nous avons utilisé dans ce travail des hypothèses importantes (dont l'hypothèse que les détections proviennent de la direction du nadir). Le couplage du modèle de noyau avec un modèle d'expansion de gas, comme le modèle DSCM, permettrait de simuler les collisions et les trajectoires complexes des molécules. Enfin, la comparaison des résultats avec les données des autres instruments de Rosetta (MIRO, VIRTIS, ALICE et ROSINA pour le gaz) devrait être développée afin de mieux contraindre les propriétés du noyau de 67P/C-G.

Appendices

Our analysis of RTOF data led to three publications: one as a first author (a) and two as a co-author (b and c). A fourth article is about to be submitted (d).

(a) **M. Hoang**, K. Altwegg, H. Balsiger, A. Beth, A. Bieler, U. Calmonte, M. R. Combi, J. De Keyser, B. Fiethe, N. Fougere, S. A. Fuselier, A. Galli, P. Garnier, S. Gasc, T. Gombosi , K. C. Hansen, A. Jäckel, A. Korth, J. Lasue, L. Le Roy, U. Mall et H. Rème : *The heterogeneous coma of comet 67P/Churyumov-Gerasimenko as seen by ROSINA:* H_2O*,* CO_2*, and CO from September 2014 to February 2016*, Astronomy and Astrophysics, 600, A77, 2017.

(b) U. Mall, K. Altwegg, H. Balsiger, A. Bar-Nun, J.-J. Berthelier, A. Bieler, P. Bochsler, C. Briois, U. Calmonte, M. R. Combi, B. Dabrowski, J. De Keyser, F. Dhooghe, B. Fiethe, S. A. Fuselier, A. Galli, P. Garnier, S. Gasc, T. I. Gombosi, K. C. Hansen, M. Hässig, **M. Hoang**, A. Jäckel, E. Kopp, A. Korth, L. Le Roy, B. Magee, B. Marty, O. Mousis, H. Rème, M. Rubin, T. Sémon, C.-Y. Tzou, J. H. Waite, and P. Wurz : *High-time resolution in situ investigation of major cometary volatiles around 67P/C-G at 3.1-2.3 AU measured with ROSINA-RTOF*, The Astrophysical Journal, 819(2), 126 , 2016.

(c) S. Gasc, K. Altwegg, H. Balsiger, J.-J. Berthelier, A. Bieler, U. Calmonte, B. Fiethe, S. A. Fuselier, A. Galli, T. I. Gombosi, **M. Hoang**, J. De Keyser, A. Korth, L. Le Roy, U. Mall, H. Rème, M. Rubin, T. Sémon, C.-Y. Tzou, J. H. Waite, and P. Wurz : *Change of outgassing pattern of 67P/Churyumov-Gerasimenko during the March 2016 equinox as seen by ROSINA.*, MNRAS, 2017.

(d) **M. Hoang**, P. Garnier, H. Gourlaouen, J. Lasue, H. Rème, K. Altwegg, H. Balsiger, U. Calmonte, B. Fiethe, A. Galli, S. Gasc, A. Jäckel, U. Mall, M. Rubin, T. Semon, C.-Y Tzou, J. H. Waite, P. Wurz: *Two-years with comet 67P:* H_2O*,* CO_2 *and CO as seen by ROSINA/RTOF*, to be submitted.

A&A 600, A77 (2017)
DOI: 10.1051/0004-6361/201629900

Astronomy & Astrophysics

The heterogeneous coma of comet 67P/Churyumov-Gerasimenko as seen by ROSINA: H_2O, CO_2, and CO from September 2014 to February 2016

M. Hoang[1,2], K. Altwegg[3], H. Balsiger[3], A. Beth[4], A. Bieler[3,5], U. Calmonte[3], M. R. Combi[5], J. De Keyser[6], B. Fiethe[7], N. Fougere[5], S. A. Fuselier[8,9], A. Galli[3], P. Garnier[1,2], S. Gasc[3], T. Gombosi[5], K. C. Hansen[5], A. Jäckel[3], A. Korth[10], J. Lasue[1,2], L. Le Roy[3], U. Mall[10], H. Rème[1,2], M. Rubin[3], T. Sémon[3], D. Toublanc[1,2], C.-Y. Tzou[3], J. H. Waite[8], and P. Wurz[3]

[1] University of Toulouse, UPS-OMP, IRAP, 31400 Toulouse, France
e-mail: `margaux.hoang@irap.omp.eu`
[2] CNRS, IRAP, 9 avenue colonel Roche, BP 44346, 31028 Toulouse Cedex 4, France
[3] University of Bern, Physikalisches Institut, 3012 Bern, Switzerland
[4] Department of Physics, Imperial College London, London SW7 2AZ, UK
[5] University of Michigan, Department of Atmospheric Oceanic and Space Science, Ann Arbor, MI 48109, USA
[6] Royal Belgian Institute for Space Aeronomy (BIRA-IASB), 1180 Brussels, Belgium
[7] Technical University of Braunschweig, 38106 Braunschweig, Germany
[8] Southwest Research Institute, San Antonio, TX 78238, USA
[9] Department of Physics and Astronomy, University of Texas at San Antonio, San Antonio, Texas, TX 78249, USA
[10] Max-Planck Institute für Sonnensystemforschung, 37077 Göttingen, Germany

Received 14 October 2016 / Accepted 3 February 2017

ABSTRACT

Context. The ESA Rosetta mission has been investigating the environment of comet 67P/Churyumov-Gerasimenko (67P) since August 2014. Among the experiments on board the spacecraft, the ROSINA experiment (Rosetta Orbiter Spectrometer for Ion and Neutral Analysis) includes two mass spectrometers to analyse the composition of neutrals and ions and a COmet Pressure Sensor (COPS) to monitor the density and velocity of neutrals in the coma.
Aims. We study heterogeneities in the coma during three periods starting in October 2014 (summer in the northern hemisphere) and ending in February 2016 (end of winter in the northern hemisphere). We provide a detailed description of the main volatiles dynamics (H_2O, CO_2, CO) and their abundance ratios.
Methods. We analysed and compared the data of the Reflectron-type Time-Of-Flight (RTOF) mass spectrometer with data from both the Double Focusing Mass Spectrometer (DFMS) and COPS during the comet escort phase. This comparison has demonstrated that the observations performed with each ROSINA sensor are indeed consistent. Furthermore, we used a Direct Simulation Monte Carlo (DSMC) model to compare modelled densitites with in situ detections.
Results. Our analysis shows how the active regions of the main volatiles evolve with the seasons with a variability mostly driven by the illumination conditions; this is the case except for an unexpected dichotomy suggesting the presence of a dust layer containing water deposited in the northern hemisphere during previous perihelions hiding the presence of CO_2. The influence of various parameters is investigated in detail: distance to the comet, heliocentric distance, longitude and latitude of sub-satellite point, local time, and phase angle.

Key words. comets: individual: 67P/Churyumov-Gerasimenko – comets: general – planets and satellites: atmospheres

1. Introduction

After 10 years of travel, the Rosetta spacecraft arrived at comet 67P/Churyumov-Gerasimenko (67P) in August 2014 and started to study the weakly active nucleus with its onboard instruments. The spacecraft escorted the comet through its perihelion in August 2015 at 1.24 AU from the Sun. After 20 months of study, Rosetta recorded a large amount of in situ data and helped us to understand the composition and evolution of the coma of the comet along its orbit. Among the onboard instruments, the Rosetta Orbiter Spectrometer for Ion and Neutral Analysis (ROSINA) produced important results. We owe these results to the data from its two mass spectrometers, the Reflectron-type Time-Of-Flight (RTOF) mass spectrometer and the Double Focusing Mass Spectrometer (DFMS), and to data from the COmet Pressure Sensor (COPS). All three sensors are commonly operated through a data processing unit (DPU). RTOF has a wide mass range and a high temporal resolution (Scherer et al. 2006), while DFMS has high mass resolution and sensitivity (Balsiger et al. 2007). Both sensors were designed to measure the composition of the cometary neutral gas along with cometary ions. The third instrument, COPS, measures total density and bulk velocity of the gas (Balsiger et al. 2007).

A strong chemical heterogeneity in the coma during the summer in the northern hemisphere was revealed using the DFMS data by Hässig et al. (2015). These authors studied H_2O, CO_2, and CO variations in the coma and found diurnal and latitudinal variations of H_2O with a more homogeneous behaviour of CO_2 and CO, which probably originated from deeper layers inside the comet, whose rotation axis is tilted by 52 deg relative to its orbit. A high CO_2/H_2O ratio ($\geqslant 2$) region was located in the southern part of the bigger lobe, whereas the highest water densities were observed when the spacecraft was located above the neck area. Temporal variations of H_2O, CO_2, and CO seen by RTOF between 3.1 and 2.3 AU were given in Mall et al. (2016). Luspay-Kuti et al. (2015) demonstrated that minor species density variations are correlated with major species H_2O or CO_2 while CH_4 shows a different pattern. Bieler et al. (2015) compared the three different models, purely geometrical, hydrodynamic, and Direct Simulation Monte Carlo (DSMC), and reproduced COPS data. Fougere et al. (2016) used DSMC model to fit DFMS measurements, when assuming that the activity of the comet is largely driven by solar illumination, including areas of higher activity.

Important results about the coma of 67P were also obtained from other instruments on board Rosetta, such as the ultraviolet imaging spectrometer called ALICE, with measurements of near-nucleus atomic hydrogen and oxygen emissions. These revealed an unexpected influence of electrons, rather than photons, on the break up of molecules (Feldman et al. 2015). Biver et al. (2015) also published a map of water vapour in the coma of 67P based on the Microwave Instrument for the Rosetta Orbiter data (MIRO), showing a very inhomogeneous distribution of water in the coma with the highest density above the active neck region. The active zones, such as the neck region, related to cliffs and pits – possibly due to sink-hole collapse – were mapped and discussed by Vincent et al. (2015, 2016) with the OSIRIS experiment (Optical, Spectroscopic, and Infra-red Remote Imaging System). The VIRTIS (Visible and InfraRed Thermal Imaging Spectrometer) team detailed the dynamics of 67P surface properties and the loss of a dust layer due to increased water sublimation during the approach to the Sun (Filacchione et al. 2016). They also revealed a cyclic pattern, which modifies the activity and water ice production rate on the surface of the comet (De Sanctis et al. 2015).

In this paper, we focus on the spatial and temporal variation of the densities of the main volatile species H_2O, CO_2, and CO provided by the RTOF instrument. The characterization of water and carbonic molecules in the coma is essential to understand the structure of cometary nuclei and thus the composition of the primordial solar system. We first describe the RTOF instrument briefly (further details are given by Gasc 2015). Then, we show that the density and dynamics of the main volatiles are complex and depend on several parameters such as comet-spacecraft distance, Sun-comet distance, the longitude and latitude of the sub-satellite point, and phase angle. A mapping of the coma reveals a heterogeneous seasonal production at the surface and a significant temporal variability correlated with heliocentric distance.

2. Description of the instruments and datasets

2.1. Description of the instruments

The RTOF mass spectrometer was designed to measure cometary neutral gas and cometary ions and, in particular, is able to detect heavy organic molecules with a very good mass resolution ($m/\Delta m = 500$ at 50% level). This spectrometer is able to detect ions and molecules from 1 amu/e to 300 amu/e and has a high temporal resolution of 200 s (Scherer et al. 2006; Balsiger et al. 2007).

Spectra from the RTOF are recorded as abundance versus time of flight. To convert those spectra into abundance versus mass to charge ratio, a mass calibration is applied on each RTOF spectrum (Gasc et al. 2017). The instrument can be operated in different modes. In one of them, RTOF uses a gas calibration unit (GCU) to record spectra for mass calibration. The unit contains a well-calibrated gas mixture with helium, carbon dioxide, and krypton.

Table 1. Description of RTOF neutral modes used in this work.

Mode	SS M0521	OS M0524
Extraction frequency	10 kHz	10 kHz
Filament emission	200 μA	200 μA
Acquisition time	200 s	400 s

Notes. See Gasc et al. (2017) for further details.

The RTOF is actually two mass spectrometers in one instrument, each with its own ion source and detector optimized for different measurements. The channel with electron impact storage ions source or storage source (SS) samples the neutral gas, while the orthogonal extraction ion source channel or orthogonal source (OS) analyses cometary ions but can also measure neutral gas. These two channels are never used at the same time owing to power, data rate, and DPU data compression considerations. When cometary neutral gas enters, it is ionized by one of the ion sources. The charged particles are extracted towards the drift tube at a frequency of 2 kHz, 5 kHz, or 10 kHz. These particles finally reach a detector, which records the time of flight of each molecule that is proportional to the square root of the mass of the species. In this paper, the RTOF data discussed are signatures of volatiles detected with the SS M0521 and OS M0524 mode (see Table 1).

A typical spectrum recorded in SS mode is shown in Fig. 1 with H_2O (mass 18.01 u/e), CO (mass 27.99 u/e), and CO_2 (mass 43.98 u/e).

Analysis of the data was performed with the Spectra Analyser software developed and provided by S. Gasc for mass scaling, peaks fitting, and temporal evolution analysing. Using GCU mode, a defined quantity of a gas mixture is introduced into the ion source that can be used to calibrate the time-of-flight spectra into mass to charge scale. The fitting method, which is based on a pseudo-Voigt function, takes background, offset, and electronic noise into account. This method gives us a molecule abundance per 200 or 400 s for each mass depending on the mode. We then convert abundance [counts/s] into density [cm^{-3}]. The method used is explained in Gasc et al. (2017). The CO_2/H_2O and CO/H_2O ratios are calculated for each spectrum provided by RTOF.

The DFMS is a high mass resolution ($m/\Delta m = 3000$ at 1% level) and high sensitivity mass spectrometer with a mass range of 1–150 amu that is designed to measure the composition of the cometary neutral gas and cometary ions (Balsiger et al. 2007). The gas is first ionized in the instrument by electron impact. The mass analyser is a combination of a 90 deg deflection electrostatic analyser and a 60 deg deflection magnetic analyser. A mass scan is achieved mass-by-mass by varying the sensor potentials. The integration time per mass is 20 s, leading to a lower temporal resolution for each species than for RTOF (e.g. about 40 min for H_2O).

The COPS instrument consists of two separate sensors, i.e. the nude gauge (NG) and the ram gauge (RG). The NG measures in situ the total ambient neutral number density (with no separation between the species), whereas the RG measures the ram pressure of the expanding cometary atmosphere.

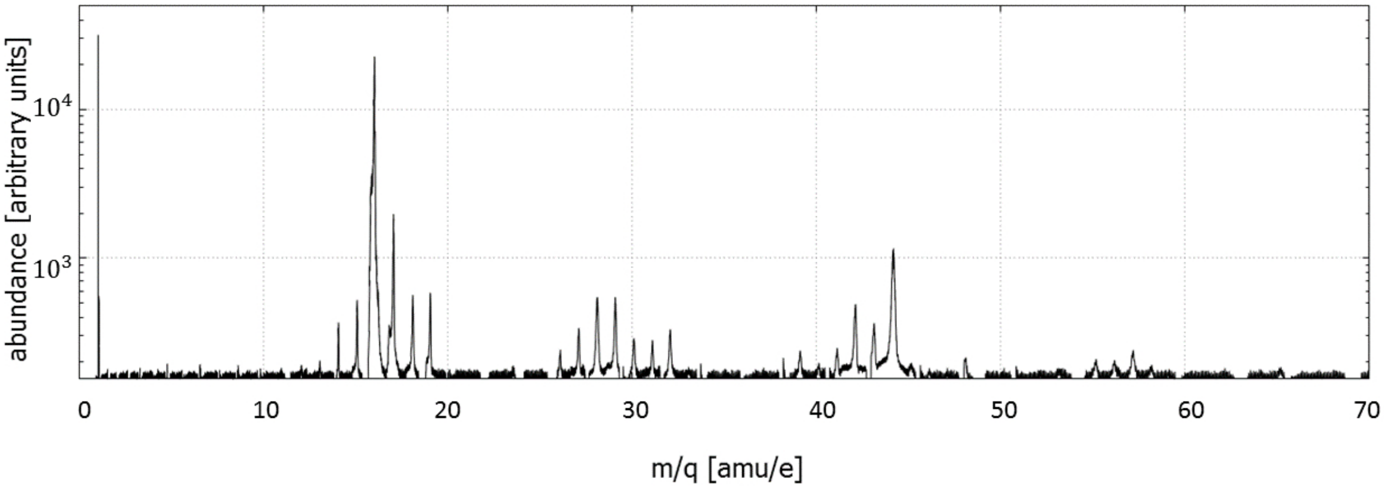

Fig. 1. Typical RTOF spectrum recorded in storage source (SS) mode showing H_2O (mass 18.01 u/e), CO (mass 27.99 u/e), CO_2 (mass 43.98 u/e), and their fragments.

In this paper, we used COPS nude gauge data, which were calibrated using the following processes. First, we removed the background density (1.2×10^6 cm^{-3}, which corresponds to 5×10^{-11} mbar at 293 Kelvin). Second, sharp neutral density peaks are seen by COPS when thrusters are fired during spacecraft maneuvers or wheel off-loadings or when the spacecraft changes orientation, where cold parts of the spacecraft previously in shadow may get illuminated by the Sun. Thus, COPS nude gauge data acquired during a maneuver or when the nadir off-pointing angle is greater than 5 deg are ignored. Lastly, a correction is applied of COPS neutral density to the sensitivity of different gas species using relative abundances from either RTOF or DFMS.

To compare RTOF and DFMS data, we have to take into account the specific sensitivity and fragmentation pattern of each species and mode, which are different for both instruments.

Densities of H_2O, CO_2, and CO are calculated via the equations below, which derive the relative abundances from the mass spectrometers and scale the results to the COPS total densities (Gasc et al. 2017), as follows:

$$n_{H_2O} = \frac{n_{COPS}}{\left(\frac{1}{\beta_{H_2O}} + \frac{r_{CO}}{\beta_{CO}} + \frac{r_{CO_2}}{\beta_{CO_2}}\right)}$$

$$n_{CO_2} = r_{CO_2}.n_{H_2O}$$

$$n_{CO} = r_{CO}.n_{H_2O},$$

where n_i are specific densities in [cm^{-3}], β_i are scale factors relative to N_2, and r_i are ratios of the densities relative to H_2O.

The CO_2/H_2O and CO/H_2O ratios needed to obtain the volatiles densities are defined as

$$r_{CO_2} = \frac{c_{CO_2}}{c_{H_2O}}.\frac{S_{H_2O}}{S_{CO_2}}.\frac{f_{H_2O\rightarrow H_2O}}{f_{CO_2\rightarrow CO_2}}$$

$$r_{CO} = \frac{c_{CO}}{c_{H_2O}}.\frac{S_{H_2O}}{S_{CO}}.\frac{f_{H_2O\rightarrow H_2O}}{f_{CO\rightarrow CO}} - r_{CO_2}.f_{CO_2\rightarrow CO},$$

where c_i is the number of detections within 200 or 400 s, S_i is the species; sensor and emission dependent sensitivity; and $f_{i\rightarrow j}$ is the relative fragmentation or isotopic ratio, where i is the parent and j one of the fragments

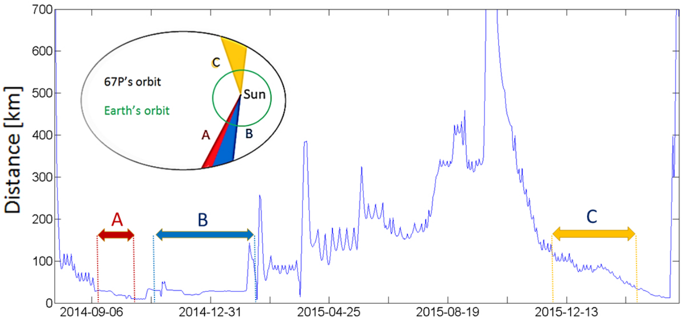

Fig. 2. Evolution of the distance between the spacecraft and 67P. Studied periods: period A, from 10 September to 30 October 2014; period B, from 1 November 2014 to 15 February 2015; and period C, from 1 December 2015 to 15 February 2016.

2.2. Description of the datasets

The data were analysed for three periods. During those periods, Rosetta observed almost the entire surface of the comet, whose rotation period is 12.4 h (Sierks et al. 2015) and covered heliocentric distances from 3.45 to 1.2 AU (see Fig. 2). The other periods could not be included in this study because of their low signal-to-noise ratio (essentially when the spacecraft was at large distances).

The first studied period started on 10 September 2014 and ended on 30 October 2014. The distance between Rosetta and 67P decreased from 30 km to 10 km and allowed a first close approach to the comet. During period A, the heliocentric distance decreased from 3.45 to 3.05 AU, and RTOF recorded almost 15 000 spectra in SS mode (2100 measurements for DFMS).

The second period followed the first closely. It started on 1 November 2014 and ended on 1 February 2015. During this period, the sublimation of water highly increased and became strong in places where the solar irradiation heated the cometary surface sufficiently. At the beginning of this period, the heliocentric distance was 3.05 AU and the estimated production rate was 2×10^5 kg per day. It reached 7×10^5 kg per day at the end of the period, around 2.4 AU (Hansen et al. 2016). The data from the second period were taken in OS mode. The spacecraft orbited the comet at an altitude of about 20 km during the majority of this period except in mid-November 2014 with a fly-by at 16 km

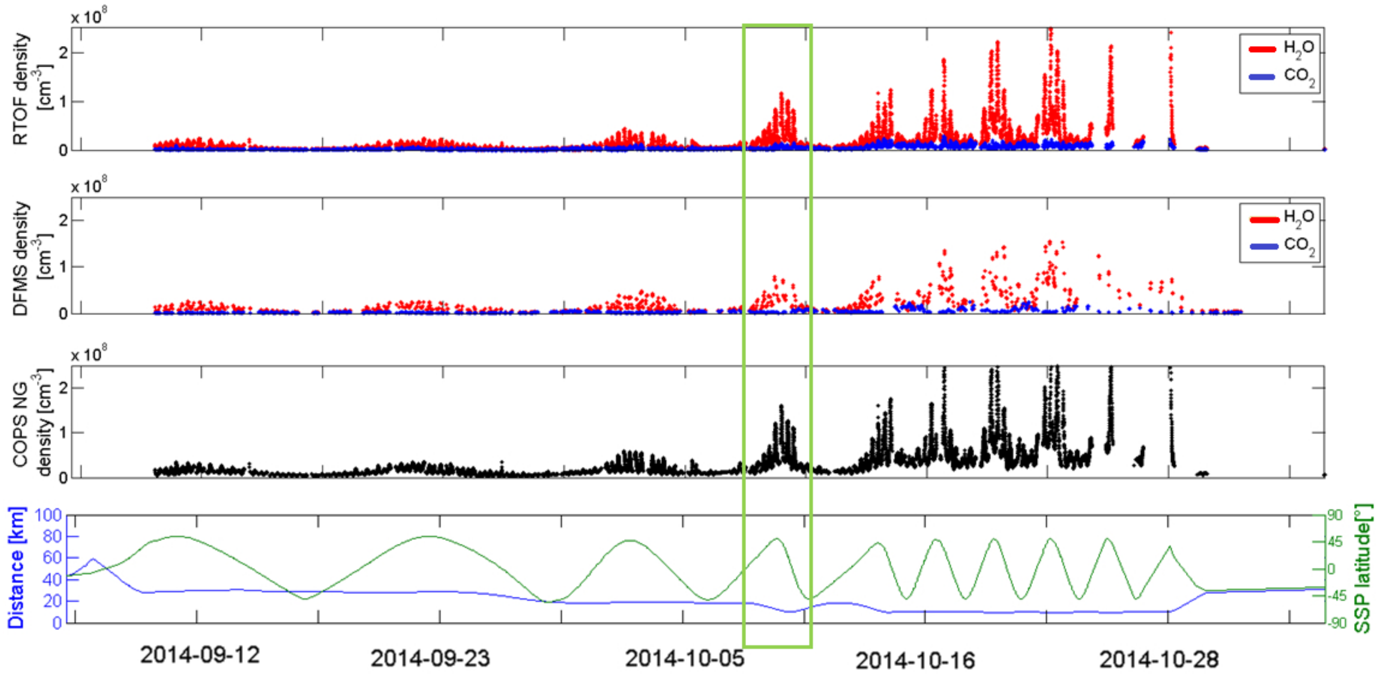

Fig. 3. Measured densities for H_2O (in red) and CO_2 (in blue) by RTOF (*upper panel*) and DFMS (*second panel*) for period A. *Third panel*: COPS total density from the nude gauge. The *lower panel* provides the variation of the distance between the comet and the spacecraft in blue and the variation of the sub-satellite point latitude in green. A zoom of the green rectangle area is shown in the next figure.

for Philae's landing. The phase angle, i.e. the angle between the spacecraft and Sun directions from the centre of the comet, was also roughly stable near 90°.

The third studied period occurred after first equinox (10 May 2015) started on 1 December 2015 (1.8 AU) and ended on 15 February 2016 (2.2 AU). The northern hemisphere (encountering summer during period A and B became the winter hemisphere and this changed the active regions considerably. During those months, the spacecraft slowly came closer to the comet from an initial distance of 100 kilometers to a distance of about 38 km in the end of period C.

3. Results

3.1. Temporal variation

The search for gas production heterogeneities at the nucleus surface is required to associate the coma measurements with source locations at the surface, assuming a radial outflow as a first step. Owing to the irregular shape of 67P, the flow is not radial very close to the nucleus, but the flow becomes closer to a straight line as the gas expands away from the nucleus (see Fig. A.1). The field of view is 10° × 40° for RTOF and 20° × 20° for DFMS. We thus associated each detection with the corresponding sub-satellite point (SSP) in latitude and longitude in a frame centred on and rotating with the comet. Latitude 0° separates the comet in two hemispheres and when the spacecraft points to the extremity of the head of the comet, the SSP position corresponds to (0°, 0°). In this section, we describe the temporal variability of the main volatiles densities and progressively discuss the various parameters of influence.

3.1.1. Period A

The first period is used to study the RTOF and DFMS temporal variations for H_2O, CO, and CO_2 and compare the total density with COPS measurements. We then highlight the influence of different parameters (distance to comet and sub-satellite latitude and longitude).

Once the density of the main volatiles is deduced from the spectra, we can visualize the temporal evolution as in Fig. 3. All the spectra show a clear signature of H_2O, CO_2, and CO. In RTOF spectra, the H_2O peak is almost always higher than the CO_2 and CO peaks. CO detections are not visible in the RTOF panel; they are very close to CO_2 detections during period A (see Fig. 4). Nevertheless, CO_2 may exceed the H_2O detection, in particular, in the southern hemisphere (see Sect. 3.2 along with the early results by Mall et al. 2016; and Hässig et al. 2015). The COPS data, in the middle panel, show the global variation of the total gas density that reaches the spacecraft.

The global periodic pattern is well known on 67P with a clear and strong diurnal variation. H_2O densities in particular followed closely the variation of the sub-satellite point latitude. The northern hemisphere was well illuminated during this period and this led to enhanced sublimation for positive latitude regions. The diurnal variation seen in RTOF and DFMS data is well confirmed by COPS. The difference of temporal resolution can be seen in the set of data of the two spectrometers: DFMS recorded less data. The maxima of periodic variations appeared lower than in the RTOF panel.

As Rosetta came closer to the comet, the ROSINA instruments recorded a progressive increase of density with a maximum when the spacecraft reached 10 kilometers.

The variation of the sub-satellite point longitude also impacted the detection of volatiles, as found in the high frequency variations, shown in Fig. 4. For one comet rotation, we observe for H_2O two minima (1 and 3 on upper panel) and two maxima (2 and 4) directly correlated with the longitude variations and the geometrical asymmetry of 67P. The CO_2 and CO observations showed more complex density variations with detections in both hemispheres and less clear asymmetries (see also Hässig et al. 2015), as discussed further in Sect. 3. A

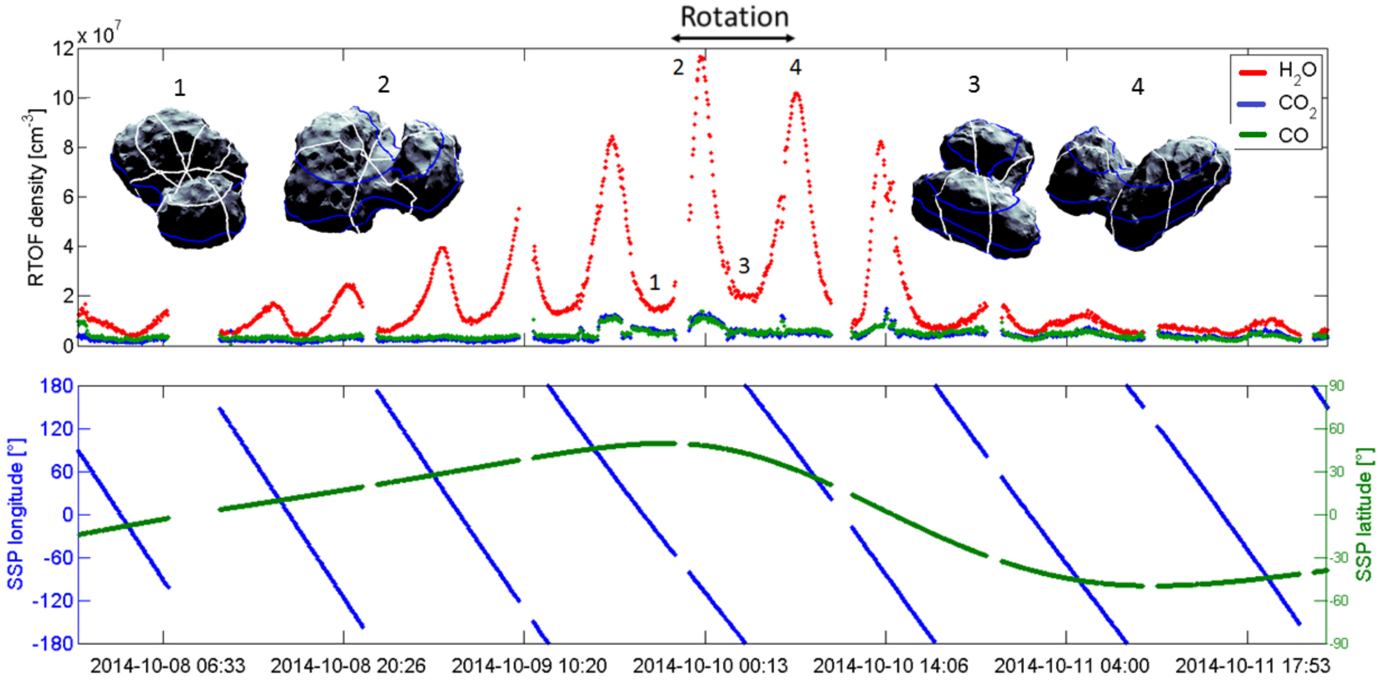

Fig. 4. Diurnal variation of main volatiles. *Upper panel*: zoom of upper panel of Fig. 3 from 8 October to 11 October with the view of the comet from the spacecraft at specific times. *Lower panel*: sub-satellite point longitude and latitude variations during the same period.

Lomb-Scargle periodogram (not shown) was applied to H_2O data to highlight periodic signals on a statistical basis and confirmed the presence of strong periodicities of about 6 and 12 h. These periodic variations are linked to the geometry of the nucleus. When SSP $= (90°, 0°)$, the spacecraft sees a large illuminated area that includes the active neck region. Since the rotation period of 67P was about 12.4 h at that time in the mission, this induces a half-diurnal variation for coma measurements with high detections each time the spacecraft is above the neck, i.e. approximately every 6.2 h. Lomb-Scargle periodograms applied to CO_2 and CO data showed a more homogeneous behaviour with a smaller 12 h periodicity; this confirmed that carbon dioxide and monoxide are more uniformly distributed than water in the top layer of the comet, as we can also see through the analysis of short time periods, following the results of Hässig et al. (2015). This behaviour of the main volatiles is in agreement with the common assumption that CO_2 and CO originates from deeper layers than H_2O (De Sanctis et al. 2010; Prialnik et al. 2004). This can be interpreted as the water sublimation is occurring from the shallow subsurface, which is very sensitive to diurnal temperature variations, while CO_2 and CO sublimate from deeper layers inside the comet that are also influenced by a seasonal effect due to obliquity in agreement with thermodynamic models of the cometary subsurface (Huebner et al. 2006; De Sanctis et al. 2010).

A similar behaviour was detected by the Deep Impact spacecraft at comet 103P/Hartley 2, where the water release was mostly originating from the illuminated part of the nucleus (A'Hearn et al. 2011).

3.1.2. Period B

In Fig. 5, we show the temporal variation of H_2O, in red, and CO_2, in blue, obtained with the period B spectra.

Beyond the sources of variability discussed above, the composition and dynamics of the coma as measured by ROSINA also depend on parameters such as the phase angle and nadir off-pointing. The phase angle was mostly constant near 90°, except at two times (start and end of period B) when it dropped significantly, leading to enhanced densities as expected (for a solar driven outgassing). Most of the variations observed in the nadir off-pointing are due to unavoidable spacecraft maneuvers that are necessary for navigation purposes or requested by other scanning instruments, such as ALICE or VIRTIS. We therefore applied a data filtering to ignore the detections when the amplitude of a slew exceeds 5°, considering that the instruments are not pointing to the comet anymore.

The second panel of Fig. 5 shows the H_2O and CO_2 densities derived from the DSMC model detailed in Bieler et al. (2015) and Fougere et al. (2016). For a given illumination, this model reproduces the collisions and trajectories of the particles from the surface to the spacecraft (including a heterogeneous activity map; see Fougere et al. 2016), allowing us to link the surface processes and the in situ reference data recorded by ROSINA. The DSMC model was successfully compared with both COPS and DFMS data. It is now also clear that it can correctly reproduce the RTOF in situ measurements (up to perihelion at least). A more detailed analysis reveals that the DSMC model reproduces well the RTOF H_2O and CO_2 variabilities except during period A (see Fig. A.2), where the DSMC model underestimates/overestimates the CO_2 density in the northern/southern hemisphere. The data are less correlated during Period A since DSMC model needs large periods of time to retrieve activity maps and CO_2 active areas may be unstable (Filaccione et al. 2016; see also the evolution of our maps from period A to B). For Period B, the ratio between the DSMC model and RTOF H_2O and CO_2 is stable around one, corresponding to a good agreement for both species.

Except during the first 15 days of November 2014, with the approach and landing of Philae, the density of H_2O accurately followed the variation of the sub-satellite point latitude. As during period A, higher water densities were measured when

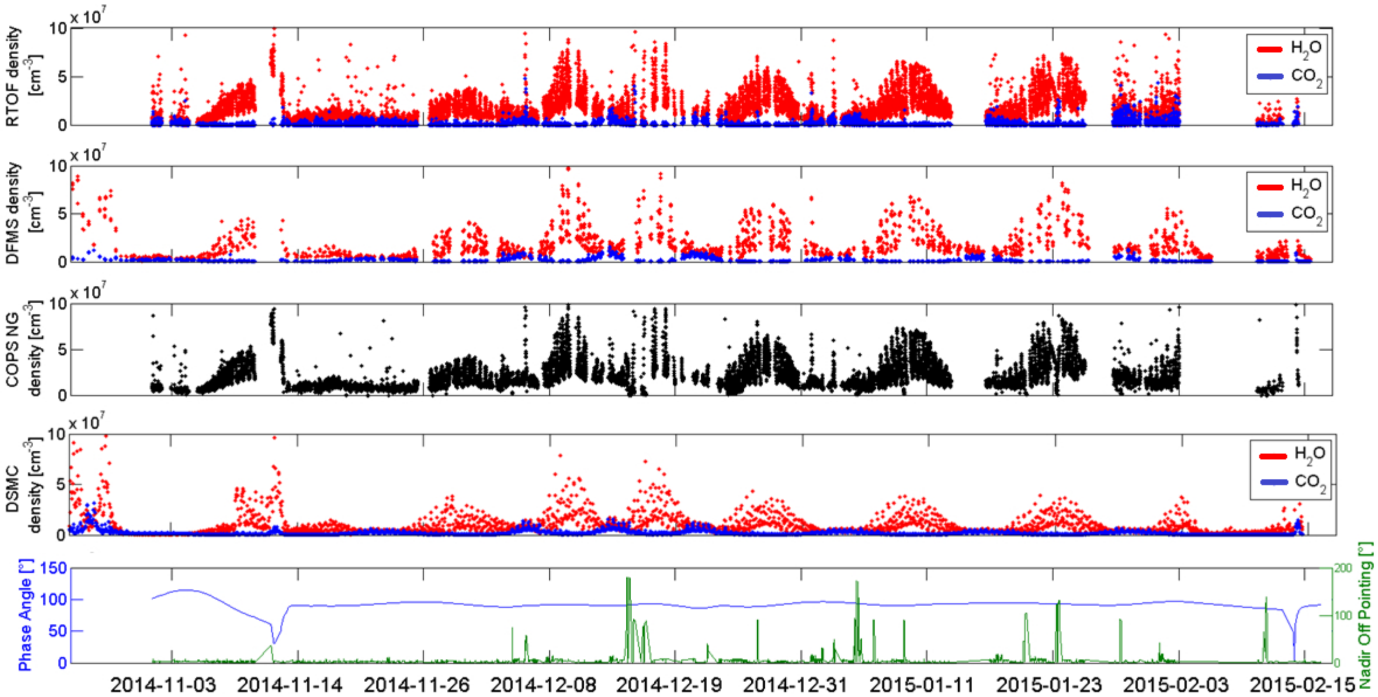

Fig. 5. Temporal evolution of H_2O and CO_2 densities detected by RTOF (*upper panel*) and DFMS (*second panel*) during period B. *Third panel*: COPS nude gauge total densities. *Fourth panel*: H_2O and CO_2 densities derived from the DSMC model (Bieler et al. 2015; Fougere et al. 2016). *Lower panel*: phase-angle variations in blue and nadir off-pointing angle variations in green.

the instrument was above the neck region in the northern hemisphere.

The largest CO_2 and CO densities correspond here to negative latitudes (southern hemisphere), whereas the situation was more complex during period A in which CO_2 and CO were also detected in the northern hemisphere (see Sect. 3.2 for detailed maps). As seen around 5 December 2014, 13 December 2014, and 3 January 2015 (Fig. 5; panels 1, 2 and 3), maximum CO_2 measurements appeared at minimum H_2O detections.

Figure 6 provides the temporal variations of CO/H_2O and CO_2/H_2O ratios from RTOF and DFMS compared with the latitude of the sub-satellite point. The correlation between the RTOF and DFMS ratios is very good, despite a significant dispersion of RTOF values partially due to the higher time resolution of RTOF; also, the anti-correlation between the ratio evolution and the variation of latitude during period B. CO and CO_2 were essentially detected from the southern hemisphere (see also Sect. 3.2).

3.1.3. Period C

The RTOF switched between SS and OS modes regularly during period C. We studied 6300 SS spectra to plot the evolution of H_2O, CO, and CO_2 in the upper panel of Fig. 7 and the corresponding DFMS and COPS densities, which are well correlated with RTOF data when both datasets are available.

In period A and B, CO and CO_2 variations were roughly anti-correlated with H_2O, meaning that they originated from different hemispheres on the comet. In this third period, CO and CO_2 variations followed the H_2O variations and seemed to be concentrated in the southern hemisphere. The total density variation also appears to be anti-correlated with the SSP latitude. As 67P passed the inbound equinox (May 2015), the illumination crossed the equator and moved to the southern hemisphere. After his first equinox, the maximum of sublimation came from negative latitudes. These observations are in agreement with the results from VIRTIS-H observations (Bockelée-Morvan et al. 2016) and from modelling (Fougere et al. 2016).

We studied the evolution of the CO_2/H_2O and CO/H_2O density ratios from RTOF and DFMS as a function of the distance to the Sun. The average trends from in situ measurements (with a more significant dispersion for the RTOF data) show a decrease in the ratios with decreasing distance to the Sun due to an enhanced H_2O outgassing at closer distances to the Sun; this is in agreement with the Snodgrass et al. (2013) predictions of outgassing rates ratios.

3.2. Spatial variation

As demonstrated above, the temporal variations observed by Rosetta are induced by the combination of different parameters, i.e. mostly the distance to the comet, the spatial variations (related to either illumination or longitude/latitude), and the distance to the Sun that plays a role in long timescales. In this section, we specifically study the spatial variations. Consequently, we first need to eliminate the influence of the distance between the spacecraft and the comet: we normalized all the densities from RTOF and DFMS to expected densities at 10 km from the nucleus. Assuming that the comet is a point source with no significant loss process at such small distances, we use a $1/r^2$ law to estimate the normalized densities.

This power law approximation was first confirmed by Hässig et al. (2015) and we were able to verify this approximation based on the COPS density measurements obtained after the 15 February 2015 fly-by (with an altitude running from 8 to 242 km in only three days), which led to a power-law statistical fit with a slope in between –1.8 and –1.9.

After removing most of the influence of the distance to the comet, the major source of variability is obviously the spatial variation due to the illumination by the Sun (and the induced sublimation process). The solar illumination is however not the

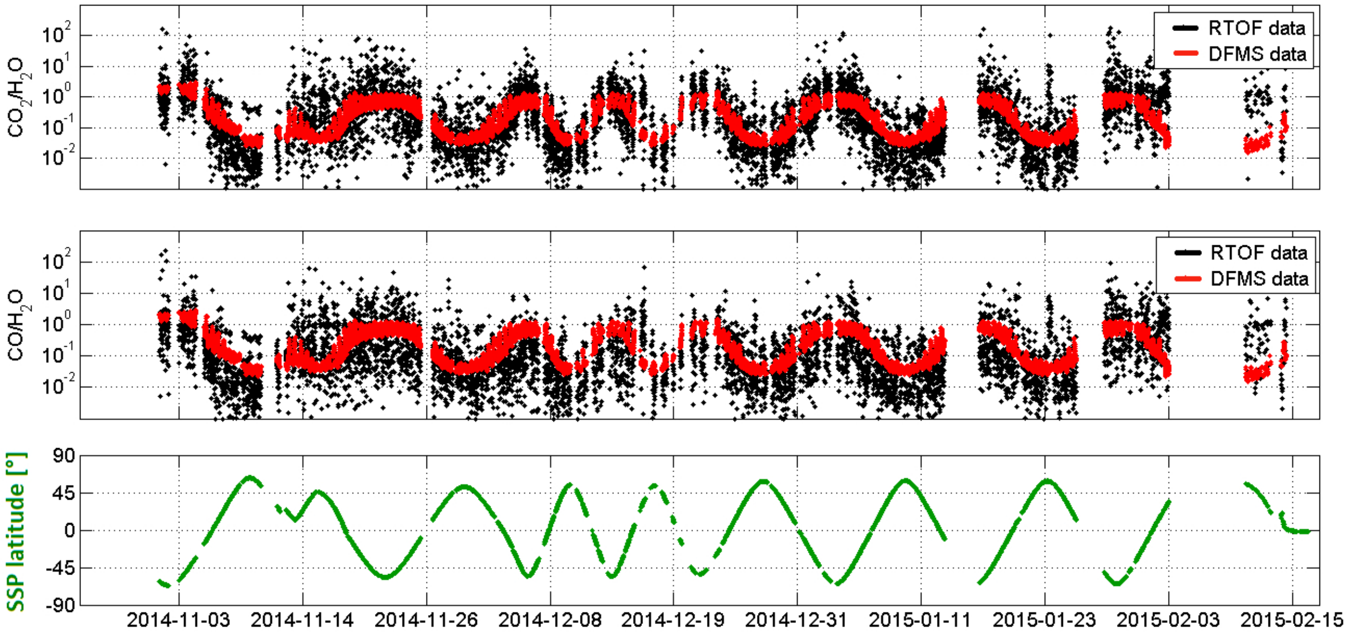

Fig. 6. CO_2/H_2O and CO/H_2O ratios from RTOF and DFMS compared with the latitude of the sub-satellite point (SSP) during period B.

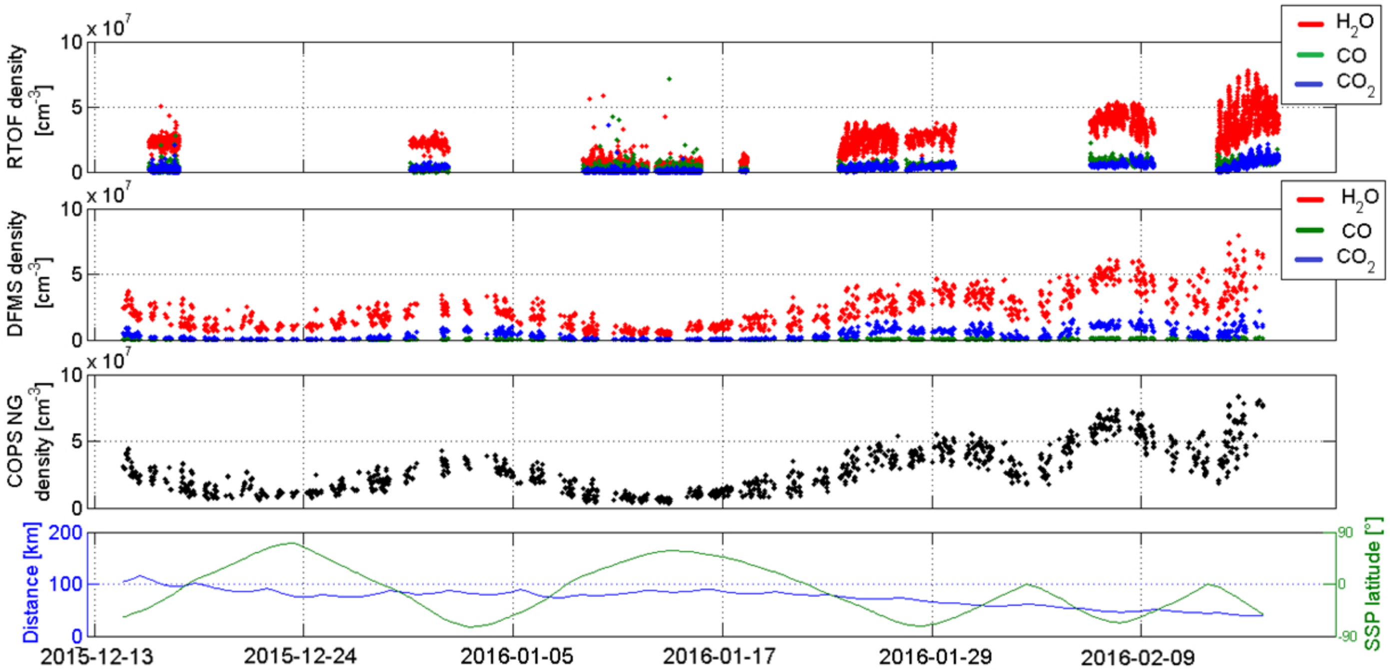

Fig. 7. Period C ROSINA data and orbitography. *Upper panel*: RTOF densities for H_2O (in red), CO (in green), and CO_2 (in blue). *Second panel*: DFMS specific densities for H_2O (in red), CO (in green), and CO_2 (in blue). *Third panel*, COPS NG total densities. *Lower panel*: variation of distance between comet and spacecraft (in blue) and variation of sub-satellite point latitude (in green).

only origin of spatial heterogeneities in the coma, there are also clear heterogeneities related to particular geographic regions (as mentioned for mostly pre-perihelion coma measurements in several studies; see Sect. 1).

To investigate the spatial heterogeneities at the surface of the comet, we created density maps using the density values normalized at 10 km distance and assuming that the recorded signal originates from the sub-spacecraft point. These maps are shown in the six lower panels in Fig. 8, showing the RTOF densities of $H_2O/CO_2/CO$ during the periods A/B/C. These are 2D maps in longitude/latitude with facets of 5 × 5 deg. The centre of each map represents the extremity of the head lobe, whereas the sides (+ or −180 deg) correspond to the Imhotep region on the big lobe. The correspondence between the morphological regions introduced by El-Maarry et al. (2015) and this 2D mapping is shown in Fig. A.3. Since most of the facets have been observed several times, each value associated with a facet is a mean value. Facets with less than 5 data points associated are coloured in white.

We use the SSP coordinates to project each RTOF measurement on the surface of the comet. We thus assume that the source region is located at the SSP. This is an important and simplifying

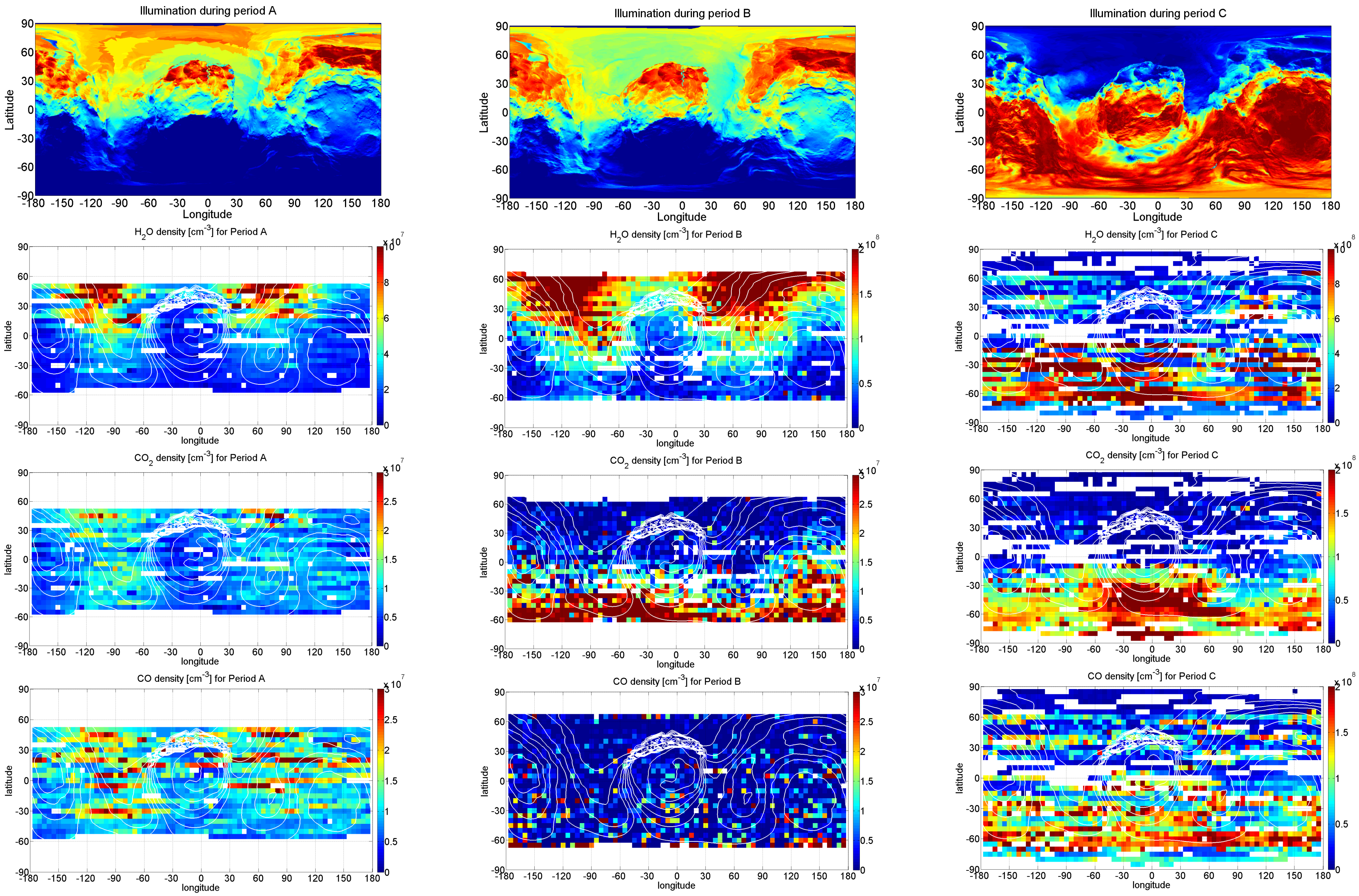

Fig. 8. Maps of illumination and densities. *Upper panels*: *left*, *middle*, and *right* figures represent 2D longitude/latitude maps of average illumination during periods A/B/C. The corresponding 2D maps of H_2O, CO_2, and CO densities in cm^{-3} measured by RTOF (*the second, third and fourth rows*, respectively) normalized at 10 km with a 1/r^2 scaling law, projected to the SSP longitude and latitude. The latitude 0 separates northern and southern hemispheres and topography lines;white contour lines in the maps are added on the maps based on the 3D shape model provided by ESA/Rosetta/MPS for OSIRIS Team MPS/UPD/LAM/IAA/SSO/INTA/UPM/DASP/IDA.

assumption; since the comet shape is complex, the spacecraft is far from the comet, the comet is fully inside the RTOF field of view, and the outflow is not purely radial from the surface. Nevertheless, those steps allow us to understand the link between the main heterogeneities in the coma and the comet surface.

To study the correlation between solar illumination and outgassing, we produced three maps of illumination, corresponding to periods A, B, and C, based on an illumation code developed for 67P (by D. Toublanc, A. Beth). The normalized intensity of the colour (maxima in red, minima in blue) at every illuminated facet is given by the cosine of the angle between the surface normal and the direction to the Sun (average over one rotation period with mean latitude conditions appropriate to each period considered). The illumination maps of periods A and B are almost identical with the illuminated regions in the northern (summer) hemisphere, mostly the Set, Ash, Ma'at, and Hapi regions, extending towards slightly lower latitudes during the period B closer to equinox (with a larger total flux not seen because of the normalization). During period C, the southern (summer) hemisphere becomes strongly illuminated, except just below the head of the comet (Sobek region) that was in shadow.

During the three periods, the influence of illumination is clearly responsible for the H_2O behaviour with a strong correlation between illuminated and active regions except for the small lobe of the comet, where fewer H_2O detections are obtained. The H_2O maps for periods A and B (upper left panels of Fig. 8) reveal an obvious and coherent inhomogeneous production. The production was very localized in the northern summer hemisphere around the neck zone with a maximum at the highest latitudes, where RTOF sometimes detected hundreds of counts per second. The illuminated neck zone thus appears responsible for the most important outgassing of water, as previously observed by several instruments (Biver et al. 2015; Hässig et al. 2015; Vincent et al. 2015). According to the analysis presented in Fig. 8, H_2O essentially originates from the Babi, Hapi, and Seth regions (see Fig. A.3).

In the second period, the maps reveal an active northern hemisphere with wider source regions for water as the comet further approaches the Sun. H_2O is predominant in the northern hemisphere before perihelion and was expected to be detected in the southern hemisphere after equinox in early May 2015, as shown and confirmed in the H_2O map for period C.

The CO_2 map from period A shows that CO_2 detections were less abundant and more diffuse than water detections. CO also appeared less localized and showed a similar behaviour to CO_2. Both species were detected above both hemispheres, mostly above the neck region and above regions close to the head (Anubis, Anuket) or to the body (Babi, Aker, Khepri) as well as from the Imhotep region.

During period B, the CO_2 densities increased and appeared more localized. Most of the detections were obtained in the southern hemisphere (essentially below 30 deg latitude south, except for the Imhotep large source region), which was the less illuminated part of the comet during the studied period. The CO outgassing was even more diffuse than CO_2 with the largest values in the southern hemisphere as well.

During period C, in which the illumination was maximum in the southern hemisphere, CO_2 and CO kept approximately the same behaviour as during period B with maximum detections in the southern hemisphere. The source regions appeared diffuse (all the more for CO) with the largest sources located below the head of the comet and below the Imhotep region. We also investigated the ratios CO_2/H_2O and CO/H_2O, which are important for understanding the coma and nucleus heterogeneities.

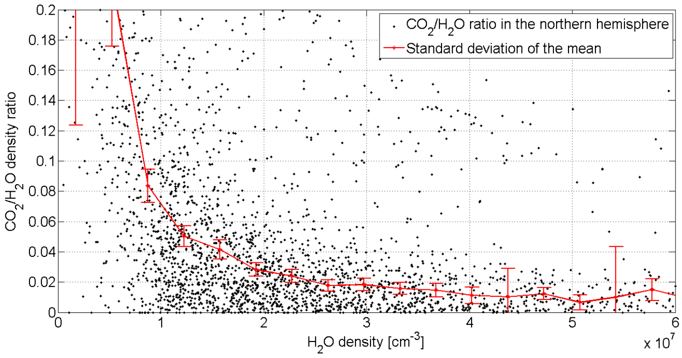

Fig. 9. CO_2/H_2O density ratio from RTOF as a function of H_2O density from 24 November 2014 to 24 January 2015. This figure is compared with the similar analysis in Fig. 11 of Bockelée-Morvan et al. (2015),which is also shown in Fig. A.1.

Overall H_2O is dominant compared to CO_2 and CO, but ratios above unity were often seen, for example in the southern hemisphere during the northern summer season. Figure 9 shows the CO_2/H_2O density ratio as a function of H_2O density from RTOF, which can be compared with the same ratio (as a function of column density) as seen by the Visible InfraRed Thermal Imaging Spectrometer (VIRTIS; see Fig. A.4, taken from Bockelée-Morvan et al. 2015) during the exact same period. Despite the different techniques and instruments (in situ versus remote sensing), the results are strikingly similar with a clear anticorrelation between the CO_2/H_2O ratio and H_2O density or column density – in agreement with the previous conclusions on the period B – down to a minimum value of 0.01–0.02 in the northern hemisphere. We also observe some CO_2 coming from both illuminated and non-illuminated parts of the nucleus, as mentioned by Bockelée-Morvan et al. (2015).

Figure 10 provides the CO_2/H_2O and CO/H_2O ratios during period B from both RTOF and DFMS in a 2D mapping similar to Fig. 8. This allows us to both investigate the ratios above specific regions of 67P (beyond the comparisons between hemispheres previously discussed) and compare the results obtained by the two ROSINA spectrometers. The two spectrometers produce very similar maps for both CO_2 and CO ratios with a much larger number of points per cell (factor 7) for RTOF owing to the very different time resolution between the instruments. Overall, the highest ratios seen by both instruments were very localized in the southern hemisphere. More precisely, the CO/H_2O ratio was highest (>0.3–0.4) in the Imhotep, Khonsu, Wosret, Neith, and Sobek regions, whereas the CO_2/H_2O was highest (>0.5) in the same regions as CO/H_2O but also in the whole latitude band [–60° –30°] (with parts of the Anhur, Bes, Atum, and Geb regions). The data do not allow us to provide conclusions on the regions below –60° latitude. The CO/H_2O ratio appeared both overall more homogeneous and with the highest detections more confined to the southern parts of the head and body of the comet, whereas CO_2 was strongly confined to and spread over the southern hemisphere in agreement with the previous conclusions on the density maps of both species and the illumination conditions of period B. Beyond period B, the CO and CO_2 ratios decreased on average while getting closer to the Sun because of an increased water outgassing. Moreover, the mapping of ratios during period C (not shown) shows a much more homogeneous distribution, in agreement with the illumination of the southern hemisphere, which leads to the highest measured densities in all three species in the same hemisphere.

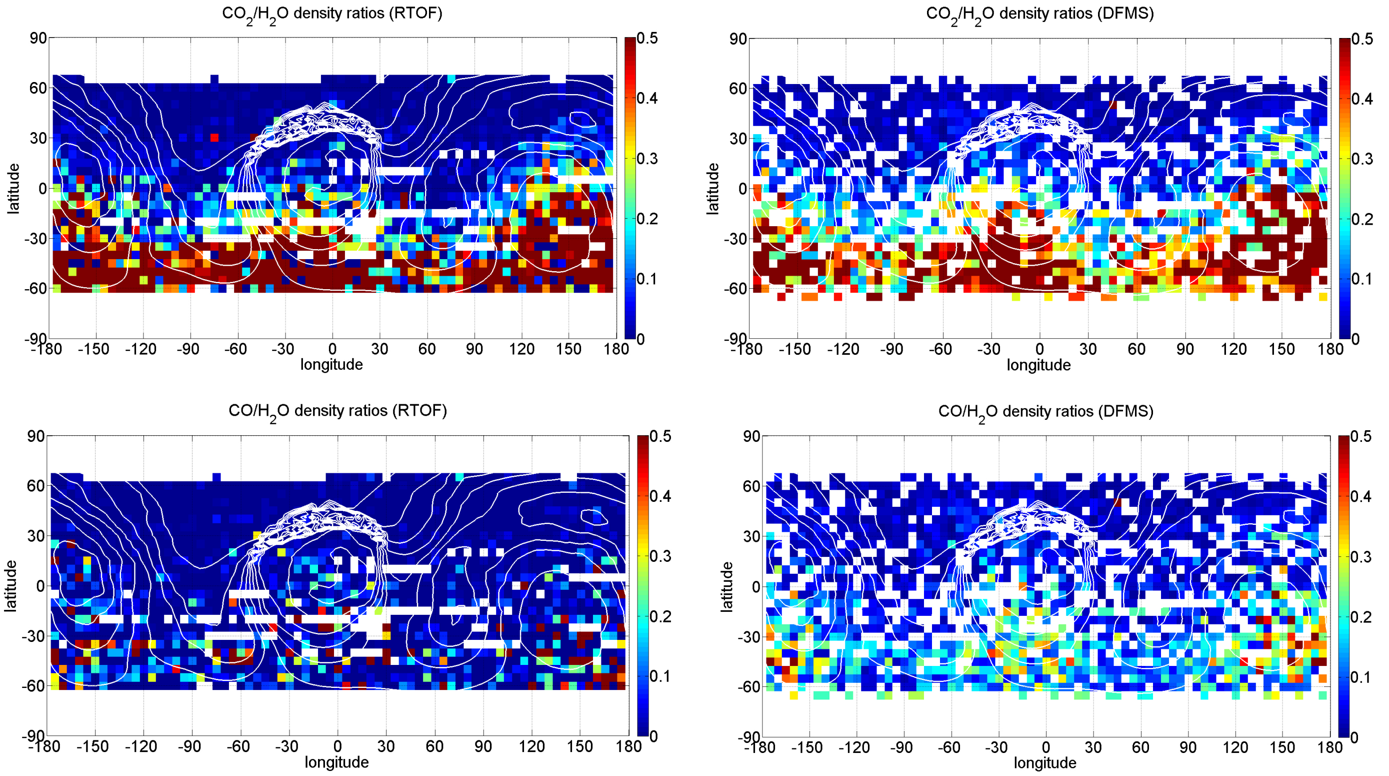

Fig. 10. Two-dimensional maps of CO_2/H_2O (*upper panels*) and CO/H_2O (*lower panels*) density ratios based on RTOF (*left*) and DFMS (*right*) data for period B.

3.2.1. Discussion

The observations about the respective production regions of H_2O, CO_2, and CO among the three periods are roughly in agreement with an illumination driven outgassing of the main volatiles. In particular, the observations during the periods A and B are in agreement with an illuminated northern hemisphere at 150–200 K allowing for increased H_2O outgassing. This agrees with the conclusions provided by the VIRTIS team (Capaccioni et al. 2015), who obtained an illuminated surface temperature from 180 to 230 K, and the MIRO team, who determined a subsurface temperature of 160–180 K (Gulkis et al. 2015). The neck region was however by far the most active part of the northern hemisphere for H_2O, as known from earlier measurements (Luspay-Kuti et al. 2015; Lee et al. 2015). This region contains a large number of active pits (Vincent et al. 2015) and cliffs (Vincent et al. 2016), which combined with the higher temperature gradients (Alí-Lagoa et al. 2015), made it the most active region when illuminated during summer on the northern hemisphere. Another interpretation could also be that ejected icy grains were redeposited on the neck (owing to its gravitational well) and covered the northern hemisphere after the active period of the previous perihelion. We may add that H_2O detections were almost absent above the northern part of the head (Ma'at region) despite strong illumination conditions. These conditions may be due to the dust coverage of this region (El-Maarry et al. 2015) with dust depleted in water ice, where the wet ice extracted from the southern hemisphere is preferentially deposited on the gravitational well of the neck region.

However, the CO_2 density was surprisingly low in the illuminated northern hemisphere during period B (many months before equinox), even if the surface temperature was sufficient to sublimate CO_2. This observation could be explained by the strong dichotomy between northern and southern surface features (El-Maarry et al. 2015): a thick dust layer could have been deposited from the last perihelion passage. During the short and intense southern summer, the ejected dust particles carried water ice towards the north. Such a dust layer would prevent the heat from penetrating deep enough to sublimate CO_2. However, it is not clear whether this interpretation can account for the change in CO_2 outgassing behaviour from period A to period B. The transition from period A, which still has significant CO_2 outgassing in the northern hemisphere (neck region), to period B, where it is essentially confined to the southern hemisphere, is even more visible when CO_2 density maps are analysed every month; there is a clear change around October and November 2014. The evolution of the dichotomy does not seem to be linked with orbitography variations: the distance was roughly stable with a slight increase during period B and the phase angle remained stabilized around 100 deg. An alternative interpretation for the low CO_2 and CO outgassing in the northern hemisphere before equinox (periods A and mostly B) could be related to the long summer period during which the northern hemisphere was illuminated. Far from the Sun, the temperature in the northern hemisphere may become sufficiently high to sublimate CO_2 but not H_2O (the sublimation ice lines of H_2O and CO_2 being approximately located at 2.6 AU and 20 AU, respectively), thus emptying the CO_2 reservoirs of the uppermost layers, whereas the southern hemisphere remains too cold to induce a significant sublimation of CO_2.

The diurnal skin depth and orbital skin depth of 67P are about a few centimeters and a few meters (Huebner et al. 2006), respectively. The H_2O measured in the coma thus originates from the first centimeters below the surface of the comet, while CO_2 probably originates from layers located at a few meters maximum below the surface to allow for sufficient seasonal driven heating, and probably at a few centimeters minimum to prevent a pure diurnal variability such as for H_2O. The same conclusions apply for CO and CO_2; CO, whose measurement interpretation is less easy owing to noise, has an even smaller diurnal variability, suggesting deeper sources in agreement with thermal models of comet nuclei.

4. Conclusions

We provide an analysis of the coma of comet 67P/Churyumov-Gerasimenko based on the ROSINA data from three periods between September 2014 and February 2016.

The influence of different parameters, such as illumination, distance spacecraft/comet, distance comet/Sun, sub-satellite point, nadir off-pointing angle, local time, and phase angle, on the outgassing detected by ROSINA was individually analysed and interpreted. As expected, the shape, attitude, and orbit directly impacts the sublimation of volatiles at the surface of the comet. Our observations reveal a strong difference of behaviour for the three main volatiles.

The analysis of RTOF data first confirms that outgassing of the main volatiles (water, carbon dioxide, and carbon monoxide) shows strong latitudinal and diurnal (longitude) variations. The H_2O density was measured maximum above strongly illuminated areas (except the small lobe) including the active neck region before May 2015 equinox and moving slowly to the southern hemisphere after. The CO_2 outgassing was in general smaller than for H_2O and was confined to the southern hemisphere (except before November 2014, where CO_2 and CO were detected above both hemispheres). The absence of CO_2 detection from the northern winter hemisphere early before the May 2015 equinox, despite a surface and subsurface temperature large enough to sublimate CO_2, suggests the presence of an icy dust layer covering the northern regions deposited after the previous perihelion, thus preventing the heat from reaching the CO_2 rich layers. This icy dust layer mainly contains water transported by the dust particles ejected from the southern hemisphere, leading to strong water outgassing during the northern summer hemisphere. Our observations (of CO_2 and, mostly, CO being more homogeneous than H_2O) are consistent with the assumption that CO_2 and CO originate from deeper layers than H_2O. Their sublimation is influenced by seasonal, diurnal, and surface heterogeneities effects.

Our study provides the first global comparison between the data recorded by the three instruments of ROSINA: DFMS, RTOF, and COPS. The comparison between those in situ data and the DSMC modelling reveals a very good correlation and understanding of the global behaviour of the main volatiles.

We analysed spectra during a large period of time, allowing the analysis of the relative dynamics of the three main volatiles and the displacement of the active regions for each species, especially after crossing the ice line and the May 2015 equinox. From our work, we conclude that the observed dynamic results from a complex combination of seasonal, diurnal, and surface heterogeneity effects.

Acknowledgements. The authors thank the following institutions and agencies, which supported this work: Work at IRAP was supported by the French space agency CNES. Work at the University of Bern was funded by the State of Bern, the Swiss National Science Foundation, and the European Space Agency PRODEX Programme. Work at the Max Planck Institute for Solar System Research was funded by the Max-Planck Society and Bundesministerium für Wirtschaft und Energie under contract 50QP1302. Work at the Southwest Research Institute was funded by NASA JPL. The results from ROSINA would not be possible without the work of the many engineers, technicians, and scientists involved in the mission, the Rosetta spacecraft, and the ROSINA instrument team over the past 20 yr, whose contributions are gratefully acknowledged. Rosetta is an European Space Agency (ESA) mission with contributions from its member states and NASA. We thank herewith the work of the whole ESA Rosetta team. All ROSINA flight data have been or will be released to the PSA archive of ESA and to the PDS archive of NASA.

References

A'Hearn, M. F., Belton, M. J., Delamere, W. A., et al. 2011, Science, 332, 1396
Alí-Lagoa, V., Delbo', M., & Libourel, G. 2015, ApJ, 810, L22
Balsiger, H., Altwegg, K., Bochsler, P., et al. 2007, Space Sci. Rev., 128, 745
Bieler, A., Altwegg, K., Balsiger, H., et al. 2015, A&A, 583, A7
Biver, N., Hofstadter, M., Gulkis, S., et al. 2015, A&A, 583, A3
Bockelée-Morvan, D., Debout, V., Erard, S., et al. 2015, A&A, 583, A6
Bockelée-Morvan, D., Crovisier, J., Erard, S., et al. 2016, MNRAS, 462, S170
Capaccioni, F., Coradini, A., Filacchione, G., et al. 2015, Science, 347, 0628
De Sanctis, M., Lasue, J., Capria, M., et al. 2010, Icarus, 207, 341
De Sanctis, M., Capaccioni, F., Ciarniello, M., et al. 2015, Nature, 525, 500
El-Maarry, M., Thomas, N., Giacomini, L., et al. 2015, A&A, 583, A26
El-Maarry, M. R., Thomas, N., Gracia-Berná, A., et al. 2016, A&A, 593, A110
Feldman, P. D., A'Hearn, M. F., Bertaux, J.-L., et al. 2015, A&A, 583, A8
Filacchione, G., Capaccioni, F., Ciarniello, M., et al. 2016, Icarus, 274, 334
Fougere, N., Altwegg, K., Berthelier, J.-J., et al. 2016, A&A, 588, A134
Gasc, S. 2015, Ph.D. Thesis, Universitaet Bern, Switzerland
Gasc, S., Altwegg, K., Jäckel, A., et al. 2017, Planet. Space Sci.
Gulkis, S., Allen, M., von Allmen, P., et al. 2015, Science, 347, 0709
Hansen, K. C., Altwegg, K., Berthelier, J.-J., et al. 2016, MNRAS, 2413
Hässig, M., Altwegg, K., Balsiger, H., et al. 2015, Science, 347, 0276
Huebner, W. F., Benkhoff, J., Capria, M.-T., et al. 2006, Heat and gas diffusion in comet nuclei (International Space Science Institute)
Lee, S., Von Allmen, P., Allen, M., et al. 2015, A&A, 583, A5
Luspay-Kuti, A., Hässig, M., Fuselier, S., et al. 2015, A&A, 583, A4
Mall, U., Altwegg, K., Balsiger, H., et al. 2016, ApJ, 819, 126
Prialnik, D., Benkhoff, J., & Podolak, M. 2004, in Comets II (Tucson: Univ. of Arizona), 1, 359
Scherer, S., Altwegg, K., Balsiger, H., et al. 2006, Int. J. Mass Spectr., 251, 73
Sierks, H., Barbieri, C., Lamy, P. L., et al. 2015, Science, 347, 1044
Snodgrass, C., Tubiana, C., Bramich, D., et al. 2013, A&A, 557, A33
Vincent, J.-B., Bodewits, D., Besse, S., et al. 2015, Nature, 523, 63
Vincent, J.-B., Oklay, N., Pajola, M., et al. 2016, A&A, 587, A14

Appendix A: Additional figures

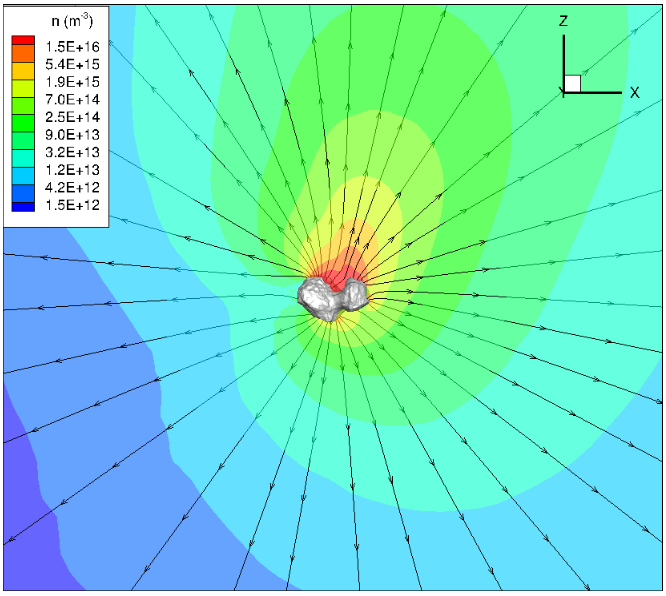

Fig. A.1. Simulation of density (*n*) and streamlines for 23 December 2014 at 12:00:00 UT from the model of Fougere et al. (2016).

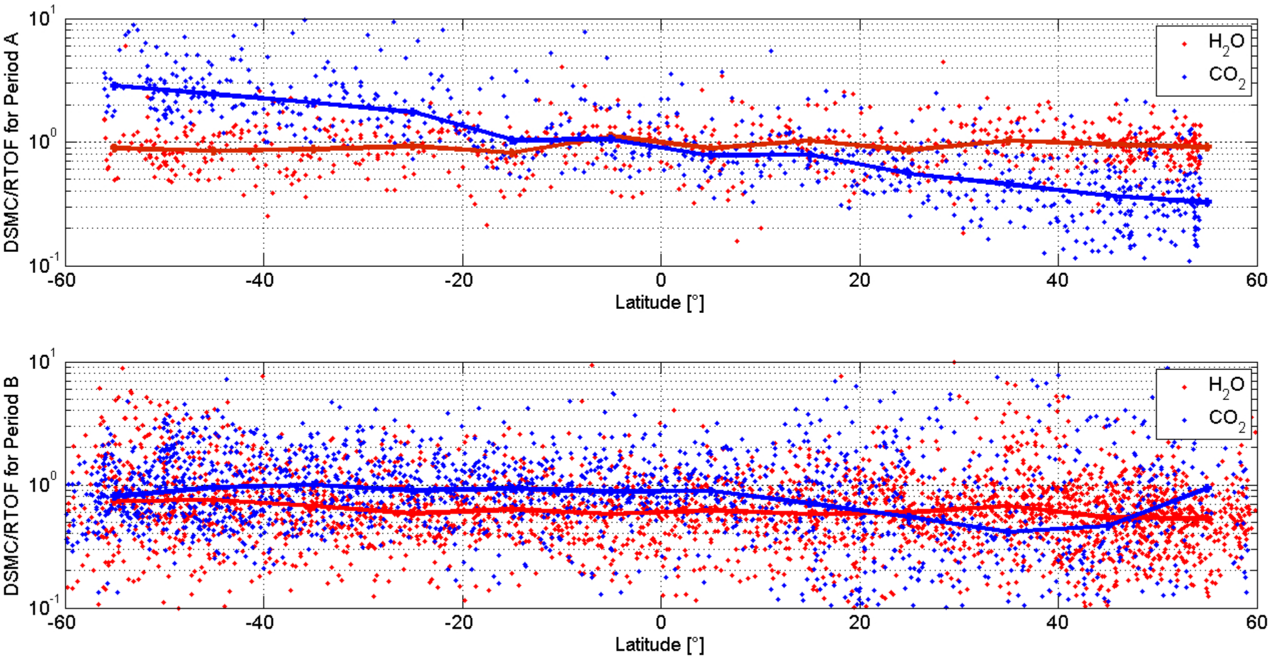

Fig. A.2. DSMC/RTOF ratio for H_2O and CO_2 for Period A (*upper panel*) and Period B (*lower panel*).

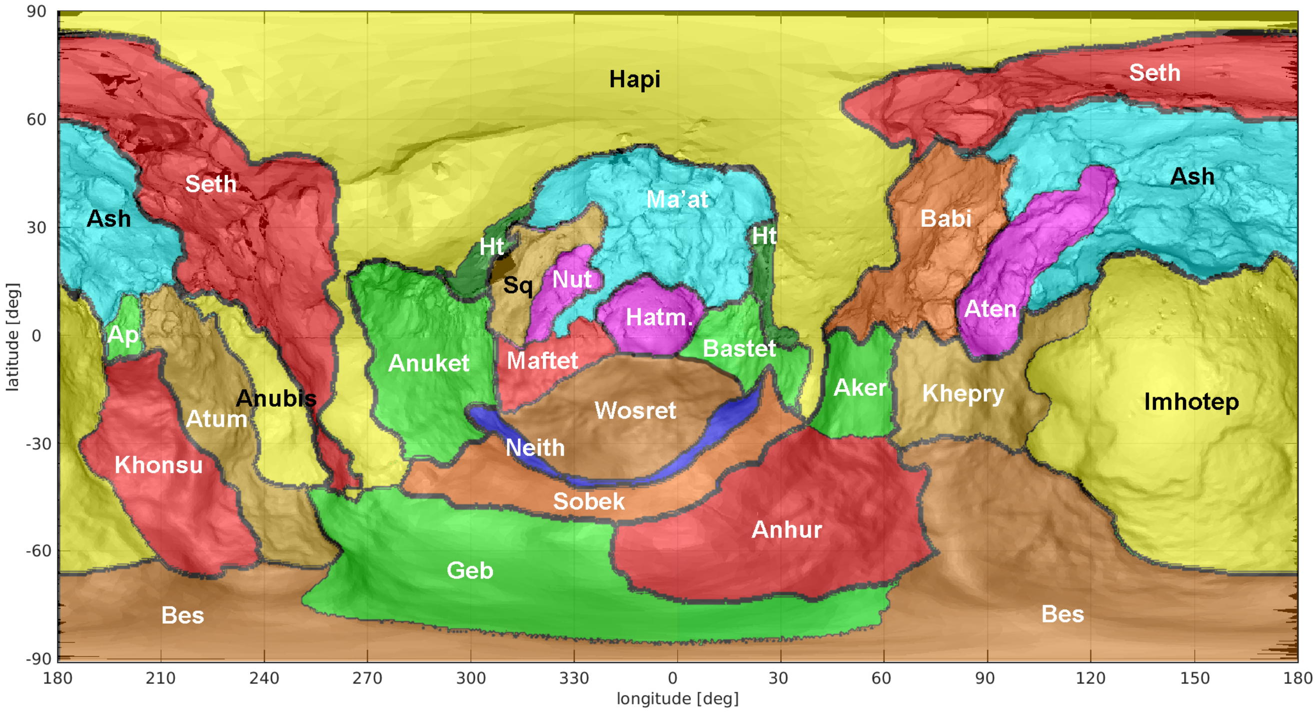

Fig. A.3. Two-dimensional longitude/latitude representation of the morphological regions defined by El-Maarry et al. (2016).

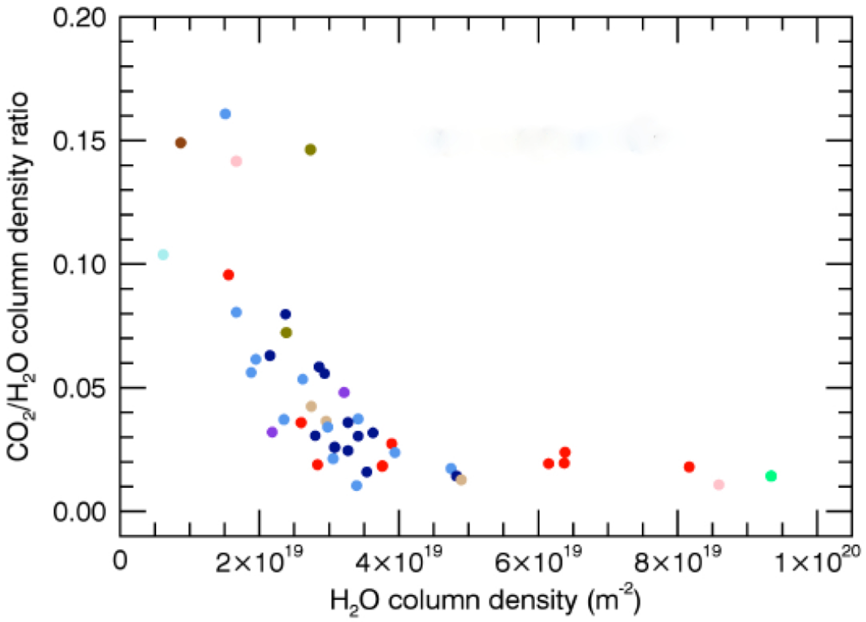

Fig. A.4. CO_2/H_2O density ratio as a function of H_2O density from Bockelée-Morvan et al. (2015), obtained from 24 November 2014 to 24 January 2015.

The Astrophysical Journal, 819:126 (9pp), 2016 March 10
doi:10.3847/0004-637X/819/2/126

HIGH-TIME RESOLUTION IN SITU INVESTIGATION OF MAJOR COMETARY VOLATILES AROUND 67P/C–G AT 3.1–2.3 au MEASURED WITH ROSINA-RTOF

U. Mall[1], K. Altwegg[2,3], H. Balsiger[2], A. Bar-Nun[4], J.-J. Berthelier[5], A. Bieler[6], P. Bochsler[2], C. Briois[7], U. Calmonte[2], M. R. Combi[6], B. Dabrowski[1], J. De Keyser[8], F. Dhooghe[8], B. Fiethe[9], S. A. Fuselier[10], A. Galli[2], P. Garnier[11,12], S. Gasc[2], T. I. Gombosi[6], K. C. Hansen[6], M. Hässig[2,10], M. Hoang[11,12], A. Jäckel[2], E. Kopp[2], A. Korth[1], L. Le Roy[2], B. Magee[10], B. Marty[13], O. Mousis[14], H. Rème[4], M. Rubin[2], T. Sémon[2], C.-Y. Tzou[2], J. H. Waite[10], and P. Wurz[2,3]

[1] Max-Planck-Institut für Sonnensystemforschung, Justus-von-Liebig-Weg 3, D-37077 Göttingen, Germany; mall@mps.mpg.de
[2] Physikalisches Institut, University of Bern, Sidlerstr. 5, CH-3012 Bern, Switzerland
[3] Center for Space and Habitability, University of Bern, Sidlerstr. 5, CH-3012 Bern, Switzerland
[4] Department of Geoscience, Tel-Aviv University, Ramat-Aviv, Tel-Aviv, Israel
[5] LATMOS/IPSL-CNRS-UPMC-UVSQ, 4 Avenue de Neptune, F-94100 Saint-Maur, France
[6] Department of Climate and Space Science and Engineering, University of Michigan, 2455 Hayward Street, Ann Arbor, MI 48109, USA
[7] Laboratoire de Physique et Chimie de l'Environnement et de l'Espace (LPC2E), UMR 6115 CNRS—Université d'Orléans, France
[8] Belgian Institute for Space Aeronomy, BIRA-IASB, Ringlaan 3, B-1180 Brussels, Belgium
[9] Institute of Computer and Network Engineering (IDA), TU Braunschweig, Hans-Sommer-Straße 66, D-38106 Braunschweig, Germany
[10] Space Science Directorate, Southwest Research Institute, 6220 Culebra Road, San Antonio, TX 78228, USA
[11] Université de Toulouse, UPS-OMP, IRAP, Toulouse, France
[12] CNRS; IRAP; 9 Av. colonel Roche, BP 44346, F-31028 Toulouse cedex 4, France
[13] Centre de Recherches Pétrographiques et Géochimiques, CRPG-CNRS, Université de Lorraine, 15 rue Notre Dame des Pauvres, BP 20, F-54501 Vandoeuvre lès Nancy, France
[14] Aix Marseille Université, CNRS, LAM (Laboratoire d'Astrophysique de Marseille) UMR 7326, F-13388, Marseille, France

Received 2015 November 15; accepted 2016 January 27; published 2016 March 7

ABSTRACT

Comets considered to be pristine objects contain key information about the early formation of the solar system. Their volatile components can provide clues about the origin and evolution of gases and ices in the comets. Measurements with ROSINA/RTOF at 67P/Churyumov–Gerasimenko have now allowed, for the first time, a direct in situ high-time resolution measurement of the most abundant cometary molecules originating directly from a comet's nucleus over a long time-period, much longer than any previous measurements at a close distance to a comet between 3.1 and 2.3 au. We determine the local densities of H_2O, CO_2, and CO, and investigate their variabilities.

Key words: comets: general – comets: individual (67P, Churyumov–Gerasimenko)

1. INTRODUCTION

Comets are thought to be built up of icy materials and dust grains. Comets may preserve both interstellar material, as well as material from the proto-solar nebula. As comets have spent extensive time far away from the Sun under very cold conditions, they are usually considered to be pristine objects that contain key information about the early formation of the solar system. Their volatile components can provide clues about the evolution of gases and ices, as the collapsing molecular cloud transforms into a mature planetary system. For example, the abundance of CO is of particular interest, as it was predicted to be the dominant C-bearing gas in the outer parts of the solar nebula where comets formed (cf. Fegley & Prinn 1989). Due to the high volatility of CO, the CO content of ices incorporated into comets is sensitive to the local conditions where the nucleus formed, or where the coldest part of the nucleus originated, assuming there was significant radial mixing of material within the nebula. The amount of CO, therefore, can contain information on the history of origin of the comets and the conditions under which they may have formed (see, e.g., Balsiger et al. 2015; Rubin et al. 2015).

A central issue of cometary science is the question of to what extent interstellar ices were chemically processed in the solar nebula before they were incorporated into cometary nuclei. A determination of the mixing ratios of cometary ices between the interstellar and proto-stellar samples is, therefore, of particular importance. As icy materials are not only present in the solar system but also in interstellar clouds and have probably been integrated into planetary bodies, they have been considered for a long time to be an important prerequisite for the formation of life on planets. From this perspective measuring the in situ composition of the volatile cometary material is also an important goal.

Typically, the most abundant molecules in cometary ices are water, carbon dioxide, and carbon monoxide, and, most recently detected, molecular oxygen (Bieler et al. 2015a), while other molecular species such as organics (e.g., HCN, NH_3, CH_4, C_2H_6, and CH_3OH) are minor (e.g., Bockelee-Morvan et al. 2004; Mumma & Charnley 2011). It is important to note that the detection of some of these species from the ground is difficult, either due to the telluric absorption of the near-infrared (NIR) in the Earth's atmosphere or due to the absence of permanent electric dipole moments for symmetric molecules, which makes detection by radio observations impossible. As comets are shedding their volatile material into interplanetary space and are ejecting dust from their surfaces, the measurement of cometary volatiles is crucial to improve our understanding of their activity and the formation of the cometary coma.

With sublimation temperatures of the major volatiles covering a wide range of temperatures (T_{sub} of H_2O ice is ~150 K, T_{sub} CO_2 ice is ~70 K and T_{sub} CO ice is ~30 K; see Figure 1)

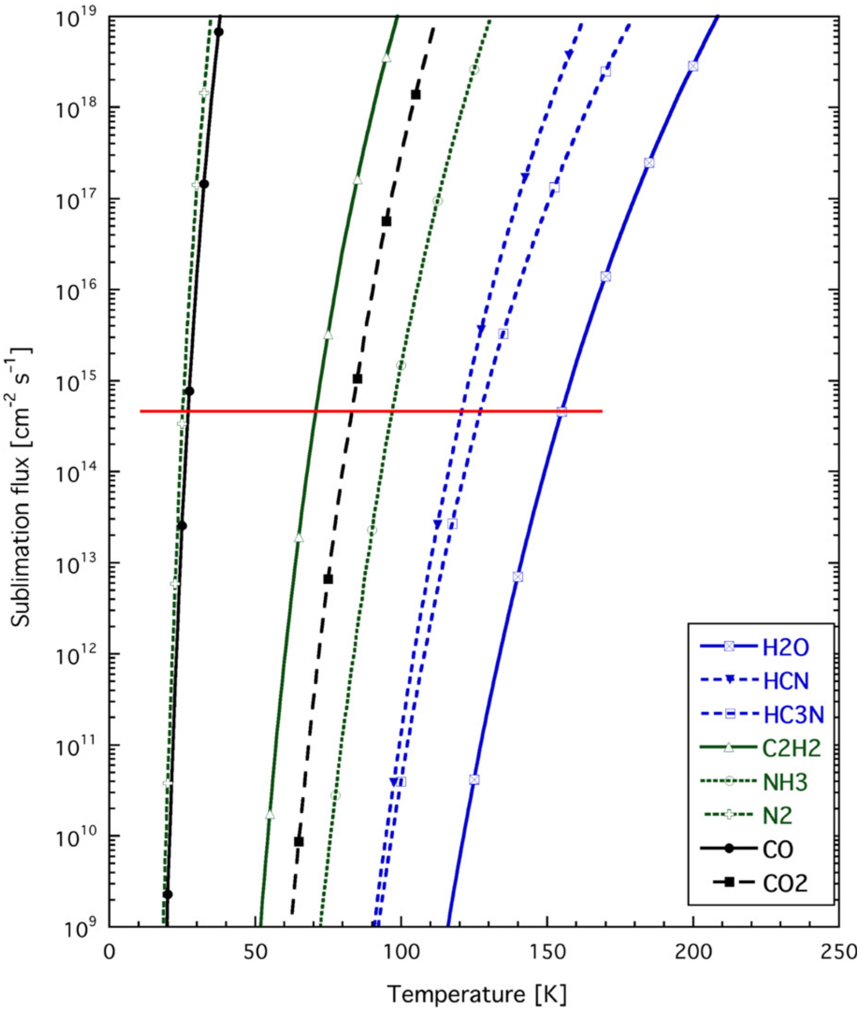

Figure 1. Sublimation fluxes for selected species relevant for Churyumov–Gerasimenko, based on Fray & Schmitt (2009). The horizontal line indicates where the sublimation flux is about 1 monolayer per second, defining the "sublimation temperature."

the activity of comets at different heliocentric distances must be partially driven by the different cometary species. This was beautifully revealed by NASA's EPOXY mission to the Jupiter family comet 103P/Hartley 2 (e.g., A'Hearn et al. 2011). This mission demonstrated the importance of CO_2 ice in lifting water ice grains at 1.07 au distance.

And yet, due to the above-mentioned observational issues there are only a few in situ measurements of H_2O, CO_2, and CO in comets. Therefore, the IR measurements of the AKARI IRC instrument of the 18 observed Oort cloud and Jupiter-family comets are particularly important because they provide a range of the major volatiles as a function of heliocentric distance: Ootsubo et al. (2012) not only provided the first homogenous database of the CO_2/H_2O ratio in more than 10 samples of comets that were compatible with earlier measurements, but also showed that the CO_2/H_2O production rate ratio is systematically higher for comets which are further than 2.5 au away from the Sun. They found that the CO/CO_2 ratio in the observed comets is smaller than unity, although they only obtained upper limits for CO in most of their observed comets. For 67P/Churyumov–Gerasimenko (67P/C–G) at 1.8 au they found a CO_2/H_2O value of about 7%.

With the *Rosetta* Mission exploring the Jupiter-family comet 67P/C–G, coma abundance measurements can now be improved. We are for the first time in a position not only to measure abundance ratios or abundances for a specific moment in time, but also to study the spatial and temporal evolution of the gas abundances in the coma over a very long time period at large distances from the Sun. It is of special interest to explore how our measurements are related to the illumination and the observation conditions at the comet.

Hässig et al. (2015) presented two periods of coma composition measurements made with the *Rosetta* Orbiter Spectrometer for Ion and Neutral Analysis (ROSINA)/DFMS instrument when *Rosetta* was close to 67P/C–G with a time resolution better (>10 measurements) than the rotation period of the comet. During the first 4 day period from 2014 August 4 to 8 *Rosetta* was above the summer hemisphere and from 2014 September 18 to 19 was above the winter hemisphere. These first measurements indicated that the cometary coma is highly heterogeneous.

In this paper, we investigate the temporal evolution of the major gas species around the cometary nucleus with the ROSINA/RTOF instrument for an extended time period between 2014 October and 2015 February, at heliocentric distances of 3.1–2.3 au. ROSINA/RTOF obtains mass spectra with a higher time resolution of 200 s and thus is better suited to resolve spatial/temporal variations in the coma than ROSINA/DFMS.

2. THE ROSINA INSTRUMENT

The ROSINA instrument suite on board the European Space Agency's (ESA) *Rosetta* spacecraft consists of two mass spectrometers: the Double Focusing Mass Spectrometer (DFMS) and the Reflectron-type Time-Of-Flight (RTOF), as well as the ROSINA COmet Pressure Sensor (COPS; Scherer et al. 2006; Balsiger et al. 2007). COPS measures the total neutral particle density with the nude gauge and ram pressure with the ram gauge. Measured values are converted on board with a reference temperature of 20°C into pressure. Lower limits are 10^{-11} mbar for the nude gauge and 10^{-9} mbar for the ram gauge. RTOF complements the DFMS with an extended mass range from 1 to >300 amu/q. While the ROSINA/DFMS spectrometer excels in mass resolution, the ROSINA/RTOF instrument shines through its measurement frequency. RTOF can measure all cometary species in a single spectrum acquired within 200 s. This ability permits one to monitor the complete mass range of cometary volatile species simultaneously.

To measure the neutral and the ionized cometary gas components, two ion sources were implemented in RTOF: the Orthogonal extraction ion Source (OS) and the Storage ion Source (SS), both of which can use the electron impact for ionization of neutral gas. The OS is dedicated to the measurement of the ionized component of the cometary atmosphere. The OS directs incoming ionized particles into the TOF section of the mass spectrometer, while the SS, dedicated to the neutral cometary gas component, ionizes neutral particles and extracts them into the TOF analyzer. The analyzer contains the 83 cm long drift tube of the time-of-flight instrument. RTOF is able to measure, with both sources simultaneously, neutrals in the storage sources and ions in the ortho source, but also with each source alone. RTOF was originally designed to measure molecules with a mass resolution up to $m/\Delta m > 4500$ at 50% peak height (Scherer et al. 2006). However, due to problems in flight with the 9 kV high voltage power converter, the instrument had to be operated at 2 kV, which naturally leads to a lower mass resolution for RTOF of ~300–400 at 50% peak height.

3. RTOF DATA ANALYSIS

3.1. Operational and Observational Conditions

The RTOF instrument can be operated in various operational measuring modes. In this investigation we have analyzed all spectra obtained with the OS sensor in measuring mode 523 between 2014 October 24 and 2015 February 17, a grand total of 10,750 spectra. During this period the *Rosetta* spacecraft orbited or passed the comet at distances between 8 and 77 km from its center and was able to monitor the comet's activity for a variety of solar illumination conditions.

3.2. Data Processing

Ions that have been created from neutral gas in the OS are extracted from the source with a frequency (10 kHz) that is defined by a high-voltage pulser. The time of extraction starts a time-of-flight measurement. After traversing the drift tube, reflected at the ion mirror and returning, an ion is measured if it hits the micro channel plate (MCP) detector (Schletti et al. 2001; Siegmund et al. 2001). The MCP produces a current pulse that is processed in the OS data acquisition board ETS-L (Equivalent Time Sampler-Light). The ion is registered as detected if the amplitude of the measured detector signal surpasses a given set threshold. The corresponding time-of-flight of a detected ion is then recorded in a spectrum which has 35152 time channels with a bin length of 1.65 ns each for measuring mode 523. For a given measuring mode the RTOF on board electronics ETS-L board produces one spectrum consisting of all the TOF measurements generated during the acquisition time of 200 s.

The analysis of a single RTOF spectrum consists of integrating the count rates of the individual peaks associated with the detected ions in the corresponding TOF channels.

Due to operational and noise issues, the measured ion signals are superimposed on a varying background that is not necessarily flat. A smoothing procedure is applied to identify the background signal, which is then subtracted from the measured spectrum. The individual channels of a spectrum are associated with their corresponding ion mass/charge ratios with the help of a calibration gas mixture. During dedicated calibration measurements this calibration gas mixture is injected into the ion source to generate those mass calibration spectra with peaks at specific known masses (He, CO_2, and Kr). With a procedure described by S. Gasc et al. (2016, in preparation), the accurate mass scale can then be found. The resulting mass spectra are then used to identify ion count peaks, which surpass a given threshold. We fitted exponentially modified Gaussian distributions to the individual peaks. With the parameters found, we computed the area of the identified peaks. Each spectrum acquired at a specific time at the comet is therefore characterized by a given number of peaks whose parameters we have determined. For each analyzed spectrum we computed ancillary data at the corresponding spectrum acquisition time with the help of the SPICE toolkit using ESA's reconstructed kernels for the orbit of *Rosetta* and 67P/C–G, and the associated shape model of the comet. In the main body of Figure 2 the integrated count rate of all the RTOF spectra for the investigated data period is displayed. It is seen that the mass spectra are dominated by the three compounds, H_2O, OH, CO_2, and minor species like CO. As ROSINA operates in an extremely tenuous coma, great care has to be taken to ensure that ROSINA cometary gas measurements are not accidently contaminated by gas molecules released during spacecraft maneuvers. The contamination effects on ROSINA and the identification of species originating from such maneuvers were studied in detail during the long flight of *Rosetta* from Earth to the comet (Schläppi et al. 2010). The right insert, which is marked red in the main body of Figure 2, shows an enlargement of the middle part of the spectrum (time-of-flight bin numbers from 0.5 to 2.5 times 10^4) to show the minor species. The left insert shows a correlation plot of the OH versus the H_2O count rate computed for each spectrum.

3.3. Results

As molecules break into fragments under electron ion impact ionization in a mass spectrometer, the fragmentation patterns for RTOF need to be measured in the laboratory with the flight spare instrument under conditions duplicating the situation in

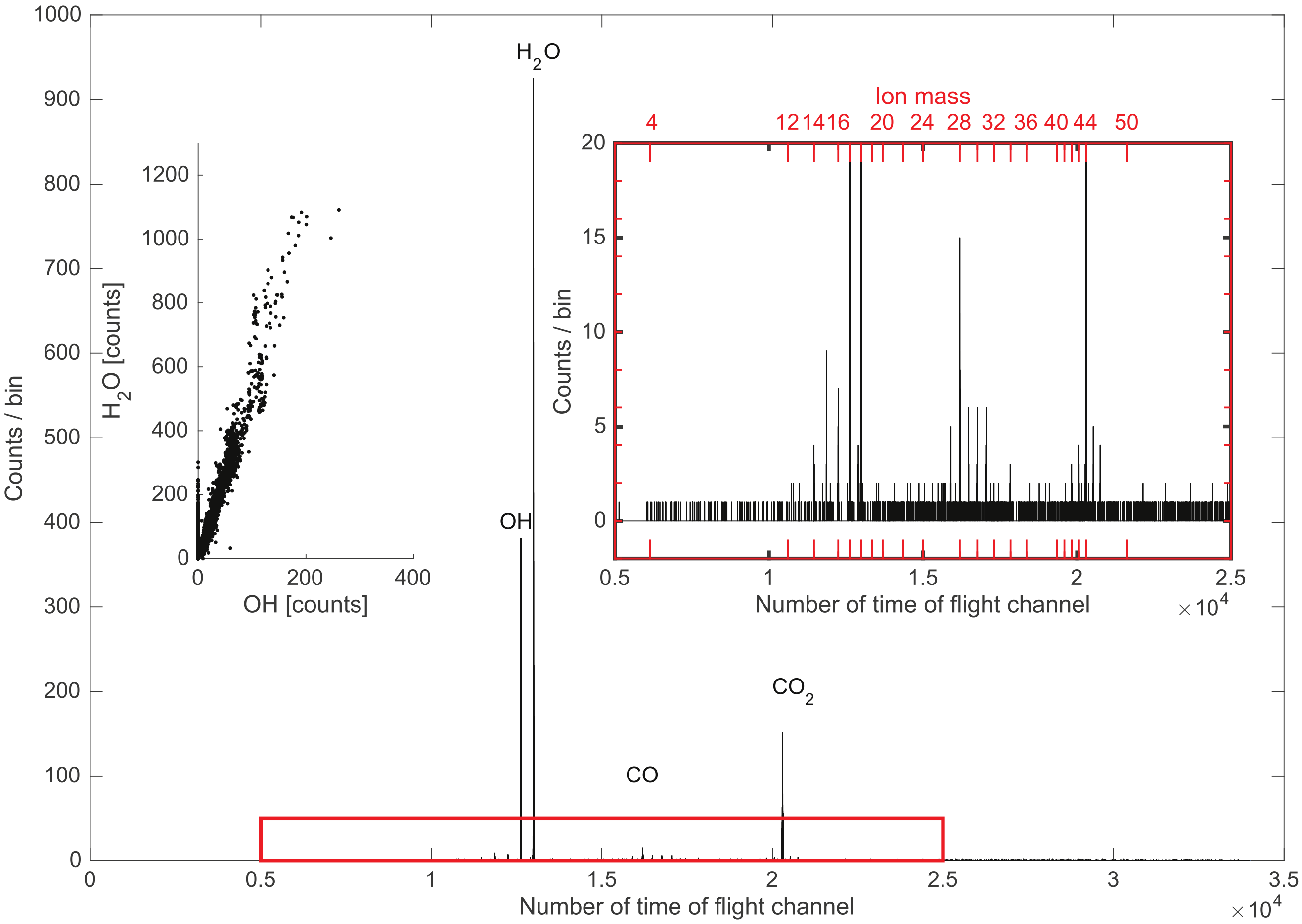

Figure 2. Sum of accumulated count rate of identified ion peaks in the investigated time interval (main part of figure). The right upper insert shows a zoomed fraction of the main ion histogram. The left insert shows the correlation between OH and the H_2O molecule.

flight. Gasc (2015) has done these laboratory calibration measurements. We used the sensitivity values and fragmentation calibration by S. Gasc et al. (2016, in preparation, Table 3: Relative fragmentation ratios) for the OS RTOF measurement. The relative fragmentation ratio is defined as the precursor ion intensity (taken to be 100%) over the fragment ion intensity. In our study we considered the fragmentation of H_2O (100%) into OH^+ ($23.35 \pm 0.53\%$) and O^+ ($1.16 \pm 0.06\%$), for CO_2 into CO^+ ($3.86 \pm 0.21\%$) and O^+ ($5.07 \pm 0.22\%$) and C^+ ($1.20 \pm 0.10\%$), and for CO into O^+ ($0.08 \pm 0.04\%$) and C^+ ($0.77 \pm 0.02\%$). These values, together with an electron emission current of 200 μA for the OS filament, are then used to convert the count rates into densities.

Figure 3 shows in the upper panel the total COPS local density as a function of time (black line) and the deviation of the RTOF pointing direction from the Nadir pointing direction (blue line).

The COPS data shown have been cleaned from COPS measurements made during routine spacecraft maneuvers (e.g., wheel off-loading time periods). To identify additional non-routine maneuvers, which could contaminate measurements, Figure 3 also shows in the top panel the deviation from the RTOF FOV looking direction and its Nadir pointing direction. The lower panel in Figure 3 contains as a time series the local density of H_2O and CO_2. The RTOF time series, unlike the COPS measurements, have data gaps, which occurred when RTOF was switched to SS mode or RTOF was simply not in operation due to reaction wheel offloading. Both sensors have also been switched off during most (COPS) or all (RTOF) orbital correction maneuvers, occurring approximately twice per week for the time period reported here.

Investigating the correlations between the different observed species in the RTOF mass spectra, we find only the clear correlation between H_2O^+ and OH^+ signals. This correlation, shown in the left insert of Figure 2, demonstrates that the OH^+ peak seen in the spectra is a fragment of an H_2O molecule; the measurements were taken so close to the nucleus that the contribution of OH from photo-dissociation in the coma is negligible. The correlation shows the fragmentation ratio found by S. Gasc et al. (2016, in preparation) of ~23%.

The more or less continuous COPS total density measurements around the comet clearly show the total density fluctuating with a cometary rotation period of 12.4 hr. To visualize that RTOF indeed sees molecules from the comet, Figure 4 zooms in on the 8 day period from DOY 371 to DOY 379, superimposed on the COPS data. In this time interval RTOF observed mostly H_2O molecules. It is important to point out that COPS measures the local total particle density, i.e., including all major and minor species, as it is not possible to separate those with COPS. Most of the time the coma is dominated by neutral water and therefore a close match can be expected to the RTOF H_2O observations. The figure shows the

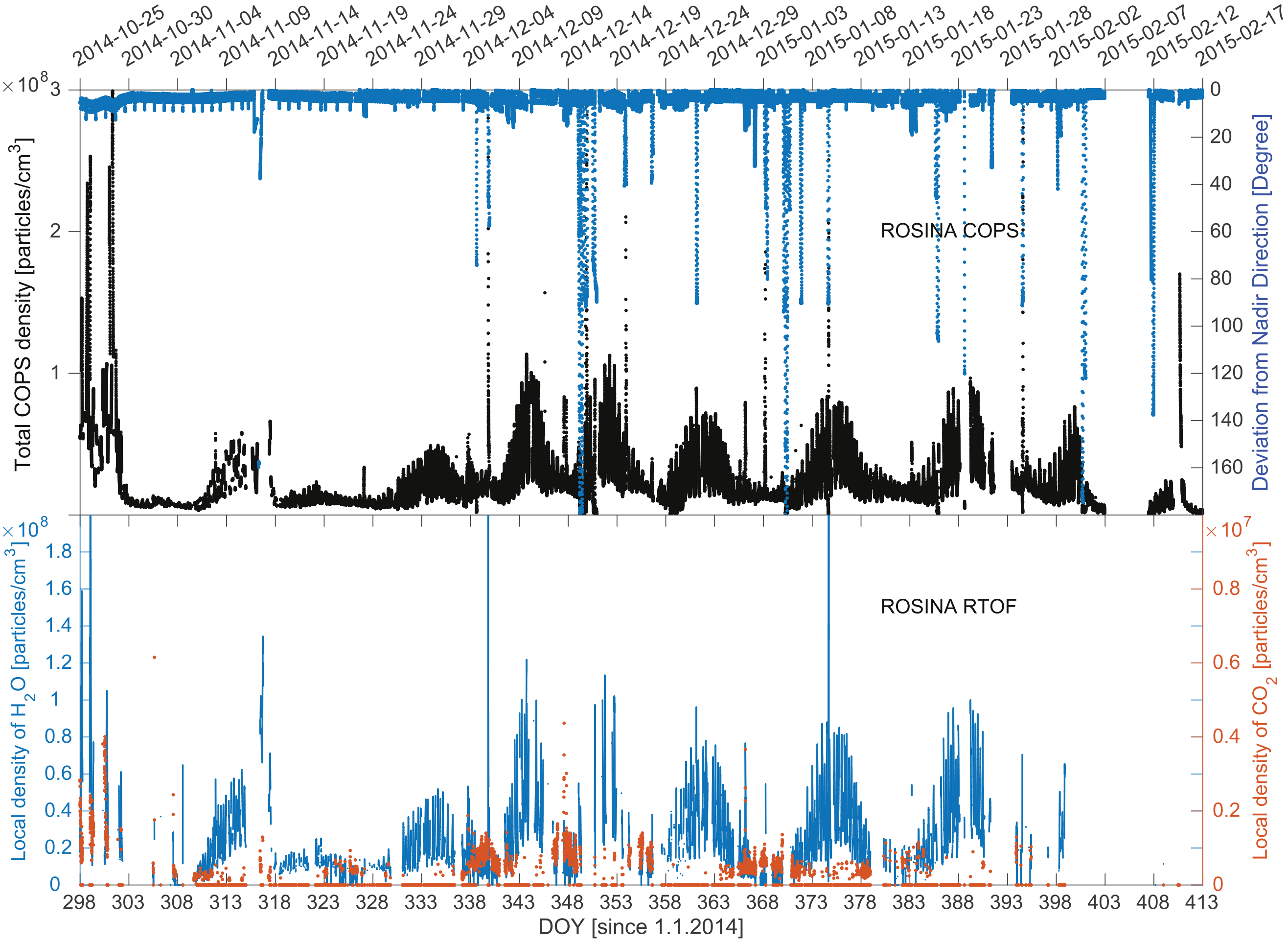

Figure 3. Time series of COPS total pressure measurements (upper panel) and H_2O (blue) and CO_2 (red) measurements with RTOF OS (lower panel).

synchronous variations of the two independent measurements, which in turn implies that during this period, H_2O was indeed the dominating gas species in the coma. Clearly visible in the figure is an additional space manoeuver, which generates the spike in the observed densities.

The RTOF local density time series from Figure 3 suggest that the H_2O and CO_2 densities are anti-correlated. We show in Figure 5 the density ratio CO_2/H_2O for the data period displayed in Figure 3.

As all measurements in the time ordered sequence shown in Figure 3 are made at different locations around the comet, we investigated which part of the comet is in the field of view of the RTOF instrument at a particular point in time. Under the assumption that RTOF detects neutral gas species, always originating from the surface of the comet, and flying into the center of the RTOF field of view direction, we can compute for each measurement the corresponding latitude and longitude values on the comet (sub-spacecraft footpoint). It must be very clear that such a simple mapping procedure can only give a rough idea about the place of origin of the measured neutrals. Bieler et al. (2015b) have investigated this issue by modeling the neutral coma of 67P/C–G with 3D kinetic and hydrodynamic codes. The large collisional mean free path of the particles leaving the cometary surface, the large fractions of concave surfaces of the nucleus shape and a rapidly changing temperature distribution of the particle emitting surface area make this tracking to the surface origin a complex problem. Furthermore, RTOF's projected field of view was always larger than the comet itself, which means that gas can come from almost everywhere on the nucleus facing *Rosetta*. However, the fact that the overall longitude, latitude distribution pattern of the investigated ion species remains relatively constant when the studied time interval is subdivided into smaller time intervals, lends some credibility to the employed method of projection. We conclude, therefore, that the analysis shows that under the given assumptions H_2O molecules are preferentially observed on the Northern Hemisphere, while CO_2 is leaving the comet more on the Southern Hemisphere (compare these figures with the results (Figure 4) from the DFMS instrument by Hässig et al. 2014). Note that RTOF's high time resolution translates into a high spatial resolution, especially in the longitudinal dimension. A much more sophisticated spatial analysis is in progress and will be published in a separate paper.

CO abundance measurements either inferred from ground-based or in situ measurements have shown a wide range of values. CO in the coma could originate either as a primary species or as a dissociation product from CO_2. Carbon monoxide was first detected in comet C/1975 V1 (West) by rocket UV observations (Feldman & Brune 1976). Highly different CO abundances were observed: from 2% in C/1979 Y1 (Bradfield) to 15%–20% in comets C/1975 V1 (West) and 1P/Halley. More recently, Paganini et al. (2015) reported

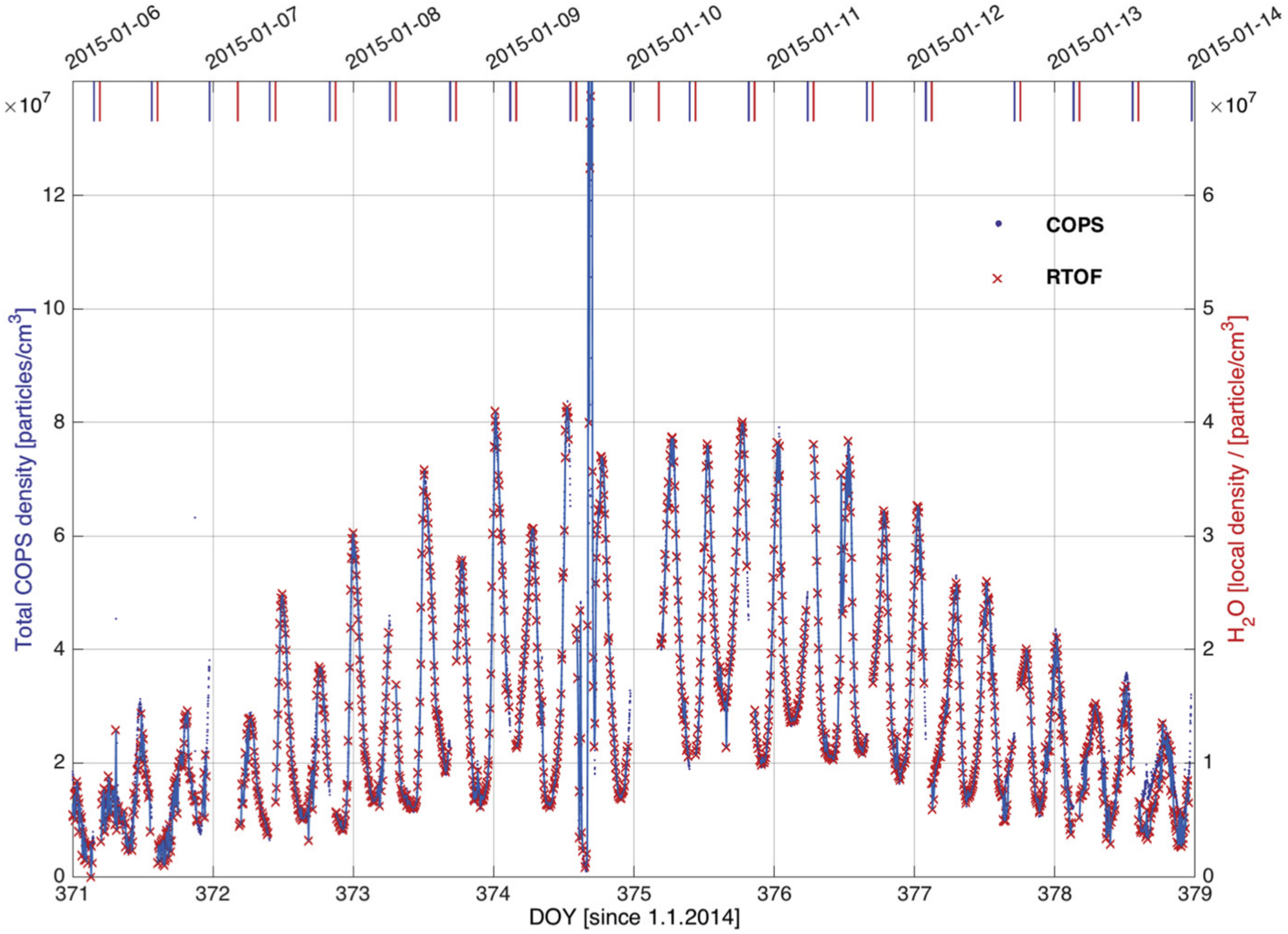

Figure 4. COPS total density and H_2O count rate for an 8 day period. Vertical lines at the top of the figure display the times of spacecraft maneuvers (blue: start, red: end of maneuver).

measurements of C/2013 R1 (Lovejoy) at pre-perihelion distances from 1.35 to 1.16 au with the Near InfraRed SPECtrometer (NIRSPEC) at the Keck Observatory. Their findings indicate that C/2013 R1, with a measured mean abundance ratio of CO/H_2O of 9.89 ± 2.03, is enriched in CO. From their compilation of the CO/H_2O abundance ratios in 23 Oort Cloud comets ranging from 0.4% to 28% they compute a median value of ~4% and arbitrarily define comets with abundances larger than twice the median CO abundance (i.e., >8%) to represent "CO-rich" comets.

Analyses of UV observations made with different fields of view, as well as the CO density evolution observed in situ by the Neutral Mass Spectrometer (NMS) on Giotto at 1P/Halley, show that the origin of CO is twofold: one part is coming from the nucleus region, and another one is from a distributed source within the coma with a scale length of the order of 10^4 km (Eberhardt et al. 1999; Cottin & Fray 2008; Mumma & Charnley 2011).

On *Rosetta*, Feldman et al. (2015) reported the detection of a weak emission from atomic CO. We have examined in the investigated data period the occurrence of RTOF spectra that show a clear CO signal. Figure 6 displays the CO local density for this time period. Also plotted are the distance of the spacecraft from the comet and the sub-solar-latitude. Unlike observations at Hyakutake and Hale–Bopp (e.g., Bockelee-Morvan 1997), where a high CO abundance was observed, we could identify only a few mass spectra that revealed a clear CO signal. Extreme care had to be taken to separate spectra taken adjacent to spacecraft maneuvers, to ensure that RTOF is not detecting the CO fragmentation remnants of spacecraft contaminations sticking to the spacecraft structure, which are released when the thermal environment changed.

4. DISCUSSION

The composition of cometary volatiles contains basic information on the nature of comets and their formation mechanisms. This information originated for a long time only from measurements of the cometary dissociation products, observed mostly from far away. Cometary in situ exploration with the possibility for close fly-bys has changed this situation drastically. As comets display huge variation in the abundance of volatiles, high-resolution mass spectrometry is now able to provide the necessary information to come up with an accurate chemical inventory for individual comets, thereby removing a lot of ambiguities. Abundance measurements of cometary volatiles are often quoted as ratios. Such ratios are used in various classification schemes of comets (e.g., A'Hearn 1995; Fink 2009; Mumma & Charnley 2011; Le Roy et al. 2015). The variability of these ratios is therefore important. Many of these

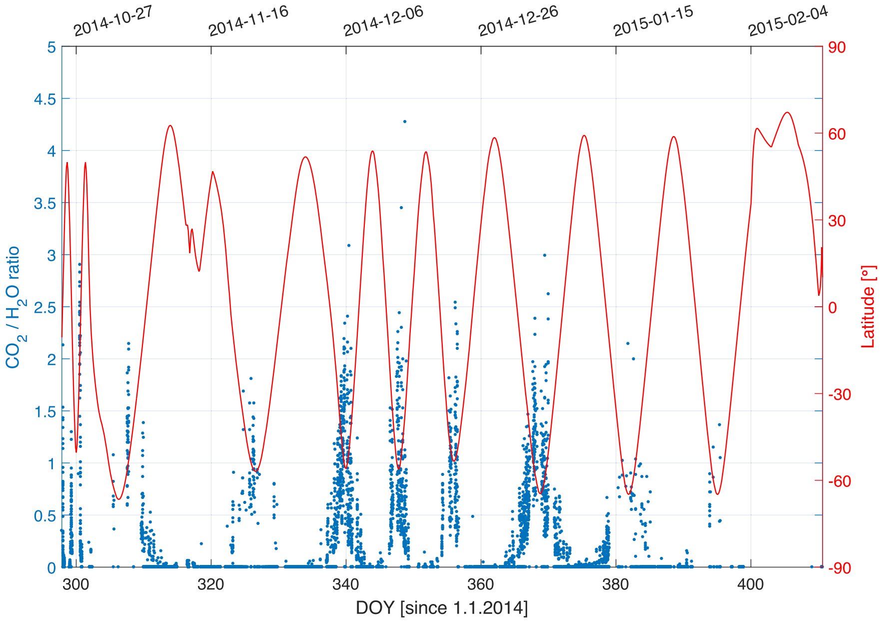

Figure 5. CO_2/H_2O ratio (left) and the latitude of the sub-spacecraft point (right) for the investigated time period.

observations have been the result of relatively short period measurements with remote sensing instrumentation, taking into account the integrated coma along the viewing direction. Some of these ratios also result from measurements over large areas of the inner coma, thus providing a global average of the production rate of these species, and also include molecular species that sublimated from the nucleus and those that were generated in subsequent chemical processes in the coma. From the in situ measurement of the CO density in the coma of Comet Halley we know, for example, that for this comet only about 1/3 of the CO originates directly from the nucleus (Eberhardt et al. 1987). The remainder of the CO comes from an extended source located in the innermost 25,000 km of the coma (for a review of distributed sources in comets, see, e.g., Cottin & Fray 2008). No suitable parent molecule for this extended source could be identified at that time, and Eberhardt et al. (1987) concluded that the CO evaporated from CHON-type dust grains in the coma either as CO or as a short-lived parent. In the case of 67P/C–G not much dust was observed (Rotundi et al. 2015).

ROSINA/RTOF has now allowed, for the first time, a direct in situ high-time resolution measurement of cometary molecules originating directly from a comet's nucleus over a long time-period, much longer than any previous measurements at a close distance to the comet. With the present study we have made with ROSINA/RTOF the first step to record precisely the heliocentric variation of cometary abundances to investigate processes responsible for the production of the most abundant cometary parent molecules. These and the forthcoming measurements at 67P/C–G have then to be used to investigate the question of to what extent molecular abundance ratios vary and what causes the observed variability in the coma. The presented RTOF measurements indeed reveal a high variability but also a distinct pattern. Our measurements show a clear north–south asymmetry in the abundance of the major volatiles (see Figure 5). The ultimate issue to be resolved is the question of whether this asymmetry can arise from a comet whose building blocks originated from a single reservoir or whether the comet was formed through fusion of material from a different origin. To answer this question we need to draw interferences from the measured volatile inventory in the coma to the composition of the volatiles in the nucleus; we have to turn our attention to the question of whether we can infer from a measurement of released trapped gases in the ice the amount of original available gas when the comet ice was formed. The underlying physics of this question was addressed in a series of laboratory experiments (see, e.g., Bar-Nun & Laufer 2003) with the goal to understand how much gas relative to its abundance in the gas phase can be trapped in water ice at a particular pressure–temperature range and how the trapped gas is then released again. Two major insights were the recognition that water ice in comets formed in the amorphous state at temperatures below ~50 K, and that amorphous water ice has a very high capacity for trapping various gases (Bar-Nun et al. 1985, 2007). It was found that when amorphous ice is warmed trapped gases are released in eight distinct temperature ranges as a pure manifestation of the change in the ice structure at very specific temperatures (e.g., Laufer et al. 1987).

To understand our RTOF measurements we ask what would be observable by a mass spectrometer from an amorphous icy homogenous sphere made out of equal parts of intrinsically mixed CO_2 and H_2O, which is illuminated from a fixed point in space with light. The very low albedo of comets indicates that the volatile ices must be definitely mixed with dust at the surface of the comet, although the relationship is complex (e.g., Lucey & Clark 1985). Moreover, hydrocarbon molecules on the surface will be transformed to a dark non-volatile carbonaceous crust by UV light (Riedo et al. 2010). Sunlight gets absorbed to a very large extent and heats the surface layer of the comet. Due to the low thermal conductivity of the cometary surface (Gulkis et al. 2015; Spohn et al. 2015), a good fraction of the incoming sunlight is reemitted in the NIR wavelength range back to space. The remaining part penetrates the cometary surface up to a few meters and heats the volatile material. After some time the illuminated surface reaches the necessary temperature to release the CO_2. A mass spectrometer

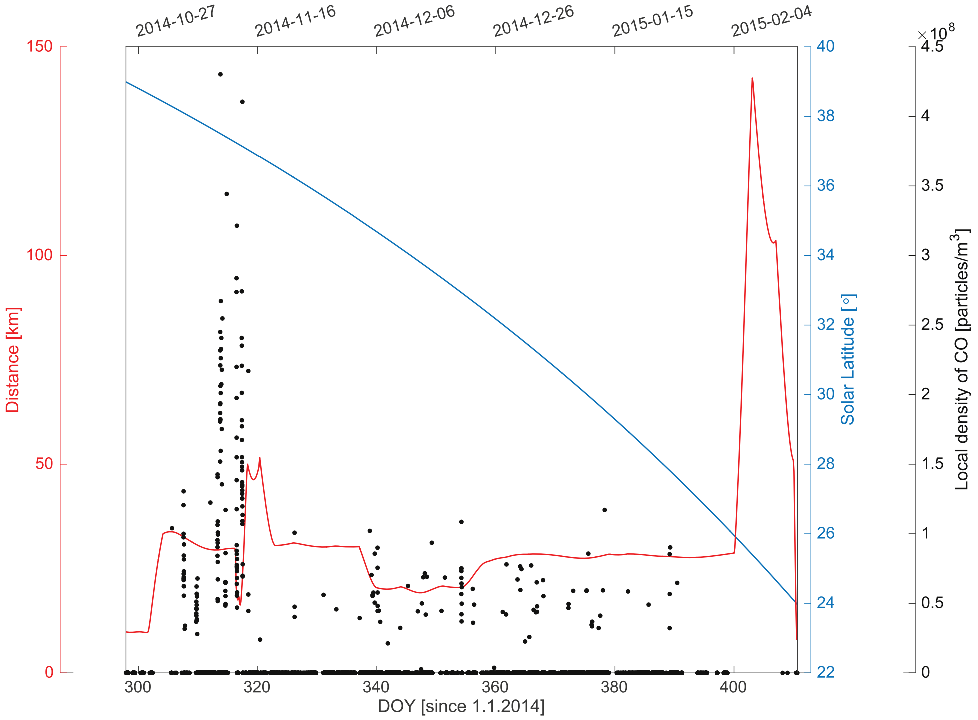

Figure 6. CO local density for the investigated time period. Also plotted are the distance of the spacecraft from the comet and the solar-latitude.

at a fixed position relative to the surface would measure during the heating process an increasing flux of the sublimating CO_2 molecules. If the surface temperature would be additionally increased to the point where the sublimation temperature of H_2O is reached, an increasing H_2O component would be seen as well. The measured ratio CO_2/H_2O could vary over a wide range depending on the particular temperature of the ice, despite the fact that the amorphous ice was formed with a fixed CO_2/H_2O vapor ratio. Comet Simulation (KOSI) experiments (see, e.g., Grün et al. 1991), which simulated cometary heating processes, showing that already on a sample surface of a few hundreds of cm^2 the temperature was not homogeneous and that the temperature pattern could change quickly in unexpected ways. At places where the ice was covered by dust, the surface temperature was significantly above 300 K. When dust was blown off, the local surface cooled down rapidly. The cover layer of dust developed during these experiments remained thin, however (<2.5 millimeters). KOSI-3 and KOSI-4 experiments revealed that inward diffusion of CO_2 can occur, which can even produce a variation of the chemical composition depending on the depth (Hsiung & Roessler 1989). It becomes clear that despite having accurate long-term local abundance measurements of the H_2O and CO_2 components of 67P/C–G's coma, we are still at the moment missing vital information to make a link to the composition of the nucleus.

Despite this, the qualitative picture holds that due to the 52° obliquity and the orientation of the spin axis of 67P/C–G strong seasonal effects exist, which leads to a highly asymmetric insolation condition. During the long time when the comet is far from the Sun, the northern cometary surface areas are only weakly illuminated during the northern summer, while during the short perihelion passage of 67P the southern regions, during the southern summer, will receive a lot of sunlight for a brief period. This leads to a highly asymmetric temperature and heat distribution on and in the upper cometary surface layers. We display in Figure 6 the solar latitude in the 67P/C–G reference frame, together with the distance between the comet and *Rosetta*. As a result of the different insolation of the Northern and Southern Hemispheres, sublimation has eroded all CO_2 from the surface on the northern side of the comet. Therefore, the observed asymmetry need not be taken necessarily as evidence that the cometary material originated from more than one reservoir. However, it becomes clear that we need precise information on the heat distribution in the upper cometary surface layers and on the erosion rate that refreshes the cometary surface layer, if we want to use two molecular species with very different sublimation temperatures to make inferences about the relative abundances of the species in the cometary surface.

Measurements with the Akari space observatory have shown that the CO_2/H_2O ratios of the investigated comets are ranging from 0.05 to 1.1 at heliospheric distances between 1.3 and 3.7 au. At distances beyond 2.7 au the ratios increase to the upper end of the interval due to the decreasing volatility of the water ice (Mumma & Charnley 2011). The RTOF measurements for Jupiter-family comet 67P/C–G reveal at heliospheric distances from 3.1 to 2.3 au a stable periodic pattern of the CO_2/H_2O ratio, which reaches from 0 to a maximum of 3–4 (see Figure 5). Clearly visible are the time variations of the observed CO_2/H_2O ratio in the view direction of the RTOF observations. The observed time variability of the measured neutral abundances is understandable when one recalls that the volatility of different ices is very different. We have also identified a weak CO component, which can vary from ~0.4% to ~30% in 23 investigated comets (see Figure 5 in Paganini et al. 2014). As our measurements were all made close to the comet, we can safely assume that we are measuring molecules originating directly from the cometary nucleus.

The authors would like to thank the following institutions and agencies, which supported this work. Work at MPS was funded by the Max-Planck Society and BMWI under contract 50QP1302. Work at UoB was funded by the State of Bern, the Swiss National Science Foundation, and by the European Space Agency PRODEX Program. Work at the Southwest Research Institute was supported by subcontract #1496541 and #1296001 from the Jet Propulsion Laboratory. Work at BIRA-IASB was supported by the Belgian Science Policy Office via PRODEX/ROSINA PEA 90020. This work has been carried out thanks to the support of the A*MIDEX project (no. ANR-11-IDEX-0001-02) funded by the (Investissements d'Avenir) French Government program, managed by the French National Research Agency (ANR). This work was supported by CNES grants at IRAP, LATMOS, LPC2E, UTINAM, CRPG, and by the the European Research Council (grant No. 267255). A. Bar-Nun thanks the Ministry of Science and the Israel Space agency. Work at the University of Michigan was funded by NASA under contract JPL-1266313. ROSINA would not give such outstanding results without the work of the many engineers and technicians involved in the mission, in the *Rosetta* spacecraft, and in the ROSINA instrument over the last 20 years, whose contributions are gratefully acknowledged. *Rosetta* is an ESA mission with contributions from its member states and NASA. We acknowledge the work of the ESA *Rosetta* team. U. Mall would like to thank Prof. Johannes Geiss (ISSI) for discussions on cometary science, and ISSI for their hospitality.

REFERENCES

A'Hearn, M. A. 1995, Icar, 118, 223
A'Hearn, M. A., Belton, M. J. S., Delamere, W. A., et al. 2011, Sci, 332, 1396
Balsiger, H., Altwegg, K., Bar-Nun, A., et al. 2015, SciA, e1500377
Balsiger, H., Altwegg, K., Bochsler, P., et al. 2007, SSRv, 128, 745
Bar-Nun, A., Herman, G., Laufer, D., & Rappaport, M. L. 1985, Icar, 63, 317
Bar-Nun, A., & Laufer, D. 2003, Icar, 161, 157
Bar-Nun, A., Notescoa, G., & Owen, T. 2007, Icar, 190, 655
Bieler, A., Altwegg, K., Balsiger, H., et al. 2015a, Natur, 526, 679
Bieler, A., Fougere, N., Toth, et al. 2015b, A&A, 583, A7
Bockelee-Morvan, D. 1997, in IAU Symp. 178, Molecules in Astrophysics: Probes 46 and Processes, ed. E. F. van Dishoeck (Dordrecht, NL: Kluwer), 447
Bockelee-Morvan, D., Crovisier, J., Mumma, M. J., & Weaver, H. A. 2004, in Comets II, ed. M. C. Festou, H. U. Keller, & H. A. Weaver (Tucson: Univ. Arizona Press), 391
Cottin, H., & Fray, N. 2008, SSRv, 138, 179
Eberhardt, P. 1999, SSRv, 90, 45
Eberhardt, P., Krankowsky, D., Schulte, et al. 1987, A&A, 187, 481
Fegley, B., Jr., & Prinn, R. G. 1989, in The Formation and Evolution of Planetary Systems, ed. H. A. Weaver, & L. Danly (Cambridge: Cambridge Univ. Press), 171
Feldman, P. D., A'Hearn, M. F., Bertaux, J.-P., et al. 2015, A&A, 583, A8
Feldman, P. D., & Brune, W. H. 1976, AJ, 209, L45
Fink, U. 2009, Icar, 201, 311
Fray, N., & Schmitt, B. 2009, P&SS, 57, 2053
Gasc, S. 2015, PhD thesis, Univ. Bern
Grün, E., Bar-Nun, A., Benkhoff, J., et al. 1991, in Comets in the Post-Halley Era, ed. R. L. Newburn et al. (Dordrecht, NL: Kluwer), 277
Gulkis, S., Allen, M., von Allmen, P., et al. 2015, SciA, 347, aaa0709
Hässig, M., Altwegg, K., Balsiger, H., et al. 2015, Sci, 347, 276
Hsiung, P., & Roessler, K. 1989, in Proc. Int. Workshop on Physics and Mechanics of Cometary Materials(ESA SP-302), 191
Laufer, D., Kochavi, E., & Bar-Nun, A. 1987, PhRvB, 36, 9219
Le Roy, L., Altwegg, K., Balsiger, H., et al. 2015, A&A, 583, A1
Lucey, P. G., & Clark, R. 1985, in Ices in the Solar System, ed. J. Klinger et al. (Dordrecht: Reidel), 155
Mumma, M. J., & Charnley, S. B. 2011, ARA&A, 49, 471
Ootsubo, T., Kawakita, H., Hamada, S., et al. 2012, ApJ, 752, 15
Paganini, L., Mumma, M. J., Villanueva, G. L., et al. 2014, ApJ, 791, 122
Paganini, L., Mumma, M. J., Villanueva, G. L., et al. 2015, ApJ, 801, 1
Riedo, P., Wahlström, J. A., Scheer, et al. 2010, JAP, 108, 114915
Rotundi, A., Sierks, H., Della Corte, V., et al. 2015, Sci, 347, aaa3905
Rubin, M., Altwegg, K., Balsiger, H., Bar-Nun, et al. 2015, Sci, 348, 232
Scherer, S., Altwegg, K., Balsiger, et al. 2006, IJMSp, 251, 73
Schläppi, B., Altwegg, K., Balsiger, et al. 2010, JGRA, 115, 12313
Schletti, R., Wurz, P., Scherer, S., & Siegmund, O. H. 2001, RScI, 72, 1634
Siegmund, O. H. W., Kromer, K., Wurz, et al. 2001, Proc. SPIE, 4140, 229
Spohn, T., Knollenberg, J., Ball, A. J., et al. 2015, Sci, 349, aab0464

Monthly Notices
of the
ROYAL ASTRONOMICAL SOCIETY

MNRAS **469,** S108–S117 (2017)
Advance Access publication 2017 June 7

doi:10.1093/mnras/stx1412

Change of outgassing pattern of 67P/Churyumov–Gerasimenko during the March 2016 equinox as seen by ROSINA

Sébastien Gasc,[1★] Kathrin Altwegg,[1,2] Hans Balsiger,[1] Jean-Jacques Berthelier,[3] André Bieler,[4] Ursina Calmonte,[1] Björn Fiethe,[5] Stephen Fuselier,[6,7] André Galli,[1] Tamas Gombosi,[4] Margaux Hoang,[8,9] Johan De Keyser,[10] Axel Korth,[11] Léna Le Roy,[1] Urs Mall,[11] Henri Rème,[8,9] Martin Rubin,[1] Thierry Sémon,[1] Chia-Yu Tzou,[1] Jack Hunter Waite[6] and Peter Wurz[1,2]

[1] *Physikalisches Institut, University of Bern, CH-3012 Bern, Switzerland*
[2] *Center for Space and Habitability, University of Bern, CH-3012 Bern, Switzerland*
[3] *LATMOS, F-94100 Saint-Maur, France*
[4] *Department of Climate and Space Sciences and Engineering, University of Michigan, Ann Arbor, MI 48109, USA*
[5] *Institute of Computer and Network Engineering (IDA), TU Braunschweig, D-38106 Braunschweig, Germany*
[6] *Space Science and Engineering Division, Southwest Research Institute, San Antonio, TX 78228, USA*
[7] *University of Texas at San Antonio, San Antonio, TX 78249, USA*
[8] *Université de Toulouse – UPS – OMP – IRAP, F-31400 Toulouse, France*
[9] *CNRS – IRAP, F-31028 Toulouse cedex 4, France*
[10] *Belgian Institute for Space Aeronomy, BIRA-IASB, B-1180 Brussels, Belgium*
[11] *Max-Planck-Institut für Sonnensystemforschung, D-37077 Göttingen, Germany*

Accepted 2017 June 5. Received 2017 June 5; in original form 2017 April 13

ABSTRACT

As the spin axis of comet 67P/Churyumov–Gerasimenko (67P) is not normal to the orbital plane, 67P has strong seasonal changes in the illumination conditions on the nucleus' surface, with a short and intense summer in the Southern hemisphere. We have been monitoring these seasonal variations in the gas coma with the *Rosetta* Orbiter Spectrometer for Ion and Neutral Analysis (ROSINA) instrument suite aboard the ESA's *Rosetta* spacecraft. *Rosetta* followed 67P from its rendezvous in 2014 August, from a distance of almost 3.5 au to Sun, through perihelion at 1.24 au, and away from Sun again. In this study, we present the change of outgassing pattern during the 2016 March equinox based on measurements acquired with the ROSINA instruments: while H_2O, O_2 and NH_3 abundances rapidly decreased during this period, CO_2, CO, H_2S, CH_4 and HCN abundances decreased much less and showed a strong south–north heterogeneity for the whole period, thus not following Sun. Sublimation temperatures of the pure ices are found to be uncorrelated with the slope of the decrease for the minor species. This can be interpreted as a consequence of two different ice phases, water ice and CO_2 ice, in which the minor species are embedded in different relative abundances.

Key words: comets: individual: 67P/Churyumov–Gerasimenko.

1 INTRODUCTION

Comet 67P/Churyumov–Gerasimenko (hereafter 67P) was accompanied by the European Space Agency's *Rosetta* spacecraft for more than 2 yr along its trajectory around Sun. During this period, the comet crossed equinox for the first time in 2015 May, passed perihelion in 2015 August, and the second equinox in 2016 March, a few months before the mission was concluded with a final descent on the nucleus of the comet. On board was ROSINA, the *Rosetta* Orbiter Spectrometer for Ion and Neutral Analysis instrument suite, built to monitor composition and abundance of the volatiles in the coma of the comet (Balsiger et al. 2007). ROSINA consisted of a pressure sensor and two complementary mass spectrometers, which together were well suited for this task.

67P has a changing rotation period (Keller et al. 2015) around a rotation axis tilted with respect to the orbit plane (Sierks et al. 2015). Hence, the illumination conditions on the nucleus surface are constantly changing in direction as well as in intensity given the variation in heliocentric distance from perihelion at 1.24 au to

---

★ E-mail: sebastien.gasc@space.unibe.ch

Published by Oxford University Press on behalf of the Royal Astronomical Society

aphelion at 5.68 au. Summer on the Southern hemisphere is short and intense; summer on the Northern hemisphere is the opposite. This leads to strong seasonal heterogeneities of the volatiles in the coma, which was already observed early in the mission (Hässig et al. 2015; Le Roy et al. 2015). Given the strong asymmetries observed from north to south, it becomes especially interesting to track some of the major volatiles across equinox, when both hemispheres change season. The comet has been shown to be quite heterogeneous in its morphological features on the surface (Thomas et al. 2015; El-Maarry et al. 2016). However, deriving internal structure (Weissman 1986) and associated composition and heterogeneities in the sub-surface ices remain very difficult (Fulle et al. 2016). One reason for this is the build-up of a thermally insulating dust cover due to the sublimation of volatiles (Gortsas et al. 2011). Several mechanisms of the outgassing process have been discussed in the literature, including stratification of the ices based on their volatility including transport and re-condensation inside the nucleus, sublimation from the crystalline and from amorphous ices as well as from clathrates (Prialnik, Benkhoff & Podolak 2004; Marboeuf & Schmitt 2014; Lectez et al. 2015; Rubin et al. 2015; Mousis et al. 2016). One of the main goals of the *Rosetta* mission was hence to study the development of cometary activity and the processes in the surface layer of the nucleus (Glassmeier et al. 2007). The rapid changes in the illumination conditions over a moderately short-time period during the outbound equinox in 2016 March – when *Rosetta* spent time close to the nucleus – and associated variations in the distributions of the volatiles in the coma can add crucial information to the understanding of a comet's activity. The measurements obtained by ROSINA provide boundary conditions for deriving surface outgassing (Fougere et al. 2016; Marschall et al. 2016) and outgassing properties derived from numerical models of the nucleus interior and corresponding ices (Davidsson & Gutiérrez 2005; Rosenberg & Prialnik 2009; Marboeuf & Schmitt 2014). Section 2 of this paper presents a short description of the ROSINA instrument suite, followed by the details of the data treatment of the pressure sensor and both mass spectrometers. The obtained measurements are shown in Section 3 and our conclusions follow in Section 4.

2 MATERIALS AND METHODS

2.1 Instrument descriptions

ROSINA consists of the Comet Pressure Sensor (COPS) and two mass spectrometers, the Double Focusing Mass Spectrometer (DFMS) and the reflectron-type time-of-flight (RTOF) mass spectrometer. The three instruments work together to provide absolute density measurements of the major and minor volatiles in the coma of 67P.

In this study, we use data from all three instruments. It is therefore important to keep in mind that they all detect volatile neutral species, but that there are some important differences on how they measure. All three sensors ionize neutral particles by electron impact. However, their electron energies are different: 70, 45 and 0–150 eV for RTOF, DFMS and COPS, respectively. Whereas COPS measures the total neutral density every 2 s, but transmits data in a normal mode only every minute, RTOF collects one spectrum in 100 µs, but then accumulates 2 million spectra before the accumulated spectrum is transmitted. DFMS has to measure at integer mass numbers sequentially with an integration time of 20 s which yields 50 min for a full spectrum, including overhead for voltage stepping.

While COPS measures the combined density of all the species and does not separate masses, RTOF has a mass resolution $m/\Delta m$ of 500 and a mass range in the mode used for these measurements from 1 to 120 u, and DFMS has a mass resolution of $m/\Delta m \approx$ 9000 (at FWHM and mass 28 u) covering mostly masses from 13 to 100 u. RTOF is operated in a counting mode, while DFMS measures in an analogue mode the charge deposited from the MCP on to the anode. COPS measures directly the ion current. Sensitivity for RTOF and COPS depends mainly on the ionization cross-section of the different species, while DFMS has a mass-sensitive transmission and adjustable detector gain, which has to be taken into account. For more details, the reader is referred to Balsiger et al. (2007) and Scherer et al. (2006).

2.2 Data treatment

The RTOF data in this study were acquired with the storage source, designed to study neutrals (Balsiger et al. 2007). The data reduction is similar to that described in Gasc et al. (2017) and consists of (i) the correction of the ADC pattern for each spectrum individually, (ii) the application of the mass scale for each spectrum, (iii) the fitting and the numerical integration of each peak of interest, here H_2O and CO_2, and (iv) the scaling of the RTOF relative densities to the COPS measured absolute density values. Additionally, the first 30 min after each spacecraft manoeuvre has been systematically removed to minimize the impact of the outgassing of the ion source following the switch ON and heating up of RTOF.

The DFMS data in this study were acquired in a high-resolution mode (Balsiger et al. 2007). The data reduction process is the same as presented in Le Roy et al. (2015) and Calmonte et al. (2016) and consists of (i) MCP-related intensity correction, (ii) a mass calibration, (iii) the determination of the peak area per spectrum and per species and (iv) the conversion to number density for each species. For (iii), an automatic analysis software described in Calmonte et al. (2016) has been used to determine the peak area corresponding to CH_4, NH_3, H_2O, HCN, CO, O_2, H_2S and CO_2. The well-known contribution of CO from fragmentation of CO_2 has been subtracted from the CO signal to leave only cometary parent CO. The conversion to density (iv) is based on scaling the DFMS relative abundances measurements to the measured COPS total density shown in Fig. 1 as described in Gasc et al. (2017).

2.3 Observation period

The measurements discussed in the following were obtained with ROSINA during the extension of the *Rosetta* mission between 2016 January 1 and August 1, i.e. at heliocentric distances increasing from 2.0 to 3.5 au. The total density derived from the COPS measurements as well as some relevant orbital parameters of 67P and *Rosetta* during this time period are given in Fig. 1.

The chosen time frame covers the outbound equinox that occurred on 2016 March 21 at a heliocentric distance of 2.63 au. Coincidently, this distance matches the water iceline (or water condensation front), located around 2.7 au (Jewitt et al. 2007). During the studied period, the mean cometary activity decreased with distance as expected compared to perihelion, allowing the *Rosetta* spacecraft to get closer to the nucleus, from 90 to 7 km from the comet centre. Unfortunately, no ROSINA data are available for the interval 2016 March 23–2016 April 27 due to a tail excursion that brought *Rosetta* to a distance of 1000 km from the nucleus. Apart from this excursion, *Rosetta* remained mostly in a terminator orbit and studied the nucleus of 67P with a nadir off-pointing most of the time smaller than 10°. In particular, fast slews and large off-pointing angles can lead to increased release of volatiles trapped

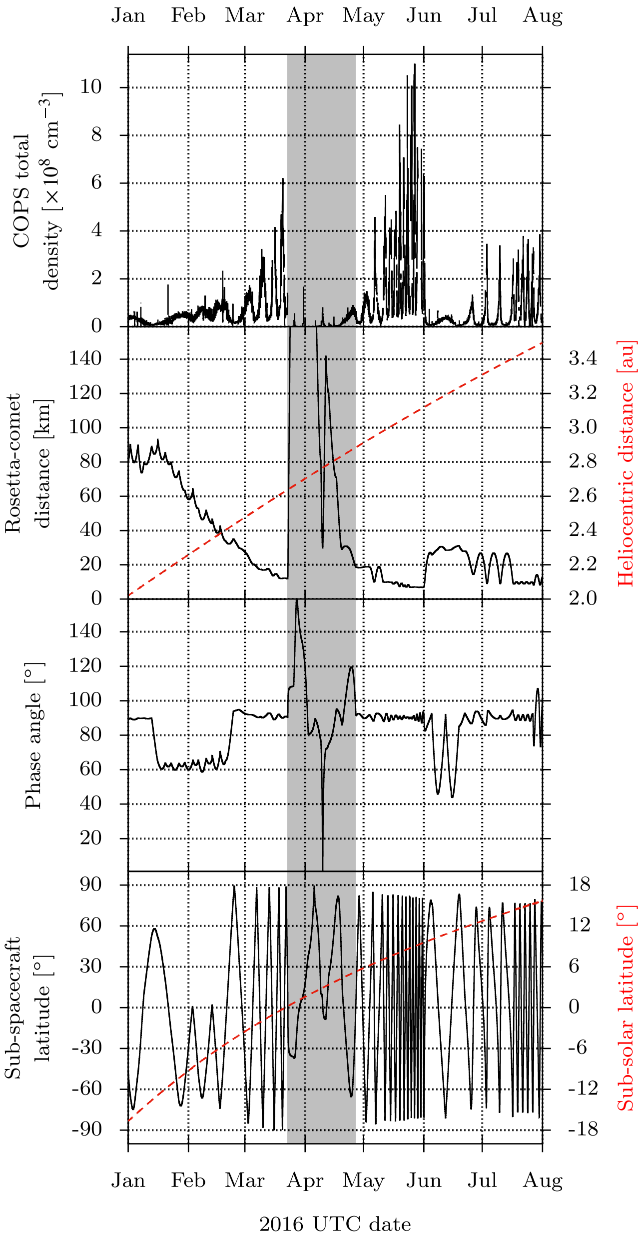

Figure 1. Top panel: COPS density. Second panel: distance from *Rosetta* to the nucleus centre (black) and heliocentric distance (dashed red). Third panel: phase angle. Bottom panel: sub-spacecraft latitude (black) and sub-solar latitude (dashed red). The period in grey corresponds to the tail excursion (2016 March 23–2016 April 27) when no measurements were acquired with the ROSINA mass spectrometers as the densities at these distances were too low.

on spacecraft surfaces that suddenly get illuminated and heat up. Furthermore, a fast-changing viewing geometry can affect the derived abundance ratios, especially in the case of DFMS, which measures each integer mass/charge ratio sequentially. As a consequence, time-periods with large slews have been removed from our analysis.

3 RESULTS

The time evolution of eight species measured by RTOF (H_2O and CO_2) and DFMS (CH_4, NH_3, H_2O, HCN, CO, O_2, H_2S and CO_2) is presented in this section. Table 1 summarizes the masses of these species and provides abundances relative to H_2O averaged over the pre-equinox period (2.0–2.7 au) and the post-equinox period (3.1–3.5 au) described in Section 2.3. As ROSINA measured abundances at the location of the spacecraft, these densities of course scale with cometocentric distance. We therefore have multiplied the measured densities with r^2, the squared distance of the *Rosetta* spacecraft to the nucleus centre, to compensate for the radial decrease of the density, an approximation consistent with recent modelling efforts of the neutral gas environment (Bieler et al. 2015b; Fougere et al. 2016).

Table 1. Average abundances relative to H_2O of the species studied in this work, for the periods 2016 January–April (2.0–2.7 au, middle column) and 2016 June–August (3.1–3.5 au, rightmost column). Species are sorted according to their abundance to H_2O for the later period.

Molecule	Abundance to H_2O pre-equinox (2.0–2.7 au)	Abundance to H_2O post-equinox (3.1–3.5 au)
CO_2	$(3.69 \pm 0.14) \times 10^{-1}$	3.31 ± 0.09
H_2O	1.00	1.00
CO	$(5.17 \pm 0.15) \times 10^{-2}$	$(5.23 \pm 0.12) \times 10^{-1}$
H_2S	$(3.77 \pm 0.10) \times 10^{-2}$	$(3.00 \pm 0.06) \times 10^{-1}$
CH_4	$(7.09 \pm 0.38) \times 10^{-3}$	$(1.08 \pm 0.03) \times 10^{-1}$
HCN	$(5.45 \pm 0.16) \times 10^{-3}$	$(4.97 \pm 0.11) \times 10^{-2}$
O_2	$(1.21 \pm 0.02) \times 10^{-2}$	$(1.97 \pm 0.03) \times 10^{-2}$
NH_3	$(3.78 \pm 0.13) \times 10^{-4}$	$(1.32 \pm 0.13) \times 10^{-4}$

3.1 RTOF

The time evolutions of the H_2O and CO_2 densities measured by RTOF are presented in Fig. 2 and cover the time period from 2016 January to June. After 2016 June, the RTOF observation times were reduced due to power limitations.

Two different trends can be observed in the RTOF data. On the one hand, CO_2 abundance decreases relatively slowly as a function of the comet's distance from Sun, while showing large variations with changing sub-spacecraft latitude. On the other hand, H_2O shows small variations with sub-spacecraft latitude but a significant decrease with the increasing heliocentric distance, correlated with the sub-solar latitude.

The anticorrelation of CO_2 with the sub-spacecraft latitude already observed by RTOF before perihelion (Mall et al. 2016) was still clearly visible after perihelion, independent of the outbound equinox. On a shorter time-scale, the high-time resolution of RTOF (200 s) translates to a high-spatial resolution in the CO_2 time series, where diurnal variations are as well still visible and similar to measurements earlier in the mission (see Fig. 3).

To a lesser extent, the RTOF H_2O measurements show the anticorrelation with the sub-spacecraft latitude observed after the inbound equinox; before the inbound equinox, water molecules were emanating more abundantly from the Northern hemisphere, which was translated into a clear correlation with the latitude (Hoang et al. 2017). The sub-solar latitude changed slowly reaching about 16° north by the end of July. This is clearly different from the situation we had at the beginning of the mission in 2014 September when Sun was almost at 50° north for the same heliocentric distances. Accordingly, while the heterogeneity for water between north and south did change after equinox, it did not reach the situation where much more water was released from the Northern hemisphere than from the south as in 2014 September (Hässig et al. 2015). The pattern we see is rather flat, indicating that water is following the

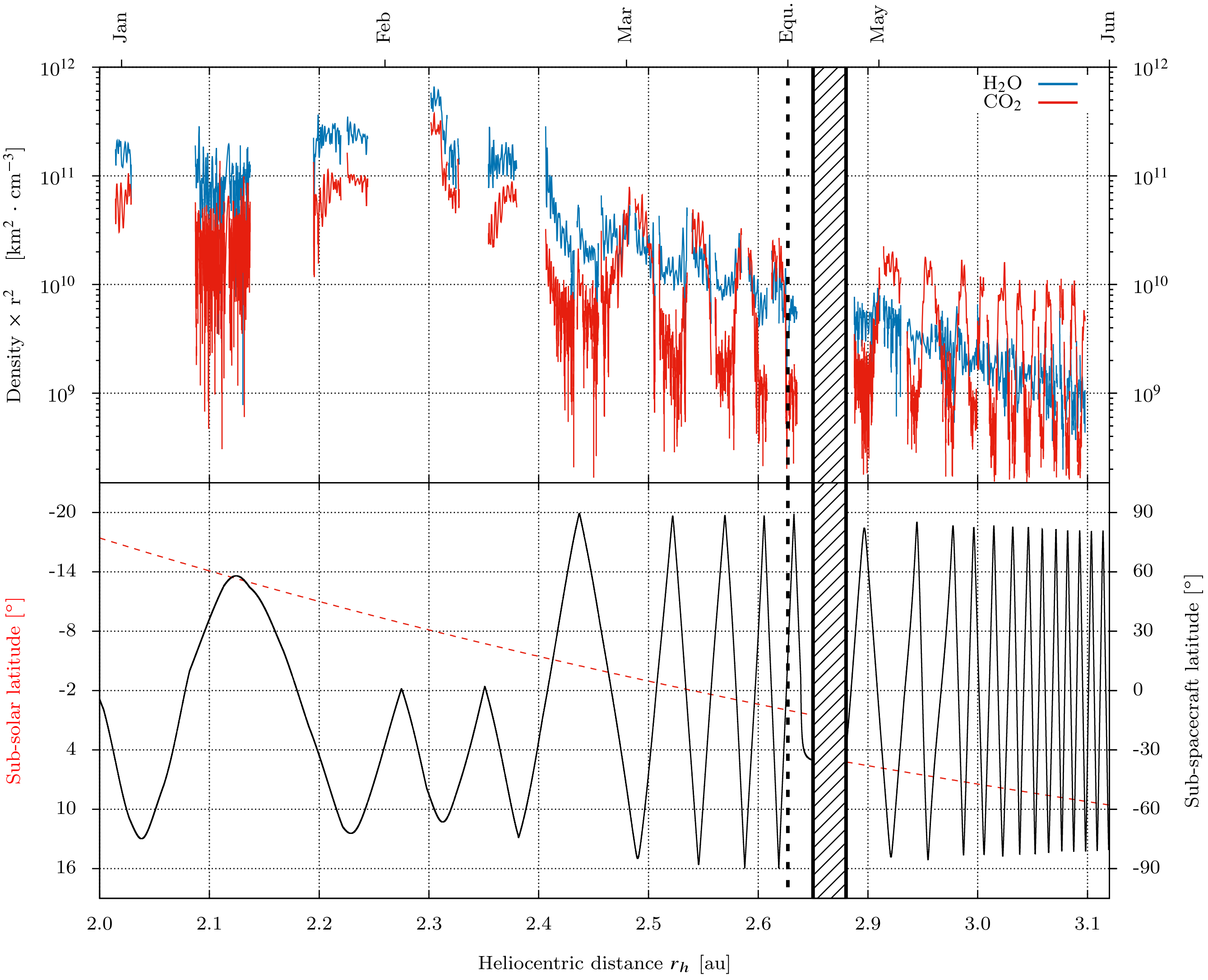

Figure 2. Top panel: evolution of H_2O (blue) and CO_2 (red) densities measured by RTOF between 2016 January and June, corresponding to a heliocentric distance ranging from 2.0 to 3.1 au. The densities derived from the RTOF measurements have been multiplied by r^2, with r the distance from the *Rosetta* spacecraft to the centre of the comet, to compensate for the decrease of the atmospheric density which follows a r^{-2} law. Bottom panel: sub-solar latitude (dashed red) and sub-spacecraft latitude (black).

sub-solar latitude to the equator and then beyond. This can be seen if looking carefully at Fig. 3, where water actually peaks around 0° latitude in 2016 May.

3.2 DFMS

The time evolutions of the densities measured by DFMS for CH_4, NH_3, H_2O, HCN, CO, O_2, H_2S and CO_2 are shown in Fig. 4. The DFMS data from 2016 May (heliocentric distance from 2.91 to 3.12 au) are not shown due to the small amount of data points for the studied species in this period.

DFMS confirms the global trend observed with RTOF for H_2O and CO_2 and allows distinction of two populations: species such as H_2O, O_2 and NH_3 show less difference in their north/south abundances than CO_2, CO, H_2S, CH_4 and HCN, which stay high over southern latitudes and are significantly lower at northern latitudes. These two populations are in agreement with the results shown by Luspay-Kuti et al. (2015), except for HCN, which in 2014 showed a significantly better correlation with H_2O than with CO_2. To quantify the different behaviour, we have fitted the data for latitudes $>30°$ (north) and $<-30°$ (south) with a power law to the heliocentric distances. The power-law indices α are given in Table 2 and the corresponding plots can be found in the Appendix. No correlation of the power-law indices α with the sublimation temperature of pure ices is observed (see Fig. 5). We have also calculated the mean ratio $R_{S/N}$ between south and north abundances for 2016 March and July. The generally steeper decrease with heliocentric distance in the south compared to north is most probably an effect of the change in sub-solar latitude: more northern parts and less southern parts are illuminated with time and therefore with heliocentric distance. Accordingly, the ratios between south and north are smaller in 2016 May than in 2016 March.

The strong heterogeneity of the coma can be mostly explained by solar insolation. In addition, however, some inhomogeneity of the nucleus surface has to be taken into account (Fougere et al. 2016), which is mostly attributed to dust coverage in the north and fresher material in the south. Fig. 6 illustrates the changes in abundance with the sub-spacecraft latitude for 2016 March. No difference between

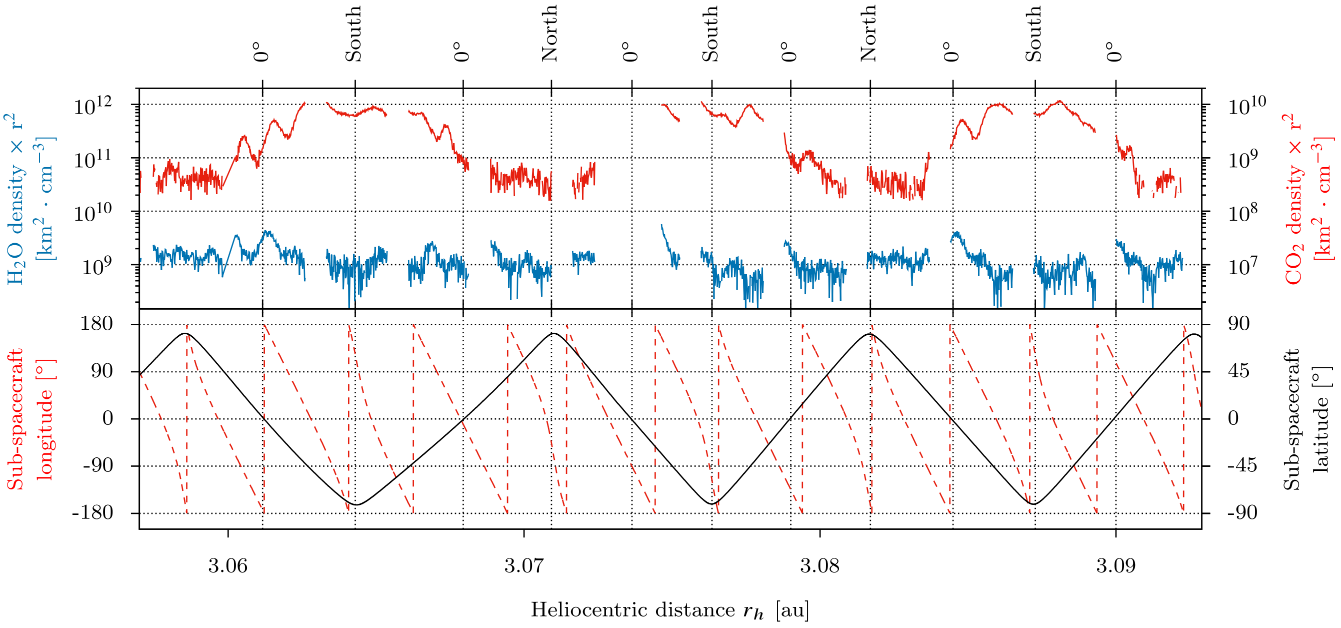

Figure 3. Top panel: evolution of H_2O (blue) and CO_2 (red) densities measured by RTOF between 2016 May 22 and 2016 May 28 (heliocentric distance from 3.057 to 3.093 au). Bottom panel: sub-spacecraft longitude (red) and sub-spacecraft latitude (black), with minimum and maximum sub-spacecraft latitudes and crossings of the equator indicated on top.

measurements acquired at dawn (local time close to 6:00) and at dusk (local time close to 18:00) can be observed. During and after the outbound equinox, the variations between the two hemispheres of H_2O, together with O_2 and NH_3, are much weaker than before the outbound equinox, but the long-term trend reveals a considerable decrease in the water sublimation. This decrease is due mostly to the increasing heliocentric distance, as the period around equinox coincided with the crossing of the snow line of water.

O_2 was known to follow H_2O in the coma of comet 67P/Churyumov–Gerasimenko before the inbound equinox with ratios of 0.01–0.1 compared with H_2O and a mean O_2/H_2O ratio from 2014 September to 2015 April of 0.0380 ± 0.0085 (Bieler et al. 2015a). After the outbound equinox, these ratios remained similar (see Table 1), with a temporal evolution of O_2 following closely the evolution of H_2O. Fig. 7 shows correlation plots for all species with respect to H_2O and CO_2 for two periods, near and post equinox (2.4–2.7 and 3.2–3.5 au, respectively). The O_2–H_2O correlation is clear for both periods. On the short term H_2O and NH_3 correlate well, but on the long term, between 3.2 and 3.5 au and after the outbound equinox, the evolution of NH_3 is flatter with distance to Sun. Most other species show very little correlation with H_2O, although some intrinsic correlation is given by the change in heliocentric distance over the periods, which affects all species, but not all alike. CO_2 and H_2O do not correlate, whereas CO, CH_4, HCN and H_2S correlate rather well with CO_2.

The species varying strongly with the sub-spacecraft latitude during equinox, i.e. CO_2, CO, H_2S, CH_4 and HCN, all had very similar trends, especially before 2016 April and the exchange of seasons between both hemispheres: detected more abundantly in the Southern hemisphere, the outgassing of these molecules decreased slowly and regularly on the long term, following the increasing heliocentric distance and thus the decrease of the solar input. These similarities were observed likely post-equinox, with a slight difference regarding H_2S, CH_4 and HCN which locally resembled water, around 3.18 au, i.e. with higher abundances at sub-spacecraft latitudes close to 0°.

4 DISCUSSIONS AND CONCLUSIONS

ROSINA, RTOF and DFMS monitored a set of eight molecules, including CH_4, NH_3, H_2O, HCN, CO, O_2, H_2S and CO_2, for several weeks throughout the outbound equinox of comet 67P. *Rosetta* orbited the comet in the terminator plane and hence covered both hemispheres of the comet repetitively. This provided the unique possibility to compare not only the different outgassing patterns of these molecules but also their temporal variations as the illumination of the nucleus was changing. Strong north/south heterogeneities have been observed, similar to observations early in the mission which were also performed beyond 3 au (Hässig et al. 2015), although in the pre-perihelion period the total outgassing was always dominated by H_2O (Fougere et al. 2016). Water seems to follow the sub-solar latitude, which was expected given its rather high sublimation temperature (Hansen et al. 2016). CO_2 does not trend the same way, as the Southern hemisphere remained its main source and, hence, towards the end of the mission, the southern, winter hemisphere dominated the outgassing of 67P through CO_2.

The general decrease over the period in abundances varies greatly from species to species. It does not follow the sublimation temperatures of pure ices (Table 2). The smallest decrease is seen in CO_2, which exhibits at the same time the highest variation between north and south during equinox. The power law with heliocentric distance is roughly −2 for the Southern hemisphere and −0.7 for the northern part. That means the outgassing of CO_2 is not an instant response to solar illumination, but rather due to heat diffusion into and thermal inertia of deeper layers below the surface. On the other hand, H_2O seems to follow the subsolar latitude. The power law with an exponent of −7 and −11 for north and south, respectively, shows that temperatures of the nucleus are below the sublimation temperature of water on both hemispheres, even at subsolar

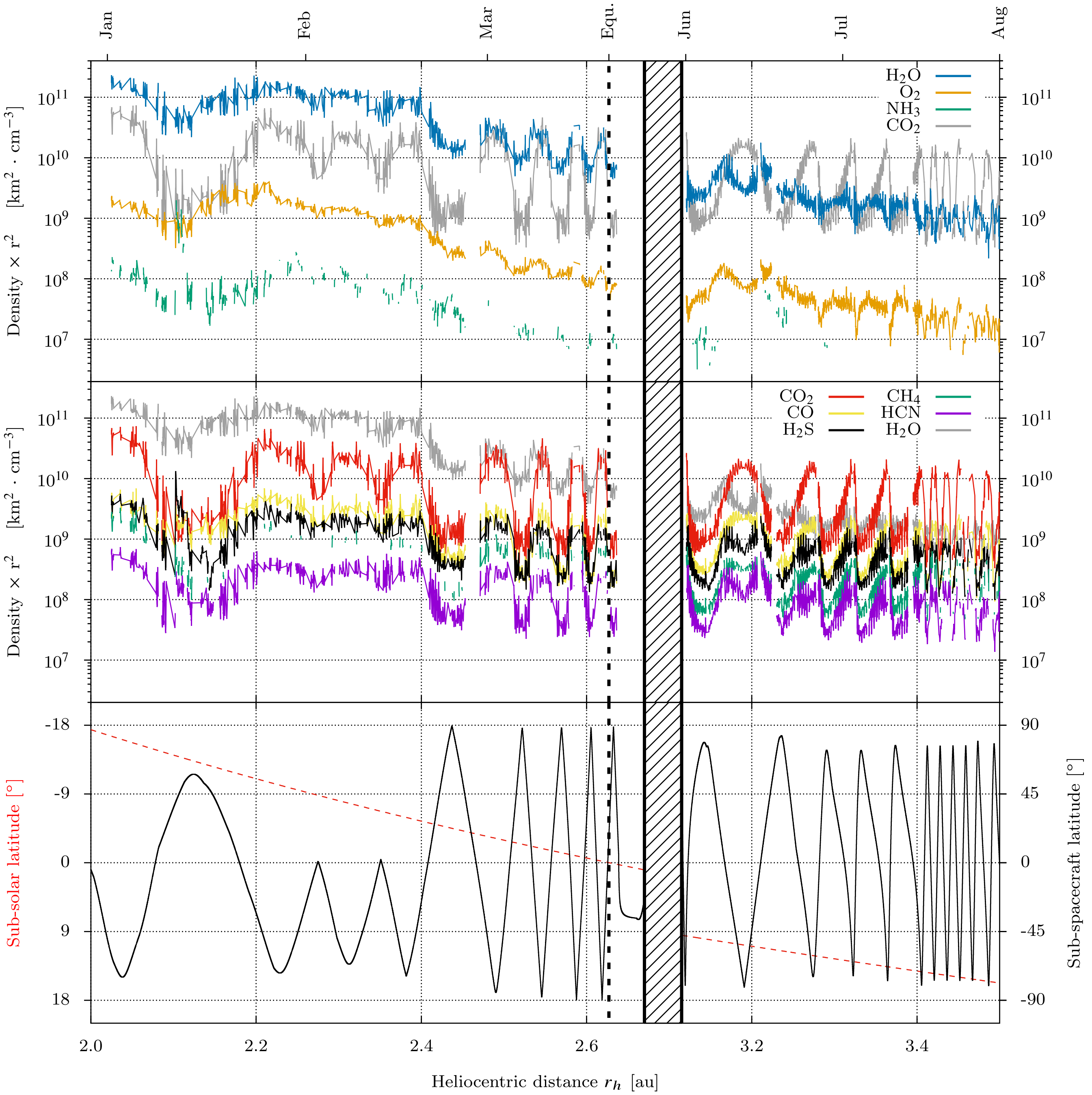

Figure 4. Evolution of the most abundant species detected by DFMS between 2016 January and August, at heliocentric distances ranging from 2.0 to 3.5 au. In the same way as for the RTOF measurements, the DFMS densities have been multiplied by r^2, the squared distance from the *Rosetta* spacecraft to the cometary nucleus. Top panel: H_2O, O_2 and NH_3; CO_2 is added in grey for comparison. Middle panel: CO_2, CO, H_2S, CH_4 and HCN; H_2O is added in grey for comparison. Bottom panel: sub-spacecraft latitude (black) and sub-solar latitude (red).

latitudes. O_2 is a special case. Its exponents of −6.7 to −8.9 for the power law are close to the water, although its volatility is very high, second only to CO, confirming the close relationship between water and O_2 (Bieler et al. 2015a). Molecular oxygen, O_2, which, according to Bieler et al. (2015a), hints at formation inside pre-solar water ices by irradiation processes, leads to a close relation between the two molecules (cf. Mousis et al. 2016) despite grossly different sublimation temperatures (see Table 2). If we include earlier findings, e.g. the lack of correlation of molecular nitrogen, N_2, with water (Balsiger et al. 2015) and the correlation of O_2 with water, we end up with two species, N_2 and O_2, with almost indistinguishable desorption patterns as a function of temperature (Collings et al. 2004) but vastly different outgassing profiles measured at the comet.

After equinox, CO_2 remained dominant in the Southern hemisphere, more abundant than on the better illuminated Northern hemisphere. The same applied to CO, H_2S, CH_4 and HCN, although some of them with a less strong north/south variation in the measured density. According to Collings et al. (2004), species that are co-deposited with water at cold temperatures, where water is amorphous, desorb in three steps: the first step is close to the

Table 2. Other properties of the species studied in this work. Sublimation temperatures T_{sub} are derived from Fray & Schmitt (2009) (sublimation from pure ices). The power-law indices α were calculated for latitudes $>30°$ (north) and $<-30°$ (south), via a fit of the data with a power law to the heliocentric distances. Mean ratios $R_{\mathrm{S/N}}$ between north and south abundances for 2016 March and July are given in the two rightmost columns. Species are sorted according to their slope α – south with heliocentric distance for the Southern hemisphere.

Molecule	Mass [u/e]	T_{sub} [K]	α – North	α – South	$R_{\mathrm{S/N}}$ – March	$R_{\mathrm{S/N}}$ – July
H_2O	18.01	144	– 7.32 ± 0.04	– 11.42 ± 0.05	2.68 ± 0.06	0.62 ± 0.02
O_2	31.99	30	– 6.66 ± 0.05	– 8.92 ± 0.05	1.72 ± 0.04	0.81 ± 0.01
NH_3	17.03	102	– 4.88 ± 0.18	–	–	–
H_2S	33.99	80	– 1.74 ± 0.05	– 3.59 ± 0.03	4.66 ± 0.11	2.31 ± 0.04
CH_4	16.03	36	– 2.26 ± 0.07	– 3.21 ± 0.03	–	3.88 ± 0.10
HCN	27.01	126	– 1.57 ± 0.05	– 2.76 ± 0.03	4.80 ± 0.18	2.72 ± 0.06
CO_2	43.99	86	– 0.68 ± 0.05	– 2.18 ± 0.04	22.20 ± 0.66	11.53 ± 0.21
CO	27.99	28	– 2.21 ± 0.05	– 1.83 ± 0.03	9.98 ± 0.24	6.07 ± 0.09

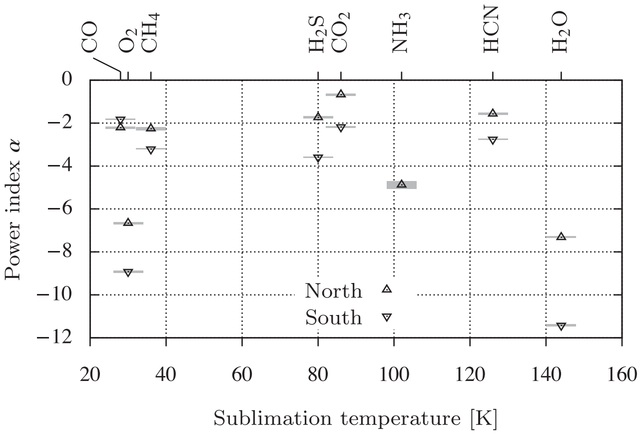

Figure 5. Power-law indices α versus sublimation temperature, for the studied species and for latitudes $>30°$ (north) and $<-30°$ (south). The grey boxes represent the error on α.

sublimation temperatures of pure ices, the second step, which is the same for all species more volatile to water, happens at ≈120 K, where water converts from amorphous to crystalline (volcano desorption) and the third step happens at the sublimation temperature of water. The behaviour of the species studied here does not follow this scheme. There are clear differences in desorption patterns between species that cannot be explained by their volatility. For example, CH_4 (36 K) and HCN (126 K) have very different sublimation temperatures, but show very similar slopes with heliocentric distances. O_2 and CH_4 have very similar sublimation temperatures, but have completely different slopes. This cannot be explained by pure ices, but hints at mixtures of species and ice types. The heterogeneity seen in most species between north and south might have their origin in the hemispherical differences between the northern and southern surfaces of the comet. The intense summer in the south sets free fresh material and the outgassing of volatiles continuously sheds any accumulated dust mantle. Kramer et al. (2017) showed that sources of enhanced gas activity were correlated to the location of dust outbursts observed within 3 months around perihelion (2015 July–September). Furthermore, these gas sources remained active until the end of the mission, much longer compared to the dust outbursts that typically last for only a few minutes and dust itself appears to be dry (De Keyser et al. 2017). In the north, lower outgassing rates and back-fall of dust (Agarwal et al. 2016; Keller et al. 2017) possibly quench the outgassing rate. If such grains contain any volatiles such as water, outgassing from back-fall would certainly be dominated by these species. Species of higher volatility would be long lost by the time of redeposition. Therefore, higher relative abundance of water is not in contradiction to the scenario proposed by Keller et al. (2017).

There exist models of desorption from cometary nuclei and laboratory experiments where species more volatile than water desorb and migrate outwards and inwards where they freeze out again (e.g. Mekler, Prialnik & Podolak 1990, and references therein; Notesco & Bar-Nun 2000, and references therein). However, most of the models and all of the experiments take into account much larger relative abundances of the minor species. In our data, relative abundances, except for CO_2, were all in the 1 per cent range before and around equinox and therefore very minor. It cannot be expected that pure ices of these minor species exist in the comet. Their sublimation temperature, with the exception of CO_2, may therefore be irrelevant because for desorption of a minor species in a matrix of volatiles and dust, van der Waals forces in the host matrix, which are different from the pure ices, are responsible. The continuous strong outgassing from the southern parts over many months and even years with very little water is probably indicative of CO_2 ice. CO_2 was found to be abundant in the coma over the Southern hemisphere already at the beginning of the *Rosetta* mission (Hässig et al. 2015) after the southern part had been in shadow for 5 yr. Experimentally, it has been shown by Fayolle et al. (2011) that with an intimate mixture of H_2O:CO_2 of 5:1, the topmost layer saturates quickly with H_2O molecules and the pores become void of more volatile species below the sublimation temperature of H_2O and the surface layer is then impenetrable for CO_2. This would suppress CO_2 outgassing quite rapidly, once the temperature of the surface layer is below the sublimation temperature of water. This clearly does not happen at the comet (Fig. 2). Our conclusion is that the ices cannot be intimately mixed, be it due to primordial separation or by evolution.

Therefore, a possible explanation for the observed sublimation temperature-independent diversity in desorption could be that minor species are partly embedded in CO_2 and partly in H_2O ices. Their different power laws with heliocentric distance are then indicative for the ratio between how much is embedded in CO_2 and are therefore co-desorbed with CO_2 and how much is embedded in water and is released by the volcano effect or by sublimation of water. Good examples are H_2S and HCN, which generally follow CO_2 (power-law indices of −1.57 to −3.59), but show some signature of the water release not seen in CO_2 like the double peak at, e.g. 3.18 au (Fig. 4). This means that the nucleus consists partly of CO_2 dominated ices, partly of H_2O dominated ones. If this is a primordial heterogeneity or due to differentiation because of

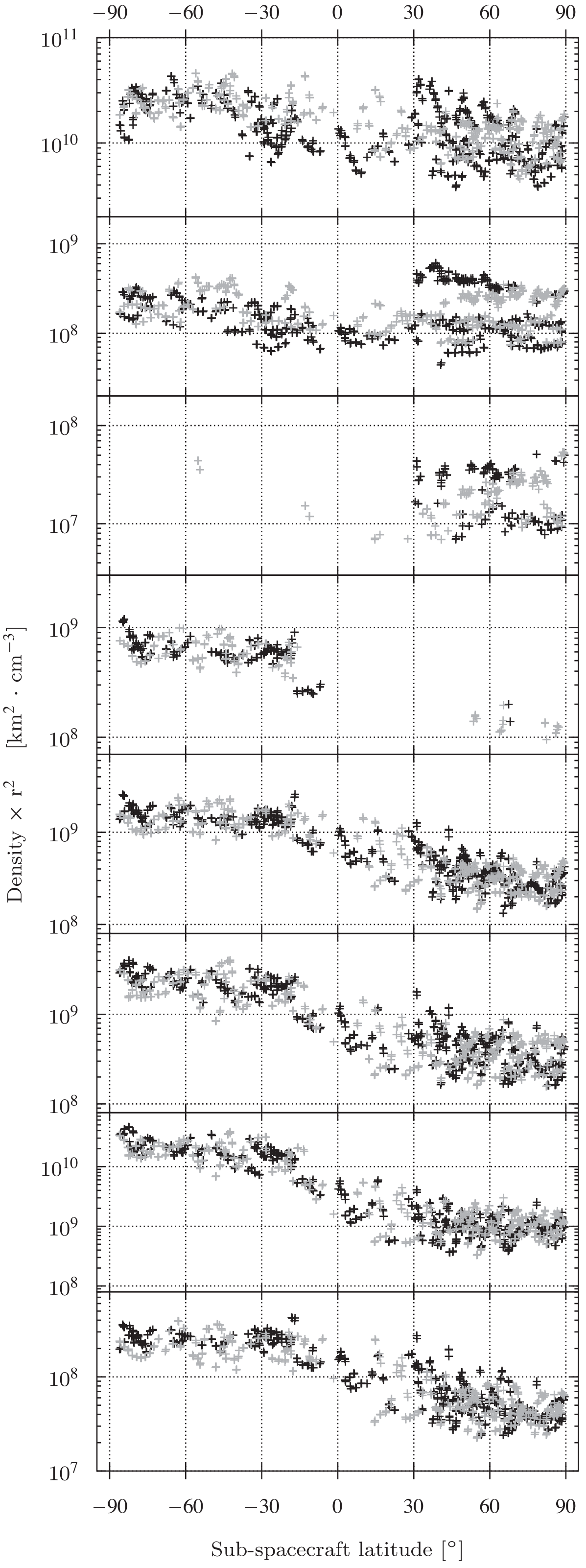

Figure 6. Evolution of the studied species with respect to the sub-spacecraft latitude for the time period 2016 February 19–2016 March 23 (2.40–2.63 au). Grey points represent measurements acquired at dawn (local time close to 6:00), whereas black points represent measurements acquired at dusk (local time close to 18:00).

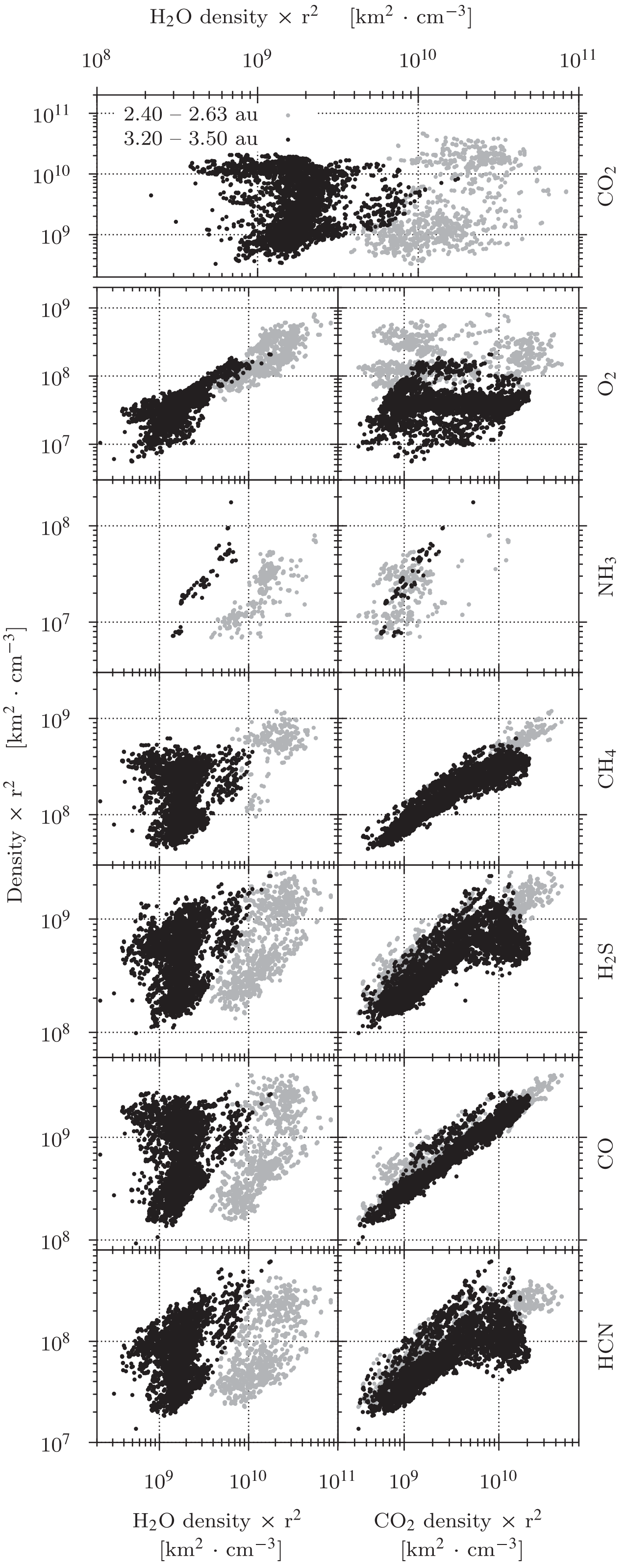

Figure 7. Top: scatter plot of CO_2 versus H_2O. Lower left graphs: scatter plots of the studies species versus H_2O. Lower right graphs: scatter plots of the studies species versus CO_2. The measurements shown here belong to the time period 2016 February 19–2016 March 23 (2.40–2.63 au, grey), and June 13–August 1 (3.20–3.50 au, black).

evolution is hard to say. There is, however, no indication that polarity of the species plays a role, as one might expect that polar species are more likely to be embedded in water and apolar ones in CO_2. Furthermore, also how each molecule is embedded in the ice, either through trapping, formation in the ice through radiation, grain-surface chemistry or refreezing, affects probably the structure and therefore the van der Waals forces in the matrix and the later desorption. Clearly, more laboratory work on low mixing ratios in H_2O and, in particular, CO_2 ice has to be done.

Before the end of the *Rosetta* mission, the comet transitioned to be dominated by highly volatiles. Towards outbound equinox in 2016 March at ≈2.6 au, the CO_2 abundance increased with respect to H_2O and, while the turnover was not instant, CO_2 became the dominant molecule in the coma of the comet, at least at the location of *Rosetta* in the terminator plane. This behaviour is associated with the low sublimation temperature and is in line with what has been observed at other comets, such as CO (possibly with contribution from CO_2) versus the water fragment OH at Hale-Bopp (Biver et al. 2002).

ACKNOWLEDGEMENTS

The authors thank the following institutions and agencies, which supported this work. Work at the University of Bern was funded by the State of Bern, the Swiss National Science Foundation and the European Space Agency PRODEX (PROgramme de Développement d'EXpériences scientifiques) Program. This work was supported by CNES (Centre National d'Etudes Spatiales) grants at LATMOS (Laboratoire Atmosphères, Milieux, Observations Spatiales) and IRAP (Institut de Recherche en Astrophysique et Planétologie). Work at the University of Michigan was funded by NASA under contract JPL-1266313. Research at Southwest Research Institute is funded by NASA through JPL contract No.196541. Work by JHW at the Southwest Research Institute was funded by NASA JPL subcontract NAS703001TONMO710889. Work at BIRA-IASB was supported by the Belgian Science Policy Office via PRODEX/ROSINA PEA90020 and 4000107705 and by the F.R.S.-FNRS grant PDR T.1073.14 'Comparative study of atmospheric erosion'. Work at the Max Planck Institute for Solar system Research was funded by the Max-Planck Society and Bundesministerium für Wirtschaft und Energie under contract 50QP1302. ROSINA would not give such outstanding results without the work of the many engineers, technicians and scientists involved in the mission, in the *Rosetta* spacecraft and in the ROSINA instrument team over the past 20 yr, whose contributions are gratefully acknowledged. *Rosetta* is an European Space Agency (ESA) mission with contributions from its member states and NASA. We thank herewith the work of the whole ESA *Rosetta* team. All ROSINA flight data have been released to the PSA archive of ESA and to the PDS archive of NASA.

REFERENCES

Agarwal J. et al., 2016, MNRAS, 462, S78
Balsiger H. et al., 2007, Space Sci. Rev., 128, 745
Balsiger H. et al., 2015, Sci. Adv., 1
Bieler A. et al., 2015a, Nature, 526, 678
Bieler A. et al., 2015b, A&A, 583, A7
Biver N. et al., 2002, Earth Moon Planets, 90, 5
Calmonte U. et al., 2016, MNRAS, 462, S253
Collings M. P., Anderson M. A., Chen R., Dever J. W., Viti S., Williams D. A., McCoustra M. R. S., 2004, MNRAS, 354, 1133
Davidsson B. J. R., Gutiérrez P. J., 2005, Icarus, 176, 453
De Keyser J. et al., 2017, MNRAS, this issue
El-Maarry M. R. et al., 2016, A&A, 593, A110
Fayolle E. C., Öberg K. I., Cuppen H. M., Visser R., Linnartz H., 2011, A&A, 529, A74
Fougere N. et al., 2016, MNRAS, 462, S156
Fray N., Schmitt B., 2009, Planet. Space Sci., 57, 2053
Fulle M., Altobelli N., Buratti B., Choukroun M., Fulchignoni M., Grün E., Taylor M. G. G. T., Weissman P., 2016, MNRAS, 462, S2
Gasc S. et al., 2017, Planet. Space Sci., 135, 64
Glassmeier K.-H., Boehnhardt H., Koschny D., Kührt E., Richter I., 2007, Space Sci. Rev., 128, 1
Gortsas N., Kührt E., Motschmann U., Keller H. U., 2011, Icarus, 212, 858
Hansen K. C. et al., 2016, MNRAS, 462, S491
Hässig M. et al., 2015, Science, 347, aaa0276
Hoang M. et al., 2017, A&A, 600, A77
Jewitt D., Chizmadia L., Grimm R., Prialnik D., 2007, in Reipurth V. B., Jewitt D., Keil K., eds, Protostars and Planets V. Univ. Arizona Press, Tucson, p. 863
Keller H. U., Mottola S., Skorov Y., Jorda L., 2015, A&A, 579, L5
Keller H. U. et al., 2017, MNRAS, this issue
Kramer T., Läuter M., Rubin M., Altwegg K., 2017, MNRAS
Le Roy L. et al., 2015, A&A, 583, A1
Lectez S., Simon J.-M., Mousis O., Picaud S., Altwegg K., Rubin M., Salazar J. M., 2015, ApJ, 805, L1
Luspay-Kuti A. et al., 2015, A&A, 583, A4
Mall U. et al., 2016, ApJ, 819, 126
Marboeuf U., Schmitt B., 2014, Icarus, 242, 225
Marschall R. et al., 2016, A&A, 589, A90
Mekler Y., Prialnik D., Podolak M., 1990, ApJ, 356, 682
Mousis O. et al., 2016, ApJ, 823, L41
Notesco G., Bar-Nun A., 2000, Icarus, 148, 456
Prialnik D., Benkhoff J., Podolak M., 2004, in Festou M. C., Keller H. U., Weaver H. A., eds, Modeling the Structure and Activity of Comet Nuclei. Univ. Arizona Press, Tucson, p. 359
Rosenberg E. D., Prialnik D., 2009, Icarus, 201, 740
Rubin M. et al., 2015, Science, 348, 232
Scherer S. et al., 2006, Int. J. Mass Spectrom., 251, 73
Sierks H. et al., 2015, Science, 347, aaa1044
Thomas N. et al., 2015, Science, 347, aaa0440
Weissman P. R., 1986, Nature, 320, 242

APPENDIX: SUPPLEMENTARY MATERIAL

The densities of the eight studied molecules have been fitted using the non-linear least-squares Marquardt–Levenberg algorithm, for latitudes >30° (north) and <−30° (south), and based on the following power law:

$$n \cdot r^2 = C \cdot r_\mathrm{h}^{\alpha}$$

with n the density of the fitted species, r the distance of the *Rosetta* spacecraft to the nucleus centre, r_h the heliocentric distance, α the fitted power-law indices and C a constant parameter. The fit was done using logarithmic values to account for the small weight of the low densities on the y axis:

$$f_\mathrm{fit}(r_\mathrm{h}) = \alpha \cdot \log_{10}(r_\mathrm{h}) + \log_{10}(C)$$

The data points, their associated fit and the fitted value of α are shown in Figs A1 and A2.

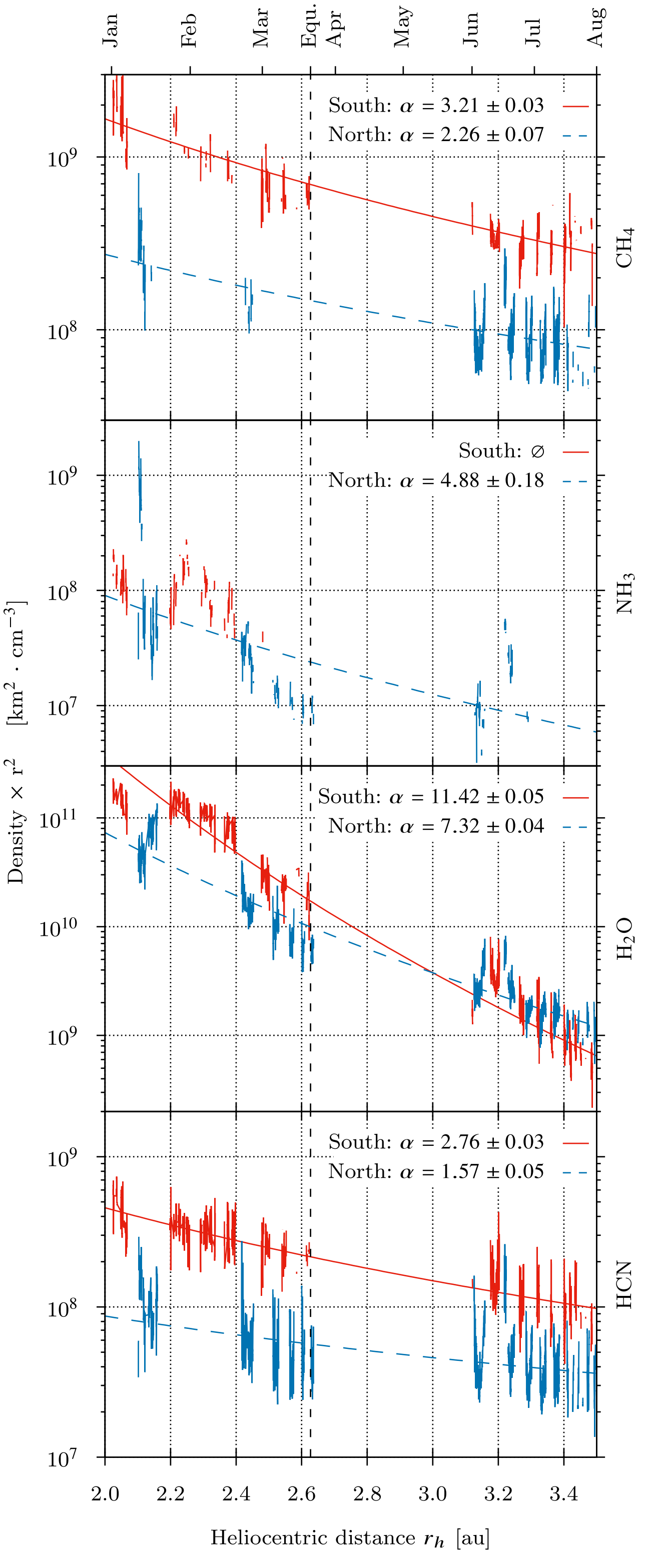

Figure A1. From top to bottom: densities ($\times r^2$) of CH_4, NH_3, H_2O and HCN, fitted with a power law to the heliocentric distance, for sub-spacecraft latitudes >30° (north – dashed blue) and <−30° (south – red).

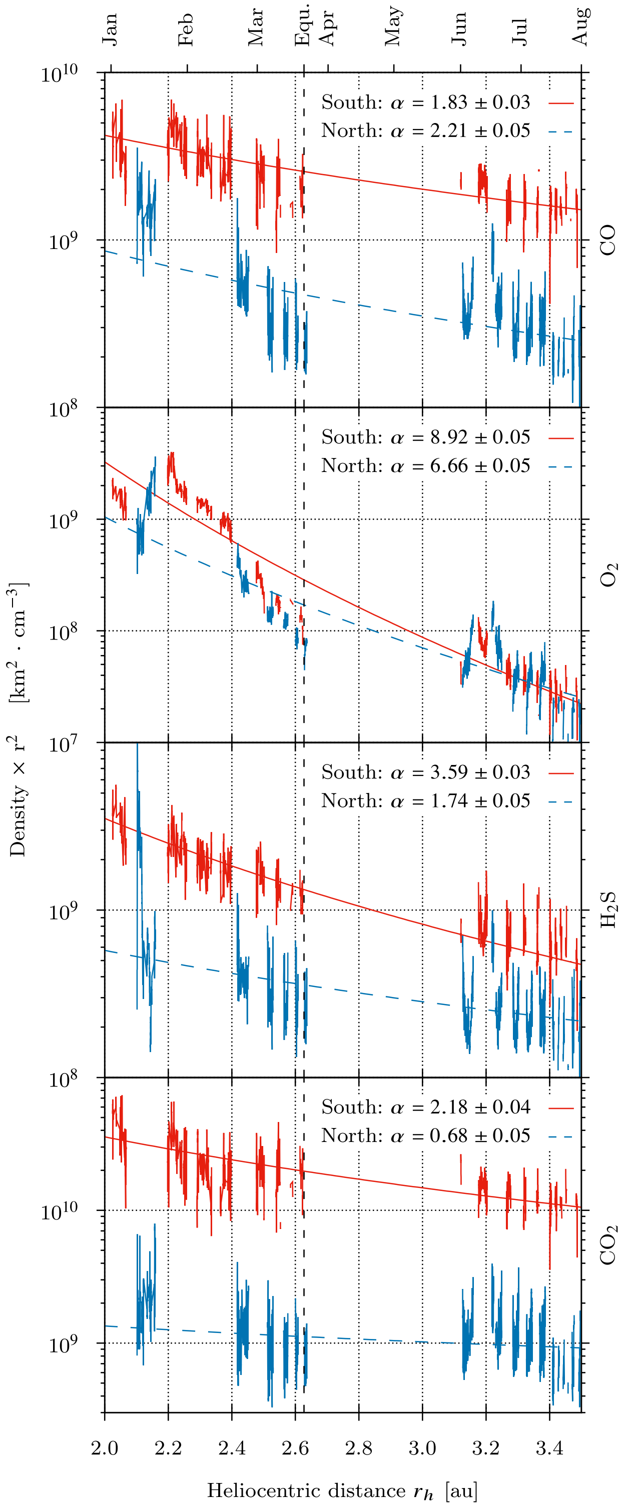

Figure A2. From top to bottom: densities ($\times r^2$) of CO, O_2, H_2S and CO_2, fitted with a power law to the heliocentric distance, for sub-spacecraft latitudes >30° (north – dashed blue) and <−30° (south – red).

This paper has been typeset from a TEX/LATEX file prepared by the author.

Bibliography

Jessica Agarwal, V Della Corte, PD Feldman, B Geiger, S Merouane, I Bertini, D Bodewits, S Fornasier, E Grün, P Hasselmann, et al. Evidence of sub-surface energy storage in comet 67P from the outburst of 2016 july 03. *Monthly Notices of the Royal Astronomical Society*, 469(Suppl_2):s606–s625, 2017.

Michael F A'Hearn, Susan Hoban, Peter V Birch, Craig Bowers, Ralph Martin, and Daniel A Klinglesmith. Cyanogen jets in comet Halley. *Nature*, 324(6098):649–651, 1986.

Michael F A'Hearn, MJS Belton, WA Delamere, J Kissel, KP Klaasen, LA McFadden, KJ Meech, HJ Melosh, PH Schultz, JM Sunshine, et al. Deep impact: excavating comet Tempel 1. *science*, 2005.

Michael F A'Hearn, Michael JS Belton, W Alan Delamere, Lori M Feaga, Donald Hampton, Jochen Kissel, Kenneth P Klaasen, Lucy A McFadden, Karen J Meech, H Jay Melosh, et al. EPOXI at comet Hartley 2. *Science*, 332(6036):1396–1400, 2011.

Victor Alí-Lagoa, M Delbo', and G Libourel. Rapid temperature changes and the early activity on comet 67P/Churyumov-Gerasimenko. *The Astrophysical Journal Letters*, 810(2):L22, 2015.

Kathrin Altwegg, Hans Balsiger, and J Geiss. Composition of the volatile material in Halley's coma from in situ measurements. In *Composition and Origin of Cometary Materials*, pages 3–18. Springer, 1999.

Kathrin Altwegg, Hans Balsiger, Akiva Bar-Nun, Jean-Jacques Berthelier, Andre Bieler, Peter Bochsler, Cristelle Briois, Ursina Calmonte, Michael R Combi, Johan De Keyser, et al. 67P/Churyumov-Gerasimenko, a Jupiter family comet with a high D/H ratio. *Science*, 347(6220):1261952, 2015.

Kathrin Altwegg, Hans Balsiger, Akiva Bar-Nun, Jean-Jacques Berthelier, Andre Bieler, Peter Bochsler, Christelle Briois, Ursina Calmonte, Michael R Combi, Hervé Cottin, et al. Prebiotic chemicals -amino acid and phosphorus- in the coma of comet 67P/Churyumov-Gerasimenko. *Science Advances*, 2(5):e1600285, 2016.

François Arago. *The Comet...* Number 65. J. Winchester, 1843.

Archeurope Educational Resources. Anglo-Saxon Archaeology. `https://http://anglosaxon.archeurope.info`, 2018. Accessed: 2018-07-01.

Philip J Armitage. *Astrophysics of planet formation*. Cambridge University Press, 2010.

Hans-Ulrich Auster, I Apathy, G Berghofer, A Remizov, R Roll, KH Fornacon, KH Glassmeier, G Haerendel, I Hejja, E Kührt, et al. ROMAP: Rosetta magnetometer and plasma monitor. *Space science reviews*, 128(1-4):221–240, 2007.

Hans-Ulrich Auster, Istvan Apathy, Gerhard Berghofer, Karl-Heinz Fornacon, Anatoli Remizov, Chris Carr, Carsten Güttler, Gerhard Haerendel, Philip Heinisch, David Hercik, et al. The nonmagnetic nucleus of comet 67P/Churyumov-Gerasimenko. *Science*, 349(6247):aaa5102, 2015.

Hans Balsiger, Kathrin Altwegg, F Bühler, J Geiss, AG Ghielmetti, BE Goldstein, R Goldstein, WT Huntress, W-H Ip, AJ Lazarus, et al. Ion composition and dynamics at comet Halley. *Nature*, 321(6067s):330, 1986.

Hans Balsiger, Kathrin Altwegg, and J Geiss. D/H and 18O/16O ratio in the hydronium ion and in neutral water from in situ ion measurements in comet Halley. *Journal of Geophysical Research: Space Physics*, 100(A4):5827–5834, 1995.

Hans Balsiger, Kathrin Altwegg, Peter Bochsler, P Eberhardt, J Fischer, S Graf, A Jäckel, E Kopp, U Langer, M Mildner, et al. ROSINA–Rosetta orbiter spectrometer for ion and neutral analysis. *Space Science Reviews*, 128(1-4):745–801, 2007.

Hans Balsiger, Kathrin Altwegg, Akiva Bar-Nun, Jean-Jacques Berthelier, Andre Bieler, Peter Bochsler, Christelle Briois, Ursina Calmonte, Michael Combi, Johan De Keyser, et al. Detection of argon in the coma of comet 67P/Churyumov-Gerasimenko. *Science Advances*, 1(8):e1500377, 2015.

Akiva Bar-Nun, G Herman, D Laufer, and ML Rappaport. Trapping and release of gases by water ice and implications for icy bodies. *Icarus*, 63(3):317–332, 1985.

Akiva Bar-Nun, Idit Kleinfeld, and E Kochavi. Trapping of gas mixtures by amorphous water ice. *Physical Review B*, 38(11):7749, 1988.

Akiva Bar-Nun, G Notesco, and T Owen. Trapping of N2, CO and Ar in amorphous ice - Application to comets. *Icarus*, 190(2):655–659, 2007.

M Antonella Barucci, G Filacchione, Sonia Fornasier, A Raponi, JDP Deshapriya, F Tosi, Clement Feller, M Ciarniello, Holger Sierks, F Capaccioni, et al. Detection of exposed H2O ice on the nucleus of comet 67P/Churyumov-Gerasimenko-as observed by Rosetta OSIRIS and VIRTIS instruments. *Astronomy & Astrophysics*, 595:A102, 2016.

Michael JS Belton, Peter Thomas, J Veverka, Peter Schultz, Michael F A'Hearn, Lori Feaga, Tony Farnham, Olivier Groussin, Jian-Yang Li, Casey Lisse, et al. The internal structure of Jupiter family cometary nuclei from Deep Impact observations: The 'talps' or layered pile' model. *Icarus*, 187(1):332–344, 2007.

Jean-Loup Bertaux. Estimate of the erosion rate from H2O mass-loss measurements from SWAN/SOHO in previous perihelions of comet 67P/Churyumov-Gerasimenko and connection with observed rotation rate variations. *Astronomy & Astrophysics*, 583:A38, 2015.

Jean-Pierre Bibring, P Lamy, Y Langevin, A Soufflot, M Berthé, J Borg, F Poulet, and S Mottola. CIVA. *Space Science Reviews*, 128(1-4):397–412, 2007.

Jean-Pierre Bibring, Y Langevin, J Carter, P Eng, B Gondet, L Jorda, S Le Mouélic, S Mottola, C Pilorget, F Poulet, et al. 67P/Churyumov-Gerasimenko surface properties as derived from CIVA panoramic images. *Science*, 349(6247):aab0671, 2015.

Jens Biele, Stephan Ulamec, Michael Maibaum, Reinhard Roll, Lars Witte, Eric Jurado, Pablo Muñoz, Walter Arnold, Hans-Ulrich Auster, Carlos Casas, et al. The landing (s) of Philae and inferences about comet surface mechanical properties. *Science*, 349 (6247):aaa9816, 2015.

Andre Bieler, Kathrin Altwegg, Hans Balsiger, Jean-Jacques Berthelier, Ursina Calmonte, Michael Combi, Johan De Keyser, Björn Fiethe, Nicolas Fougere, Stephen Fuselier, et al. Comparison of 3d kinetic and hydrodynamic models to ROSINA-COPS measurements of the neutral coma of 67P/Churyumov-Gerasimenko. *Astronomy & Astrophysics*, 583: A7, 2015.

Nicolas Biver, Dominique Bockelée-Morvan, P Colom, J Crovisier, B Germain, E Lellouch, JK Davies, WRF Dent, R Moreno, G Paubert, et al. Long-term evolution of the outgassing of comet Hale-Bopp from radio observations. *Earth, Moon, and Planets*, 78 (1-3):5–11, 1997.

Nicolas Biver, Dominique Bockelée-Morvan, Pierre Colom, Jacques Crovisier, Florence Henry, Emmanuel Lellouch, Anders Winnberg, Lars EB Johansson, Marcus Gunnarsson, Hans Rickman, et al. The 1995–2002 long-term monitoring of comet c/1995 o1 (hale-bopp) at radio wavelength. In *Cometary Science after Hale-Bopp*, pages 5–14. Springer, 2002.

Nicolas Biver, M Hofstadter, S Gulkis, D Bockelée-Morvan, M Choukroun, E Lellouch, FP Schloerb, L Rezac, WH Ip, C Jarchow, et al. Distribution of water around the nucleus of comet 67P/Churyumov-Gerasimenko at 3.4 au from the Sun as seen by the MIRO instrument on Rosetta. *Astronomy & Astrophysics*, 583:A3, 2015.

Dominique Bockelée-Morvan, J Crovisier, MJ Mumma, and HA Weaver. The composition of cometary volatiles. *Comets II*, page 391, 2004.

Dominique Bockelée-Morvan, V Debout, S Erard, C Leyrat, F Capaccioni, G Filacchione, N Fougere, P Drossart, Gabriele Arnold, M Combi, et al. First observations of H2O and CO2 vapor in comet 67P/Churyumov-Gerasimenko made by VIRTIS onboard Rosetta. *Astronomy & Astrophysics*, 583:A6, 2015.

Hermann Boehnhardt, Jean-Pierre Bibring, Istvan Apathy, Hans Ulrich Auster, Amalia Ercoli Finzi, Fred Goesmann, Göstar Klingelhöfer, Martin Knapmeyer, Wlodek Kofman, Harald Krüger, et al. The Philae lander mission and science overview. *Phil. Trans. R. Soc. A*, 375(2097):20160248, 2017.

DC Boice, LA Soderblom, DT Britt, RH Brown, BR Sandel, RV Yelle, BJ Buratti, J Oberst, N Thomas, et al. The Deep Space 1 encounter with comet 19P/Borrelly. *Earth, Moon, and Planets*, 89(1-4):301–324, 2000.

Tycho Brahe. *De mundi aetherei recentioribus phaenomenis.* Tampachius, 1602.

John C. Brandt and R. D. Chapman. *Introduction to Comets.* Cambridge University Press, 2004.

Don Brownlee, Peter Tsou, Jérôme Aléon, Conel MO'D Alexander, Tohru Araki, Sasa Bajt, Giuseppe A Baratta, Ron Bastien, Phil Bland, Pierre Bleuet, et al. Comet 81P/Wild 2 under a microscope. *science*, 314(5806):1711–1716, 2006.

Ursina Calmonte, Kathrin Altwegg, Hans Balsiger, Jean-Jacques Berthelier, André , G Cessateur, F Dhooghe, EF Van Dishoeck, B Fiethe, SA Fuselier, et al. Sulphur-bearing species in the coma of comet 67P/Churyumov-Gerasimenko. *Monthly Notices of the Royal Astronomical Society*, 462(Suppl_1):S253–S273, 2016.

AoGoWo Cameron and JoWo Truran. The supernova trigger for formation of the solar system. *Icarus*, 30(3):447–461, 1977.

Fabrizio Capaccioni, Angioletta Coradini, Gianrico Filacchione, S Erard, G Arnold, P Drossart, MC De Sanctis, D Bockelée-Morvan, MT Capria, F Tosi, et al. The organic-rich surface of comet 67P/Churyumov-Gerasimenko as seen by VIRTIS/Rosetta. *Science*, 347(6220):aaa0628, 2015.

Maria Teresa Capria, Angioletta Coradini, Maria Cristina De Sanctis, E Mazzotta Epifani, and P Palumbo. Thermal modeling of the active Centaur P/2004 A1 (LONEOS). *Astronomy & Astrophysics*, 504(1):249–258, 2009.

Maria Teresa Capria, Simone Marchi, Maria Cristina De Sanctis, Angioletta Coradini, and Eleonora Ammannito. The activity of main belt comets. *Astronomy & Astrophysics*, 537:A71, 2012.

Maria Teresa Capria, Fabrizio Capaccioni, Gianrico Filacchione, Federico Tosi, Maria Cristina De Sanctis, Stefano Mottola, Mauro Ciarniello, Michelangelo Formisano, Andrea Longobardo, Alessandra Migliorini, et al. How pristine is the interior of the comet 67P/Churyumov-Gerasimenko? *Monthly Notices of the Royal Astronomical Society*, 469(Suppl_2):S685–S694, 2017.

Chirs Carr, E Cupido, CGY Lee, A Balogh, T Beek, JL Burch, CN Dunford, AI Eriksson, Reine Gill, KH Glassmeier, et al. RPC: the Rosetta plasma consortium. *Space Science Reviews*, 128(1-4):629–647, 2007.

Valérie Ciarletti, Anny Chantal Levasseur-Regourd, Jérémie Lasue, C Statz, Dirk Plettemeier, Alain Hérique, Yves Rogez, and Wlodek Kofman. CONSERT suggests a change in local properties of 67P/Churyumov-Gerasimenko's nucleus at depth. *Astronomy & Astrophysics*, 583:A40, 2015.

Luigi Colangeli, JJ Lopez Moreno, P Palumbo, J Rodriguez, E Bussoletti, V Della Corte, F Esposito, M Herranz, JM Jeronimo, A Lopez-Jimenez, et al. GIADA: the grain impact analyser and dust accumulator for the Rosetta space mission. *Advances in Space Research*, 39(3):446–450, 2007.

Michael R Combi and AH Delsemme. Neutral cometary atmospheres. I-an average random walk model for photodissociation in comets. *The Astrophysical Journal*, 237:633–640, 1980.

Michael R Combi and William H Smyth. Monte Carlo particle-trajectory models for neutral cometary gases. I-Models and equations. *The Astrophysical Journal*, 327:1026–1059, 1988.

Michael R Combi, Brent J Bos, and William H Smyth. The OH distribution in cometary atmospheres-A collisional Monte Carlo model for heavy species. *The Astrophysical Journal*, 408:668–677, 1993.

Angioletta Coradini, Fabrizio Capaccioni, P Drossart, G Arnold, E Ammannito, F Angrilli, A Barucci, G Bellucci, J Benkhoff, G Bianchini, et al. VIRTIS: An imaging spectrometer for the Rosetta mission. *Space Science Reviews*, 128(1-4):529–559, 2007.

Hervé Cottin, Yves Bénilan, Marie-Claire Gazeau, and François Raulin. Origin of cometary extended sources from degradation of refractory organics on grains: polyoxymethylene as formaldehyde parent molecule. *Icarus*, 167(2):397–416, 2004.

Harmon Craig. Standard for reporting concentrations of deuterium and oxygen-18 in natural waters. *Science*, 133(3467):1833–1834, 1961.

Jacques Crovisier, Dominique Bockelée-Morvan, E Gerard, H Rauer, N Biver, P Colom, and L Jorda. What happened to comet 73P/Schwassmann-Wachmann 3? *Astronomy and Astrophysics*, 310:L17–L20, 1996.

Jacques Crovisier, K Leech, D Bockelée-Morvan, E Lellouch, TY Brooke, MS Hanner, B Altieri, HU Keller, and T Lim. The spectrum of comet Hale-Bopp as seen by ISO. In *The Universe as seen by ISO*, volume 427, page 137, 1999.

Björn JR Davidsson and Pedro J Gutiérrez. Nucleus properties of Comet 67P/Churyumov-Gerasimenko estimated from non-gravitational force modeling. *Icarus*, 176(2):453–477, 2005.

Björn JR Davidsson, Pedro J Gutiérrez, Olivier Groussin, Michael F A'Hearn, Tony Farnham, Lori M Feaga, Michael S Kelley, Kenneth P Klaasen, Frédéric Merlin, Silvia Protopapa, et al. Thermal inertia and surface roughness of Comet 9P/Tempel 1. *Icarus*, 224(1):154–171, 2013.

Detlef de Niem, E Kuehrt, S Hviid, and B Davidsson. Low velocity collisions of porous planetesimals in the early solar system. *Icarus*, 301:196–218, 2018.

Imke De Pater and Jack J Lissauer. *Planetary sciences*. Cambridge University Press, 2015.

Maria Cristina De Sanctis, Jérémie Lasue, Maria Teresa Capria, G Magni, D Turrini, and A Coradini. Shape and obliquity effects on the thermal evolution of the Rosetta target 67P/Churyumov-Gerasimenko cometary nucleus. *Icarus*, 207(1):341–358, 2010.

Maria Cristina De Sanctis, F Capaccioni, M Ciarniello, G Filacchione, M Formisano, S Mottola, A Raponi, F Tosi, D Bockelée-Morvan, S Erard, et al. The diurnal cycle of water ice on comet 67P/Churyumov-Gerasimenko. *Nature*, 525(7570):500–503, 2015.

Armand H Delsemme and Polydore Swings. Hydrates de gaz dans les noyaux cométaires et les grains interstellaires. In *Annales d'astrophysique*, volume 15, page 1, 1952.

Francesca E DeMeo and Benoît Carry. Solar System evolution from compositional mapping of the asteroid belt. *Nature*, 505(7485):629, 2014.

GB Donati. Discovery of comet v., 1858. *Monthly Notices of the Royal Astronomical Society*, 18:271, 1858.

Bertram D Donn. The formation and structure of fluffy cometary nuclei from random accumulation of grains. *Astronomy and Astrophysics*, 235:441–446, 1990.

Francois Dulieu, M Minissale, and D Bockelée-Morvan. Production of 02 through dismutation of H2O2 during water ice desorption: a key to understanding comet O2 abundances. *Astronomy & Astrophysics*, 597:A56, 2017.

Martin J Duncan and Harold F Levison. A disk of scattered icy objects and the origin of Jupiter-family comets. *Science*, 276(5319):1670–1672, 1997.

P Eberhardt, M Reber, D Krankowsky, and RR Hodges. The d/h andˆ 18ˆ o/ˆ 16ˆ o ratios in water from comet p/halley. *Astronomy and Astrophysics*, 302:301, 1995.

Peter Eberhardt. Comet Halley's gas composition and extended sources: Results from the neutral mass spectrometer on giotto. In *Composition and Origin of Cometary Materials*, pages 45–52. Springer, 1999.

Peter Eberhardt, R Meier, D Krankowsky, and RR Hodges. Methanol and hydrogen sulfide in comet 1P/Halley. *Astronomy and Astrophysics*, 288:315–329, 1994.

Kenneth Essex Edgeworth. The evolution of our planetary system. *Journal of the British Astronomical Association*, 53:181–188, 1943.

Pascale Ehrenfreund and Steven B Charnley. Organic molecules in the interstellar medium, comets, and meteorites: a voyage from dark clouds to the early Earth. *Annual Review of Astronomy and Astrophysics*, 38(1):427–483, 2000.

Mohamed Ramy El-Maarry, N Thomas, Lorenza Giacomini, M Massironi, M Pajola, R Marschall, A Gracia-Berná, H Sierks, C Barbieri, Philippe L Lamy, et al. Regional surface morphology of comet 67P/Churyumov-Gerasimenko from Rosetta/OSIRIS images. *Astronomy & Astrophysics*, 583:A26, 2015.

Bruce Fegley. Chemical and physical processing of presolar materials in the solar nebula and the implications for preservation of presolar materials in comets. *Space Science Reviews*, 90(1-2):239–252, 1999.

Paul D Feldman, Michael F A'Hearn, Jean-Loup Bertaux, Lori M Feaga, Joel Wm Parker, Eric Schindhelm, Andrew J Steffl, S Alan Stern, Harold A Weaver, Holger Sierks, et al. Measurements of the near-nucleus coma of comet 67P/Churyumov-Gerasimenko with the ALICE far-ultraviolet spectrograph on Rosetta. *Astronomy & Astrophysics*, 583: A8, 2015.

Ignacio Ferrín. Atlas of secular light curves of comets. *Planetary and Space Science*, 58 (3):365–391, 2010.

Michel Festou, Hans Rickman, and Lars Kamél. Using comet light-curve asymmetries to predict comet returns. *Nature*, 345(6272):235, 1990.

Michel C Festou. The density distribution of neutral compounds in cometary atmospheres. I-Models and equations. *Astronomy and Astrophysics*, 95:69–79, 1981.

Michel C Festou. On the existence of distributed sources in comet comae. In *Composition and Origin of Cometary Materials*, pages 53–67. Springer, 1999.

Gianrico Filacchione, Fabrizio Capaccioni, Mauro Ciarniello, Andrea Raponi, Federico Tosi, Maria Cristina De Sanctis, Stéphane Erard, Dominique Bockelée Morvan, Cedric Leyrat, Gabriele Arnold, et al. The global surface composition of 67P/CG nucleus by Rosetta/VIRTIS.(i) prelanding mission phase. *Icarus*, 274:334–349, 2016.

A Ercoli Finzi, F Bernelli Zazzera, Carlotta Dainese, F Malnati, PG Magnani, E Re, P Bologna, S Espinasse, and A Olivieri. SD2–How to sample a comet. *Space science reviews*, 128(1-4):281–299, 2007.

Sonia Fornasier, PH Hasselmann, MA Barucci, C Feller, S Besse, C Leyrat, L Lara, Pedro J Gutierrez, Nilda Oklay, Cécilia Tubiana, et al. Spectrophotometric properties of the nucleus of comet 67P/Churyumov-Gerasimenko from the OSIRIS instrument onboard the Rosetta spacecraft. *Astronomy & Astrophysics*, 583:A30, 2015.

Sonia Fornasier, S Mottola, Horst Uwe Keller, MA Barucci, B Davidsson, Clement Feller, JDP Deshapriya, H Sierks, C Barbieri, PL Lamy, et al. Rosetta's comet 67P/Churyumov-Gerasimenko sheds its dusty mantle to reveal its icy nature. *Science*, 354(6319):1566–1570, 2016.

Nicolas Fougere, Kathrin Altwegg, J-J Berthelier, Andre Bieler, Dominique Bockelée-Morvan, Ursina Calmonte, F Capaccioni, Michael R Combi, Johan De Keyser, V Debout, et al. Three-dimensional direct simulation Monte-Carlo modeling of the coma of comet 67P/Churyumov-Gerasimenko observed by the VIRTIS and ROSINA instruments on board Rosetta. *Astronomy & Astrophysics*, 588:A134, 2016.

M Fulle, AC Levasseur-Regourd, Neil McBride, and E Hadamcik. In situ dust measurements from within the coma of 1p/halley: First-order approximation with a dust dynamical model. *The Astronomical Journal*, 119(4):1968, 2000.

Marco Fulle, V Della Corte, A Rotundi, P Weissman, A Juhasz, K Szego, R Sordini, M Ferrari, S Ivanovski, F Lucarelli, et al. Density and charge of pristine fluffy particles from comet 67P/Churyumov-Gerasimenko. *The Astrophysical Journal Letters*, 802(1): L12, 2015.

Marco Fulle, Francesco Marzari, V Della Corte, Sonia Fornasier, H Sierks, A Rotundi, C Barbieri, Philippe L Lamy, R Rodrigo, D Koschny, et al. Evolution of the dust size distribution of comet 67P/Churyumov-Gerasimenko from 2.2 au to perihelion. *The Astrophysical Journal*, 821(1):19, 2016.

Sébastien Gasc, Kathrin Altwegg, Hans Balsiger, Jean-Jacques Berthelier, André Bieler, Ursina Calmonte, Björn Fiethe, Stephen Fuselier, André Galli, Tamas Gombosi, et al. Change of outgassing pattern of 67P/Churyumov-Gerasimenko during the march 2016 equinox as seen by ROSINA. *Monthly Notices of the Royal Astronomical Society*, 469 (Suppl_2):S108–S117, 2017a.

Sébastien Gasc, Kathrin Altwegg, Annette Jäckel, Léna Le Roy, Martin Rubin, Björn Fiethe, Urs Mall, and Henri Rème. Sensitivity and fragmentation calibration of the time-of-flight mass spectrometer RTOF on board ESA's Rosetta mission. *Planetary and Space Science*, 2017b.

Karl-Heinz Glassmeier, Hermann Boehnhardt, Detlef Koschny, Ekkehard Kührt, and Ingo Richter. The Rosetta mission: flying towards the origin of the solar system. *Space Science Reviews*, 128(1-4):1–21, 2007.

Fred Goesmann, Helmut Rosenbauer, Reinhard Roll, Cyril Szopa, Francois Raulin, Robert Sternberg, Guy Israel, Uwe Meierhenrich, Wolfram Thiemann, and Guillermo Munoz-Caro. COSAC, the cometary sampling and composition experiment on Philae. *Space Science Reviews*, 128(1-4):257–280, 2007.

Tamas I Gombosi and Harry LF Houpis. An icy-glue model of cometary nuclei. *Nature*, 324(6092):43, 1986.

Rodney Gomes, Harold F Levison, Kleomenis Tsiganis, and Alessandro Morbidelli. Origin of the cataclysmic Late Heavy Bombardment period of the terrestrial planets. *Nature*, 435(7041):466, 2005.

J Mayo Greenberg. 6. From Dust to Comets. In *International Astronomical Union Colloquium*, volume 39, pages 491–497. Cambridge University Press, 1977.

J Mayo Greenberg, AJ Yencha, JW Corbett, and HL Frisch. Ultraviolet effects on the chemical composition and optical properties of interstellar grains. In *Les Spectres des Astres dans l'Infrarouge et les Microondes*, pages 425–436, 1972.

J Mayo Greenberg et al. Making a comet nucleus. *Astronomy and Astrophysics*, 330:375, 1998.

Olivier Groussin, JM Sunshine, LM Feaga, L Jorda, PC Thomas, J-Y Li, MF A'Hearn, MJS Belton, S Besse, B Carcich, et al. The temperature, thermal inertia, roughness and color of the nuclei of Comets 103P/Hartley 2 and 9P/Tempel 1. *Icarus*, 222(2): 580–594, 2013.

Eberhard Grün, Akiva Bar-Nun, J Benkhoff, A Bischoff, H Düren, H Hellmann, P Hesselbarth, P Hsiung, HU Keller, J Klinger, et al. Laboratory simulation of cometary processes: Results from first KOSI experiments. In *International Astronomical Union Colloquium*, volume 116, pages 277–297, 1989.

A Guilbert-Lepoutre, J Lasue, C Federico, A Coradini, R Orosei, and ED Rosenberg. New 3D thermal evolution model for icy bodies application to trans-Neptunian objects. *Astronomy & Astrophysics*, 529:A71, 2011.

S Gulkis, M Frerking, J Crovisier, G Beaudin, P Hartogh, P Encrenaz, T Koch, C Kahn, Y Salinas, R Nowicki, et al. MIRO: Microwave instrument for Rosetta orbiter. *Space Science Reviews*, 128(1-4):561–597, 2007.

Samuel Gulkis, Mark Allen, Paul von Allmen, Gerard Beaudin, Nicolas Biver, Dominique Bockelée-Morvan, Mathieu Choukroun, Jacques Crovisier, Bjorn JR Davidsson, Pierre Encrenaz, et al. Subsurface properties and early activity of comet 67P/Churyumov-Gerasimenko. *Science*, 347(6220):aaa0709, 2015.

Bastian Gundlach and Jürgen Blum. Outgassing of icy bodies in the Solar System–II: Heat transport in dry, porous surface dust layers. *Icarus*, 219(2):618–629, 2012.

Kenneth C Hansen, K Altwegg, J-J Berthelier, A Bieler, N Biver, D Bockelée-Morvan, U Calmonte, F Capaccioni, MR Combi, J De Keyser, et al. Evolution of water production of 67P/Churyumov-Gerasimenko: An empirical model and a multi-instrument study. *Monthly Notices of the Royal Astronomical Society*, page stw2413, 2016.

Paul Hartogh, Dariusz C Lis, Dominique Bockelée-Morvan, Miguel de Val-Borro, Nicolas Biver, Michael Küppers, Martin Emprechtinger, Edwin A Bergin, Jacques Crovisier, Miriam Rengel, et al. Ocean-like water in the Jupiter-family comet 103P/Hartley 2. *Nature*, 478(7368):218, 2011.

Harvard University. Central Bureau for Astronomical Telegrams. `http://cbat.eps.harvard.edu/`, 2018. Accessed: 2018-06-26.

L Haser. Distribution d'intensité dans la tête d'une comète. *Bulletin de la Societe Royale des Sciences de Liège*, 43:740–750, 1957.

Myrtha Hässig, K Altwegg, H Balsiger, A Bar-Nun, Jean-Jacques Berthelier, A Bieler, P Bochsler, Christelle Briois, U Calmonte, M Combi, et al. Time variability and heterogeneity in the coma of 67P/Churyumov-Gerasimenko. *Science*, 347(6220):aaa0276, 2015.

Eric Herbst. Chemistry in the interstellar medium. *Annual Review of Physical Chemistry*, 46(1):27–54, 1995.

KL Heritier, Kathrin Altwegg, J-J Berthelier, A Beth, CM Carr, J De Keyser, AI Eriksson, SA Fuselier, M Galand, TI Gombosi, et al. On the origin of molecular oxygen in cometary comae. *Nature communications*, 9(1):2580, 2018.

K Hirao and T Itoh. The Sakigake/Suisei encounter with comet 1P/Halley. In *Exploration of Halley's Comet*, pages 39–46. Springer, 1988.

Margaux Hoang, Kathrin Altwegg, Hans Balsiger, A Beth, André Bieler, U Calmonte, MR Combi, J De Keyser, B Fiethe, N Fougere, et al. The heterogeneous coma of comet 67P/Churyumov-Gerasimenko as seen by ROSINA: H2O, CO2, and CO from September 2014 to February 2016. *Astronomy & Astrophysics*, 600:A77, 2017.

Xuanyu Hu, Xian Shi, Holger Sierks, Marco Fulle, J Blum, HU Keller, E Kührt, Björn Davidsson, C Güttler, B Gundlach, et al. Seasonal erosion and restoration of the dust cover on comet 67P/Churyumov-Gerasimenko as observed by OSIRIS onboard Rosetta. *Astronomy & Astrophysics*, 604:A114, 2017.

RL Hudson and B Donn. An experimental study of the sublimation of water ice and the release of trapped gases. *Icarus*, 94(2):326–332, 1991.

Walter F Huebner, Johannes Benkhoff, Maria-Teresa Capria, Angioletta Coradini, Christina De Sanctis, Roberto Orosei, and Dina Prialnik. *Heat and gas diffusion in comet nuclei*. International Space Science Institute, 2006.

WF Huebner and J Benkhoff. From coma abundances to nucleus composition. In *Composition and Origin of Cometary Materials*, pages 117–130. Springer, 1999.

WF Huebner, DC Boice, HU Schmidt, and R Wegmann. Structure of the coma: chemistry and solar wind interaction. In *International Astronomical Union Colloquium*, volume 116, pages 907–936, 1991.

William Huggins. Spectrum analysis of comet ii. 1868. *Astronomical register*, 6:169–170, 1868.

JA Hynek. Astrophysics: A Topical Symposium. *American Journal of Physics*, 20:250–250, 1952.

Masahiro Ikoma and Hidenori Genda. Constraints on the mass of a habitable planet with water of nebular origin. *The Astrophysical Journal*, 648(1):696, 2006.

Karl Wahlberg Jansson and Anders Johansen. Formation of pebble-pile planetesimals. *Astronomy & Astrophysics*, 570:A47, 2014.

David Jewitt. The active centaurs. *The Astronomical Journal*, 137(5):4296, 2009.

David Jewitt and Jing Li. Activity in geminid parent (3200) Phaethon. *The Astronomical Journal*, 140(5):1519, 2010.

David Jewitt, J Luu, and BG Marsden. 1992 QB1. *IAU circ*, 5611(1), 1992.

Laurent Jorda, R Gaskell, C Capanna, S Hviid, P Lamy, J Ďurech, G Faury, Olivier Groussin, P Gutiérrez, C Jackman, et al. The global shape, density and rotation of Comet 67P/Churyumov-Gerasimenko from preperihelion Rosetta/OSIRIS observations. *Icarus*, 277:257–278, 2016.

Brian A Keeney, S Alan Stern, Michael F A'hearn, Jean-Loup Bertaux, Lori M Feaga, Paul D Feldman, Richard A Medina, Joel Wm Parker, Jon P Pineau, Eric Schindhelm, et al. H2O and O2 absorption in the coma of comet 67P/Churyumov-Gerasimenko measured by the ALICE far-ultraviolet spectrograph on Rosetta. *Monthly Notices of the Royal Astronomical Society*, 469(Suppl_2):S158–S177, 2017.

Horst Uwe Keller and Laurent Jorda. The morphology of cometary nuclei. In *The Century of Space Science*, pages 1235–1275. Springer, 2001.

Horst Uwe Keller, C Arpigny, C Barbieri, RM Bonnet, S Cazes, M Coradini, CB Cosmovici, WA Delamere, WF Huebner, DW Hughes, et al. First Halley multicolour camera imaging results from Giotto. *Nature*, 321(6067s):320, 1986.

Horst Uwe Keller, Cesare Barbieri, Philippe Lamy, Hans Rickman, Rafael Rodrigo, K-P Wenzel, Holger Sierks, Michael F A'Hearn, Francesco Angrilli, M Angulo, et al. OSIRIS–The scientific camera system onboard Rosetta. *Space Science Reviews*, 128 (1-4):433–506, 2007.

Horst Uwe Keller, S Mottola, Y Skorov, and L Jorda. The changing rotation period of comet 67P/Churyumov-Gerasimenko controlled by its activity. *Astronomy & Astrophysics*, 579:L5, 2015a.

Horst Uwe Keller, Stefano Mottola, Björn Davidsson, SE Schröder, Y Skorov, Ekkehard Kührt, Olivier Groussin, Maurizio Pajola, Stubbe F Hviid, Frank Preusker, et al. Insolation, erosion, and morphology of comet 67P/Churyumov-Gerasimenko. *Astronomy & Astrophysics*, 583:A34, 2015b.

Horst Uwe Keller, Stefano Mottola, Stubbe F Hviid, Jessica Agarwal, Ekkehard Kührt, Yuri Skorov, Katharina Otto, J-B Vincent, Nilda Oklay, Stephan E Schröder, et al. Seasonal mass transfer on the nucleus of comet 67P/Churyumov-Gerasimenko. *Monthly Notices of the Royal Astronomical Society*, 469(Suppl_2):S357–S371, 2017.

Lindsay P Keller, Sasa Bajt, Giuseppe A Baratta, Janet Borg, John P Bradley, Don E Brownlee, Henner Busemann, John R Brucato, Mark Burchell, Luigi Colangeli, et al. Infrared spectroscopy of comet 81p/Wild 2 samples returned by Stardust. *Science*, 314 (5806):1728–1731, 2006.

Michael S Kelley, William T Reach, and David J Lien. The dust trail of comet 67P/Churyumov-Gerasimenko. *Icarus*, 193(2):572–587, 2008.

Yong-Ki Kim, K Irikura, M Rudd, M Ali, P Stone, J Chang, JS Coursey, RA Dragoset, AR Kishore, KJ Olsen, et al. Electron-impact cross sections for ionization and excitation database. *NIST.(Accessed 2016) Available at: http://physics. nist. gov/PhysRefData/Ionization/atom_index. html*, 2005.

Jochen Kissel, DE Brownlee, K Büchler, BC Clark, H Fechtig, E Grün, K Hornung, EB Igenbergs, EK Jessberger, FR Krueger, et al. Composition of comet Halley dust particles from Giotto observations. *Nature*, 321(6067):336–337, 1986.

Jochen Kissel, Kathrin Altwegg, BC Clark, L Colangeli, H Cottin, S Czempiel, J Eibl, C Engrand, HM Fehringer, B Feuerbacher, et al. Cosima–high resolution time-of-flight secondary ion mass spectrometer for the analysis of cometary dust particles onboard Rosetta. *Space science reviews*, 128(1-4):823–867, 2007.

Goestar Klingelhöfer, J Brückner, C D'uston, R Gellert, and R Rieder. The Rosetta alpha particle X-ray spectrometer (apxs). *Space science reviews*, 128(1-4):383–396, 2007.

Wlodek Kofman, Alain Hérique, J-P Goutail, Tor Hagfors, IP Williams, Erling Nielsen, J-P Barriot, Yves Barbin, C Elachi, Peter Edenhofer, et al. The comet nucleus sounding experiment by radiowave transmission (CONSERT): a short description of the instrument and of the commissioning stages. *Space Science Reviews*, 128(1-4):413–432, 2007.

Wlodek Kofman, Alain Herique, Yves Barbin, Jean-Pierre Barriot, Valérie Ciarletti, Stephen Clifford, Peter Edenhofer, Charles Elachi, Christelle Eyraud, Jean-Pierre Goutail, et al. Properties of the 67P/Churyumov-Gerasimenko interior revealed by CONSERT radar. *Science*, 349(6247):aab0639, 2015.

Akira Kouchi and Sin-iti Sirono. Crystallization heat of impure amorphous H2O ice. *Geophysical research letters*, 28(5):827–830, 2001.

Akira Kouchi and Tetsuo Yamamoto. Cosmoglaciology: Evolution of ice in interstellar space and the early solar system. *Progress in crystal growth and characterization of materials*, 30(2-3):83–107, 1995.

Akira Kouchi, JM Greenberg, T Yamamoto, T Mukai, et al. Extremely low thermal conductivity of amorphous ice - Relevance to comet evolution. *Astrophysical Journal*, 388:L73, 1992.

Michael Küppers, Ivano Bertini, Sonia Fornasier, Pedro J Gutierrez, Stubbe F Hviid, Laurent Jorda, Horst Uwe Keller, Jörg Knollenberg, Detlef Koschny, Rainer Kramm, et al. A large dust/ice ratio in the nucleus of comet 9P/Tempel 1. *Nature*, 437(7061): 987, 2005.

Fiorangela La Forgia, L Giacomini, M Lazzarin, M Massironi, N Oklay, F Scholten, M Pajola, I Bertini, G Cremonese, C Barbieri, et al. Geomorphology and spectrophotometry of Philae's landing site on comet 67P/Churyumov-Gerasimenko. *Astronomy & Astrophysics*, 583:A41, 2015.

Philippe L Lamy, Imre Toth, and Harold A Weaver. Hubble Space Telescope observations of the nucleus and inner coma of comet 19P/1904 Y2 (Borrelly). *Astronomy and Astrophysics*, 337:945–954, 1998.

Philippe L Lamy, I Toth, HA Weaver, L Jorda, M Kaasalainen, and PJ Gutiérrez. Hubble Space Telescope observations of the nucleus and inner coma of comet 67P/Churyumov-Gerasimenko. *Astronomy & Astrophysics*, 458(2):669–678, 2006.

Philippe L Lamy, Imre Toth, Björn JR Davidsson, Olivier Groussin, Pedro Gutiérrez, Laurent Jorda, Mikko Kaasalainen, and Stephen C Lowry. A portrait of the nucleus of comet 67P/Churyumov-Gerasimenko. *Space science reviews*, 128(1-4):23–66, 2007.

LM Lara, S Lowry, J-B Vincent, PJ Gutiérrez, A Rożek, F La Forgia, N Oklay, H Sierks, C Barbieri, PL Lamy, et al. Large-scale dust jets in the coma of 67P/Churyumov-Gerasimenko as seen by the OSIRIS instrument onboard Rosetta. *Astronomy & Astrophysics*, 583:A9, 2015.

Jérémie Lasue and AC Levasseur-Regourd. Porous irregular aggregates of sub-micron sized grains to reproduce cometary dust light scattering observations. *Journal of Quantitative Spectroscopy and Radiative Transfer*, 100(1-3):220–236, 2006.

Jérémie Lasue, MC De Sanctis, A Coradini, G Magni, MT Capria, D Turrini, and AC Levasseur-Regourd. Quasi-3-D model to describe topographic effects on non-spherical comet nucleus evolution. *Planetary and Space Science*, 56(15):1977–1991, 2008.

Jérémie Lasue, R Botet, Anny Chantal Levasseur-Regourd, and Edith Hadamcik. Cometary nuclei internal structure from early aggregation simulations. *Icarus*, 203 (2):599–609, 2009.

Jérémie Lasue, R Botet, Anny Chantal Levasseur-Regourd, Edith Hadamcik, and W Kofman. Appearance of layered structures in numerical simulations of polydisperse bodies accretion: Application to cometary nuclei. *Icarus*, 213(1):369–381, 2011.

Léna Le Roy, Kathrin Altwegg, Hans Balsiger, Jean-Jacques Berthelier, Andre Bieler, Christelle Briois, Ursina Calmonte, Michael R Combi, Johan De Keyser, Frederik Dhooghe, et al. Inventory of the volatiles on comet 67P/Churyumov-Gerasimenko from Rosetta/ROSINA. *Astronomy & Astrophysics*, 583:A1, 2015.

Jui-Chi Lee, Matteo Massironi, Wing-Huen Ip, Lorenza Giacomini, Sabrina Ferrari, Luca Penasa, Mohamed Ramy El-Maarry, Maurizio Pajola, Ian-Lin Lai, Zhong-Yi Lin, et al. Geomorphological mapping of comet 67P/Churyumov-Gerasimenko's southern hemisphere. *Monthly Notices of the Royal Astronomical Society*, 462(Suppl_1):S573–S592, 2017.

J Lequeux and T. Encrenaz. *A la rencontre des comètes, de Halley à Rosetta*. Belin/Pour la Science, 2015.

A. C. Levasseur-Regourd and J. Borg. *L'exploration cométaire, de l'Antiquité Ãă Rosetta*. Nouveau monde editions, 2018.

AC Levasseur-Regourd, B Goidet, T Le Duin, C Malique, JB Renard, and JL Bertaux. Optical probing of dust in comet grigg-skjellerup from the giotto spacecraft. *Planetary and space science*, 41(2):167–169, 1993.

Anny-Chantal Levasseur-Regourd, Jessica Agarwal, Hervé Cottin, Cécile Engrand, George Flynn, Marco Fulle, Tamas Gombosi, Yves Langevin, Jérémie Lasue, Thurid Mannel, et al. Cometary dust. *Space science reviews*, 214(3):64, 2018.

Harold F Levison. Comet taxonomy. In *Completing the Inventory of the Solar System*, volume 107, pages 173–191, 1996.

John Lewis. *Physics and chemistry of the solar system*. Academic Press, 2012.

Carey M Lisse, YR Fernandez, WT Reach, JM Bauer, MF A'hearn, TL Farnham, O Groussin, MJ Belton, KJ Meech, and CD Snodgrass. Spitzer Space Telescope observations of the nucleus of Comet 103P/Hartley 2. *Publications of the Astronomical Society of the Pacific*, 121(883):968, 2009.

ALICE Lucchetti, Gabriele Cremonese, Laurent Jorda, François Poulet, J-P Bibring, Maurizio Pajola, Fiorangela La Forgia, Matteo Massironi, Mohamed Ramy El-Maarry, Nilda Oklay, et al. Characterization of the Abydos region through OSIRIS high-resolution images in support of CIVA measurements. *Astronomy & Astrophysics*, 585: L1, 2016.

Jonathan I Lunine, A Graps, DP O'Brien, A Morbidelli, L Leshin, and A Coradini. Asteroidal sources of Earth's water based on dynamical simulations. In *Lunar and Planetary Science Conference*, volume 38, page 1616, 2007.

Dmitrij F Lupishko, M di Martino, and TA Lupishko. What the physical properties of near-Earth asteroids tell us about sources of their origin? *Kinematika i Fizika Nebesnykh Tel Supplement*, 3:213–216, 2000.

Adrienn Luspay-Kuti, Olivier Mousis, Myrtha Hässig, Stephen A Fuselier, Jonathan I Lunine, Bernard Marty, Kathleen E Mandt, Peter Wurz, and Martin Rubin. The presence of clathrates in comet 67P/Churyumov-Gerasimenko. *Science advances*, 2(4): e1501781, 2016.

Jane Luu, David Jewitt, and BG Marsden. 1993 FW. *IAU circ*, 5730(1), 1993.

K Magee-Sauer, FL Roesler, F Scherb, J Harlander, and RJ Oliversen. Spatial distribution of O(1D) from Comet Halley. *Icarus*, 76(1):89–99, 1988.

Loris Magnani and Michael F A'Hearn. CO(+) fluorescence in comets. *The Astrophysical Journal*, 302:477–487, 1986.

BA Mamyrin, VI Karataev, DV Shmikk, and VA Zagulin. The mass reflectron, a new non-magnetic time-of-flight mass spectrometer with high resolution. *Zh. Eksp. Teor. Fiz*, 64:82–89, 1973.

Lucie Maquet. The recent dynamical history of comet 67P/Churyumov-Gerasimenko. *Astronomy & Astrophysics*, 579:A78, 2015.

B Marty, Kathrin Altwegg, Hans Balsiger, A Bar-Nun, DV Bekaert, J-J Berthelier, André Bieler, Christelle Briois, U Calmonte, M Combi, et al. Xenon isotopes in 67P/Churyumov-Gerasimenko show that comets contributed to Earth's atmosphere. *Science*, 356(6342):1069–1072, 2017.

Matteo Massironi, Emanuele Simioni, Francesco Marzari, Gabriele Cremonese, Lorenza Giacomini, Maurizio Pajola, Laurent Jorda, Giampiero Naletto, Stephen Lowry, Mohamed Ramy El-Maarry, et al. Two independent and primitive envelopes of the bilobate nucleus of comet 67P. *Nature*, 526(7573):402, 2015.

Y Mekler and M Podolak. Formation of amorphous ice in the protoplanetary nebula. *Planetary and Space Science*, 42(10):865–870, 1994.

Alessandra Migliorini, G Piccioni, F Capaccioni, G Filacchione, D Bockelée-Morvan, S Erard, C Leyrat, MR Combi, N , J Crovisier, et al. Water and carbon dioxide distribution in the 67P/Churyumov-Gerasimenko coma from VIRTIS-M infrared observations. *Astronomy & Astrophysics*, 589:A45, 2016.

Alessandro Morbidelli, J-M Petit, B Gladman, and J Chambers. A plausible cause of the late heavy bombardment. *Meteoritics & Planetary Science*, 36(3):371–380, 2001.

Alessandro Morbidelli, Harold F Levison, Kleomenis Tsiganis, and Rodney Gomes. Chaotic capture of Jupiter's Trojan asteroids in the early solar system. *Nature*, 435 (7041):462, 2005.

Alessandro Morbidelli, Kleomenis Tsiganis, Aurélien Crida, Harold F Levison, and Rodney Gomes. Dynamics of the giant planets of the Solar System in the gaseous protoplanetary disk and their relationship to the current orbital architecture. *The Astronomical Journal*, 134(5):1790, 2007.

Alessandro Morbidelli, Jonathan I Lunine, David P O'Brien, Sean N Raymond, and Kevin J Walsh. Building terrestrial planets. *Annual Review of Earth and Planetary Sciences*, 40, 2012.

Andrew Morse, Geraint Morgan, Dan Andrews, Simeon Barber, Mark Leese, Simon Sheridan, Ian Wright, and Colin Pillinger. Ptolemy-a GCMS to measure the chemical and stable isotopic composition of a comet. 2009.

Stefano Mottola, Gabriele Arnold, Hans-Georg Grothues, Ralf Jaumann, Harald Michaelis, Gerhard Neukum, and Jean-Pierre Bibring. The ROLIS experiment on the Rosetta lander. *Space Science Reviews*, 128(1-4):241–255, 2007.

Stefano Mottola, S Lowry, Colin Snodgrass, PL Lamy, I Toth, A Rożek, H Sierks, MF A'Hearn, F Angrilli, C Barbieri, et al. The rotation state of 67P/Churyumov-Gerasimenko from approach observations with the OSIRIS cameras on Rosetta. *Astronomy & Astrophysics*, 569:L2, 2014.

Olivier Mousis, T Ronnet, B Brugger, O Ozgurel, F Pauzat, Y Ellinger, R Maggiolo, Peter Wurz, P Vernazza, JI Lunine, et al. Origin of molecular oxygen in comet 67P/Churyumov-Gerasimenko. *The Astrophysical Journal Letters*, 823(2):L41, 2016.

Michael J Mumma and Steven B Charnley. The chemical composition of comets - Emerging taxonomies and natal heritage. *Annual Review of Astronomy and Astrophysics*, 49, 2011.

Michael J Mumma, Harold A Weaver, Harold P Larson, D Scott Davis, and Michael Williams. Detection of water vapor in Halley's comet. *Science*, 232(4757):1523–1528, 1986.

Michael J Mumma, Michael A DiSanti, Karen Magee-Sauer, Boncho P Bonev, Geronimo L Villanueva, Hideyo Kawakita, Neil Dello Russo, Erika L Gibb, Geoffrey A Blake, James E Lyke, et al. Parent volatiles in comet 9p/Tempel 1: Before and after impact. *Science*, 310(5746):270–274, 2005.

MJ Mumma, VA Krasnopolsky, and MJ Abbott. Soft X-rays from four comets observed with EUVE. *The Astrophysical Journal Letters*, 491(2):L125, 1997.

G Notesco and A Bar-Nun. Enrichment of CO over N2 by their trapping in amorphous ice and implications to comet 1P/Halley. *Icarus*, 122(1):118–121, 1996.

Jan Hendrik Oort et al. The structure of the cloud of comets surrounding the Solar System and a hypothesis concerning its origin. *Bulletin of the Astronomical Institutes of the Netherlands*, 11:91, 1950.

Maurizio Pajola, ALICE Lucchetti, Jean-Baptiste Vincent, Nilda Oklay, Mohamed R El-Maarry, Ivano Bertini, Giampiero Naletto, Monica Lazzarin, Matteo Massironi, Holger Sierks, et al. The southern hemisphere of 67P/Churyumov-Gerasimenko: Analysis of the preperihelion size-frequency distribution of boulders âĽě 7 m. *Astronomy & Astrophysics*, 592:L2, 2016.

Martin Pätzold, Bernd Häusler, Kaare Aksnes, John D Anderson, Sami W Asmar, Jean-Pierre Barriot, Michael K Bird, Hermann Boehnhardt, Werner Eidel, Eberhardt Grün, et al. Rosetta radio science investigations (RSI). *Space science reviews*, 128(1-4):599–627, 2007.

Martin Pätzold, T Andert, Matthias Hahn, SW Asmar, J-P Barriot, MK Bird, B Häusler, Kerstin Peter, Silvia Tellmann, Eberhard Grün, et al. A homogeneous nucleus for comet 67P/Churyumov-Gerasimenko from its gravity field. *Nature*, 530(7588):63, 2016.

Dina Prialnik. Crystallization, sublimation, and gas release in the interior of a porous comet nucleus. *The Astrophysical Journal*, 388:196–202, 1992.

Dina Prialnik. Modeling the structure and activity of comet nuclei. *Comets II*, 1:359–387, 2004.

Dina Prialnik and Akiva Bar-Nun. Gas release in comet nuclei. *The Astrophysical Journal*, 363:274–282, 1990.

Dina Prialnik and Akiva Bar-Nun. Crystallization of amorphous ice as the cause of comet 1P/Halley's outburst at 14 AU. *Astronomy and astrophysics*, 258:L9–L12, 1992.

Dina Prialnik and M Podolak. Radioactive heating of porous comet nuclei. *Icarus*, 117 (2):420–430, 1995.

Dina Prialnik, Johannes Benkhoff, and Morris Podolak. *Modeling the structure and activity of comet nuclei*, volume 1. Univ. of Arizona, Tucson, 2004.

Sean N Raymond, Thomas Quinn, and Jonathan I Lunine. Making other earths: dynamical simulations of terrestrial planet formation and water delivery. *Icarus*, 168(1):1–17, 2004.

Sean N Raymond, Thomas Quinn, and Jonathan I Lunine. High-resolution simulations of the final assembly of Earth-like planets. 2. Water delivery and planetary habitability. *Astrobiology*, 7(1):66–84, 2007.

PA Redhead. New hot-filament ionization gauge with low residual current. *Journal of Vacuum Science and Technology*, 3(4):173–180, 1966.

R Reinhard. The giotto encounter with comet Halley. *Nature*, 321(6067):313–318, 1986.

K Richter, MR Combi, HU Keller, and RR Meier. Multiple scattering of hydrogen Lyα radiation in the coma of Comet Hyakutake (C/1996 B2). *The Astrophysical Journal*, 531(1):599, 2000.

W Riedler, Klaus Torkar, H Jeszenszky, J Romstedt, H St C Alleyne, H Arends, W Barth, JVD Biezen, B Butler, P Ehrenfreund, et al. MIDAS - The micro-imaging dust analysis system for the Rosetta mission. *Space Science Reviews*, 128(1-4):869–904, 2007.

Frans JM Rietmeijer. Interplanetary dust particles. *Planetary materials*, 36:2–1, 1998.

Frans JM Rietmeijer. Materials: Interplanetary dust particles, micrometeorites, meteorites, and meteoric dust. *Meteors in the Earth's Atmosphere: Meteoroids and Cosmic Dust and Their Interactions with the Earth's Upper Atmosphere*, page 215, 2002.

Alessandra Rotundi, Holger Sierks, Vincenzo Della Corte, Marco Fulle, Pedro J Gutierrez, Luisa Lara, Cesare Barbieri, Philippe L Lamy, Rafael Rodrigo, Detlef Koschny, et al. Dust measurements in the coma of comet 67P/Churyumov-Gerasimenko inbound to the Sun. *Science*, 347(6220):aaa3905, 2015.

Martin Rubin, Kathrin Altwegg, Hans Balsiger, A Bar-Nun, J-J Berthelier, A Bieler, P Bochsler, Christelle Briois, U Calmonte, M Combi, et al. Molecular nitrogen in comet 67P/Churyumov-Gerasimenko indicates a low formation temperature. *Science*, 348(6231):232–235, 2015a.

Martin Rubin, Kathrin Altwegg, Ewine F van Dishoeck, and Gerhard Schwehm. Molecular oxygen in Oort cloud comet 1P/Halley. *The Astrophysical Journal Letters*, 815(1):L11, 2015b.

Roald Z Sagdeev, J Blamont, AA Galeev, VI Moroz, VD Shapiro, VI Shevchenko, and K Szegő. Vega spacecraft encounters with comet Halley. *Nature*, 321(6067s):259, 1986.

Stefan Scherer, K Altwegg, H Balsiger, J Fischer, A Jäckel, A Korth, M Mildner, D Piazza, H Reme, and P Wurz. A novel principle for an ion mirror design in time-of-flight mass spectrometry. *International Journal of Mass Spectrometry*, 251(1):73–81, 2006.

F Peter Schloerb, Stephen Keihm, Paul von Allmen, Mathieu Choukroun, Emmanuel Lellouch, Cedric Leyrat, Gerard Beaudin, Nicolas Biver, Dominique Bockelée-Morvan, Jacques Crovisier, et al. MIRO observations of subsurface temperatures of the nucleus of 67P/Churyumov-Gerasimenko. *Astronomy & Astrophysics*, 583:A29, 2015.

B Schmitt, S Espinasse, RJA Grim, JM Greenberg, J Klinger, et al. Laboratory studies of cometary ice analogues. 1989.

Megan E Schwamb. Solar System: Stranded in no-man's-land. *Nature*, 507(7493):435, 2014.

Stephen R Schwartz, Patrick Michel, Martin Jutzi, Simone Marchi, Yun Zhang, and Derek C Richardson. Catastrophic disruptions as the origin of bilobate comets. *Nature astronomy*, 2(5):379, 2018.

Klaus J Seidensticker, Dirk Möhlmann, Istvan Apathy, Walter Schmidt, Klaus Thiel, Walter Arnold, H-H Fischer, Michael Kretschmer, David Madlener, Attila Péter, et al. SESAME - an experiment of the Rosetta lander Philae: objectives and general design. *Space Science Reviews*, 128(1-4):301–337, 2007.

Zd Sekanina. The path and surviving tail of a comet that fell into the Sun. *The Astronomical Journal*, 87:1059–1072, 1982.

Holger Sierks, Cesare Barbieri, Philippe L Lamy, Rafael Rodrigo, Detlef Koschny, Hans Rickman, Horst Uwe Keller, Jessica Agarwal, Michael F A'Hearn, Francesco Angrilli, et al. On the nucleus structure and activity of comet 67P/Churyumov-Gerasimenko. *Science*, 347(6220):aaa1044, 2015.

Colin Snodgrass, C Tubiana, DM Bramich, K Meech, H Boehnhardt, and L Barrera. Beginning of activity in 67P/Churyumov-Gerasimenko and predictions for 2014–2015. *Astronomy & Astrophysics*, 557:A33, 2013.

Colin Snodgrass, Cyrielle Opitom, Miguel de Val-Borro, Emmanuel Jehin, Jean Manfroid, Tim Lister, Jon Marchant, Geraint H Jones, Alan Fitzsimmons, Iain A Steele, et al. The perihelion activity of comet 67P/Churyumov-Gerasimenko as seen by robotic telescopes. *Monthly Notices of the Royal Astronomical Society*, 462(Suppl_1):S138–S145, 2016.

Colin Snodgrass, Michael F A'Hearn, Francisco Aceituno, Viktor Afanasiev, Sefano Bagnulo, J Bauer, G Bergond, S Besse, Nicolas Biver, Dennis Bodewits, et al. The 67P/Churyumov-Gerasimenko observation campaign in support of the Rosetta mission. *Phil. Trans. R. Soc. A*, 375(2097):20160249, 2017.

LA Soderblom, TL Becker, G Bennett, DC Boice, DT Britt, RH Brown, BJ Buratti, C Isbell, B Giese, T Hare, et al. Observations of Comet 19P/Borrelly by the miniature integrated camera and spectrometer aboard Deep Space 1. *Science*, 296(5570):1087–1091, 2002.

T Spohn, J Knollenberg, AJ Ball, M Banaszkiewicz, J Benkhoff, M Grott, J Grygorczuk, Christian Hüttig, A Hagermann, G Kargl, et al. Thermal and mechanical properties of the near-surface layers of comet 67P/Churyumov-Gerasimenko. *Science*, 349(6247): aab0464, 2015.

Tilman Spohn, Karsten Seiferlin, Axel Hagermann, Jörg Knollenberg, Andrew J Ball, Marek Banaszkiewicz, Johannes Benkhoff, Stanislaw Gadomski, Wojciech Gregorczyk, Jerzy Grygorczuk, et al. MUPUS - a thermal and mechanical properties probe for the Rosetta lander Philae. *Space Science Reviews*, 128(1-4):339–362, 2007.

SA Stern, DC Slater, J Scherrer, J Stone, M Versteeg, MF A'hearn, Jean-Loup Bertaux, PD Feldman, MC Festou, Joel Wm Parker, et al. ALICE: the Rosetta ultraviolet imaging spectrograph. *Space Science Reviews*, 128(1-4):507–527, 2007.

G Strazzulla, GA Baratta, RE Johnson, and B Donn. Primordial comet mantle: irradiation production of a stable organic crust. *Icarus*, 91(1):101–104, 1991.

Czeslaw Szmytkowski, Krzysztof Maciag, and Grzegorz Karwasz. Absolute electron-scattering total cross section measurements for noble gas atoms and diatomic molecules. *Physica Scripta*, 54(3):271, 1996.

Vianney Taquet, Kenji Furuya, Catherine Walsh, and Ewine F van Dishoeck. On the origin of O2 and other volatile species in comets. *arXiv preprint arXiv:1711.02372*, 2017.

MGGT Taylor, N Altobelli, BJ Buratti, and M Choukroun. The Rosetta mission orbiter science overview: the comet phase. *Phil. Trans. R. Soc. A*, 375(2097):20160262, 2017.

SC Tegler and W Romanishin. Two distinct populations of Kuiper-belt objects. *Nature*, 392(6671):49, 1998.

Valeriy Tenishev, Michael Combi, and Björn Davidsson. A global kinetic model for cometary comae: The evolution of the coma of the Rosetta target comet Churyumov-Gerasimenko throughout the mission. *The Astrophysical Journal*, 685(1):659, 2008.

The International Astronomical Union. Minor Planet Center. `https://www.minorplanetcenter.net/iau/mpc.html`, 2018. Accessed: 2018-06-26.

Nicholas Thomas, Björn Davidsson, Mohamed Ramy El-Maarry, Sonia Fornasier, Lorenza Giacomini, AG Gracia-Berná, SF Hviid, W-H Ip, Laurent Jorda, HU Keller, et al. Redistribution of particles across the nucleus of comet 67P/Churyumov-Gerasimenko. *Astronomy & Astrophysics*, 583:A17, 2015a.

Nicolas Thomas, Holger Sierks, Cesare Barbieri, Philippe L Lamy, Rafael Rodrigo, Hans Rickman, Detlef Koschny, Horst Uwe Keller, Jessica Agarwal, Michael F A'Hearn, et al. The morphological diversity of comet 67P/Churyumov-Gerasimenko. *Science*, 347(6220):aaa0440, 2015b.

JM Trigo-Rodríguez, E García-Melendo, BJR Davidsson, A Sánchez, D Rodríguez, J Lacruz, JA De los Reyes, and Sensi Pastor. Outburst activity in comets - I. Continuous monitoring of comet 29P/Schwassmann-Wachmann 1. *Astronomy & Astrophysics*, 485(2):599–606, 2008.

Kleomeris Tsiganis, R Gomes, A Morbidelli, and HF Levison. Origin of the orbital architecture of the giant planets of the Solar System. *Nature*, 435(7041):459, 2005.

Chia-Yu Tzou. *Calibration of ROSINA-COPS and observations at comet 67P/Churyumov-Gerasimenko.* PhD thesis, Universitaet Bern, 2016.

J-B Vincent, Nilda Oklay, Maurizio Pajola, Sebastien Höfner, Holger Sierks, X Hu, Cesare Barbieri, Philippe L Lamy, R Rodrigo, Detlef Koschny, et al. Are fractured cliffs the source of cometary dust jets? insights from OSIRIS/Rosetta at 67P/Churyumov-Gerasimenko. *Astronomy & Astrophysics*, 587:A14, 2016.

Jean-Baptiste Vincent, Dennis Bodewits, Sébastien Besse, Holger Sierks, Cesare Barbieri, Philippe Lamy, Rafael Rodrigo, Detlef Koschny, Hans Rickman, Horst Uwe Keller, et al. Large heterogeneities in comet 67P as revealed by active pits from sinkhole collapse. *Nature*, 523(7558):63–66, 2015.

Kevin J Walsh, Alessandro Morbidelli, Sean N Raymond, David P O'brien, and Avi M Mandell. A low mass for mars from Jupiter's early gas-driven migration. *Nature*, 475 (7355):206, 2011.

HA Weaver, MF A'hearn, C Arpigny, DC Boice, PD Feldman, SM Larson, Ph Lamy, DH Levy, BG Marsden, KJ Meech, et al. The hubble Space Telescope (HST) observing campaign on comet Shoemaker-Levy 9. *Science*, 267(5202):1282–1288, 1995.

HA Weaver, PD Feldman, MF A'Hearn, C Arpigny, JC Brandt, and SA Stern. Post-perihelion HST observations of comet Hale–Bopp (C/1995 O1). *Icarus*, 141(1):1–12, 1999.

SJ Weidenschilling. The origin of comets in the solar nebula: A unified model. *Icarus*, 127(2):290–306, 1997.

Paul R Weissman. Are cometary nuclei primordial rubble piles? *Nature*, 320(6059):242, 1986.

Paul Wessel and David Bercovici. Interpolation with splines in tension: a Green's function approach. *Mathematical Geology*, 30(1):77–93, 1998.

Fred L Whipple. A comet model. I. The acceleration of Comet Encke. *The Astrophysical Journal*, 111:375–394, 1950.

Fred L Whipple. A Comet Model. III. The Zodiacal Light. *The Astrophysical Journal*, 121:750, 1955.

WC Wiley and Ii H McLaren. Time-of-flight mass spectrometer with improved resolution. *Review of scientific instruments*, 26(12):1150–1157, 1955.

DH Wooden, SB Charnley, and P Ehrenfreund. Composition and evolution of interstellar clouds. *Comets II*, pages 33–66, 2004.

Yunxi Yao and Konstantinos P Giapis. Dynamic molecular oxygen production in cometary comae. *Nature communications*, 8:15298, 2017.

Qingzhu Yin, SB Jacobsen, K Yamashita, J Blichert-Toft, Ph Télouk, and F Albarede. A short timescale for terrestrial planet formation from hf–W chronometry of meteorites. *Nature*, 418(6901):949, 2002.

Kevin Zahnle and Mordecai-Mark Mac Low. The collision of Jupiter and comet Shoemaker-Levy 9. *Icarus*, 108(1):1–17, 1994.

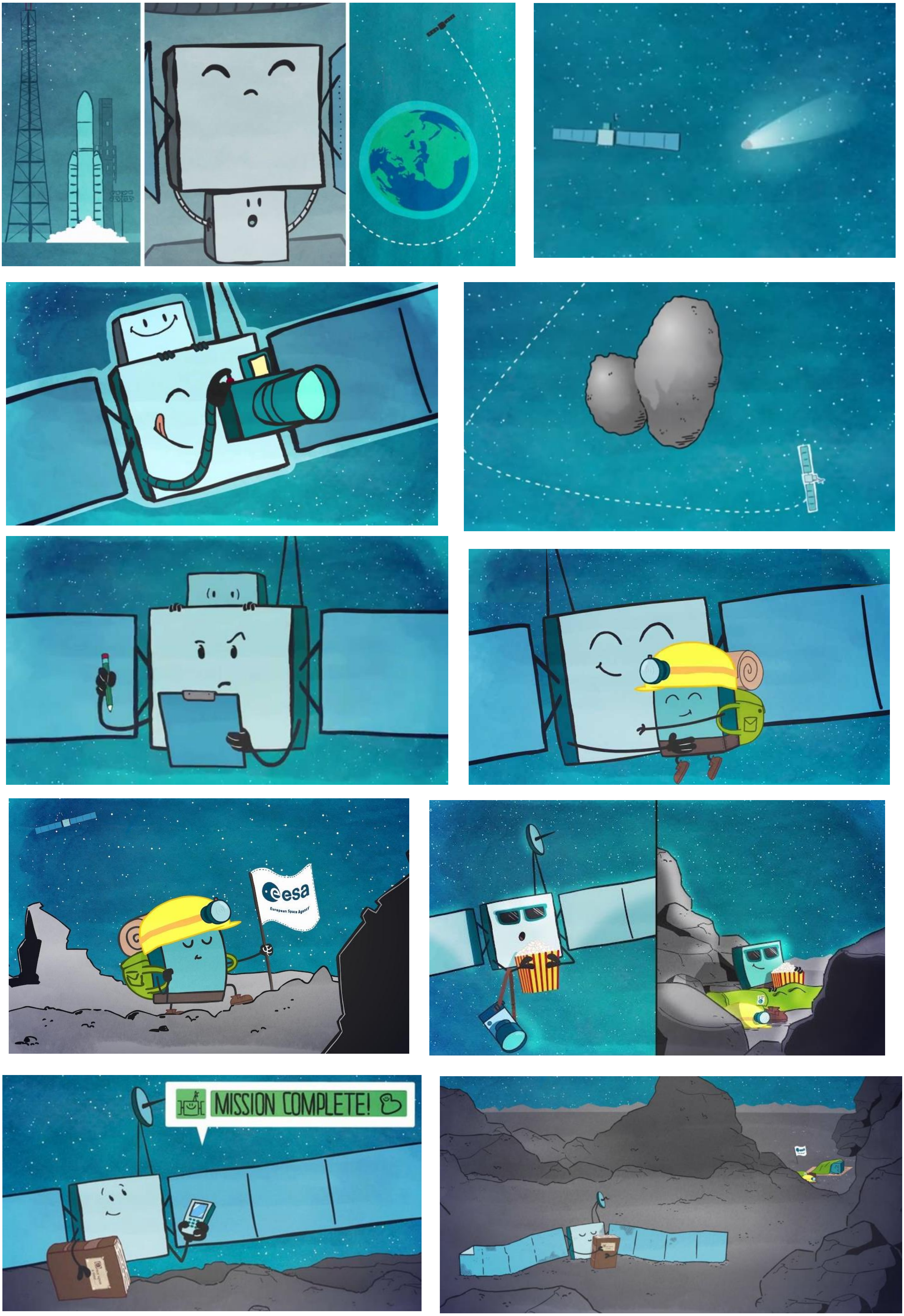
esa
European Space Agency
MISSION COMPLETE!

Page 36, Figure 3.4 *Would the reader be able to find Philae?*. Credits: OSIRIS.
Solution:

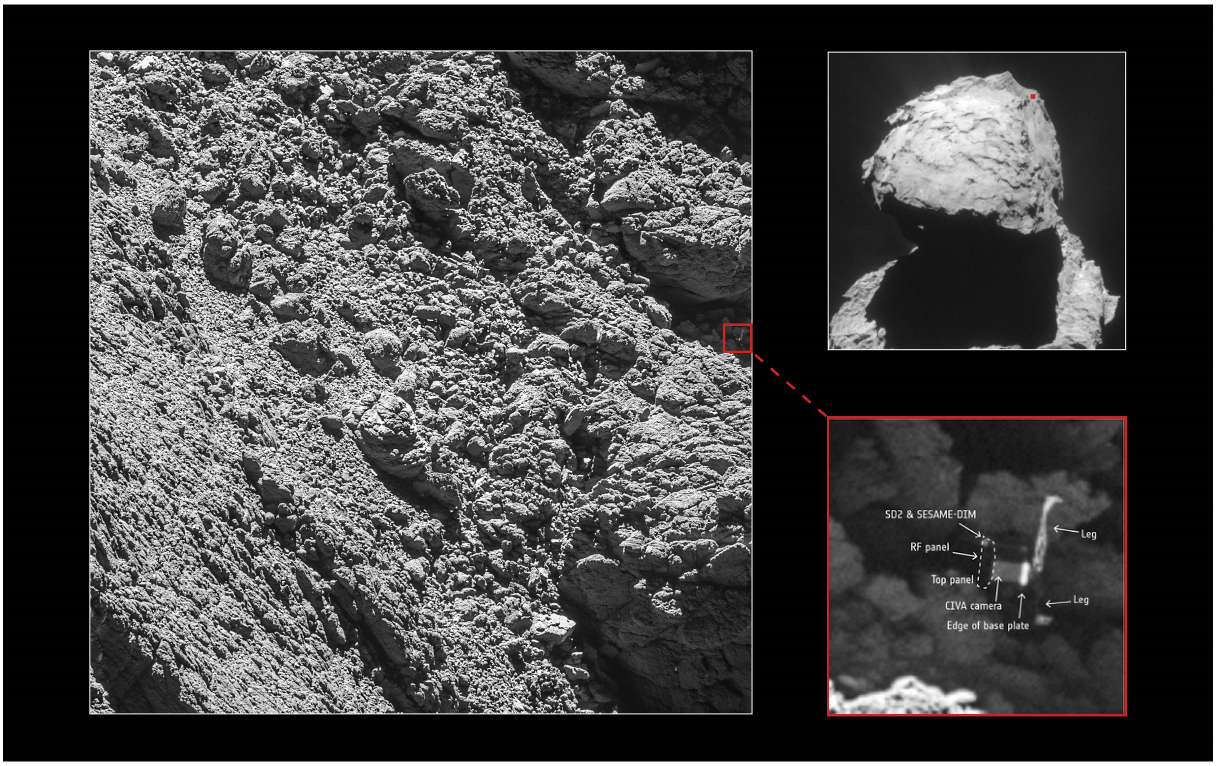

Comic of the Rosetta mission: Pictures taken from the ESA's cartoon *Once upon a time*, telling the adventures of Rosetta and Philae. Available at https://www.esa.int/.

Author: Margaux Hoang

Title: Study of the environment of comet 67P/Churyumov-Gerasimenko based on the data of ROSINA/RTOF onboard the Rosetta mission.

Supervisors: Philippe Garnier and Jérémie Lasue

Place and date of defense: Toulouse, 12th October 2018.

Abstract: The comet 67P/Churyumov-Gerasimenko (67P/C-G) has been investigated by the Rosetta space mission over two years from August 2014 to September 2016. Onboard the spacecraft, the ROSINA experiment included two mass spectrometers (DFMS and RTOF) to detect the composition of neutrals and ions, and a pressure sensor (COPS) to monitor the density and velocity of neutrals in the coma. This thesis details an analysis and discussion of the data of the RTOF instrument during the comet escort phase. We analyse 67P/C-G's coma over the mission in terms of the main volatiles concentrations (H_2O, CO_2 and CO) and their ratios. The 2-years-long Rosetta mission allows us to observe the diurnal and seasonal variabilities in the atmosphere of 67P/C-G and strong heterogeneities. This analysis shows that the illumination conditions do not explain all the coma observations, revealing the presence of surface or sub-surface heterogoeneities. Therefore, we use a thermo-physical nucleus model applied to the case of 67P/C-G to investigate the physical processes occurring inside the nucleus and leading to complex coma observations.

Keywords: Rosetta - comet - coma - 67P/Churyumov-Gerasimenko - volatiles - mass spectrometer

Discipline: Astrophysics

Research Unity: Research Institute in Astrophysics and Planetology (UMR 5277). 9, avenue du Colonel Roche - 31028 Toulouse

Auteur: Margaux Hoang

Titre: Etude de la coma de la comète 67P/Churyumov-Gerasimenko à l'aide des données de l'instrument ROSINA/RTOF à bord de la mission spatiale Rosetta.

Directeurs de thèse: Philippe Garnier et Jérémie Lasue

Lieu et date de soutenance: Toulouse, le 12 octobre 2018.

Résumé: La mission spatiale Rosetta a étudié la comète 67P/Churyumov-Gerasimenko (67P/C-G) pendant deux ans, d'août 2014 à septembre 2016. À bord de la sonde, l'expérience ROSINA était composée de deux spectromètres de masse (DFMS et RTOF) pour étudier la composition des neutres et des ions présents dans la coma, et d'un senseur de pression (COPS) pour mesurer la densité et la vitesse du gaz cométaire. Le travail présenté a pour objectif l'étude de la coma de la comète 67P/C-G grâce à l'analyse et l'interprètation des données de l'instrument RTOF, en particulier des mesures des principaux volatiles (H_2O, CO_2 et CO) et de leurs abondances relatives. Les mesures récoltées pendant les deux années de mission nous permettent d'étudier les variations diurnes et saisonnières de la coma de 67P/C-G et de mettre en évidence des hétérogénéités spatiales. Cette analyse révèle que les conditions d'illumination n'expliquent pas en totalité les observations et suggère la présence d'hétérogénéités de surface ou sous-surface. Nous appliquons un modèle thermo-physique de noyau cométaire au cas de 67P/C-G pour étudier les processus physiques à l'intérieur du noyau responsable de la complexité des observations de la coma.

Mots-clés : Rosetta - comète - coma - 67P/Churyumov-Gerasimenko - volatiles - spectrométrie de masse

Discipline: Astrophysique, Science de l'univers et Astrophysique

Laboratoire: Institut de Recherche en Astrophysique et Planétologie (UMR 5277). 9, avenue du Colonel Roche - 31028 Toulouse